Inclusive and differential measurements of spin correlation in top-antitop quark pairs at $\sqrt{s} = 8$ TeV using the ATLAS detector

Mark Levy

A thesis submitted to the University of Birmingham
for the degree of Doctor of Philosophy

Particle Physics Group,
School of Physics and Astronomy,
University of Birmingham

July 2016

UNIVERSITY OF BIRMINGHAM

University of Birmingham Research Archive

e-theses repository

This unpublished thesis/dissertation is copyright of the author and/or third parties. The intellectual property rights of the author or third parties in respect of this work are as defined by The Copyright Designs and Patents Act 1988 or as modified by any successor legislation.

Any use made of information contained in this thesis/dissertation must be in accordance with that legislation and must be properly acknowledged. Further distribution or reproduction in any format is prohibited without the permission of the copyright holder.

Abstract

A measurement of the spin correlation strength in $t\bar{t}$ pairs is presented, using proton-proton collision data collected at the ATLAS detector with a centre of mass energy of $\sqrt{s} = 8$ TeV and an integrated luminosity of 20.3 fb^{-1}. An inclusive measurement is made, as well as a differential measurement as a function of the $t\bar{t}$ invariant mass. Additionally, these measurements are made both at detector level and unfolded to a parton level distribution. Selected events are required to have exactly two oppositely charged leptons (either electrons or muons), a large missing transverse energy and at least two hadronic jets, at least one of which must be tagged as originating from a b-quark. The azimuthal separation between the two charged leptons, $\Delta\phi$, is used to measure the degree of spin correlation. The measured distribution is compared to a Standard Model prediction and a model with no spin correlation. It is found that the results all favour the Standard Model prediction over the uncorrelated model, with the data found to be several standard deviations away from the uncorrelated scenario.

DECLARATION OF AUTHOR'S CONTRIBUTION

The operation of the Large Hadron Collider and the ATLAS experiment is only possible due to a great amount of work from thousands of physicists. The studies presented in this thesis would not be possible without this dedicated effort. Over the course of my postgraduate studies, I have contributed to the operation and development of the ATLAS detector through several data-taking shifts in the ATLAS control room and talks in conferences presenting the work of the ATLAS Top Physics working group. I also conducted studies aiming to improve the performance of the Level-1 Calorimeter Trigger (this work is presented in chapter 4 and is entirely my own work). These studies were also only possible through collaborative effort with the L1Calo working group who provided feedback and suggestions during discussions.

The measuremements presented in this thesis are the result of my own work, unless explicitly stated. I was not involved in the design or construction of the ATLAS detector, and the discussion of the structure of the detector presented in chapter 3 is provided as a necessary backdrop to the rest of the thesis.

The work presented in chapters 6 and 7 is entirely my own work. The methodologies and reconstruction techniques used are based on earlier work and recommended practices from the ATLAS Top Physics working group, and various studies conducted to determine appropriate reconstruction techniques.

ACKNOWLEDGEMENTS

I would like to extend my thanks to a number of people whose support has made this thesis possible. Firstly I would like to thank my supervisors, Miriam Watson and Christopher Hawkes. Their knowledge and support in both matters of physics and general postgraduate life has been invaluable, and I cannot overstate how much I value their contribution. Also, I must mention Simon Head, who guided me in the ways of top physics analyses and the art of making an informative and engaging presentation. Thank you for your help, and I'm heartened to know that life beyond physics can be equally as fulfilling. Thank you as well to Paul Newman and all the academic staff at Birmingham. It's been a wonderful place to study with such a friendly atmosphere and excellent knowledge of cricket.

I am extremely grateful to the Science and Technologies Funding Council (STFC) for providing me with financial support during the course of my studies. Also, thank you to the University and School of Physics and Astronomy for affording me the opportunity to do a small amount of teaching, which has been beneficial for both my development and my wallet!

Thanks as well go to the past and present occupants of W316: Tom McLaughlan, Hardeep Bansil, Benedict Allbrooke, Andy Chisholm, Richard Mudd, Andrew Daniells, Javier Murillo, Rhys Owen, Matt Baca, Andy Foster, Alasdair Winter, "Ha-mes" Broughton, Elliot Reynolds, James Kendrick and Daniel Briglin. The stimulating conversation, games of folder badminton, and friendships made will stay

with me long after my name has passed into the annals of UoB history. Special mentions go to Pete Griffith, Luca Pescatore, Didier Alexandre and Lewis Armitage, with whom I shared various adventures across Italy, Switzerland and the UK. My final mention here goes to those who survived living with me during this time: Pete and Rhys (again), Vicky, and Ally (who will have to put up with me soon!). Thank you so much, I know it can't have been easy and I hope I was sane enough sometimes to make it enjoyable!

One of the higlights of my Ph.D. experience, and indeed my life, has been the 15 months in which I lived in Geneva. Prior to my time here, I had never so much as left the UK so such an experience was an informative and an inimitable one. This, in addition to my trip to Chicago for the Fermilab summer school have opened my eyes a little wider to the world. Thank you to everyone who helped make these adventures so exciting.

A quick mention as well to the Birmingham Ballroom and Latin Dance team, particularly my long suffering partners Charlie and Alessandra. Dancing has kept me fit and has always been an enjoyable way to spend my evenings.

Finally, I would like to thank my family, particularly my mother, Valerie, and my brother, Ian. Their support, both financial and emotional, has kept me going and I hope that I have made you proud and lived up to the wonderful example you have set for me. Also, thank you to my late father and grandparents. You will always be in my thoughts.

"Look at me still talking when there's science to do."

GLaDOS, Portal, Valve Corporation, 2007

For Dad. The man who gave me the gift of science.

Contents

List of Figures **ix**

List of Tables **xii**

1 Introduction **1**

2 The Standard Model of Particle Physics and the Top Quark **4**

2.1 Standard Model of Particle Physics 4

2.2 The Top Quark 12

2.3 Top Quark Pair Production 15

2.4 Top Quark Decays 17

2.5 Single Top Production 19

2.6 Importance of Top Quark Studies 20

3 The ATLAS Detector and the Large Hadron Collider **23**

3.1 The LHC Experiments 23

3.2 Proton Acceleration and Collisions 25

3.3 The ATLAS Experiment 27

3.4 ATLAS Geometry 28

3.5 ATLAS Subcomponents 30

3.6 The ATLAS Trigger System 38

4 The Level-1 Calorimeter Trigger and Reduction in Trigger Rate Acceptance **41**

4.1 The Level-1 Calorimeter Trigger 41
4.2 EM Sliding Window Algorithm 44
4.3 Reducing Trigger Rate Acceptance 45
4.4 Rates and Efficiency Measurements 47
4.5 Conclusions of EM Isolation Study 56

5 Spin Correlation in Top Quark Pairs 58

5.1 Spin Correlation 59
5.2 Spin Correlation as a Function of the $t\bar{t}$ System Invariant Mass 68
5.3 Previous Measurements 70
5.4 Analysis Strategy 80

6 Event Selection and Analysis Techniques 82

6.1 Monte Carlo Simulation 82
6.2 Object Selection 88
6.3 Event Selection 94
6.4 Data Driven Background Estimations 98
6.5 M_{T2} for $t\bar{t}$ Reconstruction 106
6.6 Unfolding: Uses and Challenges 112
6.7 Control Plots and Yields 126

7 Analysis Results 136

7.1 Extracting Spin Correlation 136
7.2 Systematic Uncertainties 139
7.3 Procedure to Assess Systematic Uncertainties in Unfolded Distributions 156
7.4 Detector Level Measurement Results 161
7.5 Unfolded Measurement Results 171
7.6 Discussion of Results 174

8 Concluding Remarks 181

References **184**

A Systematic Errors for Unfolded Measurements **195**

B MC Samples Used in Analysis **206**

B.1 MC Samples Used for Analysis 206

B.2 MC Samples Used in Systematic Uncertainty Assessment 210

List of Figures

2.1 Top-antitop quark pair production 15

2.2 PDF distribution examples 16

2.3 Example top-antitop quark decay 19

2.4 Single top production mechanisms 21

3.1 The LHC ring and interaction points 24

3.2 LHC Injection Mechanism 25

3.3 ATLAS Schematic 28

3.4 Inner Detector Schematic 30

3.5 The ATLAS Calorimeter System 33

3.6 EM Calorimeter Accordion Geometry 36

3.7 Muon Spectrometers 37

3.8 ATLAS Magnet Systems 38

3.9 ATLAS Trigger Schematic 40

4.1 Trigger Tower Granularities 42

4.2 Level-1 Calorimeter Architecture 43

4.3 Level-1 Calorimeter Sliding Window Diagram 45

4.4 Rate Reduction using EM Isolation 48

4.5 Efficiency of EM Isolation Triggers 51

4.6 Rates vs. Integrated Efficiencies of Isolation Triggers 53

4.7 Pile-up dependence of Isolation Triggers 55

5.1 Predicted spin correlation asymmetry values for different quantisation bases 65
5.2 Parton level distribution of $\Delta\phi$ distribution at $\sqrt{s} = 8$ TeV 67
5.3 Differential $t\bar{t}$ production cross sections as a function of $M_{t\bar{t}}$ 69
5.4 Parton level distribution of $\Delta\phi$ distribution at $\sqrt{s} = 8$ TeV for different $M_{t\bar{t}}$ ranges. 71
5.5 Summary of $\sqrt{s} = 7$ TeV spin correlation results at an integrated luminosity of 4.6 fb^{-1} 74
5.6 Data distribution of spin correlation observables at $\sqrt{s} = 7$ TeV . . . 75
5.7 $\Delta\phi$ distribution from previous 8 TeV spin correlation ATLAS analysis in combined dilepton channel 77
5.8 Unfolded measurements from CMS at 8 TeV. 79

6.1 Dilepton invariant mass distributions in the Z mass window for events with 1 b-tagged jet, before data driven normalisation. 102
6.2 Dilepton invariant mass distributions in the Z mass window for events with ≥ 2 b-tagged jets, before data driven normalisation. 103
6.3 Dilepton invariant mass distributions in the Z mass window for events with 1 b-tagged jet, after data driven normalisation. 104
6.4 Dilepton invariant mass distributions in the Z mass window for events with ≥ 2 b-tagged jets, after data driven normalisation. 105
6.5 Fractional difference between true and reconstructed $M_{t\bar{t}}$ values. . . . 113
6.6 Data/simulation comparisons of reconstructed $M_{t\bar{t}}$. 114
6.7 Response matrices for the combined dilepton channel calculated using simulated data. 119
6.8 Closure testing of unfolding method for inclusive measurements in the eμ and combined dilepton channels. 123
6.9 Closure testing of unfolding method for differential measurements in the eμ channel. 124

6.10 Closure testing of unfolding method for differential measurements in the combined dilepton channel. 125
6.11 Control plots for e^+e^- channel. 127
6.12 Control plots for $\mu^+\mu^-$ channel. 128
6.13 Control plots for $e^\pm\mu^\mp$ channel. 129
6.14 Control plots for charged leptons in the e^+e^- channel. 130
6.15 Control plots for charged leptons in the $\mu^+\mu^-$ channel. 131
6.16 Control plots for charged leptons in the $e^\pm\mu^\mp$ channel. 132
6.17 Control plots for jets in all channels. 133

7.1 Linearity test of the f_{SM} fitting procedure in the eμ channel. 138
7.2 Linearity test of the $f_{t\bar{t}}$ fitting procedure in the eμ channel. 138
7.3 Envelope plots used to calculate PDF systematic uncertainty for the inclusive detector level measurement. 149
7.4 Plots illustrating procedure for assessing f_{SM} uncertainty resulting for varying top masses. 151
7.5 Normalised p_T distributions for dilepton system in the Z boson mass window, used for assessing systematic uncertainty relating to Z/γ^* + *jets* background shape. 154
7.6 Data/Monte Carlo comparisons of inclusive $\Delta\phi$ distributions at detector level. 163
7.7 Data/Monte Carlo comparisons of $\Delta\phi$ distributions at detector level in the mass range $M_{t\bar{t}} \leq 415$ GeV. 164
7.8 Data/Monte Carlo comparisons of $\Delta\phi$ distributions at detector level in the mass range 415 GeV$< M_{t\bar{t}} \leq 505$ GeV. 165
7.9 Data/Monte Carlo comparisons of $\Delta\phi$ distributions at detector level in the mass range $M_{t\bar{t}} > 505$ GeV. 166
7.10 Data/Monte Carlo comparisons of inclusive $\Delta\phi$ distributions at detector level, illustrating the f_{SM} fit. 167

7.11 Data/Monte Carlo comparisons of $\Delta\phi$ distributions at detector level in the mass range $M_{t\bar{t}} \leq 415$ GeV, illustrating the f_{SM} fit. 168
7.12 Data/Monte Carlo comparisons of $\Delta\phi$ distributions at detector level in the mass range 415 GeV$< M_{t\bar{t}} \leq 505$ GeV, illustrating the f_{SM} fit. 169
7.13 Data/Monte Carlo comparisons of $\Delta\phi$ distributions at detector level in the mass range $M_{t\bar{t}} > 505$ GeV, illustrating the f_{SM} fit. 170
7.14 Unfolded $\Delta\phi$ distributions in the eμ channel for inclusive and differential mass range measurements. 172
7.15 Unfolded $\Delta\phi$ distributions in the combined dilepton channel for inclusive and differential mass range measurements. 173
7.16 Summary of f_{SM} results for inclusive measurement. 177
7.17 Summary of f_{SM} results for measurement in range $M_{t\bar{t}} \leq 415$ GeV. . 178
7.18 Summary of f_{SM} results for measurement in range 415 GeV$< M_{t\bar{t}} \leq$ 505 GeV. 179
7.19 Summary of f_{SM} results for measurement in range $M_{t\bar{t}} > 505$ GeV. . 180

List of Tables

2.1 Summary of quark properties in the SM. 6

2.2 Summary of lepton properties in the SM. 7

2.3 Summary of force and mediating gauge boson properties in the SM. . 8

5.1 Spin analysing powers for top quark decay products. 60

5.2 Results from previous ATLAS 8 TeV spin correlation analysis 76

6.1 The yields and calculated scale factors for the various channels and control regions described, for events with exactly one b-tagged jet. . . 101

6.2 The yields and calculated scale factors for the various channels and control regions described, for events with at least 2 b-tagged jets. . . 101

6.3 Testing of the M_{T2} combinatoric assignment methodology 110

6.4 Data and Monte Carlo yields for signal and background contributions for the inclusive measurement. 134

6.5 Data and Monte Carlo yields for signal and background contributions for the differential measurement in mass range $M_{t\bar{t}} \leq 415$ GeV. 134

6.6 Data and Monte Carlo yields for signal and background contributions for the differential measurement in mass range 415 GeV$\leq$ $M_{t\bar{t}}$ $\leq$ 505 GeV. 135

6.7 Data and Monte Carlo yields for signal and background contributions for the differential measurement in mass range $M_{t\bar{t}} > 505$ GeV. 135

7.1 The alternative PDF sets used for assessing the PDF systematic uncertainties and the total number of variations for each set. 146
7.2 Calculated values for each parameter in the fit function used for the Z p_T reweighting. The fit function is of the form $w = mZ_{p_T} + c$ . . . 153
7.3 Summary of the systematic uncertainties for the detector level measurements in all channels. 158
7.4 Summary of f_{SM} measurements and associated uncertainties for the detector level measurement. 162
7.5 Calculated χ^2 values for each unfolded distribution in the eμ channel. 176
7.6 Calculated χ^2 values for each unfolded distribution in the combined dilepton channel. 176

A.1 The unfolded results and uncertainties for each bin of the inclusive unfolded measurement in the eμ channel for bins 1-10 196
A.2 The unfolded results and uncertainties for each bin of the inclusive unfolded measurement in the eμ channel for bins 11-20 197
A.3 The unfolded results and uncertainties for each bin of the inclusive unfolded measurement in the combined dileptonic channel in bins 1-10 198
A.4 The unfolded results and uncertainties for each bin of the inclusive unfolded measurement in the combined dileptonic channel in bins 11-20 199
A.5 The unfolded results and uncertainties for each bin of the inclusive unfolded measurement where $M_{t\bar{t}} \leq 415$ GeV in the eμ channel 200
A.6 The unfolded results and uncertainties for each bin of the differential unfolded measurement where 415 GeV$< M_{t\bar{t}} \leq 505$ GeV in the eμ channel. 201
A.7 The unfolded results and uncertainties for each bin of the differential unfolded measurement where $M_{t\bar{t}} > 505$ GeV in the eμ channel 202

A.8 The unfolded results and uncertainties for each bin of the differential unfolded measurement where $M_{t\bar{t}} \leq 415$ GeV in the combined dilepton channel 203
A.9 The unfolded results and uncertainties for each bin of the differential unfolded measurement where 415 GeV$< M_{t\bar{t}} \leq 505$ GeV in the combined dilepton channel 204
A.10 The unfolded results and uncertainties for each bin of the differential unfolded measurement where $M_{t\bar{t}} > 505$ GeV in the combined dilepton channel 205

B.1 Top quark signal MC simulation samples 206
B.2 Diboson MC simulation samples 207
B.3 Z/γ^* + jets MC simulation samples where $10 < M_{ll} \leq 40$ GeV 207
B.4 Z/γ^* + jets MC simulation samples $40 < M_{ll} \leq 60$ GeV 208
B.5 Z/γ^* + jets MC simulation samples $60 < M_{ll} \leq 2000$ GeV 208
B.6 Z/γ^* + jets + heavy flavour MC simulation samples $60 < M_{ll} \leq 1000$ GeV 209
B.7 Top quark signal alternative MC simulation samples 210
B.8 Top quark MC simulation signal with altered ISR/FSR 210
B.9 Top quark MC simulation signal with altered colour reconnection strength and underlying event 210
B.10 Top quark MC simulation signal with altered top mass values 211
B.11 Alternativee Wt-channel single top MC simulation sample using diagram subtraction scheme 211

Chapter 1

INTRODUCTION

The top quark is the heaviest known fundamental particle in nature. Its existence was first postulated in the 1970s as an addition to the existing theories of particle physics, as part of a third generation of quarks (with the bottom quark). The actual discovery of the top quark was made in 1995 at the Fermilab Tevatron, and subsequent studies at the Tevatron and at the Large Hadron Collider (LHC) have probed the properties and decays of the top. The top quark has a measured mass of $m_t = 173.21 \pm 0.51 \pm 0.71$ GeV and a predicted mean lifetime of $\approx 5 \times 10^{-25}$ s [1]. The lifetime of the top is small to such a degree that it decays before it can undergo strong interactions and therefore cannot be bound into hadrons. This offers a unique opportunity to study properties of the bare quark which would otherwise be lost. One of these properties is the degree of correlation between the spins of the top (t) and antitop ($\bar{t}$), where they are produced together in a $t\bar{t}$ system.

The LHC is the largest particle accelerator that has been constructed to date, and is situated at CERN close to Geneva, Switzerland. The LHC experiments began taking data in 2010. Since this date, the centre of mass (c.m.) energy produced by proton-proton collisions has increased and before the first long shutdown in 2013, it had achieved a c.m. energy of $\sqrt{s} = 8$ TeV. Following the long shutdown, the LHC was successfully restarted and began taking data at $\sqrt{s} = 13$ TeV in the latter half of 2015. The proton-proton collisions at such high energies allow for a large number

of $t\bar{t}$ pairs to be produced, both at 8 TeV and 13 TeV.

There are 4 main experiments which utilise the events generated by the LHC. Two of these are general purpose detectors (ATLAS and CMS) which are appropriate places to study top properties. This thesis will concentrate on the full dataset yielded from the $\sqrt{s} = 8$ TeV run by the ATLAS detector.

The spin correlation in top-antitop pairs is a property predicted to high precision by the Standard Model and a study of this will act as a test of the Standard Model. The degree of spin correlation has been measured several times at ATLAS and CMS and so far has been found to be in good agreement with prediction. This analysis will aim to further these measurements by producing an "unfolded" distribution which tests the accuracy of the prediction after removing detector-generated biases. In addition, theory also predicts that the degree of spin correlation varies as a function of the invariant mass of the $t\bar{t}$ system ($M_{t\bar{t}}$). This thesis will present a differential analysis of the spin correlation in different $M_{t\bar{t}}$ ranges, which tests this prediction.

The structure of this thesis is as follows. Chapter 2 presents a brief outline of some of the general theory involved in the Standard Model, with greater focus on the aspects which relate to the top quark. Chapter 3 discusses the structure and function of the LHC as well as the ATLAS detector. Chapter 4 presents the author's study of methods with which to reduce the rate of acceptance of events within the first level of the elecromagnetic calorimeter trigger (L1Calo) at the ATLAS detector. Chapter 5 discusses the more detailed theory regarding spin correlation in top-antitop quark pairs. Chapter 6 is an explanation of the Monte Carlo methods used to estimate the signal and background contributions for the observables to be investigated, as well as a rationale for the decisions made on how to select objects. It also describes the unfolding techniques to be used within the analysis as well as the method of

reconstruction of top quarks in a system where there are unconstrained variables. Chapter 7 presents the bulk of the analysis, including results and assessment of systematic uncertainties on measurements. Chapter 8 summarises the final results and conclusions of this thesis.

Chapter 2

THE STANDARD MODEL OF PARTICLE PHYSICS AND THE TOP QUARK

This chapter introduces some of the basic concepts of particle physics as well as giving a brief introduction to the top quark, its prediction and discovery, and why a study of its properties is of importance to the field. Natural units are used throughout this thesis.

2.1 Standard Model of Particle Physics

The *Standard Model of Particle Physics* (SM) is the basic framework which encapsulates the most up to date understanding of interactions at the subnuclear level. The Standard Model is used as the basis for many predictions of how particle interactions should behave and has been proven to be a robust theory, with many of these predictions verified to be correct.

In broad terms, the SM classifies all known fundamental matter particles into two categories: *quarks* and *leptons*, with the interactions between matter being mediated by virtual particles known as *gauge bosons*. It is these fundamental particles which comprise all known matter in the universe. In the SM, there are six quarks and six leptons predicted (with each quark and lepton type being known as its *flavour*),

and in each case they are subdivided into three sets of pairs known as *generations*. Both quarks and leptons are classified as *fermions* which are particles which have a $\frac{1}{2}$ integer *spin*.

Mathematically, the Standard Model is a product of three groups $\mathrm{SU}(3)_C \times \mathrm{SU}(2)_L \times \mathrm{U}(1)_Y$, with $\mathrm{SU}(3)_C$ describing *Quantum Chromodynamics*, and $\mathrm{SU}(2)_L \times \mathrm{U}(1)_Y$ describing the *electroweak* sector (where electroweak can be further broken down into the *weak nuclear force* and *Quantum Electrodynamics*). The fundamental forces which govern particle interactons in the SM are discussed further in section 2.1.3.

2.1.1 Quarks

The six known quarks are tabulated with their properties in table 2.1, organised into three generations, with each subsequent generation being of greater mass than the corresponding particle in the previous generation. Quarks can have one of two charges, either $+\frac{2}{3}e$ for "up-type" quarks or $-\frac{1}{3}e$ for "down-type" quarks, where e denotes the absolute value of the charge of an electron. The mass of quarks ranges from $\approx$ 2 MeV (the up quark) to $\approx$ 173 GeV (the top quark). Additionally, as previously mentioned, quarks are fermions and therefore all are spin-$\frac{1}{2}$.

The table shows the case for standard quarks, but for each quark listed, a corresponding *antiquark* exists, which possesses the same spin, mass and absolute value of charge as the quark, but the sign of the charge is opposite (i.e. an antiup quark has a charge of $-\frac{2}{3}e$).

All known matter is composed of quarks and leptons. Quarks in particular are able to form composite particles through interactions with the strong nuclear force, mediated by eight types of gluons (see section 2.1.3). These composite particles

Table 2.1: Properties of the six known matter quarks within the Standard Model. For the charges, e represents the absolute value of the charge of the electron. All data are taken from the Particle Data Group [1]. Antimatter quarks possess the same properties but with an opposite sign charge, and are represented in notation with a bar above the corresponding letter .

Generation I	Generation II	Generation III
up (u) $m_u = 2.3^{+0.7}_{-0.5}$ MeV Q $= +\frac{2}{3}e$	charm (c) $m_c = 1.275 \pm 0.025$ GeV Q $= +\frac{2}{3}e$	top (t) $m_t = 173.21 \pm 0.51 \pm 0.71$ GeV Q $= +\frac{2}{3}e$
down (d) $m_d = 4.8^{+0.5}_{-0.3}$ MeV Q $= -\frac{1}{3}e$	strange (s) $m_s = 95 \pm 5$ MeV Q $= -\frac{1}{3}e$	bottom (b) $m_b = 4.18 \pm 0.03$ GeV Q $= -\frac{1}{3}e$

are known as *hadrons* and can be further subdivided into two types: *baryons* and *mesons*. Baryons are composed of either three quarks or three antiquarks. The most common baryons are protons (two up quarks and one down quark) and neutrons (two down quarks and one up quark), of which the majority of known matter is formed. The reason that these are common is that both protons and neutrons are stable inside nuclei and are therefore able to exist for long periods of time. Mesons are composed of one quark and one antiquark and there are no known stable states which occur naturally. Due to the composition of these two types, a fundamental difference is introduced in that baryons are still half-integer spin fermions whereas mesons are whole-integer spin bosons. This allows mesons to act as force-mediating particles in some interactions.

In addition to a standard electrical charge, quarks have an additional quantum number component called colour charge and this is important in the formation of hadrons. There are three types of colour charge which are known as red (R), blue (B) and green (G). In order for hadrons to form, the hadron must be *colour-neutral*

and it is this requirement which leads to the fact that hadrons can consist of either three particles (antiparticles) or one particle and one antiparticle. For baryons, there must be one particle (antiparticle) of each colour charge (or anticolour) which creates a colour-neutral state and for mesons, the particle and antiparticle must have corresponding colour and anticolour. Gluons also possess colour charge and it is due to this that there are eight gluon types (the "colour-octet" model of gluons).

2.1.2 Leptons

The six known leptons are tabulated with their properties in table 2.2, and as with the quarks are organised into three generations. Again, each lepton mentioned has a corresponding antiparticle which has the opposite charge sign to its matter partner.

Table 2.2: Table presenting properties of the six known leptons within the Standard Model. For the charges, e represents the absolute value of the charge of the electron. All data are taken from the Particle Data Group [1].

Generation I	Generation II	Generation III
electron $m_e = 0.51100 \pm 1.1 \times 10^{-8}$ MeV Q $= -1e$	muon $m_\mu = 105.66 \pm 3.5 \times 10^{-6}$ MeV Q $= -1e$	tau $m_\tau = 1776.9 \pm 0.12$ MeV Q $= -1e$
electron neutrino $m_{\nu_e} < 2 \times 10^{-6}$ MeV Q $= 0$	muon neutrino $m_{\nu_\mu} < 2 \times 10^{-6}$ MeV Q $= 0$	tau neutrino $m_{\nu_\tau} < 2 \times 10^{-6}$ MeV Q $= 0$

As can be seen in table 2.2, the charge of leptons can be either $-1e$ or zero. This leads to the distinction between types of lepton: charged and neutral. The neutral leptons are known as *neutrinos*. Neutrinos are very hard to detect due to their lack of electric or colour charges, and the fact that they are almost massless. There are

a number of experiments that have been devised to directly detect neutrinos (such as IceCube [2] and Super-Kamiokande [3]). However, in the context of the ATLAS experiment they pose an experimental problem as there is no viable method of direct detection. When information is required about neutrinos, other experimental techniques are employed in order to ascertain the information needed and this is discussed in chapter 6.

2.1.3 Fundamental Forces and Mediating Particles

The Standard Model mathematically describes three fundamental forces which are the strong nuclear force, the electromagnetic force and the weak nuclear force. It currently does not incorporate a mechanism for describing gravity. A brief description of these forces follows. A summary of the force mediating gauge bosons is presented in table 2.3.

Table 2.3: Table presenting the four fundamental forces and the bosons which mediate their interactions. In the case of the graviton, its existence and properties are theorised only. For the charges, e represents the absolute value of the charge of the electron. All data are taken from the Particle Data Group [1].

Force	Mediating Boson	Mass	Charge	Spin	Range
Electromagnetic	photon (γ)	massless	0	1	Infinite
Weak	Z^0 $W^{\pm}$	91.188 ± 0.0021 GeV 80.385 ± 0.015 GeV	0 $\pm 1e$	1 1	$< 10^{-15}$m $< 10^{-15}$m
Strong	gluon (g)	massless	0	1	$< 10^{-17}$m
Gravity	graviton (G)	0	0	2	Infinite

2.1.3.1 The Electromagnetic Force

The electromagnetic (EM) force is mediated by massless virtual photons and acts on charged particles. As well as being a phenomenon seen at the subatomic level, the

EM force is felt at distances greater than the atomic nucleus and is seen in aspects of classical physics, which makes it perhaps the best known of the fundamental forces. Interactions occurring through the EM force are governed by Quantum Electrodynamics (QED).

Whilst not being directly responsible for any of the decay processes that are involved at the tree level for this analysis, the EM force is seen in the cascading process used to identify electrons and photons in the electromagnetic calorimeter. The electromagnetic calorimeter is discussed in chapter 3.

2.1.3.2 The Strong Force and Quantum Chromodynamics

The strong interaction is mediated by gluons, and as the name suggests, is the strongest of the fundamental forces over its interaction range. It is responsible for binding quarks and gluons into hadrons. The interactions which occur through the strong force are governed by *Quantum Chromodynamics* (QCD). QCD is seen as being analogous to QED, however there are some key differences. One of these is that in QED, the force mediator (the photon) does not possess any intrinsic charge, whereas the gluon possesses colour charge. Additionally, within QED there is one type of charge, but in QCD, the analogous colour charge has three distinct types (R,G,B).

The notion of colour charge was first proposed by Oscar Greenberg soon after the first predictions of the existence of quarks in 1964 [4] [5]. The addition of colour charge became necessary as a response to quarks bound in hadrons apparently violating the *Pauli Exclusion Principle* (PEP) [6]. The PEP states that no two identical fermions can occupy the same quantum state simultaneously. In the case of hadrons such as Δ^{++} baryons (uuu) which are composed of three quarks of the same flavour, this

situation would occur. In order to explain how a three quark constitutent hadron could exist, a new property was created, which could be used to define three distinct states. This prevents violation of the PEP.

Gluons themselves are massless and this should mean the strong force would have an infinite range. The reason that it is not is that the gluons carry colour charge, and can self interact. This leads to a process called *confinement*. When two quarks separate, they experience an attractive force caused by the behaviour of the gluon field generated between them. As the distance between the quarks increases, the stored energy in the system also increases. If this is compared to the attractive force felt in an electric or gravitational field, it can be seen that the behaviour of the strong force is different as in these other cases, the attractive force gets weaker with greater distance (following an inverse square relationship). At the point where the energy supplied to the quark-gluon system is great enough to break free of the confinement effect, it is energetically favourable to produce new particles from the vacuum, and new pairs of confined particles are produced.

The strong force is particularly important in the context of this analysis as top quarks are mostly produced at the LHC by gluon-gluon interactions, which are mediated by the strong force.

2.1.3.3 The Weak Force

The weak interaction is mediated by three massive bosons, $W^{\pm}$ and Z^0, and acts on all matter particles. The interaction was first proposed by Enrico Fermi in 1934 as an explanation for radioactive beta decay [7] [8]. The initial postulate was for a contact force with no range, when in fact it does act at range, but it is very small. The existence of the $W^{\pm}$ and Z^0 bosons was experimentally confirmed in 1983 [9] [10].

One key feature of the weak interaction is that it allows for flavour changing interactions through exchange of $W^{\pm}$ bosons, which carry charge. It is also theorised that it is possible to have a flavour changing interaction which occurs via the exchange of Z^0 bosons and this is known as a *Flavour Changing Neutral Current* (FCNC). This is expected to have a very small impact within the Standard Model and is forbidden at leading order (LO), where LO refers to only tree level decays. Expected contributions only come from interactions of next-to-leading order (NLO) or higher and are incorporated into the SM through quantum loops, box diagrams or "penguin" diagrams. FCNC processes have been confirmed experimentally from several sources, such as at the CDF experiment at the Fermilab Tevatron in 2005 through observation of the $B_s^0 \to \phi\phi$ process [11].

It was predicted in 1979 by Glashow, Salam and Weinberg that at high energies, the electromagnetic and weak forces can be unified to become one force (electroweak) [6]. This unification is interesting and has led to searches for a *Grand Unified Theory* (GUT) where all the fundamental forces are shown to be different facets of one theory which are "frozen out" at lower energies.

The weak interaction is of importance for this analysis as the top (antitop) quark almost exclusively decays via weak interactions into a $W^+(W^-)$ boson and a b ($\bar{\text{b}}$) quark and it is these decays, along with subsequent ones, which allow for the measurement of the correlation of the spins between the top and antitop.

2.1.4 The Higgs Mechanism

One final fundamental particle is required to complete the Standard Model; the Higgs boson. It arises as an observable consequence of a mechanism included in

the SM in order to explain why fermions and the $W^{\pm}$ and Z^0 gauge bosons have mass [12] [13] [14]. For many years, the Higgs boson was theorised but remained undetected. In July 2012, the ATLAS and CMS collaborations at the LHC independently confirmed the existence of this fundamental particle [15] [16]. The Higgs boson is the second heaviest known fundamental particle, with a mass of 125.09 ± 0.24 GeV. It also has a spin of 0 [1].

The Higgs boson coupling strength to each fermion (known as the *Yukawa coupling*) is proportional to the mass of the fermion. Therefore, it couples most strongly to the heaviest known fundamental particle; the top quark.

2.2 The Top Quark

The top quark is one of the six quarks in the Standard Model and is part of the third generation of quarks discussed in section 2.1.1. The top quark interacts mainly with other particles via the strong force (mediated by gluons) but decays exclusively via the weak nuclear force (specifically with W bosons). Due to its heavy nature, the top couples strongly to the Higgs field. The current accepted decay width of the top quark is $\Gamma = 1.41^{+0.19}_{-0.15}$ GeV, which is inferred from data and theory [1].

The existence of a third generation of quarks was initially predicted in 1973 by Kobayashi and Maskawa [17] in order to explain charge-parity (CP) violation that had been observed in kaon decay. Prior to this prediction, three quarks had been experimentally confirmed (up, down and strange) and the model in place for two generations of quarks could not explain CP violation. The top quark was postulated to be the positively charged quark in this new generation.

2.2.1 Theoretical Prediction

In a two generation model, it was noted that down-type quarks could decay into up-type quarks via the weak interaction. The object which allows this can be seen as a superposition of down-type quarks:

$$d' = V_{ud}\, d + V_{us}\, s \tag{2.1}$$

$$s' = V_{cd}\, d + V_{cs}\, s \tag{2.2}$$

where d' and s' are the superposition object states, d and s are the observable particle states and $|V_{xy}|^2$ is the probability of quark y decaying into quark x (or vice-versa). Historically, these V_{xy} were known as *Cabibbo Mixing Angles* and these superpositions can be written in matrix form:

$$\begin{pmatrix} d' \\ s' \end{pmatrix} = \begin{pmatrix} V_{ud} & V_{us} \\ V_{cd} & V_{cs} \end{pmatrix} \begin{pmatrix} d \\ s \end{pmatrix} .$$

This matrix is by construction unitary and so introduces N^2 parameters which are real and measurable (where N is the order of the matrix). The quark wavefunctions have no defined phase and so some of these parameters ($2N$-1 to be precise) have no physical meaning as they can be absorbed by arbitrary phase rotations of the quarks. In the case of a 2×2 matrix, this leaves one last parameter which describes a mixing angle. In order for CP violation to occur, there needs to be a *complex phase term* included within the theory (the phase itself is not complex). This is not possible for only two generations and so a third generation was postulated.

The addition of the third generation allowed for this unabsorbable phase to be included and so explain CP violation:

$$\begin{pmatrix} d' \\ s' \\ b' \end{pmatrix} = \begin{pmatrix} V_{ud} & V_{us} & V_{ub} \\ V_{cd} & V_{cs} & V_{cb} \\ V_{td} & V_{ts} & V_{tb} \end{pmatrix} \begin{pmatrix} d \\ s \\ b \end{pmatrix}$$

Each of these parameters is measurable and when squared, $|V_{xy}|^2$ gives the relative probability of a quark decaying to another quark. The current measured values are as follows [18]:

$$\begin{pmatrix} |V_{ud}| & |V_{us}| & |V_{ub}| \\ |V_{cd}| & |V_{cs}| & |V_{cb}| \\ |V_{td}| & |V_{ts}| & |V_{tb}| \end{pmatrix} = \begin{pmatrix} 0.974254^{+0.000071}_{-0.000097} & 0.22542^{+0.00042}_{-0.00031} & 0.003714^{+0.000072}_{-0.000060} \\ 0.22529^{+0.00041}_{-0.00032} & 0.973394^{+0.000074}_{-0.000096} & 0.04180^{+0.00033}_{-0.00068} \\ 0.008676^{+0.000087}_{-0.000150} & 0.04107^{+0.00031}_{-0.00067} & 0.999118^{+0.000024}_{-0.000014} \end{pmatrix}$$

As can be seen from the value of $|V_{tb}|$ being approximately equal to 1, the top quark almost exclusively decays to a b-quark.

2.2.2 Top Quark Discovery

In 1995, following a number of attempts to find the top quark, a joint announcement was made from the CDF and DØ experiments at the Fermilab Tevatron, a proton-antiproton collider operating at $\sqrt{s} \approx 2$ TeV, that the existence of the top quark had been confirmed, with a mass of 176 ± 18 GeV [19]. The experiments that found the top quark were the only ones at the time which could create top-antitop pairs due to the large energies required. In addition, the number of events that were found was small, so detailed studies with high precision could not be performed.

At the LHC, the c.m. energies that are available are greater than those of previous experiments. The Tevatron was able to reach an energy of 1.96 TeV [20] whereas at design capability, the LHC will reach a c.m. energy of 14 TeV. This allows it to create a far greater number of top and antitop quarks and therefore it is an

ideal collider to use in order to study the properties of the top with greater precision.

2.3 Top Quark Pair Production

There are various methods of production of the top quark, dependening on the c.m. energy. Feynman diagrams illustrating these processes for top-antitop production at lowest order are shown in figure 2.1.

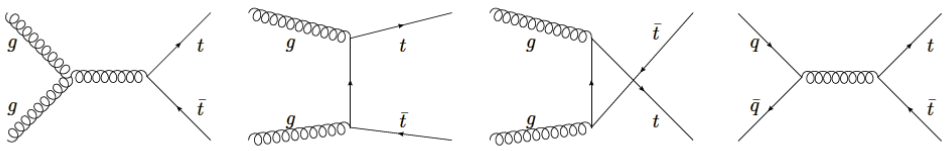

Figure 2.1: Feynman diagrams illustrating top quark pair production at lowest order through gluon-gluon scattering for the first three diagrams (left to right) and quark-antiquark annihilation in the final diagram.

The predominant method of production of top-antitop quark pairs at the LHC is via gluon-gluon fusion. This is in contrast to the Tevatron, where the main production method was via quark-antiquark interactions resulting from proton-antiproton collisions. The reason for this difference is due to the threshold production energy of the top quark and the *parton distribution function* (PDF) of the hadrons which collide at the energies present in each of the accelerators.

2.3.1 Parton Distribution Functions

When hadrons collide (in the case of the LHC, two protons; for the Tevatron, one proton and one antiproton), they do so with a longitudinal momentum. However, as these hadrons are a composite of quarks and gluons, the longitudinal momen-

tum is actually shared between these partons. The way in which the momentum is distributed is described by a parton distribution function. A PDF illustrates the probability of finding a parton with a certain fraction, x, of the hadron's total longitudinal momentum. PDFs are dependent on the hadrons and the energy scale, Q^2, at which they collide. Example PDFs are shown in figure 2.2, which shows the distributions for the proton at two values of Q^2. The energy scale varies depending on the process being considered: for the purposes of top quark production, a Q^2 of $\approx m_t^2 = O(10^4)$ GeV^2 is used.

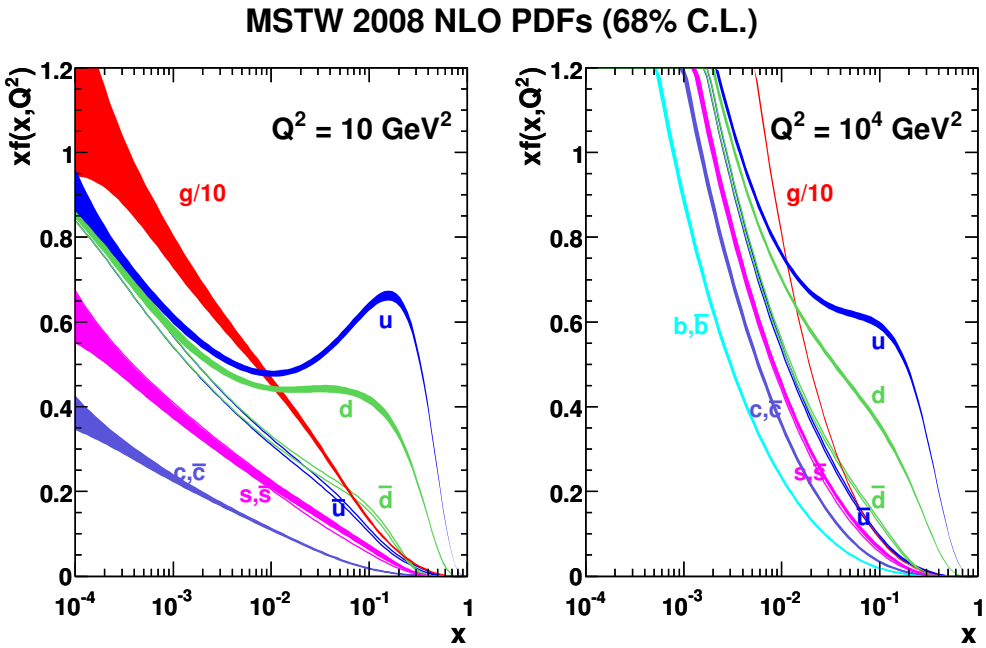

Figure 2.2: Example PDF distributions of the proton for two energy scales using the MSTW 2008 prediction set [21].

The PDF models which are used in analyses are constrained using experimental data obtained through probing techniques of the hadron collectively known as *Deep Inelastic Scattering* (DIS) [7]. There are a number of calculation methods and data sets which can be used for these PDFs, each creating a slightly different prediction. Therefore, the choice of PDF set is seen as a source of uncertainty within experi-

ments and this has to be assessed (see section 7.2.2.9).

At a c.m. energy of $\sqrt{s} = 8$ TeV, and using the required fractional momentum of each parton for top pair production (≈ 0.045), the preferred method of production of top-antitop quark pairs is gluon-gluon fusion ($\approx 90\%$ at $\sqrt{s} = 14$ TeV and $\approx 80\%$ at $\sqrt{s} = 7$ TeV [1]) with quark-antiquark and quark-gluon interactions accounting for the rest.

The prevalence of the gluon-gluon scattering method of production at the LHC also means that the cross section for top pair production at $\sqrt{s} = 14$ TeV is around 100 times higher than that at the Tevatron. This, combined with the high integrated luminosity expected per year of running, means that at design criteria, around 10^7 top pairs are predicted to be produced per year [22].

2.4 Top Quark Decays

The top quark decays almost exclusively via the weak interaction to a W boson and a b-quark. Following this initial decay, the b-quark also decays weakly to lighter quarks, which subsequently hadronise forming showers of hadrons (known as *jets*). The W boson can decay into either a lepton and the corresponding neutrino or it can decay into a quark and antiquark pair (such that the charge is conserved e.g. $W^+ \to u\bar{d}$). As there is one top and one antitop decay which behave analogously (but with the charge of the W boson flipped and the production of a $\bar{b}$ quark), there will be two b-type quarks and two W bosons produced. Given the potential decays of each W boson, this gives rise to three possible channels of analysis:

- *All hadronic*: This is where both W bosons decay into a quark and an antiquark. Experimentally, this leads to an event signature of six high transverse

momentum (p_T) jets (one for each b-quark and for each quark and antiquark from the W decays). This is the preferred decay channel, with a branching ratio of 46.2% [1]. Whilst this would give the highest number of events for a measurement, there are a number of experimental challenges, including triggering requirements and uncertainty due to jet reconstruction and separation of events from QCD multi-jet background.

- *Semi-leptonic*: This is the case in which one W boson decays leptonically and one decays hadronically. The experimental signature for this event is that of four high p_T jets, one isolated lepton and missing transverse energy (representing a neutrino which cannot be directly measured in the ATLAS detector). The branching ratio for this decay is close to that of the fully hadronic channel at 43.5% [1].

- *Dileptonic*: Here, both W bosons decay leptonically. The signature for this event is two charged leptons, a high value of missing transverse energy and two high p_T jets. As there are fewer jets in this channel, the signal is the cleanest of the three possible, with a good signal to background ratio. However the branching ratio is only 10.3% and so the number of events will be smaller [1]. This channel is further subdivided into the flavours of the leptons from the W boson decays (i.e. two electrons (ee), two muons ($\mu\mu$) or one muon and one electron (eμ)). Included within the 10.3% branching ratio is the possibility of one or both of the W bosons decaying into a τ lepton. Due to the mass of the τ lepton, these decay further, either leptonically or hadronically. If the decay is leptonic, then the event will have a signature similar to that of the other dileptonic decays, and they are experimentally difficult to distinguish. Therefore, typically some of the τ leptons that decay leptonically will be included in a dileptonic top quark decay analysis which looks for ee, $\mu\mu$ and eμ in its final state.

An example of a potential $t\bar{t}$ pair production and subsequent decay can be seen in figure 2.3.

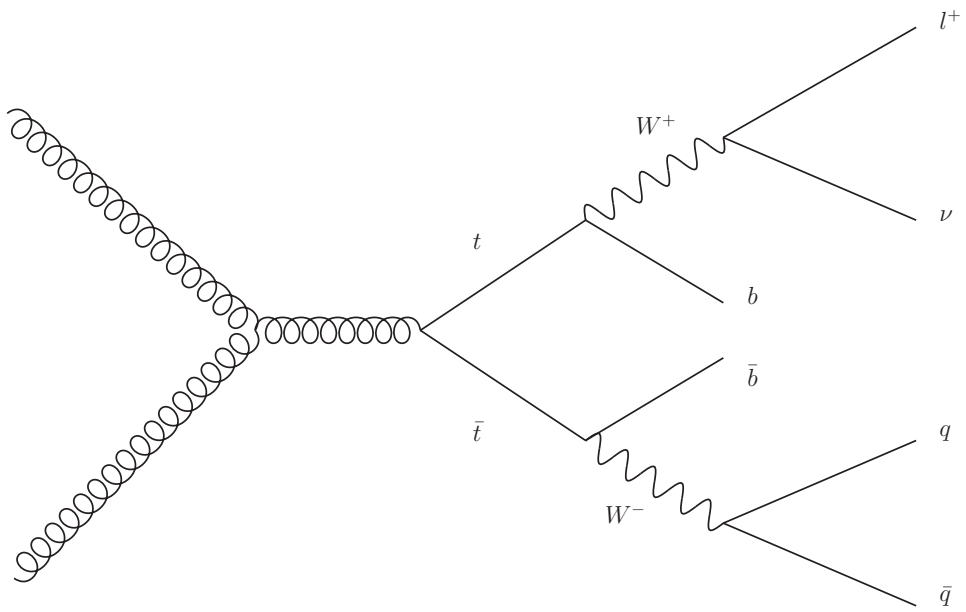

Figure 2.3: Feynman diagram illustrating a semileptonic decay chain of a top-antitop quark pair.

Each of these $t\bar{t}$ channels can and have been used for certain analyses but this analysis uses only the dileptonic channel. This is partially due to the reasons discussed above (i.e. the cleanest signal and good signal to background ratio). However, there are additional features of charged leptons which make them ideal for top quark spin studies. These will be discussed in chapter 5.

2.5 Single Top Production

Whilst the majority of top quarks observed at the LHC are produced in pairs (with a cross section at $\sqrt{s} = 8$ TeV of $\sigma = 253^{+13}_{-15}$ pb [23] [24] [25]), there are several processes which also allow for production of a lone top quark (see figure 2.4). The processes can be split into three types [26] [27]:

- *t-channel*: this channel involves production of a single top via the exchange of a space-like W boson. It also creates one other 1st or 2nd generation quark, and a b-quark. At the LHC, this is the process which accounts for the greatest amount of single top production, with a predicted cross section at $\sqrt{s} = 8$ TeV of $\sigma = 87.2^{+3.4}_{-2.4}$ pb for an assumed top mass of $m_t = 173$ GeV [28] [29].

- *s-channel*: this channel involves production of a single top via the exchange of a time-like W boson and also creates one bottom quark. This process has the lowest predicted cross section for single top production at $\sqrt{s} = 8$ TeV, $\sigma = 5.55 \pm 0.22$ pb, for an assumed top mass of $m_t = 173$ GeV [29] [30].

- *Wt-channel*: this channel results in the production of a real W boson in association with a single top quark. For $\sqrt{s} = 8$ TeV, the Wt-channel has a predicted cross section of $\sigma = 22.2 \pm 1.52$ pb [29] [31]. Due to the products of this reaction, the resulting signature of the process is similar to that of the dileptonic decay of a $t\bar{t}$ pair (see section 2.4). This becomes important when considering background contributions in a dileptonic analysis.

Studies of single top production can be used to investigate various facets of the Standard Model, such as the spin properties of the individual top, and also can provide insight into potential sources of Beyond the Standard Model (BSM) physics. However for the purposes of this analysis, which aims to study the correlation in spins between $t\bar{t}$ pairs, top quarks which are produced in isolation are only of interest as possible sources of background (most notably in the Wt-channel). This background will be discussed further in chapter 6.

2.6 Importance of Top Quark Studies

As comparatively little is known experimentally about the top quark in comparison to other quarks, its investigation has the potential to add great insight into what is

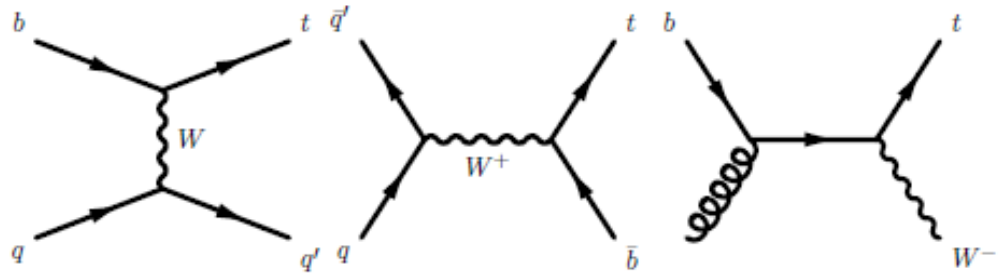

Figure 2.4: Feynman diagrams illustrating the three production methods of single top quarks at the LHC. The leftmost diagram illustrates the t-channel, the central diagram shows the s-channel and the rightmost diagram is the Wt-channel.

known about particle physics. Studies of the top quark may highlight non-standard couplings (evident as anomalous top quark production and decays), which would indicate new physics. Other studies may also illuminate rare top decays, which could again highlight new physics which is beyond the SM.

Another important property of the top quark is that it has a lifetime shorter than that of the characteristic interaction time of the strong force. The consequence of this is that top quarks are unable to form hadrons and so act as "bare" quarks, offering an opportunity to study properties of quarks which are otherwise lost when hadrons are formed. One of these is the direction of the spin of the quarks and, when produced in pairs, the degree to which the spins of the top and the antitop are correlated. This is the property which will be investigated in this thesis.

Since the inception of the LHC, the top quark has been studied extensively, both for measurements of its properties and to probe the Standard Model. One such study considers searches for flavour changing neutral currents (see section 2.1.3.3) by considering a state where one top quark decays leptonically via a W boson to a charged lepton and neutrino and the other decays via a flavour changing neutral current to two charged leptons ($t \to ql^+l^-$, $q = u, c$) [32]. Another study probes the proposed SM colour octet model through analysis of the distribution of jets arising

from the hadronic decay of a W boson produced from a top quark decay [33]. These studies, amongst others, help to highlight the diversity of measurements that can be made through top quark studies.

Chapter 5 will look in more detail at the theory behind the phenomenon of spin correlation in top-antitop quark pairs, as well as presenting an analysis strategy for the measurements made in this thesis.

Chapter 3

THE ATLAS DETECTOR AND THE LARGE HADRON COLLIDER

The Large Hadron Collider (LHC) is a particle accelerator which is housed at CERN near Geneva, Switzerland. The LHC has a circumference of 26.7 km and is approximately 100 m underground, passing through both Switzerland and France. The LHC ring has two beam pipes in which protons or heavy lead ions are accelerated in opposite directions and are made to meet at 4 interaction points on the ring. The four main LHC experiments have been built at these interaction points to study the results of these collisions (see figure 3.1). Each experiment is concerned with different areas of physics and the structure of the detectors reflects the different requirements of the experiments.

3.1 The LHC Experiments

A brief description of the four detectors is given below:

- **ATLAS** (**A** **T**oroidal **L**HC **A**pparatu**S**) [35] and **CMS** (**C**ompact **M**uon **S**olenoid) [36] are both general purpose detectors. This means that they are designed to be able to study a wide array of the properties of particles produced in proton-proton collisions. They are both cylindrical in shape and consist of a number of subsystems (such as inner detectors, calorimeters and

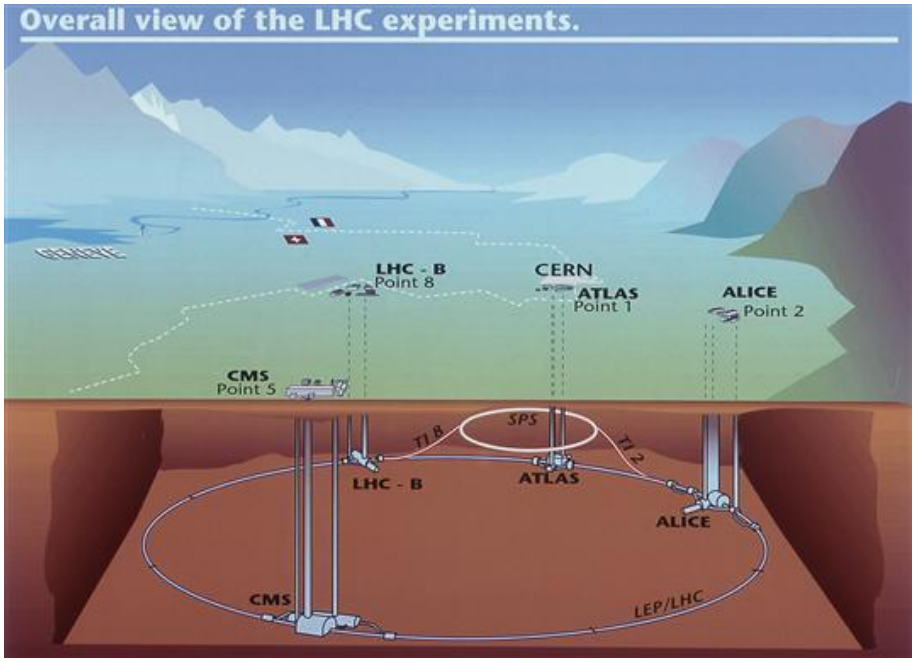

Figure 3.1: A pictorial representation of the LHC ring and the 4 interaction points [34].

muon detectors) to enable high precision particle tracking and detection. The main difference between the two is the field strength and positioning of the magnetic systems in the detector which give different momentum resolutions. A more detailed description of the ATLAS detector is given in section 3.3.

- **LHCb** [37] is an experiment which mainly considers the differences between matter and antimatter by investigation of the bottom quark. It is also particularly sensitive to processes which are considered Beyond Standard Model. The detector itself is different to the other LHC experiments in that it is not cylindrical and only looks for particles in the "forward" region (i.e. the region close in angle to the beam line). This is due to the properties of the processes that it is studying.

- **ALICE** [38] (**A** **L**arge **I**on **C**ollider **E**xperiment) is an experiment whose main concern is the lead ion-ion collisions that are run in addition to the proton-proton collisions studied by the other experiments (although the other exper-

iments also do conduct some studies using lead ion collisions). It is again a hermetic experiment and its main aim is to study the quark gluon plasma which is created by collisions of heavy ions at high energies. The purpose of the experiment is to replicate and study the conditions of matter formed in the early universe.

3.2 Proton Acceleration and Collisions

In order for protons to reach the speeds required for the high energy collisions which occur at each of the interaction points, they are first accelerated by use of the LHC injector system [39]. This consists of a series of accelerating mechanisms which gradually build up the speed of the protons before they are finally injected into the LHC (see figure 3.2).

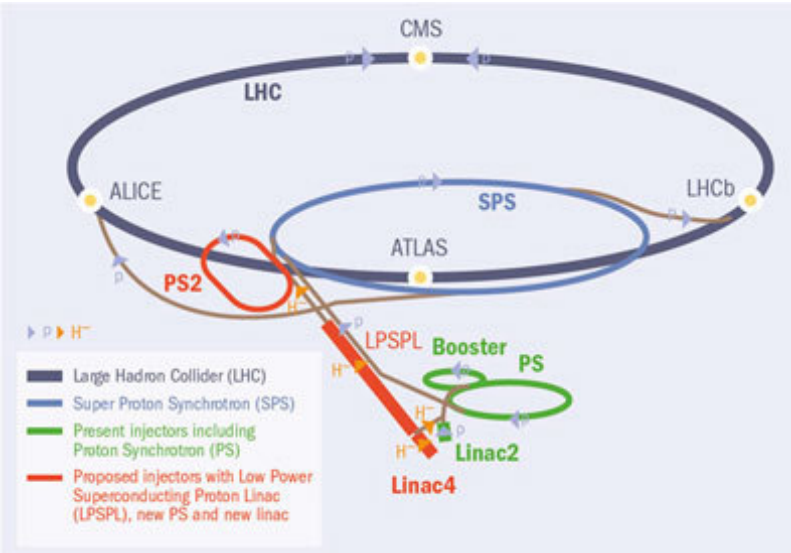

Figure 3.2: A pictorial representation of the injection system used to accelerate protons to high energies at the LHC [40].

The protons are produced from hydrogen gas which is subsequently ionised through use of an electric field to strip off electrons, leaving just protons. The protons undergo an initial acceleration through the Linac 2 [41], which accelerates the protons

to an energy of 50 MeV [39]. The protons are then passed to the Proton Synchrotron Booster (PSB) [42] [43], where the protons are accelerated further to 1.4 GeV [39], as well as being collected into *bunches*, which are collections of around 10^{11} protons, designed to increase the chance of interaction when collided. The next stage is the Proton Synchrotron (PS) which has a final accelerated energy of 25 GeV [39] for each of the proton bunches. The bunches are also brought together into groups, known as "bunch trains." The final stage before injection into the LHC is the Super Proton Synchrotron (SPS), which allows the proton bunch trains to be brought to an energy of 450 GeV [39].

The process for the acceleration of lead ions is similar, where ions are produced in Linac 3 before being subsequently accelerated. However, they do not pass into the PSB and are instead accelerated and gathered in the Low Energy Ion Ring (LEIR) before being passed to the PS [39].

Once the protons (or heavy ions) have been sufficiently accelerated, they are injected into the LHC beam pipes. Within the pipes, the particles to be collided are directed around the ring by superconducting electromagnets, which are required to be kept at temperatures of $-271.3\,^{\circ}\mathrm{C}$. These magnets bend the beams in order to direct the particles to their required collision points and Radio Frequency (RF) cavities are used to accelerate the protons to their required energies (at design energy, this will be 7 GeV for each beam). At the collision points, more magnets are used in order to bring the two beams together and focus them, thereby increasing the probability of collisions.

The proton bunches are collided at 4 points around the LHC ring and many interactions can occur per "bunch crossing" (which leads to an effect known as pile-up, where it becomes more difficult to distinguish one event from another). During the

2012 run, the bunch crossing rate was 40 MHz with a mean number of interactions per beam crossing ranging from between 15 and 40 (with some specialised runs generating $\sim$ 70 interactions).

3.3 The ATLAS Experiment

There are around 3000 scientists working on the ATLAS experiment from 38 countries. It is 25 m in diameter, 45 m in length and weighs 7000 tonnes. The experiment itself is housed in a large cavern 92 m underground which is located at "Point 1", which is the closest beam interaction point to the CERN laboratories [35].

The general purpose nature of the experiment necessitates that the detector is able to detect a wide variety of different processes. Consequently, the detector is hermetic and covers a nearly 4π solid angle around the interaction point. There are a number of subcomponents within ATLAS which are as follows:

- The Inner Detector,
- The Calorimeter System,
- The Muon Spectrometer,
- The Magnet System.

These will be described in section 3.5. The subdetectors surround the beam axis in concentric layers and are arranged into a central *barrel* region, and an *endcap* region, designed to measure particles produced in a forward direction.

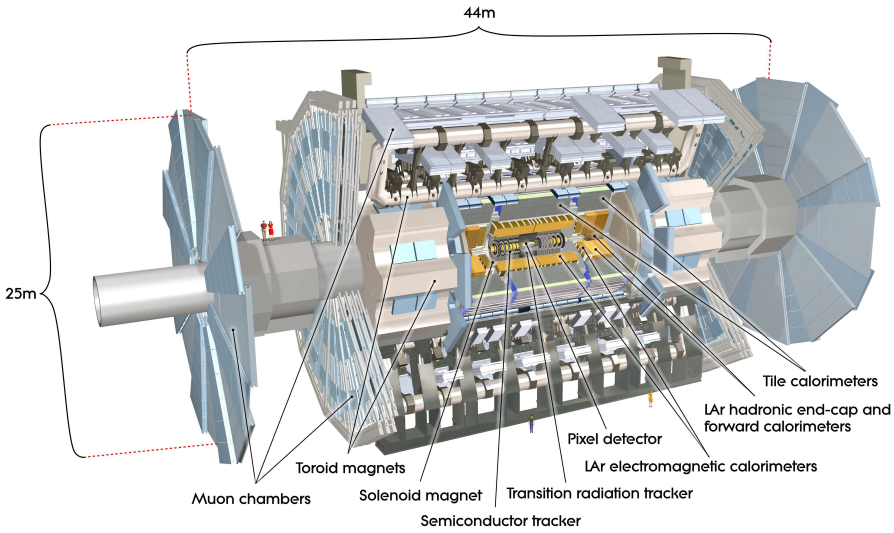

Figure 3.3: A cut-away schematic diagram of the ATLAS detector showing the various subcomponents which make up the detector as a whole [34].

3.4 ATLAS Geometry

In order to decribe the position of particles in the ATLAS detector, a geometry system is required. It is possible to do this using a standard Cartesian system (x, y, z), but it is more convenient to use a polar coordinate system.

The z-axis is defined as being along the beam and the radial component, r, is defined as the perpendicular distance from the z-azis. ϕ is defined as being the azimuthal angle around the beam and θ the angle between the beam axis and the position to be measured. However, instead of using θ, it is more convenient to use an angular variable which describes particles travelling at relativistic speeds. One such variable is the *rapidity*, y, defined as

$$y = \frac{1}{2} \ln \left[\frac{(E + p_z)}{(E - p_z)} \right], \tag{3.1}$$

where E is the energy of the particle and p_z is the longitudinal (i.e. parallel to the beam axis) component of the momentum of the particle. In the case where particles

are massless or travelling at highly relativistic speeds (which is the case here), this can be approximated to the *pseudorapidity*, η, where

$$\eta = -\ln\left[\tan\left(\frac{\theta}{2}\right)\right]. \tag{3.2}$$

The pseudorapidity is used because particle production is roughly constant across units of η and in addition, the difference in pseudorapidity between two particles is invariant under Lorentz boosts in the z-direction. Pseudorapidity runs from $-\infty \rightarrow \infty$ with $\eta = \pm\infty$ being on the beam axis, at $\theta = 0$ and $\theta = \pi$, and $\eta = 0$ at right angles to the beam direction.

Another convention used in ATLAS (and which is important for selection of events in chapters 4 and 6) is to define the separation of particles as the quantity ΔR:

$$(\Delta R)^2 = (\Delta\phi)^2 + (\Delta\eta)^2 \tag{3.3}$$

This quantity creates a cone which defines the separation of particles (or the spread of a particle shower).

It is common practice within ATLAS to measure transverse quantities (such as energies, E_T and momenta, p_T) rather than total quantities, where the transverse component refers to the component perpendicular to the beam axis. This is because momentum and energy in the direction of the beamline may be residual from beam particles whereas transverse quantities will relate to particles that have been produced as a result of particle interaction.

3.5 ATLAS Subcomponents

3.5.1 Inner Detector

The inner detector (ID) is an ensemble of three further sub-detectors (in 2012), which starts at around 5 cm from the the interaction point and extends to a radius of 1.08 m and has a length of $\sim$ 6 m. This is the first set of detectors that any particles produced from the interactions will pass through and it is concerned with high precision tracking close to the interaction point. The tracking is performed by relying on ionisation in the detectors by charged particles which pass through them. The ID detects particles within the range of $|\eta| < 2.5$ [35].

The three subcomponents of the ID are the Pixel Detector, the Semi Conductor Tracker (SCT) and the Transition Radiation Tracker (TRT). In the barrel region of ATLAS, the three detectors are arranged in concentric cylinders whilst in the end-cap region, the detectors are mounted on disks which are perpendicular to the beam axis (see figure 3.4).

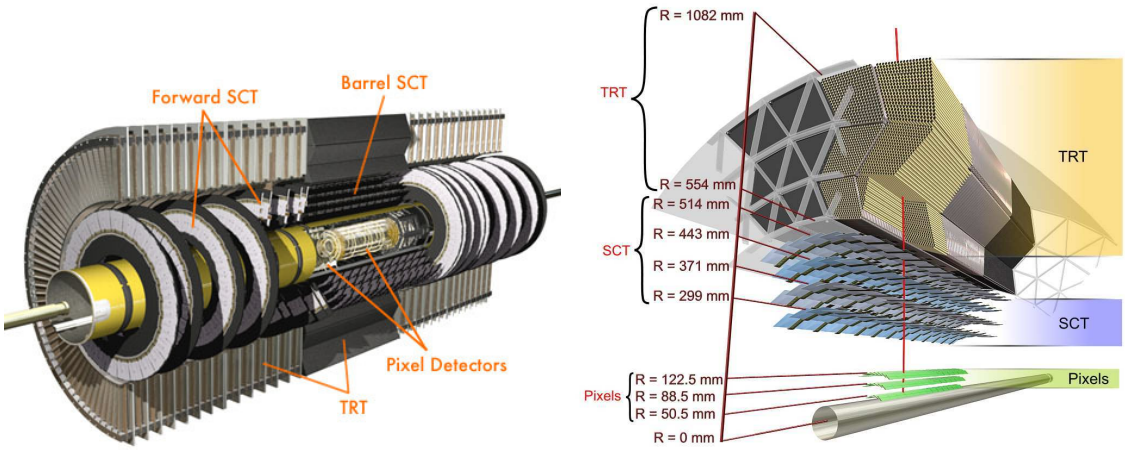

Figure 3.4: A cut away of the Inner Detector layers [34].

The Pixel Detector provides a very high granularity measurement as close to the

interaction vertex as possible. The system consists of cylindrical layers (placed at average radii of 5, 9 and 12 cm) in the barrel region, and three disks in the end-cap region at a distance of between 9 and 15 cm from the interaction point along the beam axis. The system in total consists of over 80 million silicon pixels, with each pixel measuring 50 μm by 400 μm. The size and amount of the pixels allows for extremely high precision measurements of positions of particles produced. This is important in allowing ATLAS to find short lived particles such as B-hadrons. The high granularity also allows the detector to be able to better distinguish between primary and secondary vertices and aid in reducing the effects of pile-up. Due to the proximity of the pixels to the interaction point, the pixels will be subject to a high amount of ionising radiation and will therefore become damaged more quickly than other parts of the detector. As a result, the pixels will be replaced after a few years of operation [35].

The SCT immediately surrounds the pixel detector. In the barrel region, the SCT covers the radial range 30-56 cm and is designed to provide more information about the momentum, impact parameters and vertex position of the particle interactions. The SCT consists of strips of silicon $\sim$ 12 cm in length. When a hit is recorded on a strip, the precise location of the hit cannot be determined from one strip alone. Therefore, the SCT layers are arranged into pairs which are overlapped at an angle in order to provide better spatial information. In total, there are 8 layers in the SCT mounted on carbon-fibre cylinders in the barrel region with a similar construction in the end-cap [35].

The TRT is the final layer of the ID and is composed of $\sim$ 370,000 straw detectors over the barrel and the end-cap which cover a radial range of $\sim$ 56 cm to $\sim$ 107 cm. The straws themselves are 0.4 cm in diameter and are up to 144 cm long. They are filled with xenon gas in order to detect transition radiation photons to

allow for electron identification. The resolution of the TRT is lower than the other components of the ID but this is required in order to cover a large volume. Despite the lower resolution of the TRT, it aids in particle identification and measurement by providing a large number of measurements and by increasing the length of the particle track which is measured [35].

3.5.1.1 The Insertable B-layer

During the long shutdown in 2014-2015, a new layer (the Insertable B-Layer (IBL)) was succesfully inserted into the ATLAS inner detector, placed inside the pixel detector [44]. The IBL has been inserted in order to provide improved resolutions. The IBL is closer to the interaction point than the pixel detector (a distance of ~ 3 cm) and has a higher radiation hardness, therefore making it more able to withstand the ionising radiation produced without damage. The pixels themselves are also smaller (50 μm by 250 μm), which helps to fight high occupancy (i.e. the number of particles passing through a detector cell per event) at the higher luminosities.

Whilst the IBL is of great importance for ongoing studies, the analysis presented uses data from the 2012 run and therefore will not benefit from the enhanced performance provided by it.

3.5.2 The Calorimeter System

Following the ID, the next system of detection in the ATLAS experiment is the calorimeter system. Once again, the calorimeter system itself is composed of sub-components, each tasked with performing a different function. The two main types of calorimeter are the Electromagnetic (EM) Calorimeters (ECAL) and the Hadronic Calorimeters (HCAL). See figure 3.5 for a diagram of these systems in place at ATLAS [35].

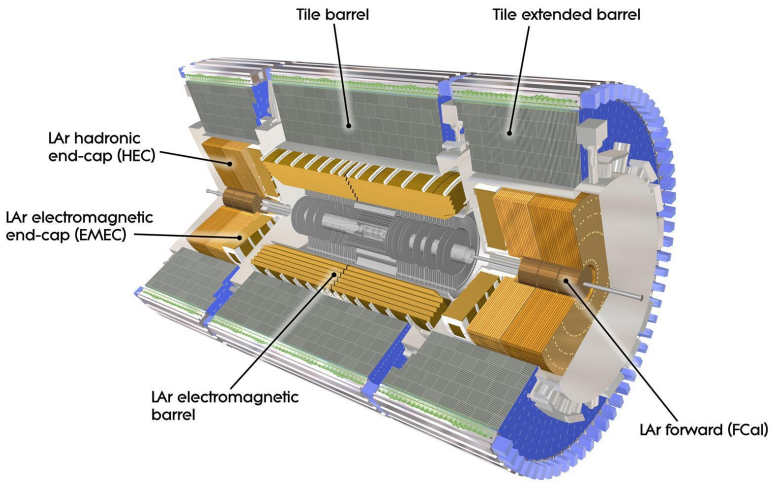

Figure 3.5: A computer generated image of the ATLAS calorimeter system [34].

The purpose of the calorimeters is to measure the energy of particles that come into contact with them by causing the particle to deposit its energy in the material of the calorimeter. Generally calorimeters can only measure the energy of specific particles and this is the reason that more than one calorimeter is required in ATLAS. The EM Calorimeter measures the energy of particles that undergo Bremsstrahlung (e.g. photons and electrons) and the Hadronic Calorimeter measures particles that interact mainly via the strong force (e.g. neutrons and pions).

The calorimeters used in ATLAS are both sampling calorimeters. This means that a high density metal is used to "absorb" a high energy particle (i.e. causes it to deposit its energy in the calorimeter through interactions with matter) and cause it to shower into other particles which are detected by the sensing (or sampling) elements of the calorimeter. By measuring the shape of the shower and the energy of the particles within the shower, it is possible therefore to gain information about the original high energy particle.

The two calorimeters cover a pseudorapidity range of $0 \leq |\eta| < 4.9$ and so have greater coverage than the ID. The calorimeters also must have a very high energy resolution (i.e. the energy measurement has a small uncertainty) to allow for extremely precise energy measurements which is important in many searches. The energy resolution, σ_E, is given by

$$\frac{\sigma_E}{E} = \frac{A}{\sqrt{E}} \oplus \frac{B}{E} \oplus C, \tag{3.4}$$

where $\oplus$ indicates addition in quadrature [45]. A represents the stochastic term, B represents the noise term and C represents a constant term. Typical values of these terms are $A = 0.1\sqrt{\text{GeV}}$, $B = 0.17$ GeV and $C = 7 \times 10^{-23}$ [45].

The precise materials and structures used in the EM Calorimeter differ from those used in the Hadronic Calorimeter. The details are as follows:

- The ECAL uses lead as the absorbing material and liquid argon as the sampling material in alternating layers. The layers are assembled together in an accordion style structure (see figure 3.6). This structure allows more active layers and provides better coverage in ϕ. In the high precision region ($0 < |\eta| < 2.5$) there are three active layers (i.e. three layers of absorbing material and sampling material) and in the more forward regions ($2.5 < |\eta| < 3.2$) there are two. The barrel region of the ECAL is split into two sections, each 3.2m long and meeting at $\eta = 0$. The barrel region covers $0 < |\eta| < 1.375$. In the end-cap region, there are two co-axial wheels on either side which cover $1.375 < |\eta| < 3.2$.

- The HCAL is located behind the ECAL. In the barrel and "extended barrel" regions ($|\eta| < 1.7$), it consists of tile calorimeters using steel as the absorber material and scintillating plastic as the sampling material. In the end-cap

regions, the HCAL uses copper and liquid argon as the sampling material. This covers the region of $1.5 < |\eta| < 3.2$ and, similarly to the ECAL, consists of two wheels in each end-cap.

- In the regions more forward of those covered by the calorimeters mentioned above, there is one further calorimeter called the Forward Calorimeter (FCAL). Housed in the same cryostats as the endcap calorimeters, the FCAL is composed of three 45 cm deep layers (FCAL1 which is an EM module and FCAL2/FCAL3 which are hadronic modules) and covers a pseudorapidity range of $3.1 < |\eta| < 4.9$. Located 4.7 m from the interaction point, the first layer of the FCAL uses copper as an absorbing material, with this changing to tungsten in the subsequent layers (in order to optimise resolution and to minimise the spread of hadronic showers in such a forward region). Liquid argon is used as the sampling material for each of the layers.

3.5.3 Muon Spectrometers

The muon spectrometer is the outermost detection system at ATLAS and surrounds the whole detector (see figure 3.7). In the barrel region, the spectrometer consists of three concentric shells at radii of 5 m, 7.5 m and 10 m. In the end-caps, the muon chambers consist of 4 wheels which are placed perpendicular to the beam axis at distances from the interaction point of $\sim$ 7.4 m, 10.8 m, 14 m and 21.5 m. Muons are important as they are evident in many processes which are being studied (including the analysis presented in this thesis). Muons are also not identified by the calorimeters due to their size, hence the spectrometers are used in order to detect and provide information about them [35].

The spectrometer is designed to both detect the presence of muons and also to give precise momentum measurement and spatial positioning. The spatial information

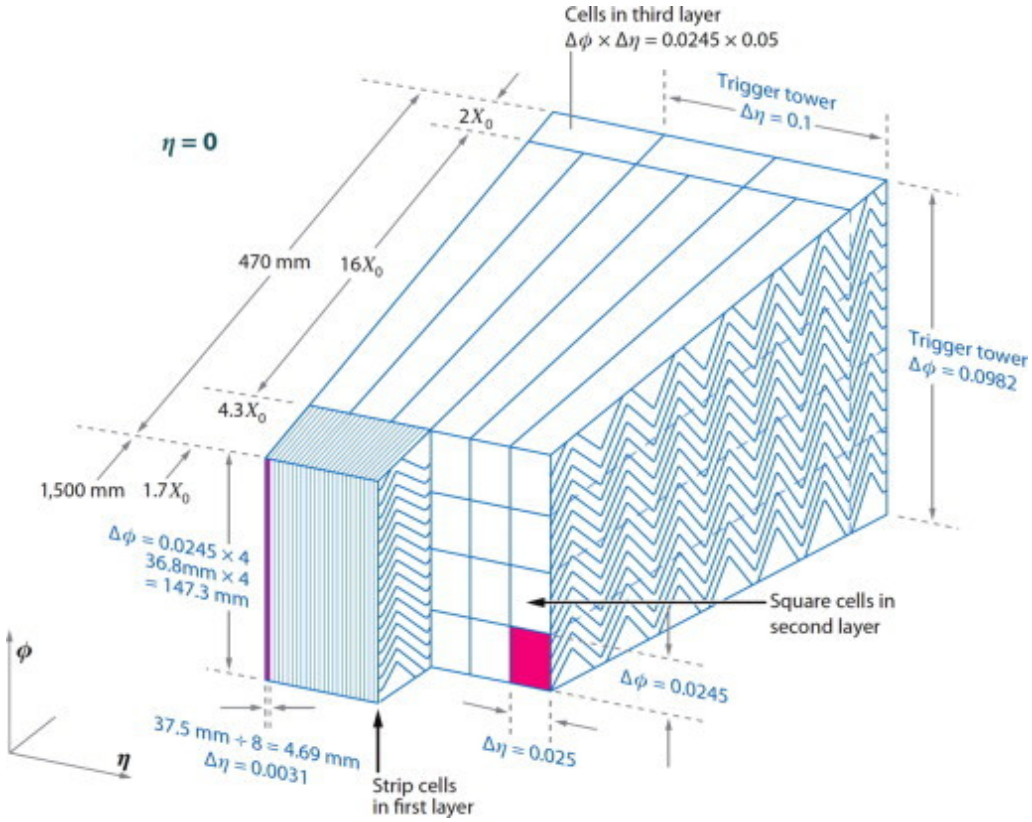

Figure 3.6: An illustration of the liquid argon EM Calorimeter "accordion" structure [34].

and momentum measurement are performed by the Monitored Drift Tube (MDT) chambers in the barrel region and by the Cathode-Strip Chambers (CSC) in the endcap region. The resolutions of the chambers are 35 and 40 μm respectively. Owing to the high precision provided by the MDT and CSC, the processing time is slow, and triggering information is required faster than these systems provide. To that end, a complementary system of Resistive Plate Chambers (RPC) in the barrel region and Thin Gap Chambers (TGC) in the end-caps were implemented in order to provide fast triggering information. The time resolution of these systems is 2-4 times faster than the precision systems.

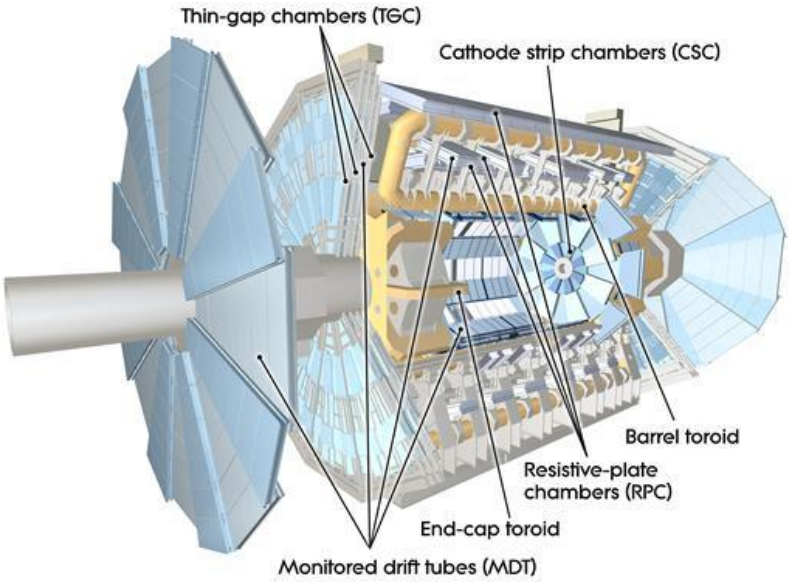

Figure 3.7: An illustration of the muon spectrometer systems surrounding the ATLAS detector [34].

3.5.4 Magnet Systems

The ATLAS detector features a system of 4 superconducting magnets consisting of one solenoid magnet and 3 toroid magnets (see figure 3.8). These magnets are important in particle identification and in the accurate momentum measurement of charged particles. The total size of the magnet system is 26 m in length with a radius of 11 m. The high energy nature of the collisions taking place necessitates that the magnetic fields must be of high strength [35].

The solenoid is placed at an average radius of 1.255 m from the beam axis and encompasses both the beam axis and the Inner Detector. It produces a field of 2 T and its main purpose is to bend the paths of particles for track measurement in the ID.

As mentioned above, the toroid system is composed of three separate magnets; one in the barrel region (consisting of eight separate coils, each housed in a cryostat) and

one for each of the end-cap regions so as to provide a magnetic field which surrounds the muon spectrometers. The magnetic field of the toroid system is 3.9-4.1 T. The main purpose of the system is to bend the muon paths to provide accurate momentum measurement of the muons. A solenoidal magnet could also provide a similar effect for the muon measurements, however the solenoid would need to encompass the entirety of the detector which would not be cost-effective. Additionally, the arrangement of the toroid magnets provides a bending direction perpendicular to the bending from the solenoid and therefore provides an independent measurement of the muon momentum.

Figure 3.8: An illustration of the barrel solenoid (left) and toroids (right) used at ATLAS [34].

3.6 The ATLAS Trigger System

At design specifications, there will be around 40 million bunch crossings per second and the proton-proton collision rate will reach $\sim$ 1 GHz. However, the amount of data recording which was possible during the first data taking run was limited to around 200 Hz [22] (although during the second run, this is expected to increase to around 1 kHz [46]). In order for this to be possible, a system of triggers is employed in order to reduce the acceptance rate whilst maximising the efficiency of good events being accepted. In total there are three levels to the trigger system (see figure 3.9)

which are as follows:

- The Level 1 Trigger (L1) looks for EM events (electrons and photons), events with high missing transverse energy E_T (which indicates the possible presence of neutrinos), high p_T muons and tau leptons.

  L1 reduces the acceptance rate to 75 kHz and must process events and pass them to the next level within 2.5 μs. The L1 trigger identifies Regions of Interest (RoIs) where the trigger has identified possible items of interest. These then get passed to the next level. The L1 Trigger is a hardware-based trigger.

- The Level 2 Trigger (L2) further reduces the acceptance rate using the RoI information passed from L1 (such as co-ordinates and energy). L2 reduces the rate to under 3.5 kHz and has a total processing time of around 40 ms. This trigger uses reconstructed information as opposed to purely hardware based decisions.

- The final level of the trigger is called the Event Filter (EF) and together with L2 is called the High-Level Trigger (HLT). The EF uses offline analysis to reduce the acceptance rate to 200 Hz. The average processing time of this trigger is 4 s. Again, this is a software based trigger. The HLT uses the full precision of the various subsystems of the detector to refine the selection of events.

Chapter 4 describes in more depth the Level 1 Calorimeter Trigger (L1Calo), which is an element of the ATLAS Level 1 trigger that is concerned with triggering on EM events. The chapter will also present work conducted by the author during the 2012-2014 shutdown, investigating ways of reducing the rate of triggering on events in order to meet acceptance rate constraints as the LHC moves towards higher c.m. energies.

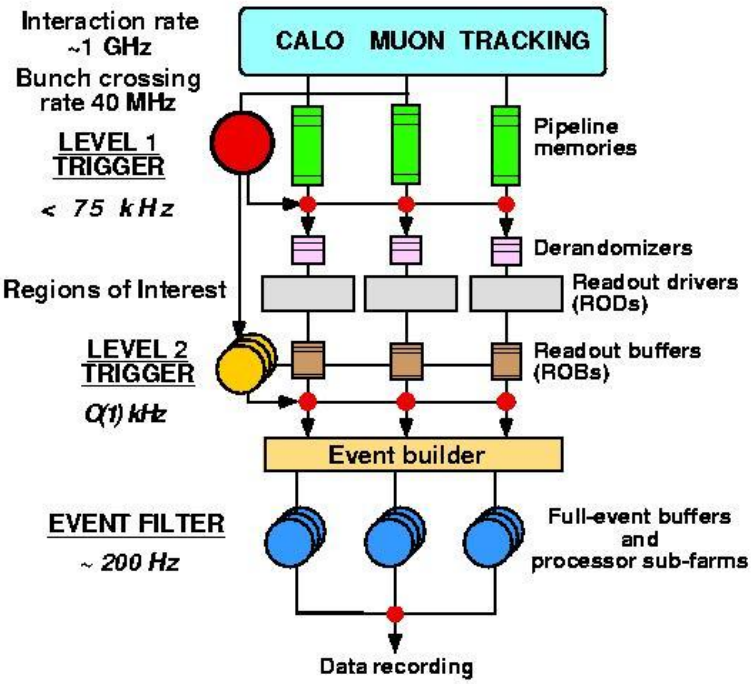

Figure 3.9: A pictorial representation of the three trigger levels used at ATLAS [47].

Chapter 4

THE LEVEL-1 CALORIMETER TRIGGER AND REDUCTION IN TRIGGER RATE ACCEPTANCE

4.1 The Level-1 Calorimeter Trigger

The Level-1 Calorimeter Trigger (L1Calo) is a digital system which uses custom electronics [47]. It is required to process and pass on all information to the next level of the trigger within 2.5 μs. The latency of the electronics themselves is less than 1 μs and with time taken for signal transfer, the total latency of the system is around 2.1 μs.

L1Calo uses information read from the two calorimeter types (EM and hadronic) both in the barrel and end-cap regions. The L1Calo system and the detector are housed in two separate caverns.

The signal input for L1Calo comes from 7200 trigger towers (TT) of reduced granularity in the calorimeters (reduced in granularity in comparison to the standard calorimeter cells). These are formed by analogue summing of energies in calorimeter cells to create towers of granularity of mostly 0.1 x 0.1 in $\Delta\phi$ x $\Delta\eta$, although this is dependent upon the position of the TT in the detector, as the granularity becomes

coarser in the more forward parts of the endcaps and the FCALs. See figure 4.1 for an illustration of the differing granularities as a function of η.

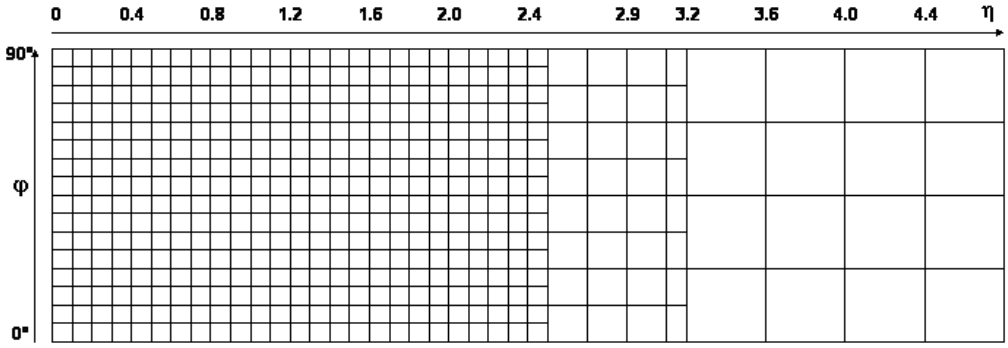

Figure 4.1: An illustration of how the trigger tower granularities vary as a function of their position in their detector [47].

There are three main sub-systems that comprise L1Calo, which are the PreProcessor (PPr), the Cluster Processor (CP) and the Jet/Energy-sum Processor (JEP) [47] (see figure 4.2).

- The PPr consists of 124 PreProcessor Modules, each of which receives 64 trigger tower signals, and its primary purpose is to convert the analogue signals received from the calorimeter into a digital signal that can be read by the processors that follow. This is performed using Flash Analogue to Digital Converters (FADCs), which convert the signals at a frequency of 40.08 MHz and a precision of 10 bits. The PPr also carries out bunch crossing identification (BCID), where each signal is linked to the correct bunch crossing that it came from. This is important in making sure the correct combination of signals are each linked to the correct BCID.

- The CP and JEP are similar in function in that they both search for certain features using digitized E_T values generated from the PPr and they both do so using overlapping, "sliding" windows of TTs (see section 4.2). The main difference is that the CP searches for electron/photon and τ/hadron signals whilst the JEP searches for jets and is the first stage of the missing E_T and

total E_T calculations.

The CP system is contained in four crates with each crate containing 14 modules (CPMs) and handling one quadrant of the calorimeter. The JEP on the other hand is a two crate system with each crate housing 16 modules (JPMs), eight of which are concerned with one quadrant of the calorimeter and the other eight handle the quadrant directly opposite in ϕ.

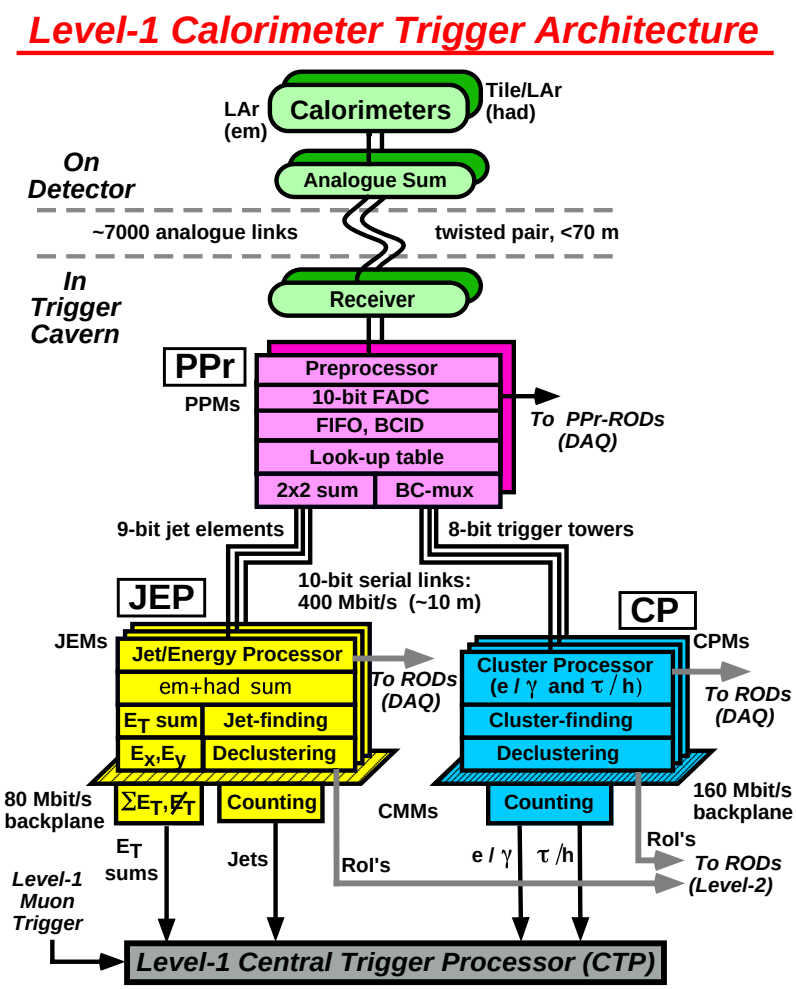

Figure 4.2: A diagram illustrating the various levels of the L1Calo Trigger [35].

Following the processing in the first three subsystems, the signals are passed to the Central Trigger Processor (CTP). The CTP compares the variety of information it receives from the CP/JEP to a series of preprogrammed requirements known as the

"trigger menu." For each item on the menu, the CTP makes an accept or reject decision. For events that are denoted as accepted, the event is passed on to the Level-2 trigger; events that are not accepted are deleted. The importance of this trigger is therefore apparent as when an event is rejected, the information cannot be retrieved.

4.2 EM Sliding Window Algorithm

The way that L1Calo selects events is by identifying Regions of Interest (RoIs) using a sliding window algorithm (see figure 4.3). The algorithm works by selecting a set of 2×2 electromagnetic TTs and comparing it to all other selections of 2×2 TTs in the surrounding area. The block which is determined to be the local energy deposit maximum is designated as a Region of Interest. The "sliding" part of the algorithm name refers to the fact that each individual tower is included in four 2×2 blocks rather than just one. Within the RoI, the maximum energy of the four possible 2×1 or 1×2 sums is defined as being the energy of the RoI. In addition to the RoI, the other regions of importance are the 2×2 block of Hadronic TTs directly behind them (HadCore), the 12 EM TTs that surround the RoI (EM Isolation Ring) and the 12 Hadronic TTs that surround the HadCore (Hadronic Isolation Ring) [47] (see figure 4.3).

Each of the four regions can be used to distinguish between types of events and, as will be shown in the next section, the EM isolation ring can be used to reduce rates of acceptance of background events whilst retaining true EM events. The need to reduce acceptance rates arises as a result of the expected increase in luminosity during the Run-2 phase of the LHC and beyond. The following section will present studies conducted in 2013 investigating potential methods of reducing the rate of event acceptance which may be implemented in the higher luminosity runs at the

LHC.

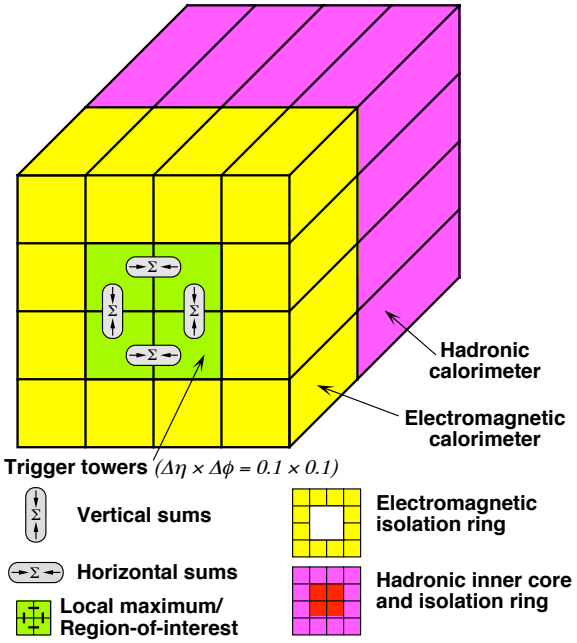

Figure 4.3: An illustration of the L1Calo sliding window algorithm and the various regions which form each window [47].

4.3 Reducing Trigger Rate Acceptance

At the end of the Run 1 data taking period in 2012, the trigger menu in the CTP had 16 available thresholds, nine of which were configured for EM events (i.e. events with a high p_T signal measured in the EM calorimeter) [47]. However, after the long shutdown period during 2013-2014 (LS1), the increase in beam energies and luminosities means that too many events meet these thresholds to allow the trigger rate constraint to be met. Therefore, more sophisticated L1 EM trigger options are required.

There are a limited number of options available for use in reducing the acceptance rate of EM events. One possibility is to increase the E_T thresholds. This would

achieve the rate reduction which is desired, for a trade off in terms of physics (i.e. electrons below this threshold would be lost).

Additional rate reduction can be gained by introducing cuts based on the contents of the various isolation regions. In the 2012 data taking period, L1Calo used a veto on the HadCore of less than or equal to 1 GeV. This chapter investigates what rate reduction can be achieved by introducing cuts requiring that E_T in the isolation region does not exceed a fixed value. The study was conducted during the long shutdown period in 2013.

This study investigates several possible hypothetical triggers which are outlined below:

- *L1_EM16HI*
- *L1_EM18VHI*
- *L1_EM25HI*

In the trigger names above, the number refers to the E_T threshold that the RoI is required to pass, the H means that the E_T in the HadCore region must be ≤ 1 GeV and the I indicates that various possible isolation cuts in the EM calorimeter have been investigated and implemented. Finally, the V in *L1_EM18VHI* indicates that the EM threshold required varies as a function of pseudorapidity:

- in the regions $|\eta| \leq 0.8$ and $2.0 < |\eta| \leq 2.5$, $E_T \geq 20$ GeV,
- in the regions $0.8 < |\eta| \leq 1.2$ and $1.6 < |\eta| \leq 2.0$, $E_T \geq 19$ GeV, and
- in the region $1.2 < |\eta| \leq 1.6$, $E_T \geq 18$ GeV.

4.4 Rates and Efficiency Measurements

4.4.1 Rate Estimations

As ATLAS uses a three tiered trigger system, any events that are accepted by L1 are subjected to two further layers of scrutiny. This makes determining the rate of acceptance of events at L1 more complex as some events that passed the L1 trigger will be removed by the HLT and hence we cannot estimate the rate accurately in standard conditions.

In order to combat this problem, L1 rates are estimated using "Enhanced Bias" data [48]. For selected runs, random events which pass L1 criteria are accepted without being subjected to further HLT trigger conditions. This means that the rate of acceptance is proportional to the number of RoIs generated from each L1 trigger item from the trigger menu. In order to produce the rate estimations seen in figure 4.4, a sample from period L in 2012 was used (referring to November 30th - December 6th 2012).

The rate reduction obtained for each of the fixed isolation L1_EMnnHI triggers (i.e. L1_EMnnHI c.f. L1_EMnnH) can be seen in figure 4.4. These show the ratio of the rate of event acceptance between the trigger when it has the isolation requirement and when it does not. This is illustrated for a range of fixed isolation values, plotted along the x-axis.

The three plots in figure 4.4 highlight the relative power of each trigger and of each isolation veto. It can be seen that the rate reduction is increased by a stricter veto (as would be expected), but also that the amount of rate reduction for each veto increases at higher E_T thresholds. For example, for an isolation veto of $I \leq 4$ GeV,

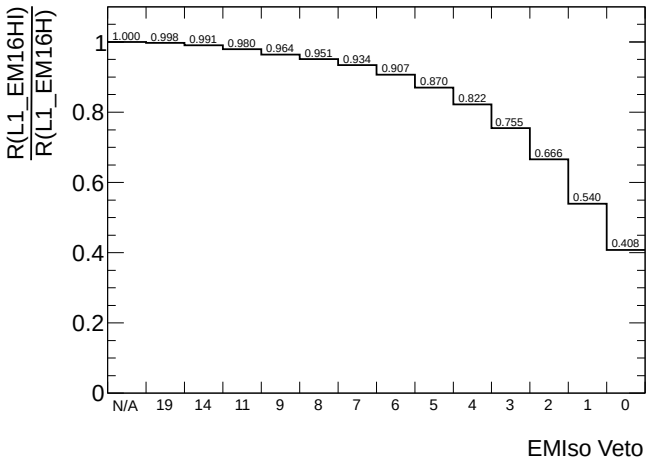

(a) *L1_EM16HI*

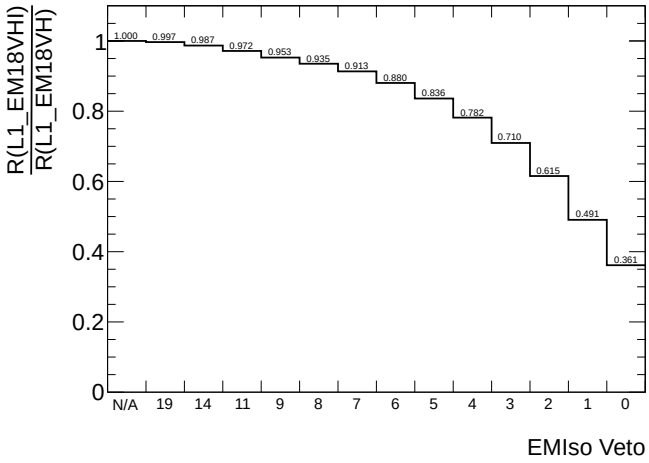

(b) *L1_EM18VHI*

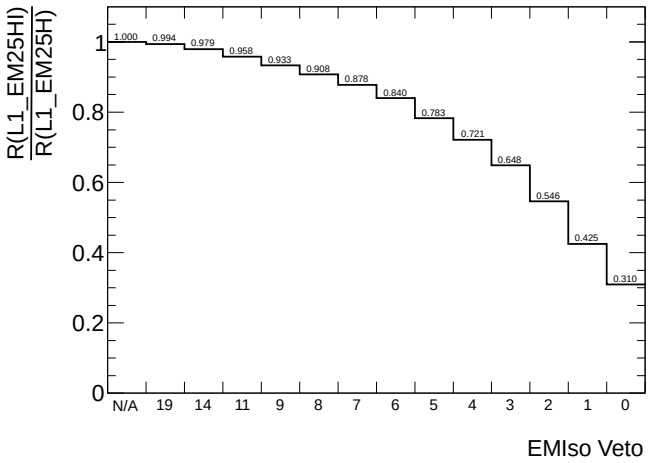

(c) *L1_EM25HI*

Figure 4.4: The rate reduction found for the three fixed L1_EMnnHI triggers for various isolation values. The energy in the EM isolation ring is required to be less than or equal to the isolation veto (given in GeV) for each of the veto values.

the rate reduction compared to no isolation is 17.8% for *L1_EM16HI*, 21.8% for *L1_18VHI* and 27.9% for *L1_EM25HI*. At higher EM thresholds, it is expected that background jet events (i.e. events which produce electrons as part of a shower of other particles) would be more energetic and deposit more energy in the isolation region, and thus the rate reduction due to isolation cuts would be expected to be higher, and this is the case.

With the higher energy threshold, a higher proportion of electrons which should be accepted will leak a sufficient amount of energy into the isolation region to cause them to be rejected. This contributes to the rate reduction. Therefore, whilst the isolation vetoes appear to offer a good of rate reduction, it must be considered that this could be caused in part by rejection of good electrons. The proportion of the rate reduction which is attributable to jet rejection compared to erroneous electron rejection will be addressed by considering the efficiency of the vetoes.

4.4.2 Efficiency Measurements

The efficiency of the trigger is measured by comparing the number of events accepted before and after an EM isolation veto. In order to do this, the Z$\rightarrow e^+e^-$ Tag and Probe Method is used.

4.4.2.1 Z$\rightarrow e^+e^-$ Tag and Probe

The Z$\rightarrow e^+e^-$ Tag and Probe method has been utilised in order to produce a sample of offline electrons which are created by a Z boson decaying to an electron-positron pair. To do this, one of the decay products of the Z boson is "tagged" (this is the product which triggered the event) and subsequently the trigger's efficiency is tested by its ability to have found the second electron (the "probe") [48]. This produces a sample of electrons which are of good purity.

The tag electron is required to meet certain criteria in order for it to be selected. These include:

- A high tranverse momentum ($p_T > 25$ GeV)
- Must be matched to an Inner Detector track
- Must be associated to an Event Filter electron (within $\Delta R < 0.15$).

If a tag electron is found, the probe electron is required to meet the same p_T requirements as the tag, and in addition :

- The tag-probe pairing must have opposite charge (i.e. electron must be matched with positron)
- The invariant mass of the system must measure $80 < m_{e^+e^-} < 100$ GeV (i.e. the invariant mass $m_{e^+e^-}$ must be close to the Z boson mass).

4.4.2.2 Efficiency Calculations

The plots presented in figure 4.5 show the efficiency turn-on curves for the three triggers for a variety of fixed isolation cuts. These curves plot the ratio of the number of probe electrons that pass the trigger when the isolation trigger is implemented compared to the total number of probe electrons as a function of E_T. The plots have been produced using 2012 period L data.

The efficiency turn-on curves appear to be consistent with expectation. Around the threshold energy, the efficiency increases because the trigger is no longer removing these electrons, giving the "turn-on region." As is apparent in all three triggers, the efficiency in the plateau region is dependent on the strictness of the isolation requirement; the tighter the restriction, the lower the efficiency in the plateau (in general). This is especially apparent for the $I = 0$ case, where this requirement

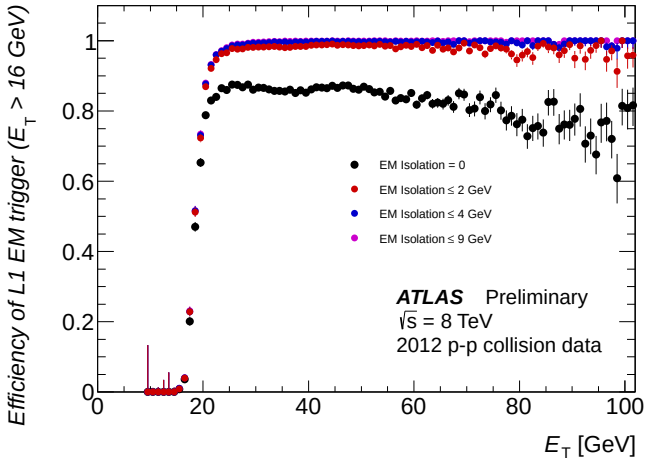

(a) *L1_EM16HI*

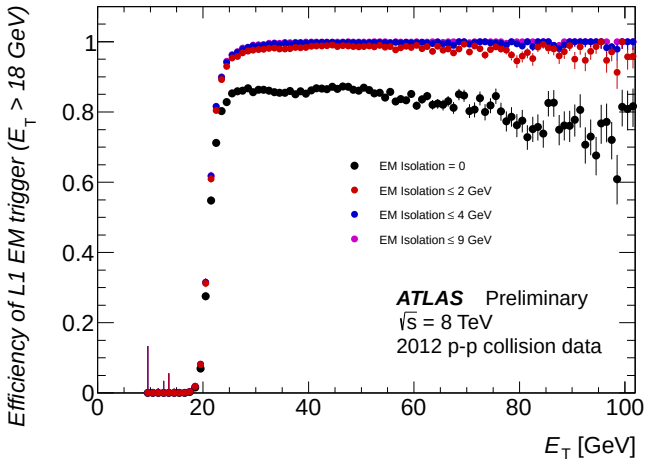

(b) *L1_EM18VHI*

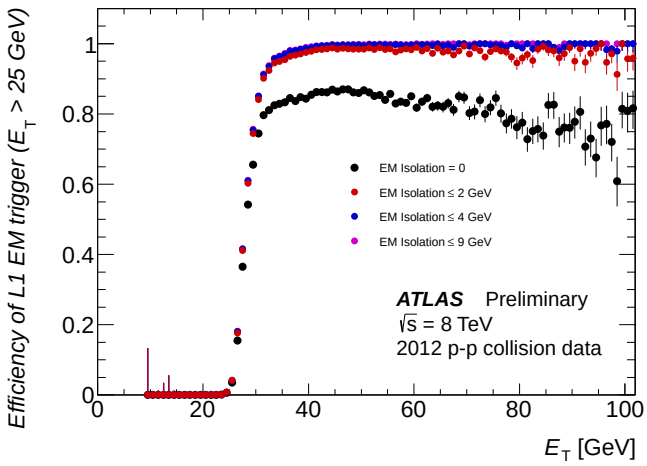

(c) *L1_EM25HI*

Figure 4.5: The efficiency turn-on curves corresponding to the three fixed L1_EMnnHI triggers for various EM isolation values.

will remove all events which have any isolation ring leakage whatsoever and a small amount of leakage is to be expected. Consequently, $I = 0$ can only be used where loss of efficiency is not of great concern.

For the other triggers, there is minimal reduction in efficiency, with noticeable effects only occurring in the high E_T region and it is the region close to the threshold E_T which is of importance for this study. The efficiency curves therefore do not highlight any significant concerns regarding use of a fixed isolation trigger.

4.4.3 Rate of Acceptance Against Efficiency

Figure 4.6 illustrates the rate reduction and corresponding efficiency for triggers at several threshold values and with various fixed isolation requirements. The value of the efficiency is taken to be the integrated efficiency between E_T values of 30 and 100 GeV. This range was selected in order to investigate the efficiency in the plateau region and to ignore the turn-on region.

Figure 4.6 also highlights the fact that higher threshold triggers (i.e. *L1_EM25HI*) exhibit greater rate reduction through requiring isolation than the lower threshold triggers, without a noticeable drop off in efficiency.

This plot will be discussed further in section 4.5.

4.4.4 Isolation Trigger Efficiency as a Function of Pile-up

The efficiencies of the triggers are also studied as a function of pile-up to see if an increase in pile-up adversely affects the triggers' usefulness. During Run 2, there will be a higher amount of pile-up per bunch crossing and at higher pile-up, the efficiency of the trigger may decrease and so this is an important effect to consider. In the data yielded in the 2012 period L run, the average pile-up ranged from 10-

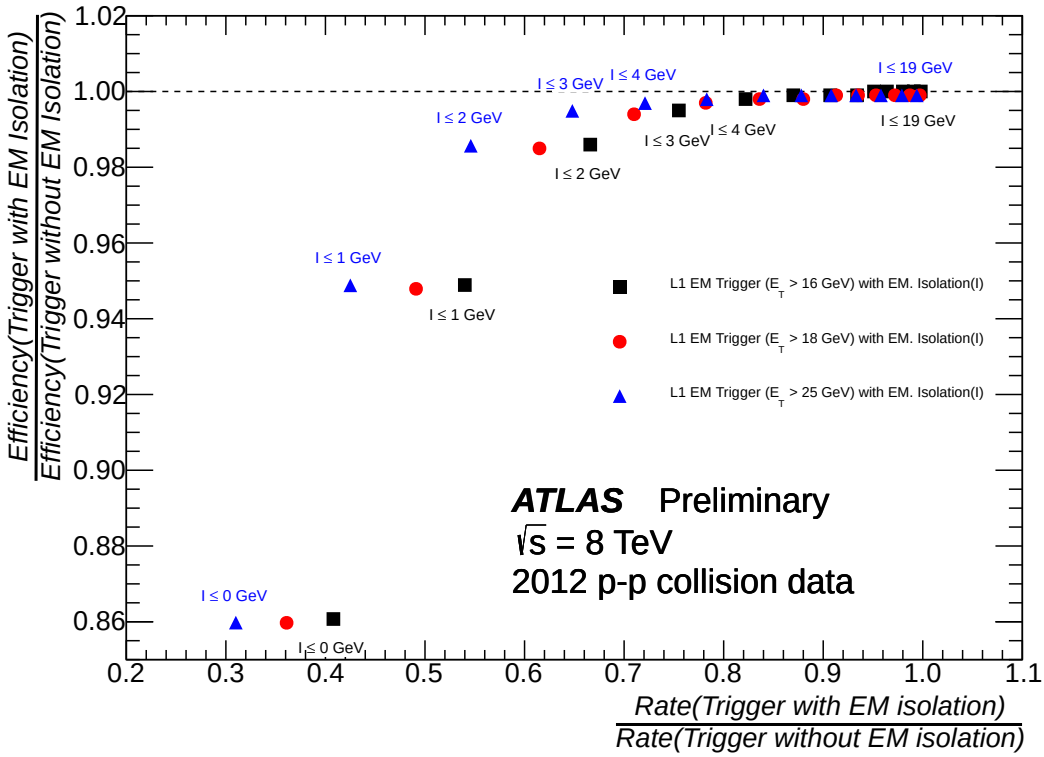

Figure 4.6: The values of rate reduction plotted against the corresponding integrated efficiency values for the three fixed isolation triggers and a variety of EM isolation values $I \leq x$, where $x = 0$, 1, 2, 3, 4, 5, 6, 7, 8, 9, 11, 14, 19 GeV.

40 interactions per bunch crossing. After LS1, pile-up will eventually increase to around 50 interactions [49].

The plots in figure 4.7 show the efficiencies of the three triggers for isolation vetoes of $I = 0$ GeV, $I \leq 2$ GeV and $I \leq 4$ GeV as a function of the average number of interactions per bunch crossing, μ. The analysis considers only probe electrons with $E_T \geq 30$ GeV.

As can be seen, the $I = 0$ case does demonstrate a strong μ dependence. However, as has already been discussed, the $I = 0$ case is not a feasible choice for our isolation veto as it cuts all events with any activity in the isolation ring and is therefore expected to be sensitive to pile-up.

The other two vetoes do not display as strong a dependence on μ. However, there is a dependence in the $I \leq 2$ GeV veto. The period L data used in these studies does not have a particularly high pile-up and further studies will be useful in determining how Run 2 levels of pileup affect the efficiencies.

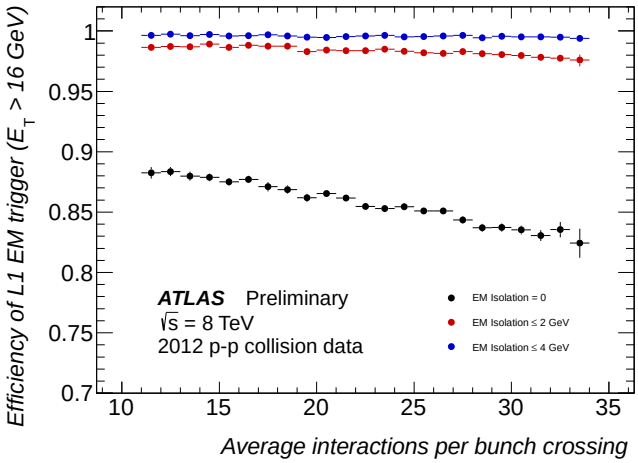

(a) *L1_EM16HI*

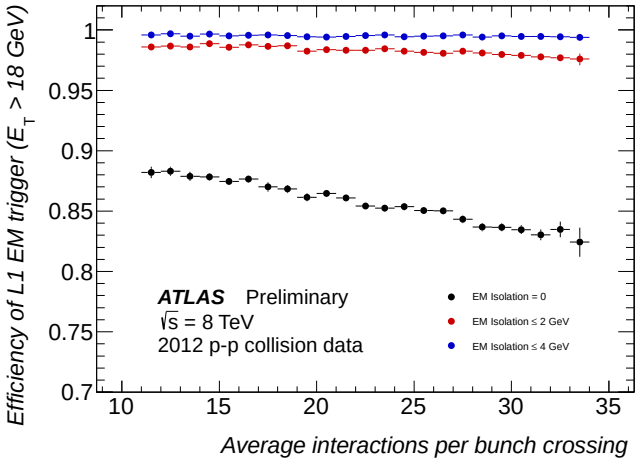

(b) *L1_EM18VHI*

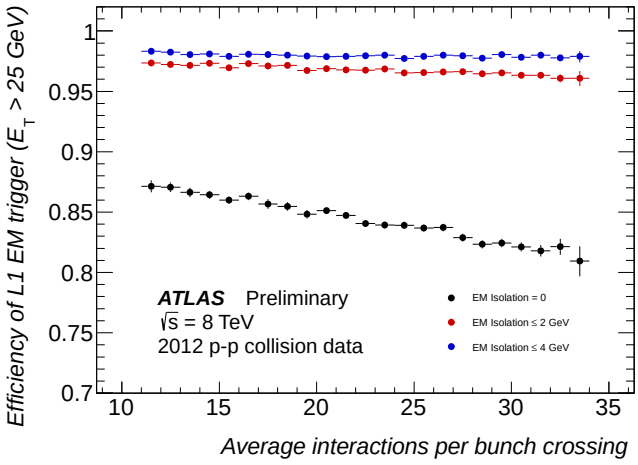

(c) *L1_EM25HI*

Figure 4.7: The efficiency of probe electrons with $E_T \geq 30$ GeV as a function of pile-up for the three fixed isolation triggers L1_EM16HI, L1_EM18VHI and L1_EM25HI. The EM isolation vetoes considered are $I = 0$ GeV, $I \leq 2$ GeV and $I \leq 4$ GeV.

4.5 Conclusions of EM Isolation Study

The optimal balance between rate reduction and efficiency loss is subjective, but one can conclude from figure 4.6 that significant rate reductions can be made at the expense of modest efficiency losses through the use of an EM isolation veto. For example, a rate reduction of 18% can be achieved at the expense of an efficiency loss of just 0.5% by introducing a veto $I \leq 5$ GeV for the L1_EM16HI trigger. Another possible working point would be a high rate reduction with a significant loss in efficiency (e.g. a rate reduction of 61% can be achieved at the expense of an efficiency loss of 13% using the strongest possible criterion where $I = 0$ for the L1_EM16HI trigger).

It is also worth noting that as the threshold energy increases, the effectiveness of the fixed isolation trigger increases, without a noticeable effect on the efficiency of the trigger. During Run 2, the thresholds are greater than in the 2012 trigger menu. This would therefore suggest that the usefulness of isolation as a discriminator will increase.

The investigation into the pile-up dependence of the isolation trigger has shown that, with the exception of the $I = 0$ case, there does not appear to be a significant impact on the efficiency of the triggers with higher pile-up. The $I = 0$ case is unlikely to be used in any possible future trigger menu as it will cut events with any EM isolation ring activity whatsoever. This is physically unfeasible as we would expect a small amount of noise in many cases and such a tight requirement will severely impact on efficiency, as can be seen from the results in section 4.4.2.2.

The studies presented are included within an ATLAS internal note, which also considered the outcomes of using a fractional EM isolation veto based on the size of the

energy deposited in the RoI [50]. The fractional isolation studies follow a similar methodology to the fixed isolation studies. The results of this area of the study conclude that a fractional isolation veto also shows good discrimination of events, with fractional vetoes offering better efficiencies for the same rate reductions when compared to a fixed isolation trigger. One issue with fractional isolation is that for low values of E_T in the RoI, the isolation value will be concurrently low and the rate reduction will be poorer than in a fixed isolation scheme

In Run 2, an isolation scheme has been implemented in some trigger objects. The scheme which has been implemented is a hybrid of the fixed isolation approach presented here and the fractional isolation shown in [50]. In this scheme, a minimum isolation cut in the EM isolation ring is applied, with a fractional isolation applied above a certain E_T threshold in the RoI. Additionally above a certain E_T threshold, no isolation is applied. This hybrid has been adopted in order to optimise the rate reduction whilst maintaining a high efficiency across all values of E_T.

Chapter 5

SPIN CORRELATION IN TOP QUARK PAIRS

The top quark is the heaviest particle in the Standard Model of Particle Physics. It is also the quark with the shortest lifetime ($\approx 5 \times 10^{-25}$ s) and as such decays before it can hadronise. This also means that it decays before the spins of the top and antitop can become uncorrelated due to the effects of QCD. Both of these facts allow the degree of spin correlation in top-antitop quark pairs to be measured by use of angular distributions of the decay products of the top.

The degree of spin correlation is predicted precisely from the Standard Model and thus observations made can be compared to this prediction, with any significant deviations being highlighted as a possible source of Beyond Standard Model (BSM) physics. BSM models can alter the degree of spin correlation by either:

- A modification to the production mechanism of the $t\bar{t}$ pairs predicted by the SM. Potential modifications include $t\bar{t}$ pairs produced by a high mass Z' boson [51] [52] or a heavy Higgs boson [53], or,
- Altering the expected decay of the top quark, such as where a top quark decays into a b-quark and a theoretical charged spin-0 Higgs boson [54] [55].

In addition, the amount of spin correlation in top-antitop quark pairs is predicted to vary as a function of the invariant mass of the produced top-antitop pair, $M_{t\bar{t}}$. By performing a differential measurement with respect to $M_{t\bar{t}}$, this analysis aims to

test the accuracy of this prediction also.

5.1 Spin Correlation

Due to the short lifetime of the top quark, spin correlation cannot be directly experimentally measured. As a result, the spin correlation must be measured by other means, such as using angular distributions of the decay products of the top quarks. As discussed in section 2.4, the top quark almost exclusively decays into a W boson and a b-quark. Following this, there are three final states into which a $t\bar{t}$ quark pair can decay, which are:

- All hadronic channel, where both W bosons decay hadronically;
- Semi-leptonic channel, where one W boson decays hadronically and one leptonically;
- Dilepton channel, where both W bosons decay leptonically.

To decide which channel to use, the first consideration is the *spin analysing power* of the decay products of the top quark, which determines the amount of information about the top quark's spin carried by the angular distribution of the decay product. The value of the spin analysing power, α_i, can be between 1 and -1 , with the maximum amount of information being given by a value of $\pm$ 1.

In table 5.1, we see the spin analysing powers for the possible decay products of the top quark, calculated at leading order and next to leading order. The relationship between the spin analysing power and the single differential angular distribution of the top quark decay products is shown in equation 5.1 [56].

$$\frac{1}{\Gamma}\frac{d\Gamma}{d\cos(\theta_i)} = \frac{1}{2}(1 + \alpha_i \cos(\theta_i)) \tag{5.1}$$

Table 5.1: The spin analysing powers, α_i, for various top quark decay products at leading order (LO) and next to leading order (NLO) (LO being tree level decays and NLO including corrections for additional internal loops). The signs are reversed for antiparticles [57].

	b-quark	W^+	l^+	d quark or $\bar{s}$ quark	u quark or c quark
α_i(LO)	-0.41	0.41	1	1	-0.31
α_i(NLO)	-0.39	0.39	0.998	0.97	-0.32

where Γ is the top quark decay width and θ_i is the angle between the decay product i of the top quark and the spin direction of the top in the top quark rest frame. Here we see that the spin analysing power acts as a multiplicative factor, and that a larger magnitude of α_i maximises the information given by the angular distribution.

As can be seen from table 5.1, maximum information is found by using either charged leptons or down type quarks at leading order, with a small correction at next to leading order. The caveat in using down type quarks is that they are difficult to identify experimentally whereas as charged leptons are relatively easy to reconstruct. Therefore in this analysis, the dilepton channel is used. The experimental benefits and detractions of using this channel are discussed in section 2.4.

Equation 5.1 can be modified in order to define the correlation between the decay products of the top and antitop. This is shown in equation 5.2 [56].

$$\frac{1}{\sigma}\frac{d^2\sigma}{d\cos(\theta_+)d\cos(\theta_-)} = \frac{1}{4}(1 - C\cos(\theta_+)\cos(\theta_-)) \tag{5.2}$$

where σ is the cross section for the measurement, $\theta_\pm$ is the angle between the direction of flight of the decay product in the (anti)top rest frame and the *spin quantisation basis*, and C is defined as the spin correlation strength and includes information regarding the spin analysing powers of the decay products. The spin quantisation basis is a geometry, measured in the $t\bar{t}$ rest frame, which is chosen in order to maximise the measurable amount of correlation. Choices of basis will be

discussed in section 5.1.1. The asymmetry A, which is related to C, is defined in terms of the fractional difference between the number of top-antitop quark pairs where the spins are aligned and anti-aligned with respect to each other:

$$A = \frac{N_{like} - N_{unlike}}{N_{like} + N_{unlike}} = \frac{N(\uparrow\uparrow) + N(\downarrow\downarrow) - N(\uparrow\downarrow) - N(\downarrow\uparrow)}{N(\uparrow\uparrow) + N(\downarrow\downarrow) + N(\uparrow\downarrow) + N(\downarrow\uparrow)} \tag{5.3}$$

In this equation, $N(\uparrow\uparrow) + N(\downarrow\downarrow)$ represents the number of events where the spin directions of the top and antitop are aligned and $N(\uparrow\downarrow) + N(\downarrow\uparrow)$ represents the number of events where the spins are anti-aligned. The asymmetry A is not directly the strength of the spin correlation, which is defined fully as being:

$$C = 4A|\alpha_+\alpha_-| \tag{5.4}$$

to take into account the spin analysing powers of the decay products. However, in the case where the dilepton channel is being used for the analysis and therefore the spin analysing power is approximately 100%, the approximation of $C \approx 4A$ is valid and will be used.

5.1.1 Choice of Quantisation Basis

In order to measure the degree of spin correlation using the angular distributions of the decay products, it becomes necessary to define a spin vector against which to measure the angular distributions. Whilst the choice of the basis is arbitrary, certain geometries will allow for the degree of observed correlation to be maximised, such that the spins are either fully correlated or anti-correlated. The SM predicted degree of spin correlation, A, is dependent on the choice of quantisation basis.

Due to there being no single process through which all $t\bar{t}$ pairs are produced at the LHC, it is not possible to construct a basis with fully observed correlation (or

anti-correlation), however it is still in the interests of the analysis to maximise what can be observed. Therefore, several geometries have been considered and are discussed below, beginning with geometries that were used at the Fermilab Tevatron, before proceeding onto schemes more applicable for the LHC. For this discussion, it is assumed that two vectors are created: one to define an angular distribution of the top quark decay products and a corresponding vector for the antitop decay products. In the definitions below, these vectors will be referred to as $\bar{a}$ and $\bar{b}$ respectively.

5.1.1.1 Beam Line Basis

In this scheme, the basis vector is defined as being the direction of flight of one of the incoming partons. To simplify this, in the case of the LHC, the vector is defined as being the direction of the incoming beam, $\bar{m}$:

$$\hat{\mathbf{a}} = -\hat{\mathbf{b}} = \hat{\mathbf{m}}. \tag{5.5}$$

This is the easiest basis to form as the geometry is already defined within the laboratory frame. However at the LHC, it is not very useful for the purposes of measuring spin correlation. This scheme is relevant for lower velocity processes (in particular when $\beta \approx 0$, where β is the speed of the particle expressed as a fraction of the speed of light). At the LHC, where the value of β is close to 1, this is not a practical basis to use and the degree of spin correlation that can be measured is minimal. At the CDF experiment, where there were much lower energies and different dominant production processes, this was the preferred basis although measurements were also made using the helicity basis [58].

5.1.1.2 Off Diagonal Basis

The off diagonal basis has been formed in order to generate a geometry in which the observable unlike-spin correlation in $t\bar{t}$ pairs is 100% (i.e. $A = -1$) for the $q\bar{q} \to t\bar{t}$

process as well as for unlike-helicity gluon-gluon fusion. The basis is chosen such that the spins of the top and antitop are parallel with respect to each other. A key feature of its formulation is that for these processes, in the high and low energy limits ($\beta \to 1$ / $\beta \to 0$), this basis becomes equivalent to the helicity and beam line bases respectively. This basis is defined by creating a vector which has an angle ψ to the incoming quark using the following formula:

$$\tan\psi = \frac{\beta^2 \sin\theta \cos\theta}{1 - \beta^2 \sin\theta} \tag{5.6}$$

where θ is the angle between the top quark and the incoming parton in their c.m. frame. One point to consider is that whilst this is optimal for experiments such as the Fermilab Tevatron where the dominant production process is $q\bar{q} \to t\bar{t}$, at the LHC the dominant process is a mixture of like and unlike-helicity gluon-gluon fusion, which would suggest this may not be a sensible basis for maximising the observable spin correlation (see figure 5.1) and therefore the off diagonal basis should not be considered.

5.1.1.3 Helicity Basis

The helicity basis is more applicable for measurements at the LHC as it performs well for high β interactions and also for a variety of production processes (i.e. gluon-gluon and quark-antiquark interactions). This basis maximises the observable like-spin correlation (i.e. $A = 1$) for gluon-gluon fusion processes in which the gluons have the same sign of helicity. The definition of this framework requires a boost from the laboratory frame into the rest frame of the $t\bar{t}$ system. The spin quantisation vector is defined as the direction of flight of the top quark subsequent to this boost:

$$\hat{\mathbf{a}} = -\hat{\mathbf{b}} = \hat{\mathbf{n}} \tag{5.7}$$

where $\bar{n}$ is the aforementioned direction of the top quark in the $t\bar{t}$ rest frame. The standard nomenclature of this basis requires that the antitop is measured relative to a vector in the opposite direction to that of the top quark. This basis does not offer a maximal measure of spin correlation but does provide a more sensitive measurement than the beam line basis.

5.1.1.4 LHC Maximal Basis

The ideal situation at the LHC would be to find an analogous basis to the off diagonal but which maximises the observable spin correlation for the $gg \to t\bar{t}$ process (i.e. to a value of $A = \pm 1$. However, this has been shown to be impossible [59]. Therefore, a basis has been devised which results in the maximum amount of observable spin correlation in top quark pairs produced through gluon-gluon fusion; a value of around 46% for a c.m. energy of 8 TeV. For this basis, an optimal spin quantisation axis is calculated on an event by event basis. The derivation and calculation of this maximal basis can be seen in [59].

A prediction of the degree of spin correlation for various centre of mass energies measured using each of the bases discussed can be seen in figure 5.1.

5.1.2 $\Delta\phi$ as an Observable

Equation 5.2 relates the spin correlation strength to the $\cos(\theta_+)\cos(\theta_-)$ distribution. However, this analysis will instead investigate the azimuthal angular separation distribution, $\Delta\phi$, between the charged lepton decay products of the W bosons which themselves arise from the decay of the top and antitop. The $\Delta\phi$ distribution is measured in the laboratory frame.

$\Delta\phi$ is predicted to be sensitive to the degree of spin correlation in top-antitop quark

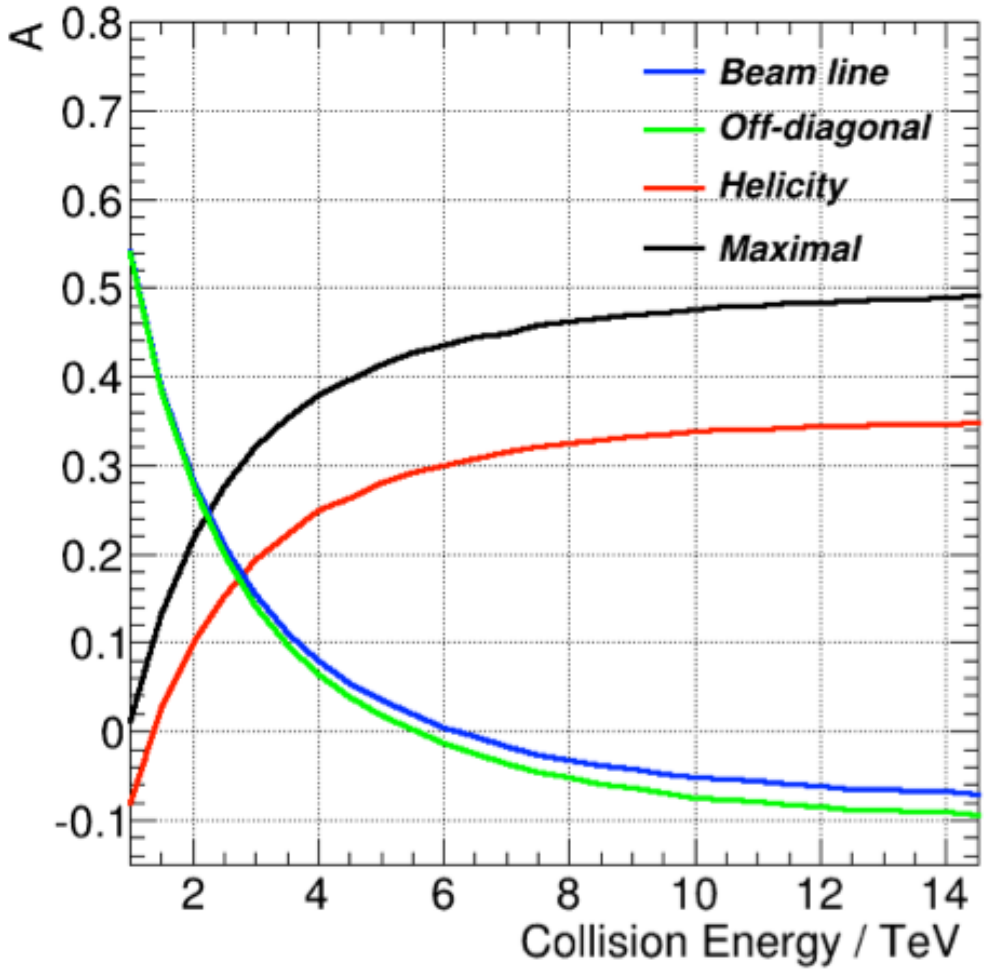

Figure 5.1: Predicted spin correlation asymmetry values for different quantisation bases in proton-proton collisions for a number of c.m. energies [56]. The prediction has been made using the MC@NLO generator [60].

pairs [61], and has the additional benefit of not needing reconstruction of the top and antitop quarks, which has inherent experimental challenges. Note that in this analysis there will be measurements of the inclusive spin correlation in top-antitop quark pairs, as well as differential measurements in particular invariant mass ranges of the top-antitop system ($M_{t\bar{t}}$). For the differential measurement, reconstruction of the $t\bar{t}$ system will be required so this benefit of using $\Delta\phi$ as an observable is only applicable in the inclusive measurement. The distribution is still beneficial as the $\Delta\phi$ angle is relatively simple to measure and has good resolution in the ATLAS detector.

In the high energy limit where the velocity v of the charged leptons is close to c, the direction of the top spin is approximated to its helicity. In this scenario, the charged leptons are preferentially produced with the same direction of flight if the spin directions of the top quarks are anti-parallel in their rest frame (i.e. have the same spin). Conversely, if the spins of the top and antitop are parallel in their rest frame (so have opposite spins), then correspondingly the decay products will preferentially be produced back to back. This indicates that the azimuthal angle difference between the decay products is a source of information about the spin correlation of the top quarks.

One consideration is how the azimuthal direction of the decay products is affected by boosts of the system. However, this is not expected to be a major factor in the analysis as the most significant boost of the $t\bar{t}$ system is in the z-direction (beam line), which has negligible impact on the ϕ of the decay products.

Therefore using $\Delta\phi$ as an observable is a viable means of measuring the spin correlation. In figure 5.2, the theoretical parton level $\Delta\phi$ distribution for both the SM correlated and also an uncorrelated model (i.e. one produced such that $A = 0$) can be seen for the dilepton decay chain for $t\bar{t}$ pairs produced at $\sqrt{s} = 8$ TeV.

For the case where there is no spin correlation ($A = 0$), then there will be no preferred production of decay products with an aligned or anti-aligned momentum due to spin correlation (although the $\Delta\phi$ distribution will not be flat as other effects have an impact on this quantity). However, as the degree of spin correlation increases, then there will be a preferential production of decay products with a smaller azimuthal angle difference, i.e. the gradient of the $\Delta\phi$ distribution will decrease.

A measurement of spin correlation using $\Delta\phi$ means that none of the quantisation

bases described in section 5.1.1 are used. A consequence of this is that the distribution does not offer a direct measurement of the asymmetry value of A. Instead, a template fit method is used which compares data to two simulated scenarios: one with an SM level of spin correlation and one with zero spin correlation. The fit gives a value of f_{SM}, which provides an estimate of how closely the data follows one scenario over the other. A value of $f_{SM} = 1$ implies that the amount of correlation is precisely in line with the SM prediction, whereas $f_{SM} = 0$ corresponds to the spins being entirely uncorrelated. If $0 < f_{SM} < 1$, the implication is that the spins are less correlated than predicted in the SM. In the case where $f_{SM} > 1$, this implies that the spins are more correlated than predicted in the SM. A more detailed description of the template fitting procedure and testing of the method is presented in section 7.1.

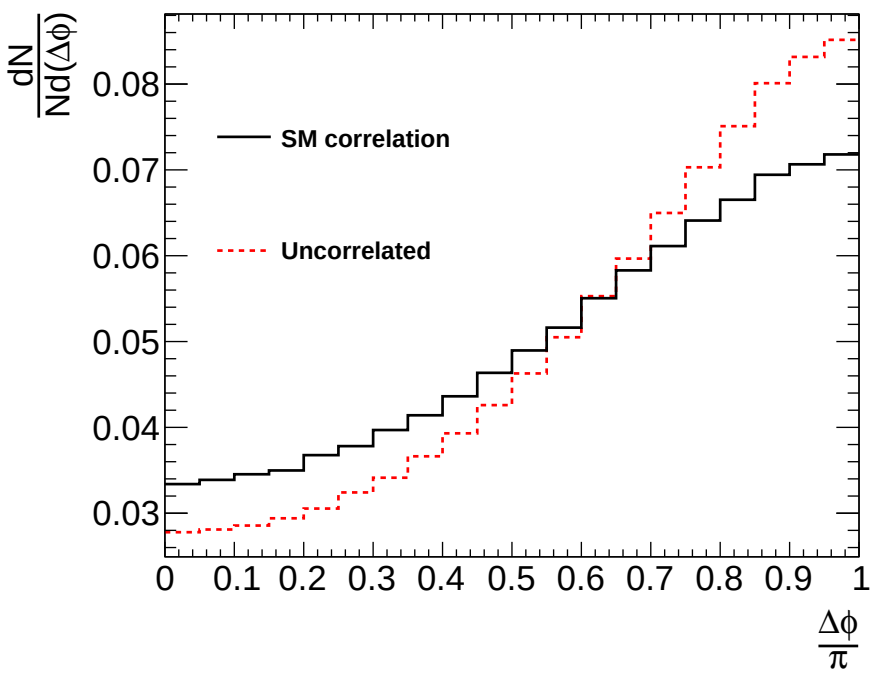

Figure 5.2: Parton level distribution of the $\Delta\phi$ distribution in the combined dilepton channel at $\sqrt{s} = 8$ TeV using the MC@NLO Monte Carlo generator [60] for an SM model of spin correlation and an uncorrelated model.

5.2 Spin Correlation as a Function of the $t\bar{t}$ System Invariant Mass

The dominant process for $t\bar{t}$ production at the LHC is gluon-gluon fusion. Gluons themselves have an helicity and so when they undergo fusion, this can be a like- or unlike-helicity process [62]. This fact is one of the reasons why a quantisation basis which leads to 100% observable correlation cannot be created for a gluon-gluon fusion process [61].

This phenomenon also leads to the effect that the amount of spin correlation varies as a function of $M_{t\bar{t}}$. For lower values of $M_{t\bar{t}}$ (less than $\approx$ 400 GeV), the like-helicity gluon-gluon fusion dominates the production of $t\bar{t}$ pairs, but this dominance decreases as $M_{t\bar{t}}$ increases [62]. This is because the squared matrix element for production of $t\bar{t}$ pairs from like-helicity gluon fusion is suppressed in the high energy limit, i.e. where $\beta \to 1$, and conversely at low energy, unlike-helicity gluon fusion is suppressed [62]. In a low energy limit, it would be expected that more $t\bar{t}$ pairs are produced at the mass threshold and therefore have a lower invariant mass, which explains this effect. Figure 5.3 illustrates the expected $t\bar{t}$ differential production cross sections for like- and unlike-helicity gluons, as well as for quark-antiquark processes at the LHC with a c.m. energy of 14 TeV. The behaviour is similar at a c.m. energy of 8 TeV.

When considering the propagation of helicities in the gluon to the spins of the $t\bar{t}$ pairs, it is found that the only non-zero contributions to the squared matrix element for production comes when:

$$g_L g_R \to t_\uparrow \bar{t}_\downarrow \text{ or } t_\downarrow \bar{t}_\uparrow \quad \text{and} \quad g_R g_L \to t_\uparrow \bar{t}_\downarrow \text{ or } t_\downarrow \bar{t}_\uparrow \tag{5.8}$$

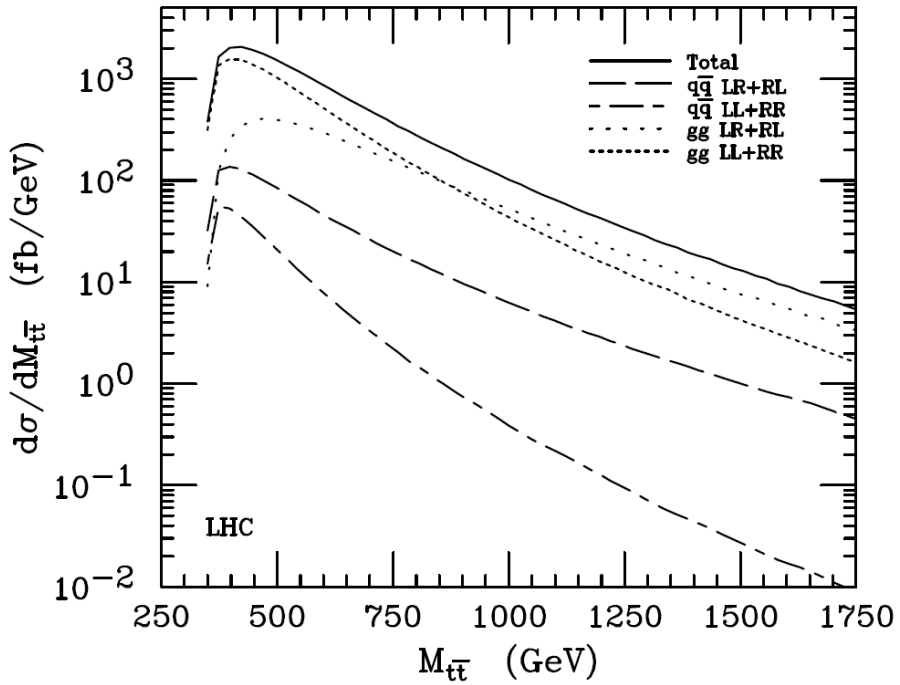

Figure 5.3: Predicted differential $t\bar{t}$ production cross sections as a function of $M_{t\bar{t}}$ at a centre of mass energy of 14 TeV at the LHC. This has been further separated into the expected cross sections for like and unlike-helicity gluon fusion and quark-antiquark processes [62].

$$g_R g_R \to t_\uparrow \bar{t}_\uparrow \text{ or } t_\downarrow \bar{t}_\downarrow \quad \text{and} \quad g_L g_L \to t_\uparrow \bar{t}_\uparrow \text{ or } t_\downarrow \bar{t}_\downarrow \tag{5.9}$$

when using the helicity spin quantisation basis [62]. This, in conjunction with figure 5.3 implies that at low $M_{t\bar{t}}$, it would be expected to see more spin correlation in $t\bar{t}$ pairs, and vice-versa.

In measuring the $\Delta\phi$ of the charged lepton decay products of $t\bar{t}$ pairs, this effect is also expected to be noticeable. As mentioned in section 5.1.2, $t\bar{t}$ pairs with like spins are expected to decay preferentially to products with a smaller opening angle than those with unlike spins. It is logical therefore to conclude that for pairs with invariant mass close to the production threshold, a comparative increase in low $\Delta\phi$ events should be observed. Reference [62] suggests implementing an $M_{t\bar{t}}$ cut in order to maximise the degree of measurable spin correlation by utilising this logic.

For this analysis, rather than using a single cut, several distinct regions of $M_{t\bar{t}}$ will be considered, the $\Delta\phi$ distributions measured in each and a subsequent value of f_{SM} generated. It is expected that at low $M_{t\bar{t}}$, there will be a greater distinction between the SM prediction and the uncorrelated prediction due to the higher amount of observable correlation. Experimentally, this should make it easier to determine whether data is more adherent to an SM or uncorrelated regime. At higher values of $M_{t\bar{t}}$ the reverse is true and the difference between the SM and uncorrelated cases will be small. An example of the two cases at several values of $M_{t\bar{t}}$ is presented in figure 5.4.

5.3 Previous Measurements

Several measurements of spin correlation strength have been made previously, both at the LHC and the Tevatron, which will be discussed below.

5.3.1 Spin Correlation Measurements at the Tevatron

The DØ Collaboration at Fermilab performed a measurement of spin correlation using the dilepton channel [63]. The analysis used an integrated luminosity of 125 pb^{-1} at a proton-antiproton centre of mass energy $\sqrt{s} = 1.8$ TeV. However, due to the low production cross section at the Tevatron, this corresponded to only 6 dilepton events. This analysis measured the double differential $\cos\theta_+ \cos\theta_-$ distribution, where θ_+, θ_- are the angles between the charged lepton and the spin quantisation basis in the rest frame of the parent top and antitop quark respectively.

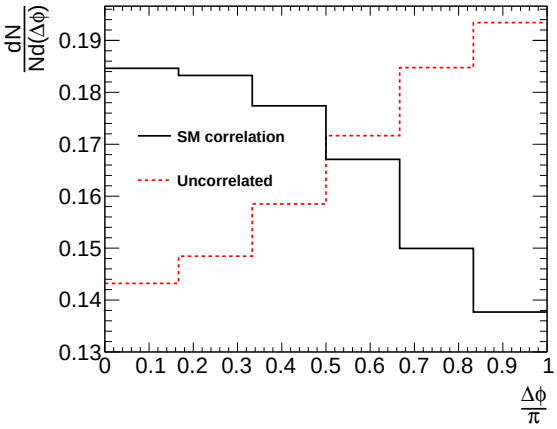

(a)

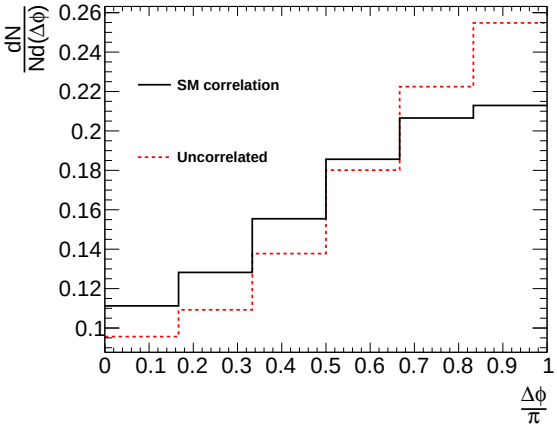

(b)

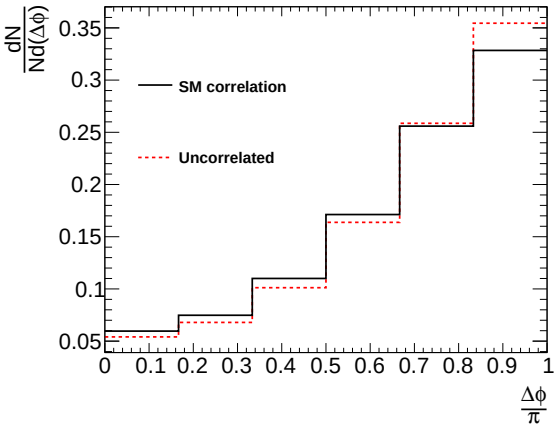

(c)

Figure 5.4: Parton level distribution of the $\Delta\phi$ distribution in the combined dilepton channel at $\sqrt{s} = 8$ TeV using the MC@NLO Monte Carlo generator [60] for an SM model of spin correlation and an uncorrelated model in various $M_{t\bar{t}}$ ranges: a) $M_{t\bar{t}} \leq 415$ GeV, b) 415 GeV$< M_{t\bar{t}} \leq 505$ GeV and c) $M_{t\bar{t}} > 505$ GeV. The reason for this choice of ranges is discussed in chapter 6.

The measurement uses the off diagonal basis for its quantisation basis which is optimal for the $q\bar{q} \to t\bar{t}$ process at the Tevatron. In order to determine the degree of spin correlation, the asymmetry (A) in the $\cos\theta_+ \cos\theta_-$ distribution is measured (taking the difference in number of events where $\cos\theta_+ \cos\theta_- > 0$ and $\cos\theta_+ \cos\theta_- < 0$). With perfect detector response, this value relates to the correlation strength, C as

$$A = \frac{C}{4} \tag{5.10}$$

however, due to loss of sensitivity, a linear relationship was determined relating A and C

$$A = 0.112 + 0.088C \tag{5.11}$$

The analysis measured an asymmetry value of $A = 0.31 \pm 0.22$, giving a value $C = 2.3 \pm 2.5$. The uncertainties were highly dominated by statistical effects. A subsequent likelihood fit to data yielded $C > -0.25$ at 68% confidence level, which is in line with the SM prediction of $C = 0.88$ [63]. However, the result is extremely limited and would be in agreement with a number of potential models, therefore further studies were required to provide more conclusive evidence.

5.3.2 Spin Correlation Measurements at the LHC at $\sqrt{s}$ = 7 TeV

The advent of data collection at the LHC offered a chance to study spin correlation in far greater detail, with the $\sqrt{s} = 7$ TeV run in 2011 offering as many $t\bar{t}$ pairs as the full Tevatron dataset. At ATLAS, a number of early measurements were made, using both the partial [64] and full [65] $\sqrt{s} = 7$ TeV datasets, with integrated luminosities of 2.1 fb^{-1} and 4.6 fb^{-1} respectively. Both of these offered a measurement of spin correlation using the $\Delta\phi$ observable in the dilepton channel, as presented in section 5.1.2, and the analysis in [65] also considered a number of other observables,

including the double differential distribution measured in [63], measured in both the helicity and LHC maximal bases, and the $\Delta\phi$ distribution using the semileptonic channel.

The analysis in [65] also measures the "S-ratio" in the dilepton channel, which provides a ratio of matrix elements for top quark production and decay from like-helicity gluon-gluon fusion [61]. This can be expressed as

$$S = \frac{(|\mathcal{M}|^2_{LL} + |\mathcal{M}|^2_{RR})_{corr}}{(|\mathcal{M}|^2_{LL} + |\mathcal{M}|^2_{RR})_{uncorr}}, \tag{5.12}$$

which experimentally translates to

$$S = \frac{m_t^2 \left\{(t.l^+)(t.l^-) + (\bar{t}.l^+)(\bar{t}.l^-) - m_t^2(l^+.l^-)\right\}}{(t.l^+)(\bar{t}.l^-)(t.\bar{t})}, \tag{5.13}$$

where $t, \bar{t}$ and $l^{\pm}$ are the four momenta of the top, the antitop and the charged leptons, respectively, and m_t is the mass of the top quark [65].

The result in [64] gave an f_{SM} value of $1.30 \pm 0.14\,(\text{stat})\,^{+0.27}_{-0.22}\,(\text{syst})$, corresponding to a spin correlation strength in the helicity basis of $A_{helicity} = 0.40 \pm 0.04\,(\text{stat})\,^{+0.08}_{-0.07}\,(\text{syst})$, which is in agreement with the SM prediction of 0.31.

For the analysis using the full $\sqrt{s} = 7$ TeV dataset [65], a measurement of f_{SM} was made for each of the distributions observed. A summary of these results is shown in figure 5.5. As can be seen, all of the results favour a correlated schema (i.e. $A = 1$) over an uncorrelated one, with each result being consistent with the SM prediction of spin correlation. Figure 5.6 illustrates the measured distributions in the dilepton channel with comparisons to both the SM prediction and an uncorrelated scenario.

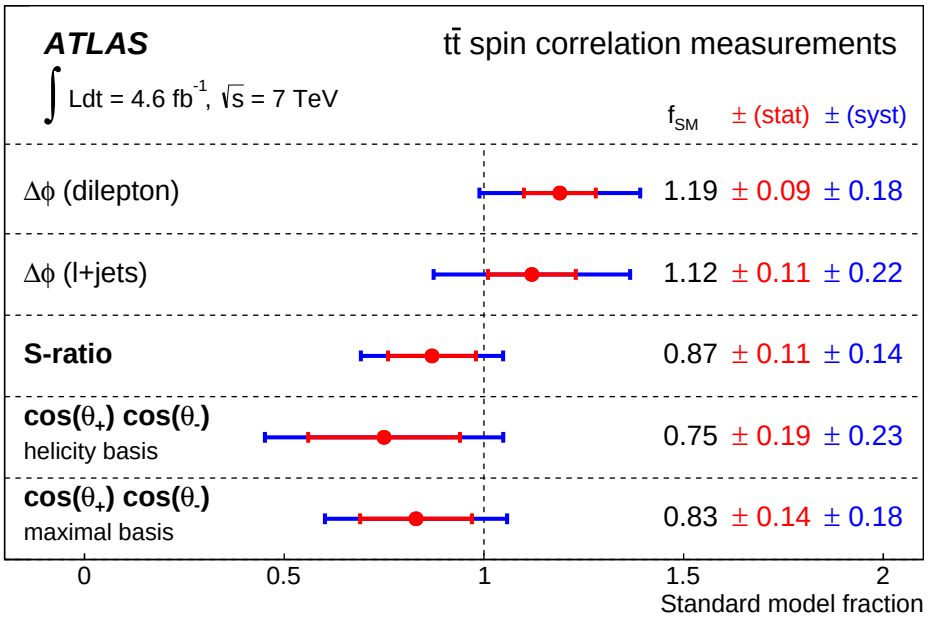

Figure 5.5: A summary of spin correlation results at $\sqrt{s} = 7$ TeV for an integrated luminosity of 4.6 fb^{-1}. The results presented show the measured f_{SM} values in comparison to a SM prediction of $f_{SM} = 1$. The results heavily favour correlated behaviour over uncorrelated [65].

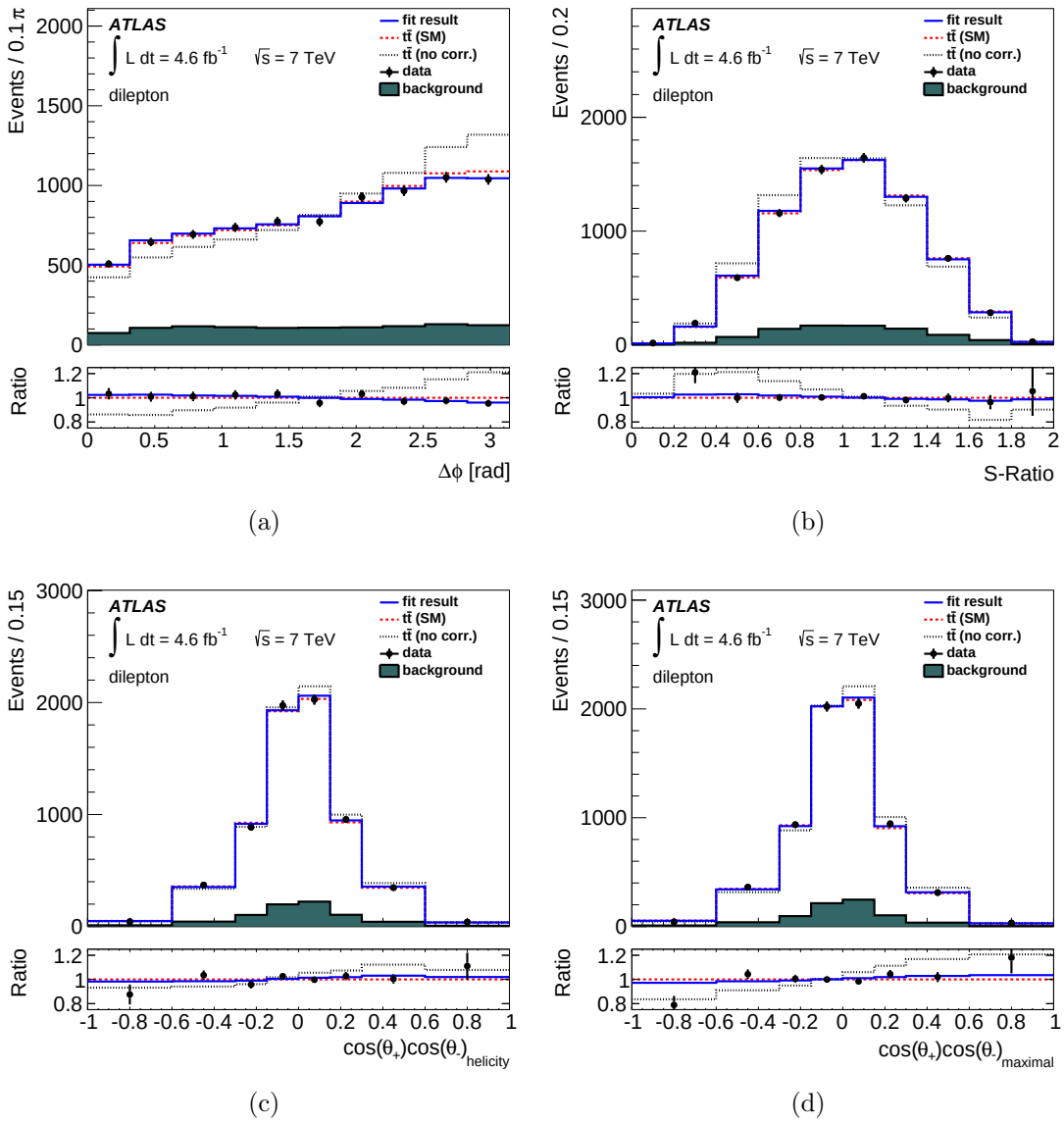

Figure 5.6: Measured data distributions sensitive to spin correlation in the dilepton channel for a centre of mass energy $\sqrt{s} = 7$ TeV. a) is the $\Delta\phi$ distribution, b) the S-ratio, c) the $\cos\theta_+ \cos\theta_-$ distribution measured in the helicity basis and d) the $\cos\theta_+ \cos\theta_-$ distribution measured in the LHC maximal basis [65]. For comparison, the expected SM correlation and uncorrelated distributions are also shown. Results presented are based on the same dataset and so are not statistically independent.

5.3.3 LHC Spin Correlation Measurements at $\sqrt{s} = 8$ TeV

5.3.3.1 Measurements at ATLAS

Following the LHC energy increase, new spin correlation measurements were made. One such measurement follows a similar procedure to that used in this analysis [66] and uses a dataset with an integrated luminosity of 20.3 fb^{-1}. This paper concentrated on the $\Delta\phi$ distribution in the dilepton channel to measure spin correlation. The channel was broken down further into ee, $\mu\mu$ and $e\mu$ channels as well as an overall combined measurement. Values of f_{SM} were calculated for each and can be seen in table 5.2. The measurement for the combined channel is shown in figure 5.7. Due to the increased statistics, the main uncertainty arises from systematic sources, in contrast to the statistics limited measurement at the Tevatron [63]. The statistical uncertainty varies in each of the channels because roughly double the number of $e\mu$ events are expected in comparison to the ee and $\mu\mu$ channels. Again, the results favour an SM level of correlation over an uncorrelated model.

Table 5.2: Tabulated f_{SM} results from previous ATLAS 8 TeV measurement, with an integrated luminosity of 20.3 fb^{-1} [66]. The three separate dilepton channels were measured, as well as a measurement of the three channels combined.

Channel	f_{SM}
ee	$1.18 \pm 0.12\,(\text{stat})\ \pm 0.15\,(\text{syst})$
$\mu\mu$	$1.23 \pm 0.12\,(\text{stat})\ \pm 0.19\,(\text{syst})$
$e\mu$	$1.19 \pm 0.07\,(\text{stat})\ \pm 0.11\,(\text{syst})$
Combined	$1.20 \pm 0.05\,(\text{stat})\ \pm 0.11\,(\text{syst})$

The analysis presented in this thesis uses a similar technique, with the same data as the analysis in [66], but will enhance the measurement by decreasing the bin width to allow for finer structure to be observed, as well as additional measurements of the $\Delta\phi$ distributions in various $M_{t\bar{t}}$ ranges and unfolded measurements for each of these.

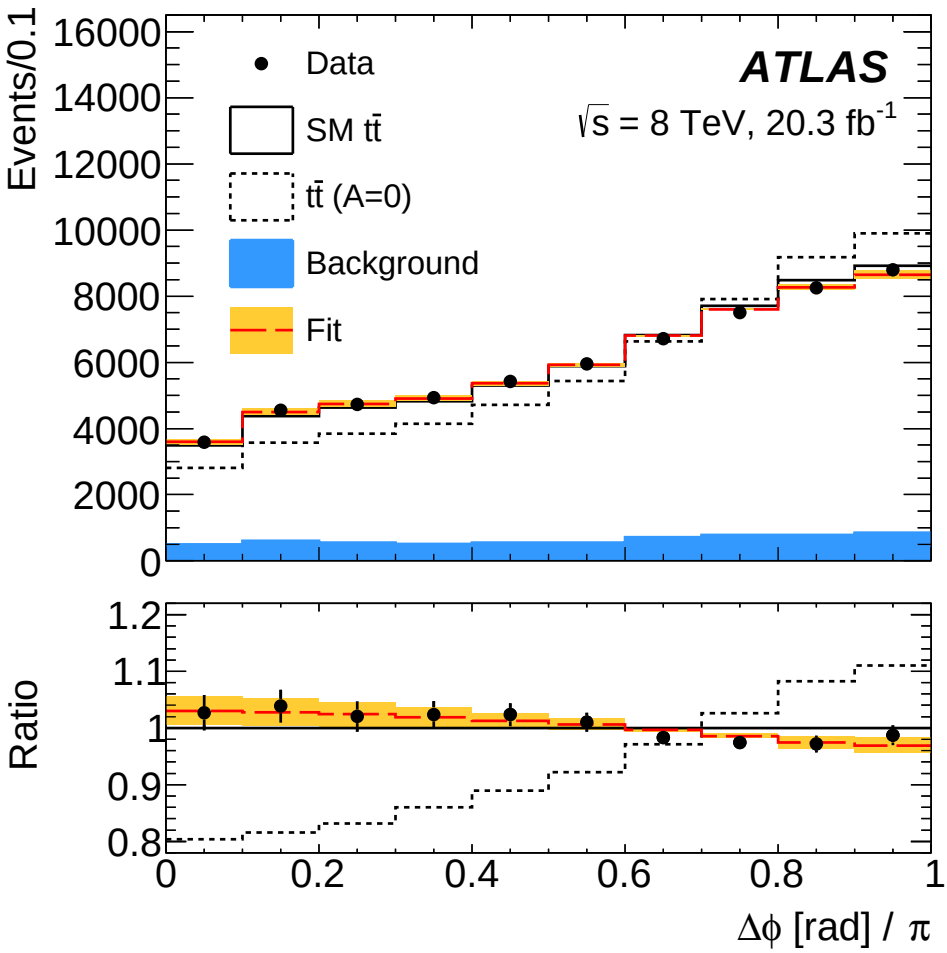

Figure 5.7: The $\Delta\phi$ distribution for the previous ATLAS 8 TeV measurement in the combined dilepton channel. The measurement strongly favours the SM correlation prediction over an uncorrelated model [66].

5.3.3.2 Measurements at CMS

CMS has also investigated spin correlation using a dilepton analysis with the 8 TeV dataset [67], with a total integrated luminosity of 19.5 fb^{-1}. In a similar vein to the analysis presented in this thesis, the CMS analysis measured the spin correlation using the $\Delta\phi$ variable inclusively, as well as taking double differential measurements binned by $M_{t\bar{t}}$, the rapidity of the $t\bar{t}$ system, $y_{t\bar{t}}$, and the transverse momentum of the system, $p_T^{t\bar{t}}$. The analysis in [67] also unfolds the measured distributions to parton level.

The spin correlation was determined by defining an asymmetry based on the observables measured. The first, based on the $\Delta\phi$ variable, is defined as

$$A_{\Delta\phi} = \frac{N(\Delta\phi > \frac{\pi}{2}) - N(\Delta\phi < \frac{\pi}{2})}{N(\Delta\phi > \frac{\pi}{2}) + N(\Delta\phi < \frac{\pi}{2})}, \tag{5.14}$$

which allows for discrimination between $t\bar{t}$ events with correlated and uncorrelated spins. The second more directly measures the spin correlation strength C in the helicity basis, using the observable:

$$A_{c_1c_2} = \frac{N(c_1c_2 > 0) - N(c_1c_2 < 0)}{N(c_1c_2 > 0) + N(c_1c_2 < 0)} \tag{5.15}$$

where $c_1 = \cos\theta_{l^+}$, $c_2 = \cos\theta_{l^-}$, and $\theta_{l^\pm}$ is the angle between the direction of flight of the charged leptons in the rest frame of the (anti)top and the spin quantisation basis. The spin correlation strength is related to $A_{c_1c_2}$ in the following way:

$$C_{hel} = -4A_{c_1c_2}. \tag{5.16}$$

The measured values for these observables following unfolding were $A_{\Delta\phi} = 0.094 \pm 0.005\,(\text{stat}) \pm 0.012\,(\text{syst})$ and $A_{c_1c_2} = 0.102 \pm 0.010\,(\text{stat}) \pm 0.012\,(\text{syst})$, both of which are in agreement with the SM NLO predictions of $0.107^{+0.006}_{-0.009}\,(\text{theory})$ and $0.114 \pm 0.006\,(\text{theory})$, respectively. The double differential measurements in $M_{t\bar{t}}$, $y_{t\bar{t}}$ and $p_T^{t\bar{t}}$ also show similar consistency with the SM predictions (see figure 5.8).

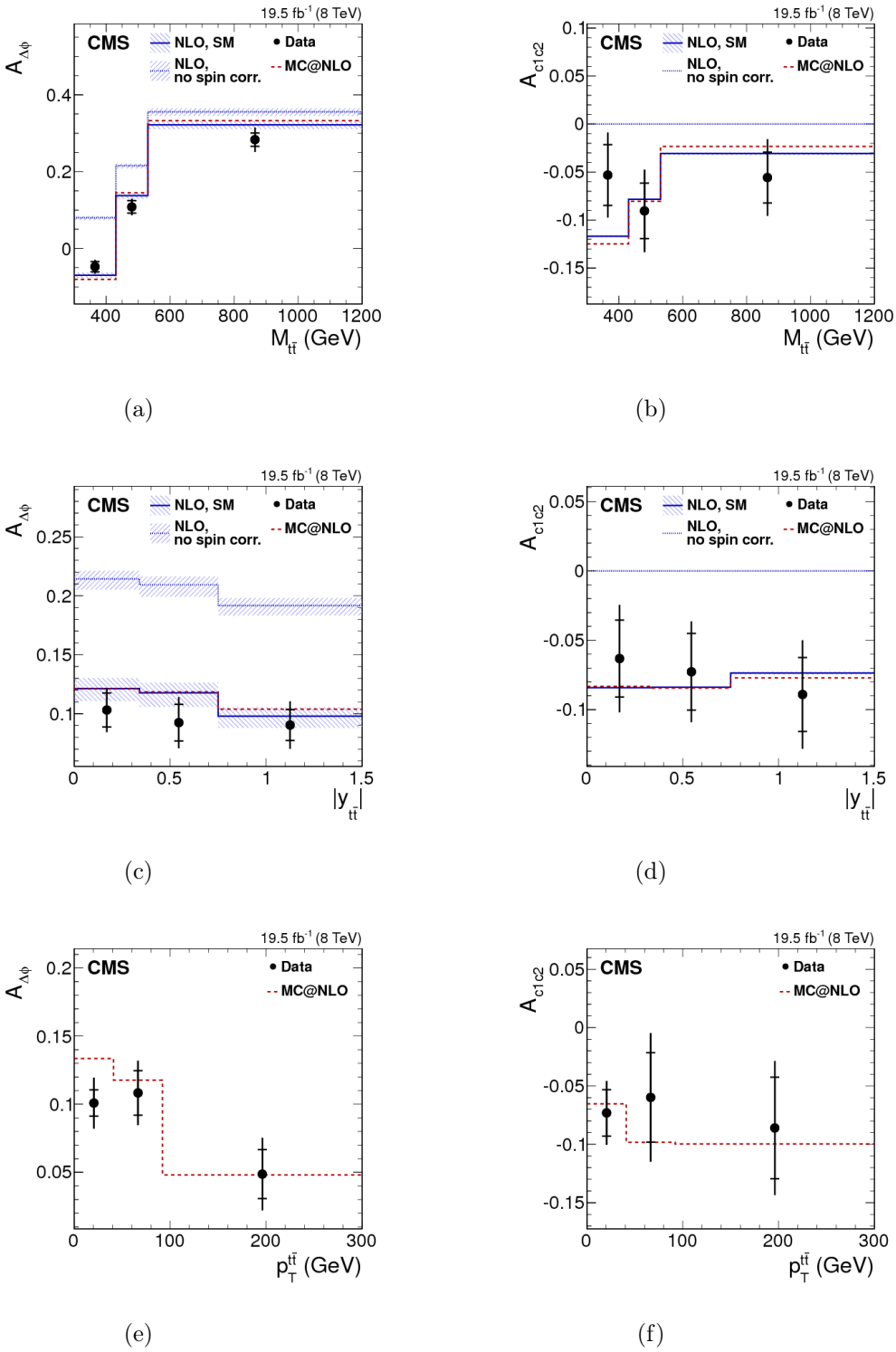

Figure 5.8: Double differential distributions of asymmetry values from CMS measurement of spin correlations after data unfolding [67]. a)-b) show asymmetries binned by $M_{t\bar{t}}$, c)-d) show asymmetries binned by $y_{t\bar{t}}$ and e)-f) show asymmetries binned by $p_T^{t\bar{t}}$. Also included for comparison are theoretical predictions for these asymmetries for SM and uncorrelated models where available, and MC simulated distributions for an SM level of correlation.

5.4 Analysis Strategy

This analysis will present a measurement of spin correlation using the $\Delta\phi$ variable between two charged leptons, which arise from the $t\bar{t} \rightarrow b\bar{b}W^+W^-(\rightarrow l^+l^-\nu\bar{\nu})$ decay. The dilepton channel will be split further into separate flavour channels (ee, $\mu\mu$ and eμ), as well as a combined channel measurement. In addition to an inclusive $\Delta\phi$ measurement, it will also be measured for various ranges of the $t\bar{t}$ invariant mass, $M_{t\bar{t}}$. The ranges used are discussed in chapter 6. The ATLAS $\sqrt{s} = 8$ TeV dataset will be used, which has an integrated luminosity of 20.3 fb^{-1}.

In order to estimate the degree of spin correlation and whether it follows an SM prediction, the data will be compared to a *Monte Carlo* (MC) simulated prediction, comprising both expected signal and background contributions for an SM and uncorrelated prediction. The MC will be subject to detector simulation to model the response of the ATLAS detector. In addition, the Monte Carlo will undergo the same quality cuts as the data in order to more accurately model the prediction. To identify leptons and jets, *object definitions* are created according to parameters determined by ATLAS working groups. Further details of the MC generators, objects and quality cuts used in this analysis are discussed in chapter 6.

An additional measurement is made by *unfolding* the data. For this, a *response matrix* is created which evaluates the expected detector response for the distribution in question. This includes resolution and acceptance effects. This detector response is then used to project a data distribution which is free from detector effects. Due to the lower number of events in the *ee* and $\mu\mu$ channels and statistical limitations in the unfolding procedure, the unfolding will be performed only in the $e\mu$ and combined dilepton channels and will unfold the data to a *parton level* in a fiducial region (see section 6.3.3). The full description of the unfolding technique is presented in

chapter 6.

The full list of measurements is as follows:

- Inclusive f_{SM} measurements for the ee, $\mu\mu$, $e\mu$ and combined dilepton channels. These will be made across the range of $0 \leq \Delta\phi \leq \pi$ in 20 bins.

- f_{SM} measurements for the ee, $\mu\mu$, $e\mu$ and combined dilepton channels in the invariant mass ranges $M_{t\bar{t}} \leq 415$ GeV, 415 GeV$< M_{t\bar{t}} \leq 505$ GeV and $M_{t\bar{t}} >$ 505 GeV. The reason for these ranges will be discussed in chapter 6. In each $M_{t\bar{t}}$ range, the measurement will be made across the range of $0 \leq \Delta\phi \leq \pi$ in 6 bins.

- Unfolded distributions in the $e\mu$ and combined dilepton channels for both the inclusive $\Delta\phi$ distribution and the differential measurements in the $M_{t\bar{t}}$ ranges and binning mentioned above.

Chapter 6

EVENT SELECTION AND ANALYSIS TECHNIQUES

In order to perform an analysis of the $t\bar{t}$ spin correlation and find its agreement with the SM, it is necessary to produce simulated samples, which can be used to make predictions of the expected measurement. Additionally, to produce a pure sample of good quality events, a number of selection cuts are included which aim to reduce background contributions to the signal. Finally, some aspects of the measurement require more sophisticated techniques, namely the reconstruction of top quarks to estimate $M_{t\bar{t}}$, and a methodology to make an unfolded measurement. This chapter will discuss each of these aspects of the analysis in turn.

6.1 Monte Carlo Simulation

The production of most of the predicted distributions for signal and background processes in this analysis is achieved using Monte Carlo simulation. These simulations are created to encapsulate as much of the theoretical prediction as possible. Typically, Monte Carlo generators will include tree level and next to leading order (NLO) processes, although this is dependent on the generator.

The simulation of an event occurs as a sequence of multiple processes:

- *Matrix Element Calculation.* This stage calculates the initial interactions be-

tween the partons in the proton-proton collision (the *hard scatter*) and encapsulates the main physics processes within the event. For the case of this analysis, this stage will simulate the creation of $t\bar{t}$ pairs, in addition to other processes which can occur.

- *Initial and Final State Radiation (ISR/FSR).* Analogously to the Bremsstrahlung radiation phenomenon experienced by electrons via the EM force, quarks can undergo QCD Bremsstrahlung which leads them to emit additional gluons. These gluons can be emitted before and after the hard scatter, leading to additional partons being included in the simulated event in the form of initial and final state radiation respectively. These partons can be included in the final state and so must be simulated accurately.

- *Multiple Parton Interactions (MPI).* When protons are brought to collision, they contain several partons. This can lead to multiple interactions within the same event in addition to the main simulated event. The distinction is made by comparing the energy of the processes, with those of lower energy seen as secondary interactions and generally classed as *soft* QCD processes [68]. These additional interactions produce extra partons which need to be simulated through the decay chain.

- *Parton showering.* Following the above steps, the partons in the simulation will continue to radiate additional partons through Bremsstrahlung processes and gluon splitting. This stage of the simulation is known as parton showering and is usually calculated with a separate generator to the one used for the Matrix Element calculation. Information is passed between the two generators in order to model this stage.

- *Hadronisation.* Following the steps above, the simulation is left with a number of quarks, gluons and leptons. However, quarks and gluons cannot be left "free" due to the confinement effects discussed in chapter 2 and thus undergo

hadronisation. This hadronisation is simulated and then any subsequent decay of these hadrons is modelled.

- *Resonance Decays.* Hadron states produced during parton showering will typically be unstable and thus decay. This decay is modelled and will produce more partons, which subsequently undergo more showering and hadronisation.

The process of simulation of an event within a detector is more complicated than a pure theoretical prediction of a proton-proton interaction. This is because typically a theoretical prediction of an interaction will need to calculate the matrix elements to determine the outcomes of the hard scatter. These products will not be immediately detectable in a detector due to their short lifetimes, and so further decay processes, showering and hadronisation become necessary and introduce potential sources of inaccuracy. However, this is a more realistic simulation of what will be actually measured in a detector.

The simulation as described above provides events assuming an experimentally perfect detector, which is not the case. Further steps are necessary to provide a complete simulation and this is achieved by passing the samples through *GEANT4* [69].

6.1.1 Signal Simulation

For $t\bar{t}$ signal events, this analysis will use the *POWHEG* Monte Carlo generator [70] to simulate the initial events, which calculates processes up to an NLO level using the CT10 PDF set [71] [72]. NLO generators consider contributions from the leading order Feynman diagrams as well as one additional loop correction to the initial process. This is interfaced with *PYTHIA 6.4* [73] to simulate parton showering in the event.

Signal simulations are produced for two possible regimes; one with an SM level of spin correlation and one where the spins of the top quark pairs are entirely uncorrelated, both of which are described using the *POWHEG+PYTHIA 6.4* generators. For the SM scenario, *POWHEG* is used to simulate the production and subsequent decay of $t\bar{t}$ pairs until the final state (i.e. $pp \to t\bar{t} \to l^+l^-\nu\bar{\nu}b\bar{b}$) before passing the event to *PYTHIA 6.4* for the parton showering. This allows information from the $t\bar{t}$ pairs to be passed to the decay products so that the expected topological effects can be simulated. In the uncorrelated scenario, events are passed to *PYTHIA 6.4* after the initial top pair production (so *POWHEG* only simulates the $pp \to t\bar{t}$ process). As a result of this, the spin information in the top quark pairs is lost and so the decay products are produced without any preferred direction which would be expected from spin correlation effects. This mimics the scenario of no spin correlation.

The signal sample produced does not include all possible decays of the $t\bar{t}$ pair but excludes events where both W bosons decay hadronically. This leaves events of the semileptonic and dileptonic channels. These events are subject to object reconstruction procedures and subsequent quality cuts to select the dileptonic events. These are discussed in sections 6.2 and 6.3 respectively.

In order to minimise statistical uncertainties in the simulation, large numbers of events are generated, before being normalised to the integrated luminosity of the dataset which is used. The computation time required to simulate fully a large number of events is high, and so to reduce this, the ATLFAST II (AFII) simulation package is used [74] for some samples. AFII uses a fast calorimeter simulation in combination with the *GEANT4* package to provide a more efficient way of generating events, with minimal effect on the accuracy of the reconstruction [75]. A list of all the samples used is presented in Appendix B.

6.1.2 Background MC simulation

Whilst the event signature and subsequent quality cuts are chosen to provide as pure a signal as possible (see section 6.3), there are still a number of other processes which produce a similar signature to the one of interest. These background processes must be taken into account when producing a prediction of the $\Delta\phi$ distributions. The majority of these backgrounds are modelled using MC simulations and are discussed below. Some applicable backgrounds are calculated using data driven methods and these are described in section 6.4.

6.1.2.1 Z/γ^* + jets Background

The process which provides the greatest source of background is the Drell-Yan process which generates a Z/γ^* (where γ^* is a virtual photon) in addition to a number of jets. The Z/γ^* decays into an oppositely charged pair of leptons, leading to an overall signature that mimics the dileptonic $t\bar{t}$ decay. An invariant mass cut is included on the charged leptons to reduce significantly this background (see section 6.3.3), however some residual events remain and these are simulated. The background from this source is expected to constitute around 10% of the dataset.

The Z/γ^* + jets sample is produced with the *ALPGEN* Monte Carlo generator [76], with up to 5 additional partons included in the initial Matrix Element calculation, using the *CTEQ6L1* PDF set [77]. This is interfaced with *PYTHIA 6.4* [78], which simulates the parton showering and the underlying event. A separate sample is generated for each charged lepton decay (i.e. e^+e^-, $\mu^+\mu^-$ and $\tau^+\tau^-$). In addition, separate samples are generated for low and high invariant mass (to account for differing production cross sections in these ranges). The sample ranges are 10 GeV$< m_{ll} <$ 40 GeV, 40 GeV$< m_{ll} <$ 60 GeV and 60 GeV$< m_{ll} <$ 2000 GeV. To

avoid double counting of final states, the MLM [79] matching scheme is used.

One additional scenario to consider is where in addition to jets, two heavy flavour quarks ($b\bar{b}$ or $c\bar{c}$) are produced. Again, *ALPGEN* is interfaced with *PYTHIA 6.4* to generate these additional heavy flavour (HF) samples where $b\bar{b}$ and $c\bar{c}$ pairs are included in the Matrix Element calculation. When using these samples, it is possible that further double counting between the heavy flavour and non-heavy flavour (inclusive) samples will be introduced. Upon parton showering, heavy flavour pairs may be produced, which in turn leads to double counting of events. This is mitigated by use of a heavy flavour overlap removal (HFOR) tool, which classifies events depending on the ΔR separation of the quarks and whether they were produced in the matrix element calculation or the parton showering [80].

Whilst this simulation offers a good shape estimation of the $\mathrm{Z}/\gamma^* +$ jets background, an additional factor is required to correct the normalisation of the background. This is calculated using a data driven technique and the methodology is described in section 6.4.

6.1.2.2 Diboson Background

Dibosonic events (WW, ZZ and WZ) can give rise to final states similar to the $t\bar{t}$ dileptonic decay and therefore give a small contribution to the background processes. The diboson background is simulated using *ALPGEN* interfaced with *HERWIG/JIMMY* to generate final states with up to three additional partons in the matrix element calculation [81].

6.1.2.3 Single Top Background

As discussed in section 2.5, top quarks can be produced singly via three possible processes. All three processes can produce a background to the signal, however only the Wt-channel does so with 2 charged leptons. The t- and s-channel processes require an object which is not a charged lepton to be identified as such (i.e. a *fake* lepton) and are therefore included in the fake lepton background estimation (see section 6.4.1.

Wt-channel single top events are simulated using *POWHEG* interfaced with *PYTHIA 6.4* [73]. Due to the possible identical final states between the Wt-channel and the $t\bar{t}$ dileptonic decay, interference is experienced at the NLO level. A correction therefore needs to be applied to account for this interference. Two possible schemes are proposed: diagram removal (DR) and diagram subtraction (DS) [82]. For the background sample used, the DR method has been adopted but an additional systematic uncertainty is assigned by considering the difference in measurement obtained when using the DS method. Both schemes are calculated using the *POWHEG+PYTHIA 6.4* simulation.

6.2 Object Selection

For this analysis, selection criteria are applied in order to define the *objects* which are used in the observable distributions, most notably electrons, muons and jets. Objects in this context refer to the collection of information received from the various ATLAS subdetectors which are representative of real particles. The selection chosen for these objects follows the recommendations of the ATLAS Top Working Group [83] and a description is given below. The selection comprises *online* and *offline* components, with online referring to information gathered during initial event

recording decisions (i.e. triggering information), and offline allowing for more detailed analysis after the event has been recorded.

6.2.1 Electrons

Electron candidates are reconstructed from clusters of energy deposits in the electromagnetic (EM) calorimeters that have additionally been matched to a track originating in the inner detector. The matched track must originate from within 2 mm of the primary vertex in the z-direction and is identified using information from the ID. In addition, the electron candidate is required to be in the region $|\eta| < 2.47$, where η is the pseudorapidity. The transition region between the barrel and endcap calorimeters, represented in $|\eta|$ space as $1.37 < |\eta| < 1.52$, is excluded. As leptons originating from a $t\bar{t}$ decay are expected to have a relatively high energy (and due to triggering requirements), the candidate is required to have tranverse energy, E_T >25 GeV. The value of E_T is defined as being the energy of the candidate (determined by the calorimeter deposit) in the direction transverse to the beam pipe.

Electron candidates are also required to be isolated in the inner detector in order to reduce possible QCD multijet backgrounds. To this end, the scalar sum of the p_T of tracks within a cone of $\Delta R = 0.3$ of the candidate track divided by the p_T of the electron candidate should be less than 0.12.

The last consideration applied is the quality of the candidate, used to help distinguish between real electrons and misidentified (fake) electrons. Two approaches can be taken: cut-based and likelihood-based. Cut-based electron objects have been used previously in several analyses, but developments in experimental techniques have led to the production of the multi-variate likelihood-based approach, which allows for greater rejection of fake electrons whilst maintaining the same efficiency.

For this reason the likelihood-based approach is taken. For this analysis, electrons are required to pass the "medium" criteria [84]. The medium criterion specifies that the candidate must have at least seven total hits in the silicon layers, of which at least two must be in the pixel detector. The likelihood approach is based on information in the EM and hadronic calorimeters, as well as from the inner detector, specifically regarding the positions of the track and the primary vertex.

Whilst the simulated events are intended to provide the best description possible, there will be some differences between the conditions in the simulated sample and the data. To minimise these differences, studies are conducted on $Z \to e^+e^-$ events taken from data, using a tag and probe method (similar to that described in chapter 4). From this, corrections are calculated for potential sources of difference between data and MC (such as the efficiency of matching a calorimeter cluster to a track and the efficiency of a genuine event firing the trigger correctly). Each of these scale factors (typically around 1-5%) is applied separately to correct the MC electron information appropriately. There is an uncertainty associated with each of these scale factors and this is treated by attributing a systematic error to the final result, according to the degree of the uncertainty [85].

Following the application of the scale factor, any residual calibrations are performed by scaling the electron energy in data and smearing the energy in Monte Carlo, using $Z \to e^+e^-$ events [85]. These corrections also have associated uncertainties which are taken into account upon calculation of the final result.

6.2.2 Muons

Muon candidates are first identified offline through matching of hits in the muon spectrometer with tracks taken from the inner detector. An algorithm called *MUID*

is used to identify and construct tracks in the spectrometer before matching these with ID tracks [86]. Candidates are required to pass the "tight" definition as well as having p_T >25 GeV and $|\eta| < 2.5$. The candidate must have a track in the inner detector less than 2 mm from the primary vertex in the z-direction. As for the electrons, muons must pass isolation requirements; within a cone of radius $\Delta R = 0.2$ around the candidate track, the calorimeter energy must be less than 4 GeV and similarly the scalar sum of the p_T of the ID reconstructed tracks within a cone of $\Delta R = 0.3$ (excluding the candidate track), must be less than 2.5 GeV. The inner detector tracks are required to have at least one pixel hit (or cross one pixel layer which is known to be inoperative) and have at least 5 hits in the SCT (which can be inoperative SCT sensors). For muons with $0.1 < |\eta| < 1.9$, the candidate is required to have at least 6 total hits in the TRT (including outliers), and of these hits, fewer than 90% of them should come from TRT outliers (sets of measurements from the TRT which cannot form a smooth particle trajectory when combined with hits from the pixel detector and the SCT).

As with the electrons, some scale factor corrections are applied to the MC in order to more accurately describe muon reconstruction within the detector. A similar approach is taken, but this time using a tag and probe methodology with $Z \to \mu^+\mu^-$ events. Again, systematic uncertainties are associated with each of these scale factors and are assigned appropriately within the final result. Similarly, energy scaling and smearing procedures are performed using $Z \to \mu^+\mu^-$ events, with associated uncertainties evaluated when obtaining a final result [87] [88].

6.2.3 Jets

A jet is the term commonly used to describe the objects associated with quark and gluon production in ATLAS. As a result of QCD Bremsstrahlung, quarks may radi-

ate additional gluons which can subsequently form additional pairs of quarks which can form bound states with the original quark (producing hadrons). This process continues until it is energetically unfavourable, however the process typically will produce a shower of a large number of gluons and quarks, which subsequently hadronise, before it reaches this stage. These showers of hadrons act as a signature of a quark having been produced and reconstructing these accurately will aid in determining the energy and direction of flight of the original quark. Leptonic jets also form as a result of EM Bremsstrahlung, but for the purposes of this analysis, the term jets will be used to refer to hadronic jets.

In ATLAS, jet objects are formed by collecting energy deposits in the calorimeters together into clusters. The topological information of the energy deposits is used to collect each deposit into a jet according to a predefined distance parameter.

Jet candidates are reconstructed using the anti-k_T algorithm with a distance parameter set to R = 0.4 [89]. The algorithm is implemented within *FASTJET*, a C++ package designed to provide a number of jet finding tools [90]. It is required that the jet $p_T > 25$ GeV, the jet must have $|\eta| < 2.5$ and the absolute value of the jet vertex fraction, JVF, must be less than 0.5. Here the JVF is defined as the scalar sum of the p_T of tracks associated with the jet which come from the primary vertex, divided by the scalar sum of the p_T of all tracks which are associated with the jet [91]. It represents a probability that a jet came from a particular vertex and a cut on the JVF helps to reduce the likelihood that an accepted jet came from a background source, such as a secondary interaction during the hard scatter or pileup.

Since the jet clustering algorithms use information from the EM calorimeters, there will be overlap between the electron identification and the jet reconstruction processes which can lead to a double counting within the event. To reduce this effect,

an overlap removal scheme is introduced, which requires that any jet which satisfies the above conditions that lies within a cone of $\Delta R < 0.2$ of an identified "good" electron is judged not to be a true jet and is removed.

6.2.3.1 *b*-tagged Jets

Heavy flavour jets are often of importance in analyses as they can act as identifying signatures in decays. Specifically in this analysis, jets originating from b-quarks can be used to identify a top decay (assuming a $t \to Wb$ decay of the top quark). Due to the relatively long lifetime of b-type hadrons, it is possible to estimate whether a jet has originated from the decay of a b quark. For this purpose, *b-tagging* algorithms have been developed to identify b jets. The algorithm used in this analysis is a multivariate algorithm called *MV1* [92].

MV1 uses information from the ID, calorimeters and the location of the event's primary vertex, which is fed into a neural net to determine whether a jet has originated from a b quark [93] [94]. The algorithm calculates likelihoods for various efficiency working points, allowing for a trade off between efficiency and accuracy. A lower working point therefore means a reduction in misidentified b-jets at the cost of removing potentially "good" events. The working point for b-tagged jets in this analysis is 70%, which is commonly used in ATLAS analyses [95]. This corresponds to a tagging efficiency of 70% (i.e. 30% of true b-quark jets will be rejected).

The MV1 algorithm has associated uncertainties, broadly classified into those associated with b-tagging, c-tagging and mis-tagging rates and these must be considered when producing an assessment of the systematic uncertainty of the result.

6.2.4 Missing Transverse Energy

In a dileptonic event, two neutrinos will be produced in the $t\bar{t}$ decay. However, neutrinos are extremely hard to detect and cannot be directly measured at ATLAS. By exploiting conservation of energy, it is possible to make an estimate of the transverse energy of all unmeasured particles in an event. Under the assumption that the partons involved in the initial collision have negligible transverse momentum, then the net transverse momentum of all final state objects should be zero. To estimate the missing transverse energy, the vector sum of all energy clusters in the calorimeters and the muon spectrometers is calculated, including those that are not associated with reconstructed objects. Any imbalances in the transverse energy are taken as the missing transverse energy (MET) [96].

Whilst this gives the total transverse energy of undetectable objects, it does not provide a way of assigning this energy in the case where there are two or more contributors to the MET. In this analysis, there are two neutrinos associated with $W \to l\nu$ decays and in order to reconstruct the initial top quarks, it is necessary to estimate the energies of the individual neutrinos. For this reason, the M_{T2} quantity has been used to estimate the energy of each neutrino. This is discussed further in section 6.5.

6.3 Event Selection

To ensure that the events chosen in the analysis are suitable, a number of quality cuts are introduced. The main purpose of these selections is to enhance the signal contribution within the observable distribution and to reject events which are likely to have arisen from background processes.

6.3.1 Data Periods and Good Run Lists

For this analysis, proton-proton collision data from the full 2012 physics run were used. These data were collected with a c.m. energy of $\sqrt{s} = 8$ TeV and correspond to a total integrated luminosity of 20.3 fb^{-1}. Whilst more data would have been recorded during this period, there will have been some running periods where there were known abnormalitites either in the detector or the beam itself. These are identified and are not used. As a result, selected data must be from periods included on a Good Run List (GRL), representing periods where there are no known abnormalities in the run [97].

6.3.2 Trigger Requirements

In the dilepton channel, we require at least one of the leptons in the event to have been matched to a relevant online trigger object. For electrons, the object must be matched to either the *EF_e24vhi_medium1* or the *EF_e60_medium1* single lepton triggers. For muons, the muon must be matched to the *EF_mu24i_tight* or the *EF_mu36_tight* single lepton triggers. For the case of the eμ channel, we require either the electron or muon to meet the requirements described above.

The naming conventions for the triggers are as follows [98]:

- The number represents the minimum p_T requirement (in GeV) at the Event Filter level for the event to trigger.
- An "i" means the candidate must pass isolation requirements; at the Level 1 EM calorimeter for electrons, and from the muon track isolation requirements for muons.
- A "v" indicates the minimum p_T threshold is variable as a function of η at the

Level 1 trigger.

- An “h” indicates the candidate must have a low amount of energy deposited in the hadronic calorimeter at Level 1.

- "medium1" and "tight" mean that the object must meet the quality criteria (electrons and muons respectively).

6.3.3 Dileptonic Event Requirements

For dileptonic event selection, the following requirements are imposed:

- It is required that there are exactly two charged leptons of opposite charge, with object quality restrictions and trigger requirements as described in sections 6.2 and 6.3.2 respectively. This helps to reduce contributions from non-dileptonic events.

- In the ee and $\mu\mu$ channels, a cut is imposed on the invariant mass of the two selected leptons, such that a dilepton candidate must satisfy $|m_{l^+l^-} - m_Z| > 10$ GeV, where m_Z is taken to be 91 GeV. The purpose of this cut is to significantly reduce the background of dilepton candidates originating from $Z \to l^+l^-$ events. The reduction in background events from introducing this cut is proportionately larger than the loss of signal events. In addition, a lower boundary on $m_{l^+l^-} > 15$ GeV is introduced in order to reduce background from low mass resonances in all dilepton channels.

- In the same flavour channels, the missing transverse energy (MET) must be larger than 30 GeV. This is because we expect a neutrino from each of the leptonically decaying W bosons and so a large value of MET. This helps to

suppress the Z/γ^* + jets background, where same flavour lepton pairs are produced without neutrinos. In the eμ channel, events are required to have an $H_T > 130$ GeV, where H_T is defined as the scalar sum of all jet and charged lepton p_T values. This is to help suppress the Z/$\gamma^* \to \tau^+\tau^-$ background (although this is expected to be small).

- There must be at least two jets in the event, at least one of which must be tagged as b-flavoured using the MV1 multi-variate analysis b-tagging algorithm, at an efficiency of 70%. As we expect at least 2 b-quarks to be produced within the event, adding the requirement that at least 1 jet in the event be identified as b-flavoured further reduces the proportion of background events in comparison to signal events.

- For the differential measurement, the events will be binned in ranges of $M_{t\bar{t}} \leq$ 415 GeV, 415 GeV$< M_{t\bar{t}} \leq$ 505 GeV and $M_{t\bar{t}} >$ 505 GeV. These have been selected in order to have roughly equal numbers of events in each of the three ranges, whilst additionally maximising the differentiation between SM correlated and uncorrelated samples at low values of $M_{t\bar{t}}$.

In assessment of the agreement between data and MC, a number of control region distributions are plotted. These consider the distributions of quantities used in event selection (i.e. the number of jets in the event, the MET and the dilepton invariant mass) and are shown in section 6.7.

6.3.4 Truth Record Requirements

For the unfolded measurement, the measured data distribution will be corrected for detector effects and then compared to simulated events which also have no detector effects (*truth level*). Truth level in this instance refers to generator level information

in simulated data. For this comparison, the simulated events at truth level will also be subjected to kinematic cuts. This is performed to unfold to a fiducial region which matches that measured in data. The cuts applied are:

- Truth electrons, muons and b-quarks are required to have $p_T > 25$ GeV
- Truth electrons, muons and b-quarks are required to have $|\eta| < 2.5$

In addition, charged leptons in truth are required to have come directly from a W boson decay. When a W boson decays leptonically, it can decay to a τ lepton and corresponding neutrino. Due to the mass of the τ lepton, it can decay further. One of its decay chains is leptonic, $\tau \rightarrow l\bar{\nu}_l\nu_\tau$, where l can be either an electron or a muon. The branching ratio for these processes is 17.41% for muons and 17.83% for electrons [1]. The result of this is that a W boson decaying to a τ can mimic the signal from an electron or muon decay, which is difficult to distinguish after detector reconstruction. For the detector level measurement, some of these decays are included as part of the measurement of each channel, in both the data and simulation. However, when unfolding, electrons and muons originating from tau leptons can be included within the detector response modelling to provide a truth level distribution which does not include $W \rightarrow \tau\nu_\tau$ decays.

6.4 Data Driven Background Estimations

6.4.1 Fake Leptons

A small contribution to the $\Delta\phi$ distribution is expected from misidentified charged leptons, or *fake* leptons. One source of fakes is jets which are erroneously reconstructed as charged leptons. This can lead to contributions from processes which would not normally be expected (such as s- and t-channel single top processes). The contribution is expected to be small and is calculated using a data driven method.

This analysis has taken a similar approach to that taken in [99]. The analysis is re-run with the same selection criteria as seen in section 6.3 with the modification that the requirement to have oppositely charged leptons is reversed, and events are only kept if the two charged leptons have the same sign. Simulation studies have shown [99] that events with same-sign leptons are dominated by contributions from misidentified leptons. Therefore, in order to calculate the contribution from fake leptons, the analysis is run with this same-sign requirement in each of the channels. The expected contributions from same-sign processes are subtracted from the data contribution. The remainder is then taken to be the estimate of the misidentified lepton contribution in the opposite sign analysis. The contribution of this background is expected to be around 1-2% of the total yield [66], and a normalisation uncertainty of 100% is assigned when calculating systematic uncertainties (see section 7.2.2.12).

6.4.2 Z+jets Data Driven Normalisation

Within the analysis, Monte Carlo simulations are used to provide an estimate of the expected signal and residual backgrounds after the above cuts. In the case of the background which originates from the decay of Z bosons with associated jets, a data driven scaling factor is calculated to correctly normalise the number of the expected events in simulation.

In order to estimate the degree to which the Z/γ^*+jets background is mismodelled in simulation, it is prudent to consider a region in which this background is dominant in comparison to the signal events and other backgrounds. To do this, the invariant mass cut described in section 6.3.3 is inverted so that values of $m_{l^+l^-}$ are close to the Z boson mass (i.e. $|m_{l^+l^-} - m_Z| \leq 10$ GeV). The $m_{l^+l^-}$ distribution is plotted for all of the backgrounds in the analysis as well as the data. This is calculated in the

ee and $\mu\mu$ channels, as well as combination of the two. A corrective scaling factor is then calculated according to the formula

$$Z_{\mathrm{SF}} = \frac{N_{\mathrm{obs}} - N^{\mathrm{MC}}_{\text{non-}Z}}{N^{\mathrm{MC}}_{Z}}, \tag{6.1}$$

where N_{obs} is the number of events seen in data, $N^{\mathrm{MC}}_{\text{non-}Z}$ is the number of events seen in simulation from non Drell-Yan sources and N^{MC}_{Z} is the number of events seen in simulation from Drell-Yan sources. This estimate is calculated for the ee and $\mu\mu$ channels (not in eμ as the expected Z+jets background is small in this channel). It is also calculated for two control regions. The first of these (CR1), is the standard event selection but with the Z veto cut inverted. The second (CR2) also removes the MET cut. Doing so increases the purity of the control region, resulting in more events in this region originating from Z/γ^*+jets.

Additionally, two sets of scale factors are calculated: one set for events with exactly one b-tagged jet and one for events with two or more b-tagged jets. The reason for this is that the Monte Carlo simulation makes poor predictions for heavy flavour content in events with vector boson + jet production and this discrepancy is exacerbated when including b-tagging as a requirement. Therefore the scale factor is expected to be greater for events with more b-tagged jets. A table showing each of the relevant numbers and corresponding calculated scale factors for events with exactly one b-tagged jet and those with at least two tags are shown in table 6.1 and table 6.2 respectively. The uncertainties on the scale factors are calculated using the statistical uncertainties on the data, the uncertainty due to limited MC statistics on the Z/γ^*+jets and an assumed uncertainty of 10% on the non-Z MC background, as used in [66].

In addition to the separate channels, the two contributions have been summed in order to give an overall scale factor for both channels. For this analysis, the scale

Table 6.1: The yields and calculated scale factors for the various channels and control regions described, for events with exactly one b-tagged jet.

Channel	Region	N_{obs}	$N^{\text{MC}}_{\text{non-}Z}$	N^{MC}_{Z}	Z_{SF}
ee	CR1	7998	1389	5283	1.25 ± 0.04
	CR2	21933	1848	15299	1.31 ± 0.02
$\mu\mu$	CR1	9586	1488	6178	1.31 ± 0.04
	CR2	26481	1986	17783	1.38 ± 0.02
l^+l^-	CR1	17584	2877	11461	1.28 ± 0.04
	CR2	48414	3834	33082	1.34 ± 0.02

Table 6.2: The yields and calculated scale factors for the various channels and control regions described, for events with at least 2 b-tagged jets.

Channel	Region	N_{obs}	$N^{\text{MC}}_{\text{non-}Z}$	N^{MC}_{Z}	Z_{SF}
ee	CR1	1744	805	605	1.55 ± 0.10
	CR2	3437	977	1717	1.43 ± 0.05
$\mu\mu$	CR1	1978	933	739	1.41 ± 0.10
	CR2	3980	1124	1986	1.44 ± 0.05
l^+l^-	CR1	3700	1738	1344	1.48 ± 0.10
	CR2	7417	2101	3703	1.44 ± 0.05

factor that has been chosen is the combined scale factor in the CR1 control region. The rationale for this is that it is the selection closest to the signal region. The distributions for these observables, both pre- and post-corrective scale factor, for events with exactly one b-tagged jet and events with at least two b-tagged jets can be seen in figures 6.1 to 6.4.

As can be seen, the agreement between data and Monte Carlo simulation is much better after the application of the scale factor correction. The agreement is better in events with exactly one b-tagged jet, but this is partially caused by statistical fluctuations as there are fewer events with 2 or more b-tagged jets. A normalisation error will be taken into account as a result of this method: a variation will be applied which encompasses all of the possible scale factors that have been calculated across the different channels and control regions. This corresponds to ± 10% for events with exactly one b-tagged jet and ± 7% for those with two or more b-tagged jets.

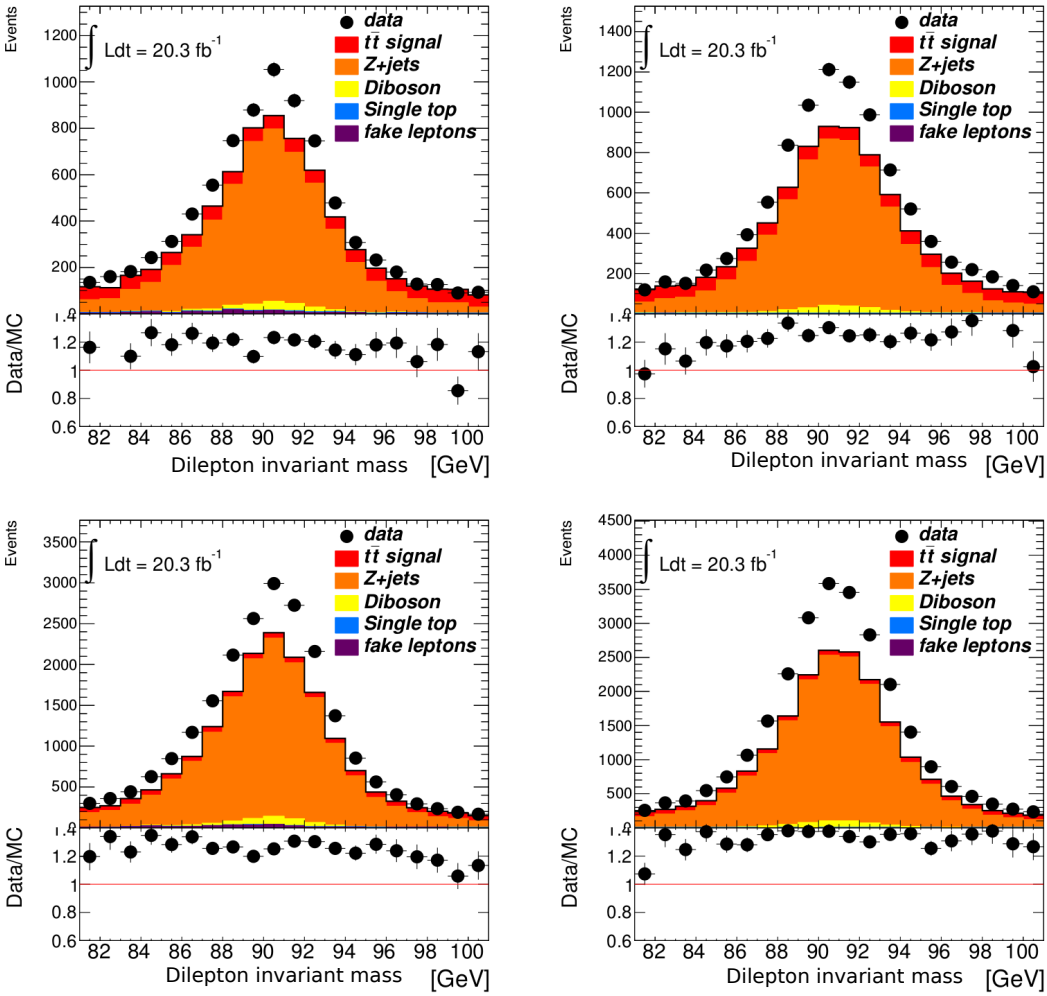

Figure 6.1: The invariant mass distributions for the ee (left) and $\mu\mu$ (right) channels within the Z mass window with (top row) and without (bottom row) the MET cuts applied (CR1 and CR2) respectively, for events with exactly 1 b-tagged jet. These distributions illustrate the data/MC discrepancy before a corrective scale factor is applied.

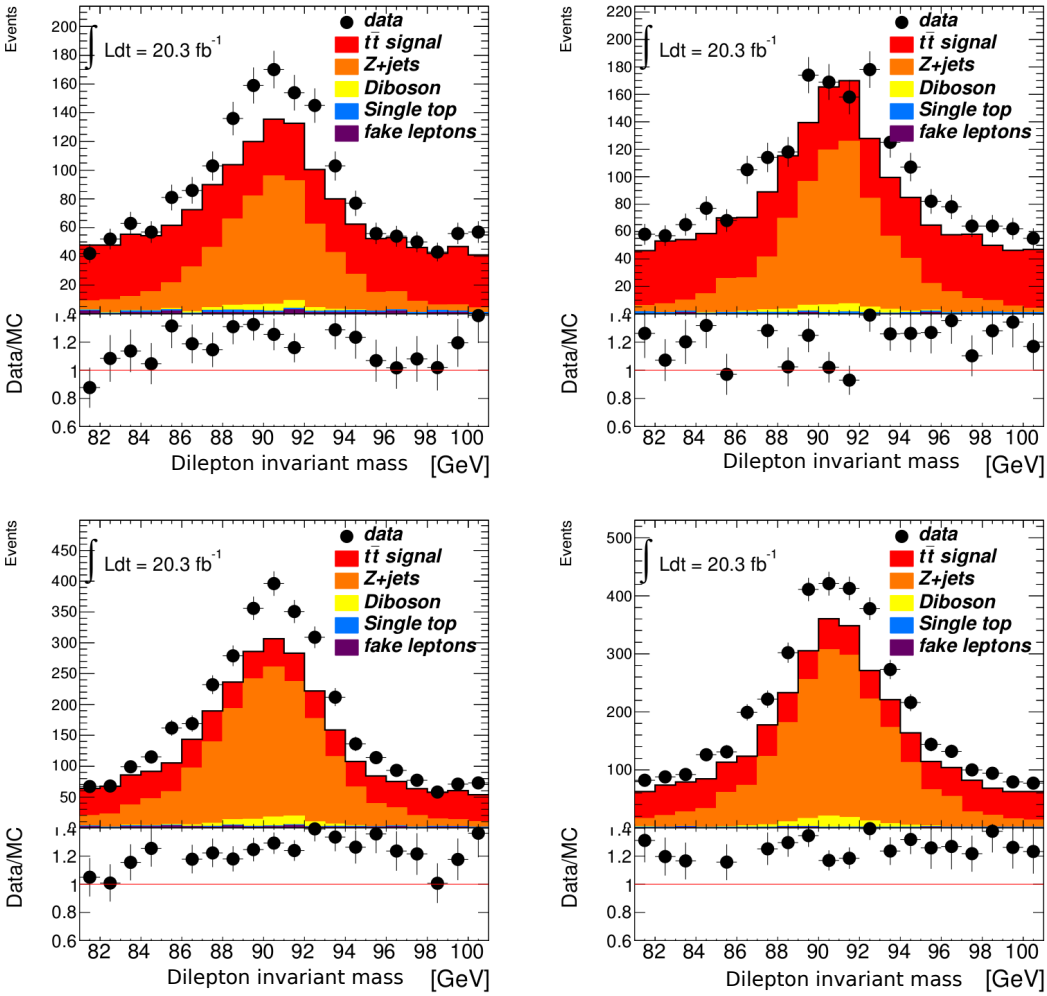

Figure 6.2: The invariant mass distributions for the ee (left) and $\mu\mu$ (right) channels within the Z mass window with (top row) and without (bottom row) the MET cuts applied (CR1 and CR2) respectively, for events with at least 2 b-tagged jets. These distributions illustrate the data/MC discrepancy before a corrective scale factor is applied.

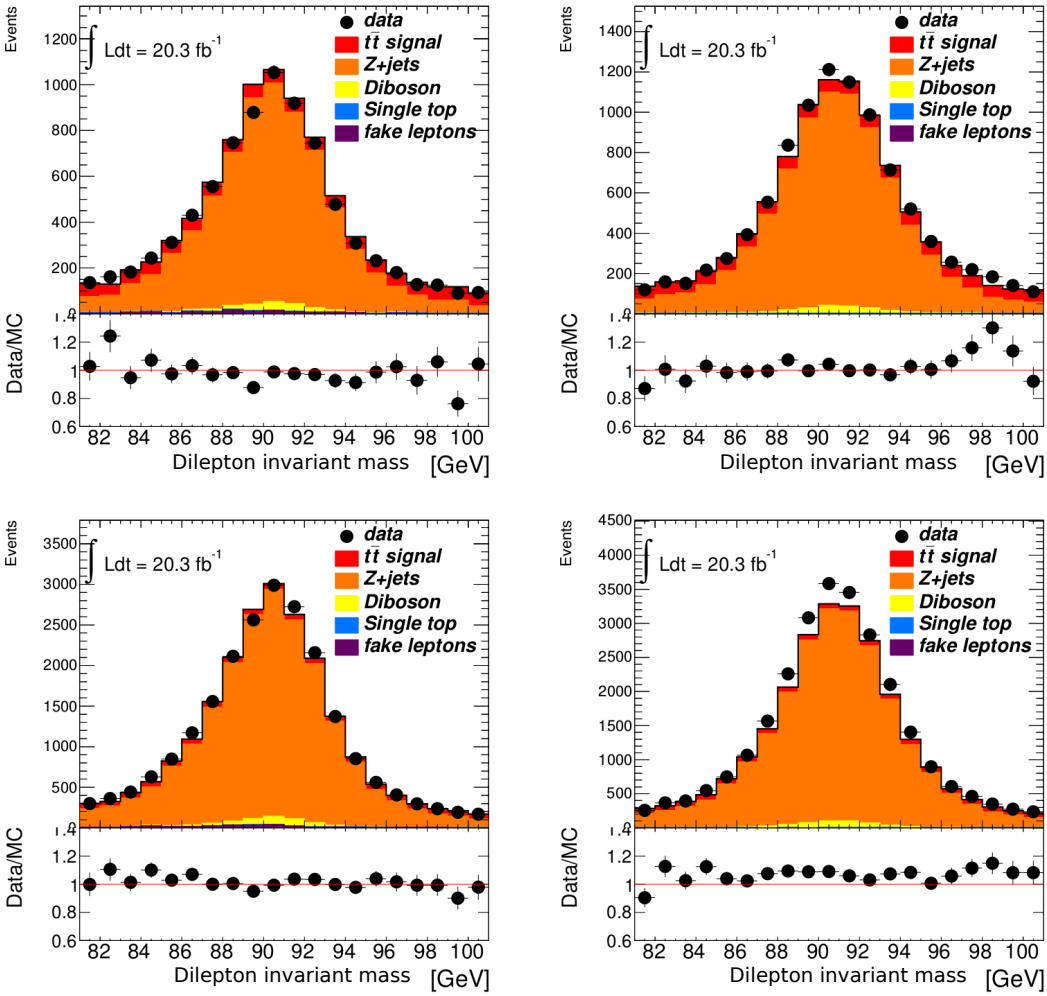

Figure 6.3: The invariant mass distributions for the ee (left) and $\mu\mu$ (right) channels within the Z mass window with (top row) and without (bottom row) the MET cuts applied (CR1 and CR2) respectively, for events with exactly 1 b-tagged jet. These distributions illustrate the data/MC discrepancy after a corrective scale factor is applied.

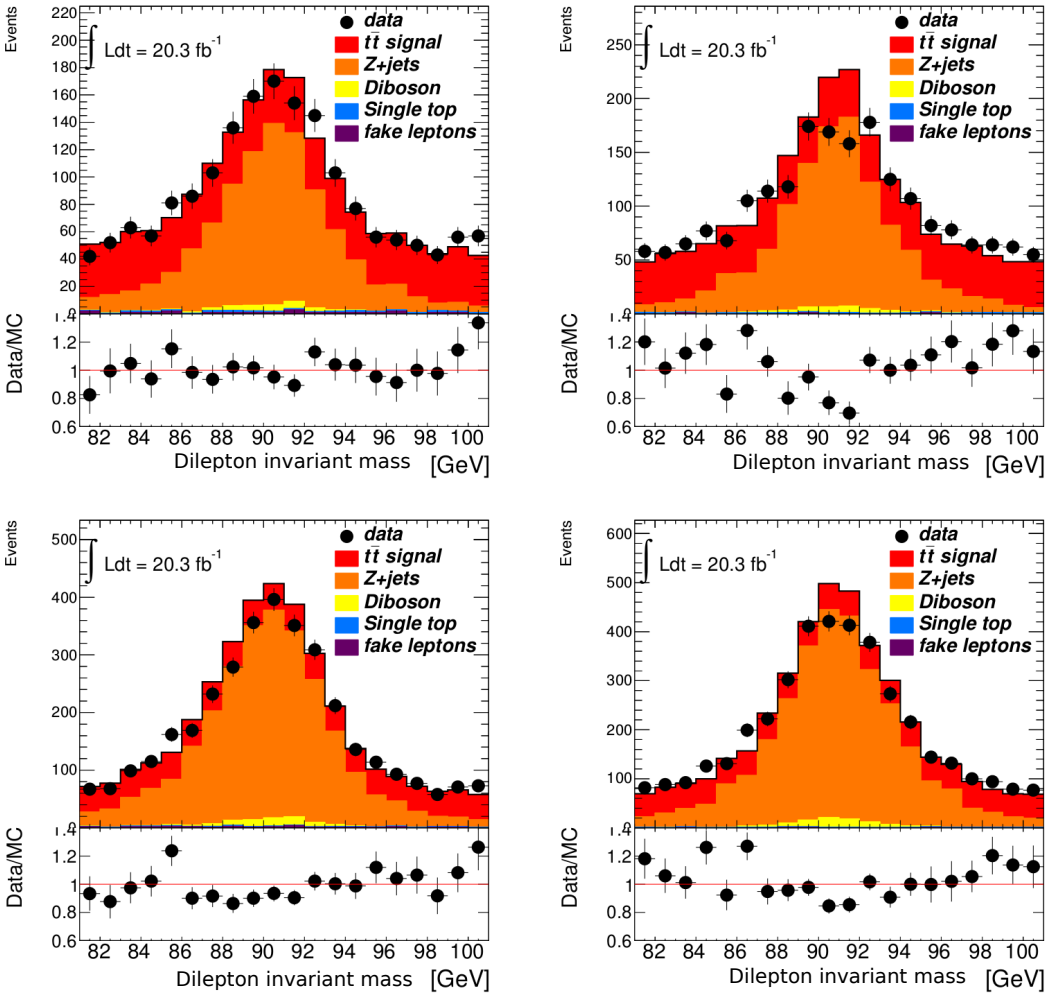

Figure 6.4: The invariant mass distributions for the ee (left) and $\mu\mu$ (right) channels within the Z mass window with (top row) and without (bottom row) the MET cuts applied (CR1 and CR2) respectively, for events with at least two b-tagged jets. These distributions illustrate the data/MC discrepancy after a corrective scale factor is applied.

6.5 M_{T2} for $t\bar{t}$ Reconstruction

In order to make a differential measurement as a function of the invariant mass ($M_{t\bar{t}}$), it becomes necessary to reconstruct the initial $t\bar{t}$ system. This is not necessary for the inclusive $\Delta\phi$ measurement as this uses quantities which are defined in terms of the decay products of the top and antitop.

As discussed in section 6.2.4, the need to reconstruct the $t\bar{t}$ system presents an extra challenge in this analysis as when faced with a total MET but two neutrinos, it is difficult to assess the momentum of each neutrino individually. In addition to this, in the $t\bar{t}$ reconstruction, we cannot a priori know which b quark should be matched to each lepton/neutrino system (as it is not possible to distinguish between the b and $\bar{b}$ from the reconstructed jets in the detector).

Therefore, to accurately measure $M_{t\bar{t}}$, a technique must be adopted to estimate the energy of each neutrino and to determine the correct combinatoric assignment of the b quarks to the decay products of each W boson. To this end, the M_{T2} event variable has been used [100] [101].

M_{T2} has been used in supersymmetry searches at both ATLAS and CMS [102] [103], where proposed new supersymmetric particles decay into weakly interacting massive particles (WIMPs) which cannot be directly measured by the detector, thus leaving an overall missing energy signature which then needs to be accurately assigned to each WIMP. M_{T2} provides an estimate of the mass of the parent supersymmetric particle. However, the use of this variable can be extended to the current analysis, where the initial parent particles have a known mass and instead of estimating the mass of the parent particle, the technique can be used to estimate the energy and momentum of the decay products (in this case, the neutrinos) [104].

M_{T2} is defined as:

$$M_{T2} = \min_{k_T^{(1)}+k_T^{(2)}=\not{p}_T} \left[\max \left\{ M_T^{(1)}, M_T^{(2)} \right\} \right] \tag{6.2}$$

where $M_T^{(1,2)}$ refers to the transverse mass of the decay products of one of the top/antitop quarks (i.e. in the decay chain $t \to W^+b \to l^+\nu b$, $M_T^{(1)}$ is the invariant transverse mass of the $l^+\nu b$ system), $k_T^{(1,2)}$ is the tranverse momentum of each of the neutrinos and $\not{p}_T$ is the total missing transverse energy in the system (MET) [104].

The calculation assigns the total MET to the neutrinos in varying proportions. From this, the tranverse mass of the decay products of each top quark is calculated and the largest of these is taken as the value of M_{T2}. The Simplex method is used to calculate the MET proportional assignment which yields the minimum value of M_{T2} [105]. This gives the final value of M_{T2} and the k_T assignment for each of the neutrinos. To perform this, the Oxbridge Kinetics library of packages has been utilised [106], with minor modifications made in order to retrieve information about the neutrinos.

As this method only assigns the transverse components of momentum, the full kinematics of each neutrino must be calculated separately. To do this, the longitudinal momentum component of each neutrino needs to be calculated, however the M_{T2} calculation only provides the transverse components. The calculation of the longitudinal component is made according to equation 6.3 [107]

$$k_{iL} = \frac{1}{E_{iT}^V} \left[p_{iL} A_i \pm \sqrt{p_{iL}^2 + \left(E_{iT}^V\right)^2} \sqrt{A_i^2 - \left(E_{iT}^V E_{iT}^\nu\right)^2} \right], \tag{6.3}$$

where E_{iT}^V is the transverse energy of the system of visible particles (i.e. the b quark

and charged lepton) in the same decay chain as neutrino i, E_{iT}^{ν} is the transverse energy of neutrino i, p_{iL} is the longitudinal component of the momentum for the visible particle system and

$$A_i = \frac{1}{2}(m_t^2 - m_{iV}^2) + \mathbf{p}_{iT}.\mathbf{k}_{iT}, \tag{6.4}$$

where $\mathbf{p}_{iT}$ is the transverse component of the momentum for the visible particle system, $\mathbf{k}_{iT}$ is the transverse component of the momentum for the neutrino and m_{iV} is the invariant mass of the visible particle system.

Due to there being fewer constraints than unknowns, the longitudinal momentum component of each neutrino has two possible solutions, leading to an overall four fold ambiguity in the possible solutions. In addition, the Simplex minimisation may converge incorrectly which can lead to some of the possible longitudinal momentum solutions being imaginary.

In reconstructing the (anti)top quark, a decision is made regarding which objects within the event are the two b quarks. This is done using information from the MV1 b-tagging algorithm (see section 6.2.3.1). Given that in our event selection we require at least one b-tagged jet, there are three possible scenarios:

- There are exactly two b-tagged jets. In this case each of these is taken as being one of the 2 b quarks resulting from the $t \to Wb$ decays.
- There are more than two b-tagged jets. In this case, the 2 jets with the highest MV1 b-tagged weight are selected.
- There is only one b-tagged jet. Here, the b-tagged jet is used in addition to one other jet which, whilst it is not tagged, has the next highest MV1 weight.

6.5.1 Combinatoric Assignment

As can be seen in equation 6.2, the calculation assumes a combinatoric assignment of b quark to lepton-neutrino system when yielding a value. In order to test which combinatoric assignment is correct, the calculation is performed twice for each event: once for each possible assignment. The assignment of b-jet to lepton-neutrino system is chosen according to the following criteria, using the methodology proposed in [108]:

- If all solutions are real for the neutrino longitudinal momenta for both assignments, then a W boson is reconstructed for each of the four possible neutrino solutions (two for the neutrino and two for the antineutrino). For each possible reconstruction, the absolute difference between its mass and the on-shell W mass is calculated and the sum of these differences is taken i.e.

$$\sum_{i=1,2,\alpha=1,2} |(m_{W,i}^{reco}(\alpha) - m_W)|, \tag{6.5}$$

  where i represents each neutrino, α is each possible longitudinal momentum solution and m_W is the on shell W boson mass [108]. The assignment that gives the lowest total difference is selected as being the correct one.

- If one assignment gives imaginary solutions and the other does not, the assignment which gives all real solutions is taken.

- If both assignments give imaginary solutions, then the event is rejected.

In order to verify the accuracy of this method, a test was performed using the SM correlated $t\bar{t}$ simulated signal sample. The combinatoric assignments for a dileptonic $t\bar{t}$ decay were made according to the criteria presented above and compared to the correct assignments using information taken from the truth record. In addition, the total number of events lost due to both assignments giving imaginary solutions was also measured. The results can be seen in table 6.3.

Table 6.3: Testing of the M_{T2} combinatoric assignment methodology. Results show the number of correctly and incorrectly assigned events according to the criteria described in section 6.5.1. Events which are rejected due to having no real solutions are included in the final category. This method results in a correct combinatoric assignment in 86.3% of cases.

Event class	Number of Events	Percentage of Total Events
Correctly assigned with no imaginary solutions	285338	53.5 ± 0.2
Correctly assigned with one imaginary solution	174857	32.8 ± 0.1
Correctly assigned	460195	86.3 ± 0.2
Incorrectly assigned with no imaginary solutions	69572	13.1 ± 0.1
Incorrectly assigned with one or more imaginary solutions	3339	0.6 ± 0.1
Incorrectly assigned	72911	13.7 ± 0.1
Total	533106	100

The accuracy of the method is seen to be 86.3% and therefore provides a good method of combinatoric assignment.

6.5.2 $t\bar{t}$ Reconstruction

Following the choice of assignment, the next stage is to reconstruct the top and antitop quarks. Whilst the combinatoric assignment has been made, there is still a four fold ambiguity in the choice of longitudinal momentum for the two neutrinos (with two possible solutions for each of the produced W bosons). In order to make a selection, once again each of the possible neutrino solutions is used to construct a W boson in conjunction with the associated charged lepton. From this point, the invariant mass of each of the reconstructed W bosons is compared to the on-shell W mass i.e.

$$|m_W^{reco}(\alpha) - m_W|, \tag{6.6}$$

where α refers to each possible logitudinal momentum and m_W is the on shell W boson mass. This is performed for each of the W bosons in isolation. The solution which gives the lowest absolute difference between the invariant mass of the $l^{\pm}\nu$ system and the on-shell W mass is taken as being the correct solution for each neutrino. This is similar to the technique adopted for combinatoric assignment but in that case, the sum of all possible differences is used as a selection criteria.

Following this choice, there is sufficient information to reconstruct the top and antitop. It is important to note that within this analysis, no information is required about the individual reconstructed top quarks, as the only quantity which is of interest is the $t\bar{t}$ invariant mass (in order to separate the analysis into the 3 $M_{t\bar{t}}$ ranges). Therefore, in testing the accuracy of this reconstruction method, the plot of $M_{t\bar{t}}$ has been considered. The MC sample used to assess the accuracy of $M_{t\bar{t}}$ is the same as is used for the full analysis. For each event which passes the selection criteria and the combinatoric assignment process, $M_{t\bar{t}}$ is calculated using the reconstruction process described above. In addition, the true $M_{t\bar{t}}$ value is recovered, using information in the Monte Carlo truth record. The two are compared and the fractional difference between them is calculated and can be seen in figure 6.5, which illustrates the $M_{t\bar{t}}$ fractional difference for both the SM correlated and uncorrelated samples. This helps to assess not only the accuracy of the reconstruction, but also if it introduces any inherent bias toward one particular correlation regime. As can be seen, the absolute fractional differences calculated are less than 0.5 for most events (with a mean of -0.008 and RMS of 0.15 for both samples), showing that the reconstruction technique is suitable for use. In addition, the difference between the two samples is within statistical uncertainties for most bins, and therefore does not appear to introduce a bias.

Figure 6.6 shows the $M_{t\bar{t}}$ distributions for the ee, $\mu\mu$ and eμ channels following

reconstruction using the technique described above. As can be seen, the agreement between data and simulation is generally good.

6.6 Unfolding: Uses and Challenges

Upon initial MC simulation, the events produced will be at a "truth" level, meaning they are free of any experimental limitations such as resolution effects. This cannot be compared directly to data as the measured values will by necessity be inclusive of these limitations. Therefore, data is often compared with MC which has been passed through full detector simulation. This method has been adopted for many analyses at the LHC.

One drawback to this approach is that the results which are produced are dependent on both the experiment and the simulation. This makes comparisons between different experiments challenging. In addition, it is not ideal for further investigations at a theoretical level, as any investigation of results will require a full detector description to be provided. A preferable scenario would involve producing a measured distribution which is free of detector effects. This removal of experimental effects is a process known as *unfolding*. This analysis has produced a measurement of spin correlation using both a detector level and unfolded approach. The following describes the approach taken in this analysis when considering unfolding.

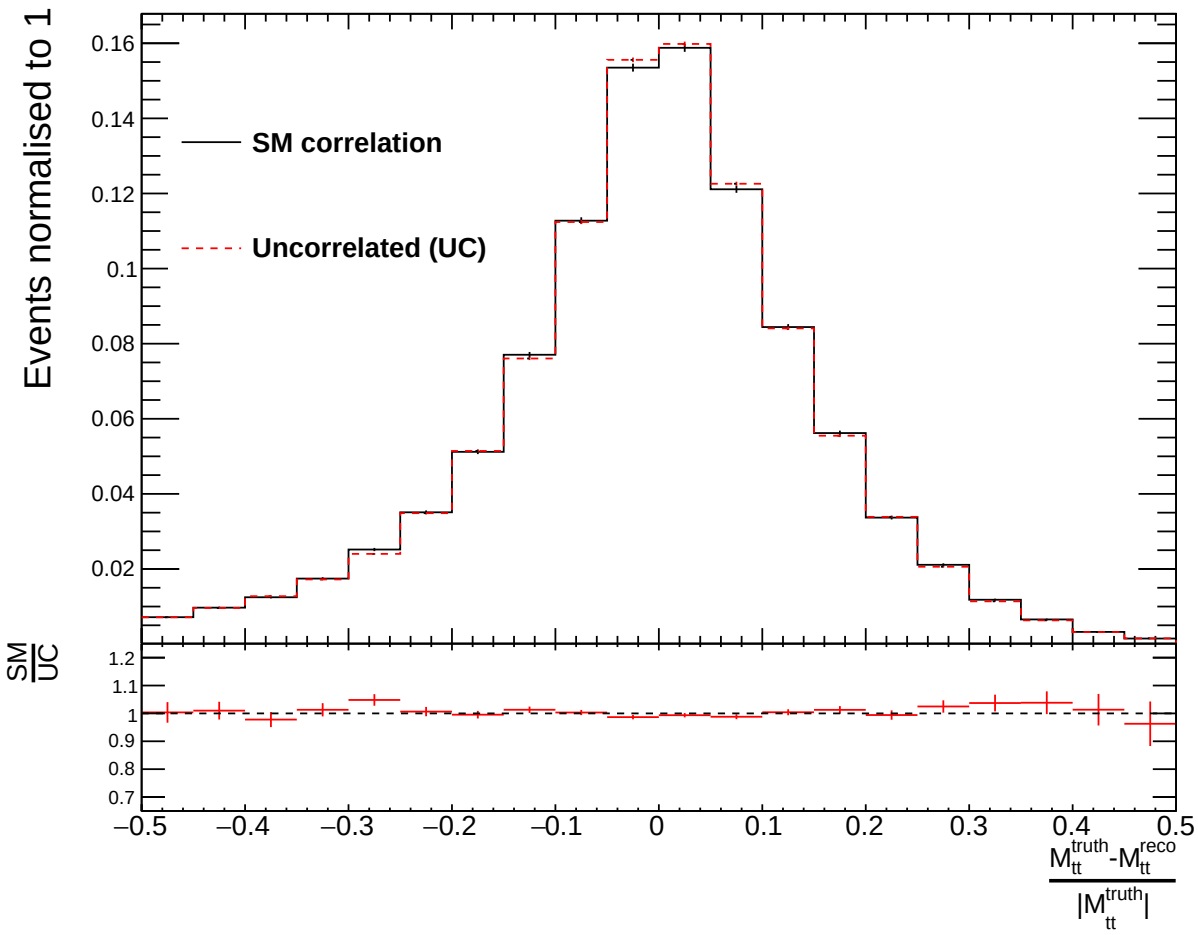

Figure 6.5: Distribution showing the normalised fractional difference between the reconstructed and true $M_{t\bar{t}}$ values, where the reconstructed $M_{t\bar{t}}$ values are obtained using the M_{T2} methodology. The events have passed all the object and event selections described in sections 6.2 and 6.3. The distributions for both the SM correlated and uncorrelated samples are used. The distribution shown is for the combined dilepton channel and a similar result is obtained for each of the separate flavour channels. Also included is a ratio of the data to MC.

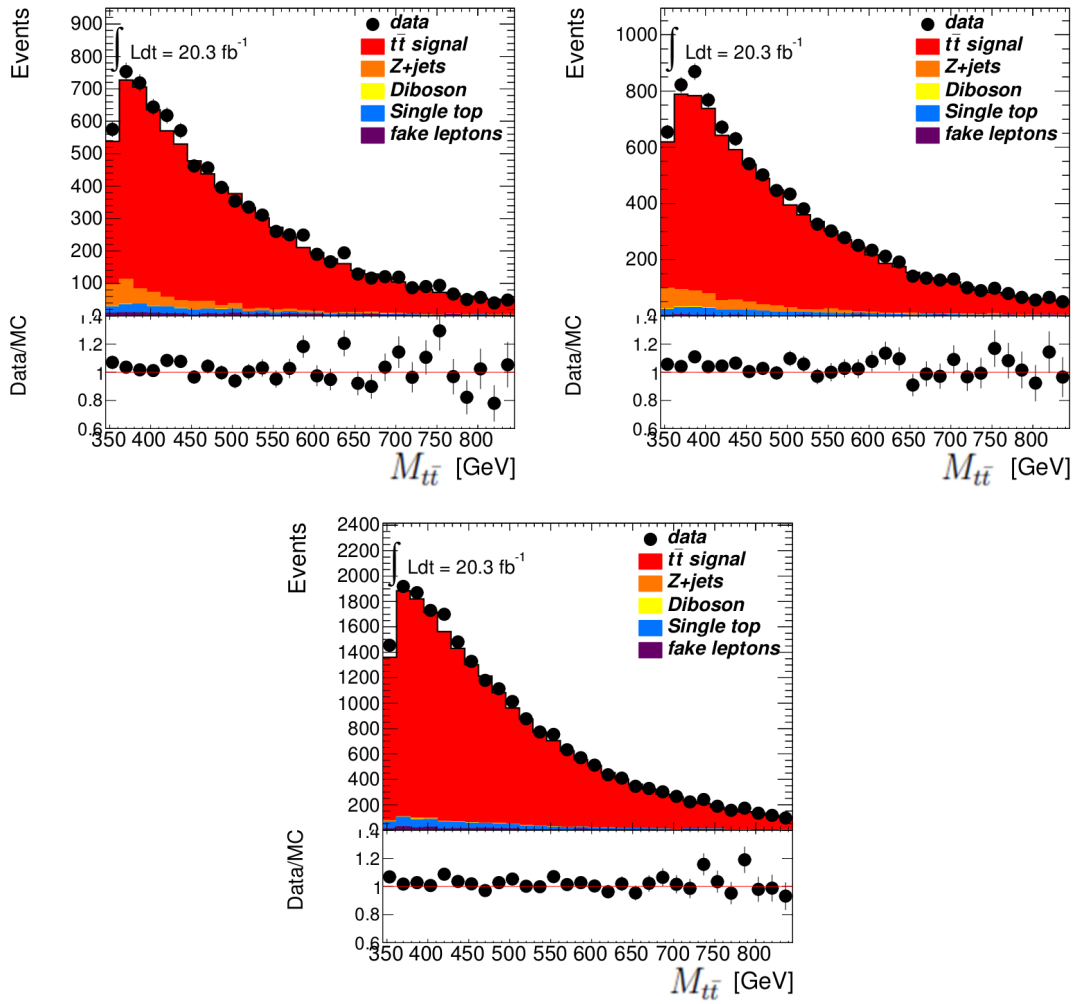

Figure 6.6: The $t\bar{t}$ invariant mass distributions for the ee, $\mu\mu$ and eμ channels following reconstruction using the M_{T2} variable. The data and MC are generally in good agreement.

6.6.1 The Unfolding Problem

When one describes the limitations of a detector, they can be broadly classed in three categories [109]:

- *Limited acceptance.* When including limited geometrical coverage and selection criteria, the probability of a genuine event being discovered is less than 1. This limited acceptance must be factored into the unfolding prescription.
- *Transformation.* When measuring a particular quantity, it is possible that a related quantity is measured instead (e.g. when attempting to measure E_T, all measurements may be systematically shifted upward, meaning it is not a true measurement of E_T).
- *Resolution effects.* In a real detector, the resolution of various components is by necessity finite and not continuous. This leads to a smearing of the measured quantity and can lead to a migration of an event from its true position into an adjacent bin.

When unfolding, each of these effects must be taken into account.

Mathematically, the relationship between a measured $g(s)$ and true $f(t)$ distribution can be described as:

$f(t) \rightarrow g(s)$ **transformation from truth to measured distributions**,

$g(s) \rightarrow f(t)$ **unfolding from measured to truth distributions**.

Using this notation, the unfolding problem can be described using a Fredholm equation of the first kind [110]:

$$g(s) = \int A(s,t) f(t) \mathrm{d}t \tag{6.7}$$

where $A(s,t)$ is the resolution function describing the convolution of all of the detector effects. Therefore, to unfold the data, it will become necessary to produce an accurate description for this $A(s,t)$. The description above assumes a continuous distribution. Experimentally, this is not the case and therefore the problem must be reformulated for a discretised distribution.

Within this analysis, histograms are used to describe the $\Delta\phi$ distribution. In the context of discretising the above equation, the histograms for the true and measured distributions can be considered to be vectors of finite length, n, in the case where the number of bins in the unfolded histogram is assumed to be the same as in the measured histogram. In this formulation, the resolution function $A(s,t)$ becomes a matrix of size n x n. This leaves us with

$$\mathbf{y} = A\mathbf{x}, \tag{6.8}$$

where $\mathbf{y}$ is the discretised form of the measured distribution, A is the matrix representing the resolution function (known as the *response matrix*) and $\mathbf{x}$ is the discretised form of the true distribution. Naively, it would appear that in order to determine the unknown $\mathbf{x}$, it is simply necessary to calculate the form of the response matrix, invert it and apply it to the measured distribution. In practice, this is not the case due to statistical fluctuations in the real and simulated distributions. However, the formulation of the response matrix is still critical to the process and the method used for this is discussed now.

6.6.1.1 Calculation of Response Matrix

To calculate the response matrix to be applied for each distribution, information is required about both the measured and truth distributions. With this in mind, Monte Carlo simulation is used. Two separate elements are calculated in order to form the total response matrix. These are the *acceptances* and the *migrations*.

The acceptances are calculated by producing $\Delta\phi$ distributions at both the truth and detector level. Using these, an efficiency value is defined as the probability that an event which is produced in bin i of the truth distribution is reconstructed in any of the bins of the detector level distribution. This will always be ≤ 1.

Another component of the acceptance calculation arises as a result of including cuts on the truth level information (see section 6.3.4). It is possible that an event which has been reconstructed has no corresponding truth information. This is a result of event smearing, where an event which has a kinematic quantity which lies marginally outside the truth fiducial region is reconstructed into the fiducial region at detector level (e.g. lepton or b-quark p_T). In order to adjust for this, a simulation study was conducted to determine the expected loss in each bin. Reconstructed $\Delta\phi$ distributions were produced which contained only events which had corresponding truth information, and for each bin a ratio was calculated between this and the distribution with all reconstructed events. Before unfolding the data, these ratios are used to reduce the data by the expected number of missing truth events in each bin.

To calculate the degree of migration, simulated data are once again used. For each event, $\Delta\phi$ is calculated for both the truth and reconstructed distributions. Using information contained within the simulated sample, it is possible to determine the migration in $\Delta\phi$ on an event by event basis. If an event is included in both the truth and reconstructed distributions, it is included within the *migration matrix*, which is an $n \times n$ matrix mapping from the true value of $\Delta\phi$ to the reconstructed $\Delta\phi$. If an event is not present in one of the distributions, then it is not included in the migration matrix and instead is accounted for as part of either the acceptance or the *missing truth events* corrections.

6.6.1.2 Differences Between Inclusive and Differential Measurement

One notable point is that the unfolding procedure is slightly more complex for the differential measurement in comparison to the inclusive. In the inclusive measurement, one quantity needs to be reconstructed, namely the $\Delta\phi$ between the charged leptons in the event ($0 \leq \Delta\phi \leq \pi$ measured in 20 bins). However, in order to make a differential measurement, the $M_{t\bar{t}}$ of the event needs to be calculated simultaneously with the $\Delta\phi$ (with the method of reconstruction described in section 6.5 and the $\Delta\phi$ placed in one of six distinct bins). This necessitates a variation on the unfolding method as both of the quantities need to be taken into account at the same time. It is not possible to unfold one quantity subsequent to the other as information will be lost in the process and the unfolding will become inaccurate.

To take this into account, when calculating the acceptances and migration matrices, the differential measurement is treated as one larger histogram of 18 bins, acting as a concatenation of the three separate $M_{t\bar{t}}$ regions. This allows for a more correct treatment of migration and acceptance effects, as a migration between $M_{t\bar{t}}$ regions can be treated at the same time as a migration between neighbouring $\Delta\phi$ bins. The resulting response matrix will therefore be an 18 x 18 matrix and data will be unfolded to a similarly concatenated 18-bin histogram, before being split again into the separate $M_{t\bar{t}}$ regions for presentation of results.

6.6.2 Calculated Response Matrices

The response matrices derived from the simulation sample with SM correlation can be seen in figure 6.7.

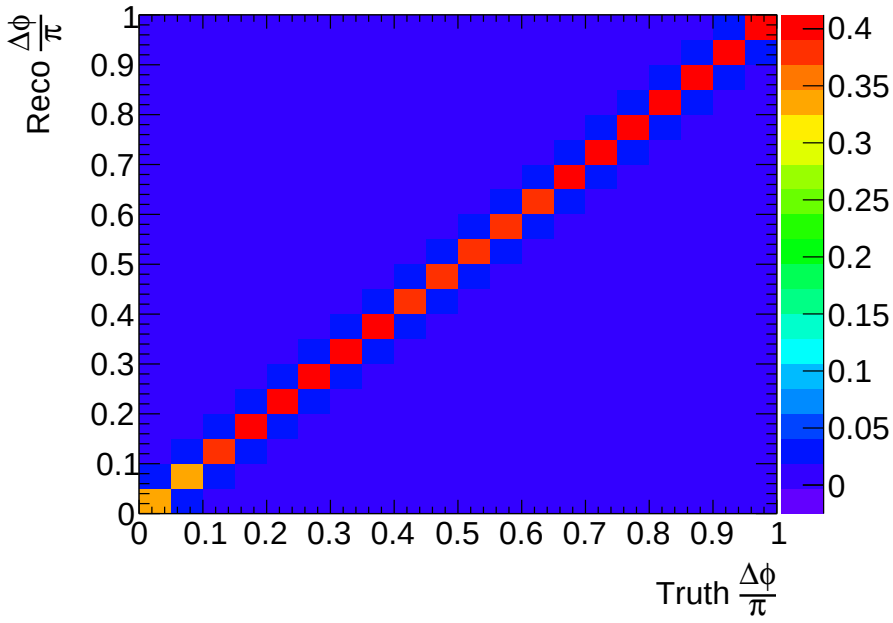

(a)

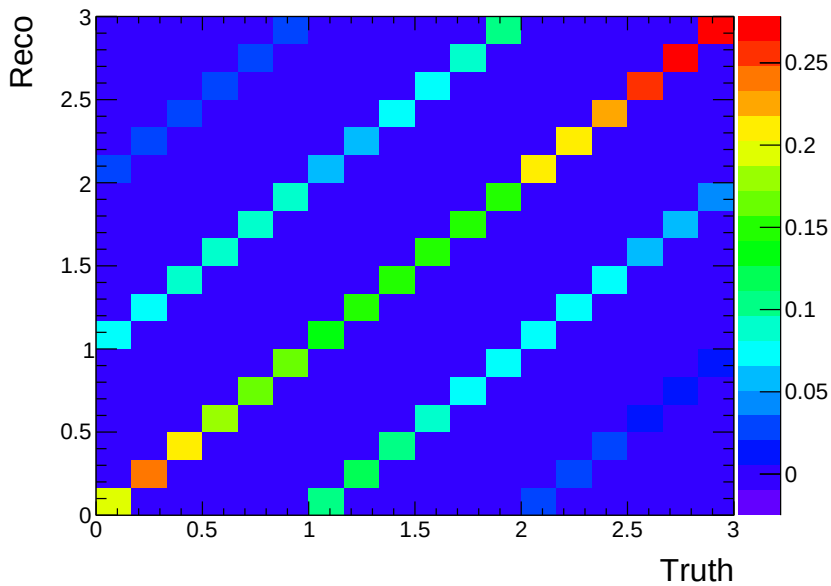

(b)

Figure 6.7: The response matrices for the combined dilepton channels using the SM correlated simulation sample: a) is the response matrix for the inclusive measurement (in bins of $\frac{\Delta\phi}{\pi}$) and b) is the response matrix for the differential measurement, which combines all three $M_{t\bar{t}}$ ranges, as described in section 6.6.1.2, where 0-1, 1-2, 2-3 represents $\frac{\Delta\phi}{\pi}$ in the mass ranges $M_{t\bar{t}} \leq 415$ GeV, 415 GeV$< M_{t\bar{t}} \leq 505$ GeV and $M_{t\bar{t}} > 505$ GeV respectively. The response matrices for the $e\mu$ channel show similar results.

Due to the fine resolution of ϕ in the detector, in comparison to the bin width, the migration of $\Delta\phi$ events between bins is very small, leading to a diagonal response matrix in the inclusive measurement. This means that a bin-by-bin unfolding approach could be taken and that a full unfolding need not be used [111]. A bin-by-bin unfolding simply corrects each measured bin by the expected acceptance correction and modifies the error analysis accordingly. However, this approach cannot be used to give an accurate error analysis for the differential analysis (as the migration in $M_{t\bar{t}}$ is noticeable). Therefore, in order to use a unified approach across all elements of the analyis, the Fully Bayesian Unfolding (FBU) method is used to unfold both the inclusive and differential measurements.

6.6.3 Fully Bayesian Unfolding

Using a Bayesian statistical approach, a methodology for unfolding a measured data distribution can be formed. Bayes' Theorem, in its purest form gives a conditional probability of observation of an event in relation to other probabilities, conditional or otherwise [110]

$$P(A|B) = \frac{P(B|A)P(A)}{P(B)}. \tag{6.9}$$

If the definition in equation 6.9 is extended to the unfolding problem that is presented here, with A representing the true distribution, $\mathbf{T}$ and B representing the measured data, $\mathbf{D}$ it can be rewritten as

$$p(\mathbf{T}|\mathbf{D}, \mathcal{M}) \propto \mathcal{L}(\mathbf{D}|\mathbf{T}, \mathcal{M}).\pi(\mathbf{T}), \tag{6.10}$$

where $\mathcal{M}$ is the reponse matrix encoding the total detector response and $\pi(\mathbf{T})$ is the prior probability density of the truth distribution (a functional representation of an initial estimate of what the data will look like). This gives an estimation of the

posterior probability distribution of the truth distribution using ingredients that are measurable in the analysis [95] [112]. For the choice of $\pi(\mathbf{T})$, this analysis uses a value of 1, i.e. it is assumed that all points are equally likely and there is no assumed prior information.

The likelihood used in equation 6.10 is given more explicitly by

$$\mathcal{L}(\mathbf{D}|\mathbf{T}, \mathcal{M}) = \prod_{i}^{N_r} \frac{R_r^{D_r}}{D_r!} e^{-R_r}, \tag{6.11}$$

where D_r is the number of events observed in the r'th bin of the measured distribution, N_r is the number of bins in the reconstructed distribution and R_r is the predicted number of events in the reconstructed distribution. R_r is estimated by using the numbers of events in each bin of the truth distribution multiplied by the appropriate coefficients from the response matrix. In addition, where background contributions are expected, these are added to the value of R_r (when unfolding data, the expected backgrounds are subtracted from the data in the calculation). This methodology assumes that the measured data are Poisson distributed, and this is expected to be the case for this analysis.

Using the above formulae, 10000 randomly distributed points are generated across the number of truth bins (so for this analysis, either 18 or 20 depending on the distribution), using a Markov Chain Monte Carlo sampling method [113]. This will give the posterior probability distribution for each of the bins. If this has been calculated correctly, the distribution should be Gaussian for each of the bins and the peak of this distribution is taken as the central value of the bin, with the width taken as the statistical error. As a check, the posterior probability is verified as being Gaussian for each bin. In order to implement the FBU procedure, the pyFBU set of packages is used, both for the estimation of likelihoods and the generation of the sampling [114].

6.6.4 Closure Testing of Response Matrices

To test the accuracy of the response matrices, a self-consistency check, known as a closure test, is performed. The simulated sample from which the matrix was calculated is unfolded using the corresponding response matrix. For a good closure test, the truth distribution from the sample should be recovered. In addition, to assess the chance of bias, the uncorrelated sample is also unfolded with this same response matrix and compared to its own truth distribution. The results of these closure tests can be seen in figures 6.8-6.10 (where the error bars represent the width of the Gaussian posterior probability distributions). They show that the response matrices accurately unfold the SM simulated samples back to their respective truth measurements. When using the response matrices to unfold the uncorrelated samples, however, we see that the unfolding is not perfect. A systematic uncertainty will therefore be assigned to this effect by unfolding data also with a response matrix calculated from the uncorrelated sample.

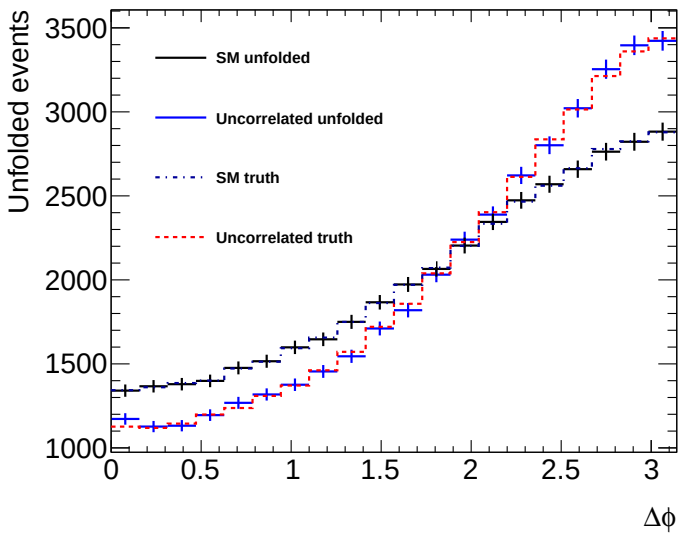

(a)

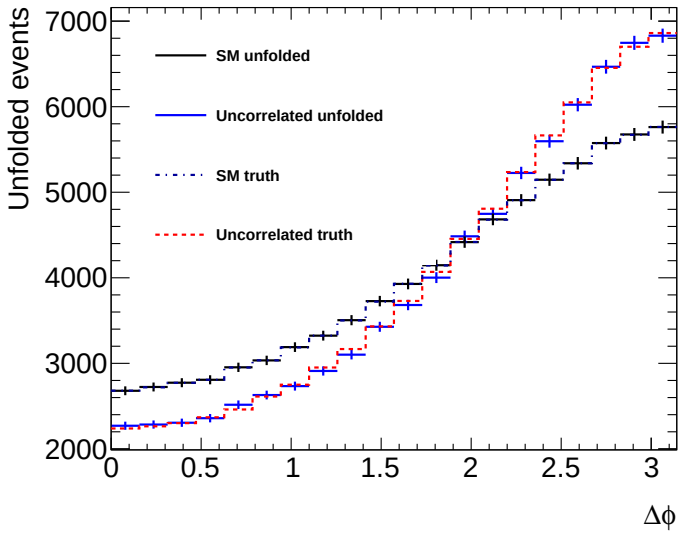

(b)

Figure 6.8: Closure tests using the Fully Bayesian Unfolding method for the inclusive measurement, where a) is the $e\mu$ channel and b) is the combined dilepton channel. The figures show the result of unfolding the detector level simulation for both the SM correlated and uncorrelated samples. The samples have been unfolded using the response matrix which has been calculated with the SM correlated sample.

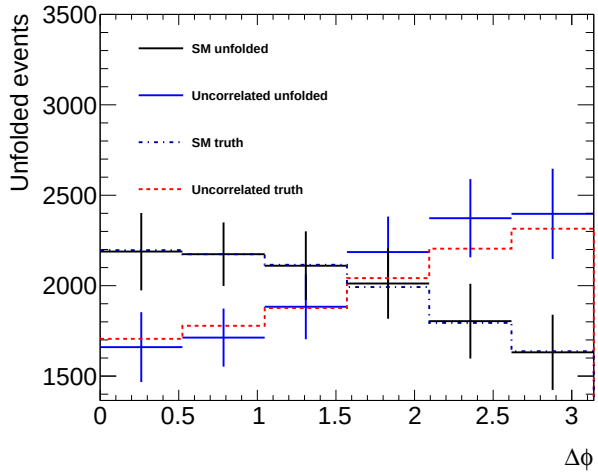

(a)

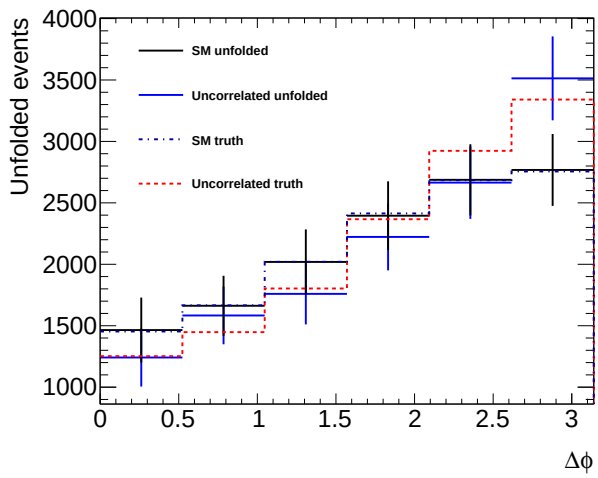

(b)

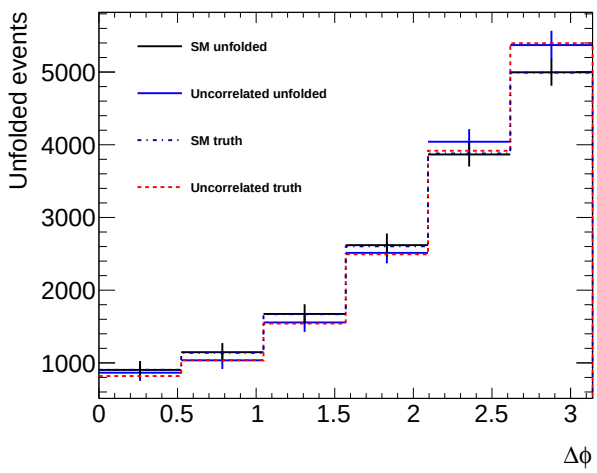

(c)

Figure 6.9: Closure tests using the Fully Bayesian Unfolding method for the eμ channel differential measurements, where a) shows the mass range $M_{t\bar{t}} \leq 415$ GeV,b) shows 415 GeV$< M_{t\bar{t}} \leq 505$ GeV and c) shows $M_{t\bar{t}} > 505$ GeV. The figures show the result of unfolding the detector level simulation for both the SM correlated and uncorrelated samples. The samples have been unfolded using the response matrix which has been calculated with the SM correlated sample.

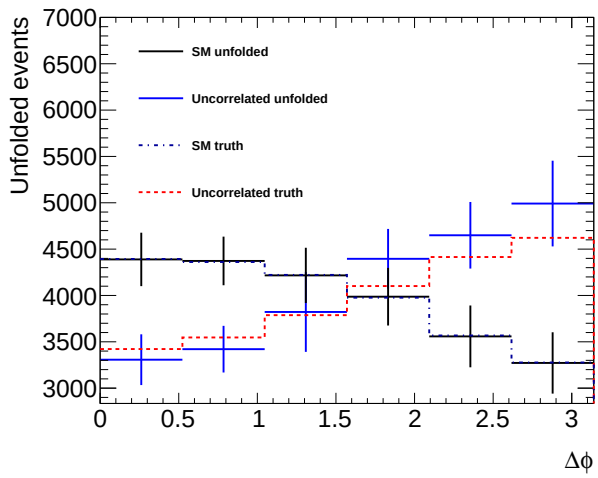

(a)

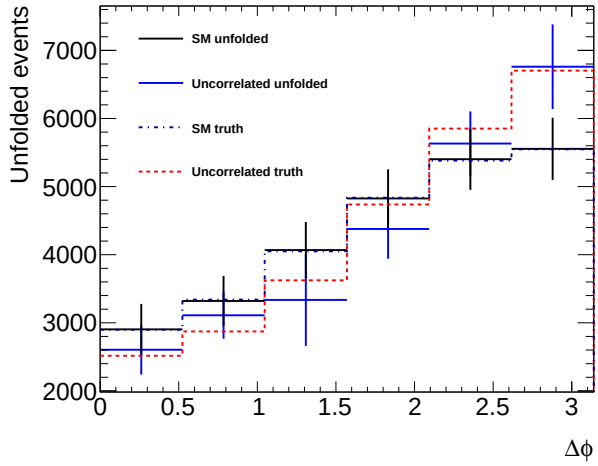

(b)

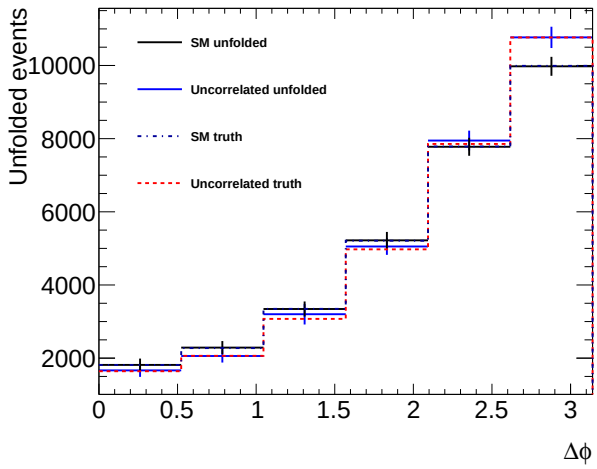

(c)

Figure 6.10: Closure tests using the Fully Bayesian Unfolding method for the combined dilepton channel differential measurements, where a) shows the mass range $M_{t\bar{t}} \leq 415$ GeV,b) shows 415 GeV$< M_{t\bar{t}} \leq 505$ GeV and c) shows $M_{t\bar{t}} > 505$ GeV. The figures show the result of unfolding the detector level simulation for both the SM correlated and uncorrelated samples. The samples have been unfolded using the response matrix which has been calculated with the SM correlated sample.

6.7 Control Plots and Yields

The plots shown in figures 6.11-6.13 show the agreement between data and Monte Carlo simulation for several distributions which act as a control to assess the accuracy of the simulation (i.e. where we expect the agreement to be good). The distributions that are shown have event selection cuts applied identical to those given in section 6.3.3, apart from the cut relating to the distribution shown, which is relaxed. These show generally good agreement. There is some excess of data in the low MET region for the same flavour channels but this is explained as being due to less accurate modelling of the Z/γ^*+jets background in this region. This region is not included in the signal region and therefore will not impact the $\Delta\phi$ measurement. Figures 6.14-6.17 show the data/Monte Carlo agreement for the properties of selected objects (i.e. lepton and jet η, ϕ and p_T), with all quality cuts included.

The yields for the signal region and associated backgrounds are shown in tables 6.4-6.7. These include statistical uncertainties as well as uncertainties that arise from normalisations. It is noted that there is a small excess of data over expectation from simulation, but these excesses are not significant.

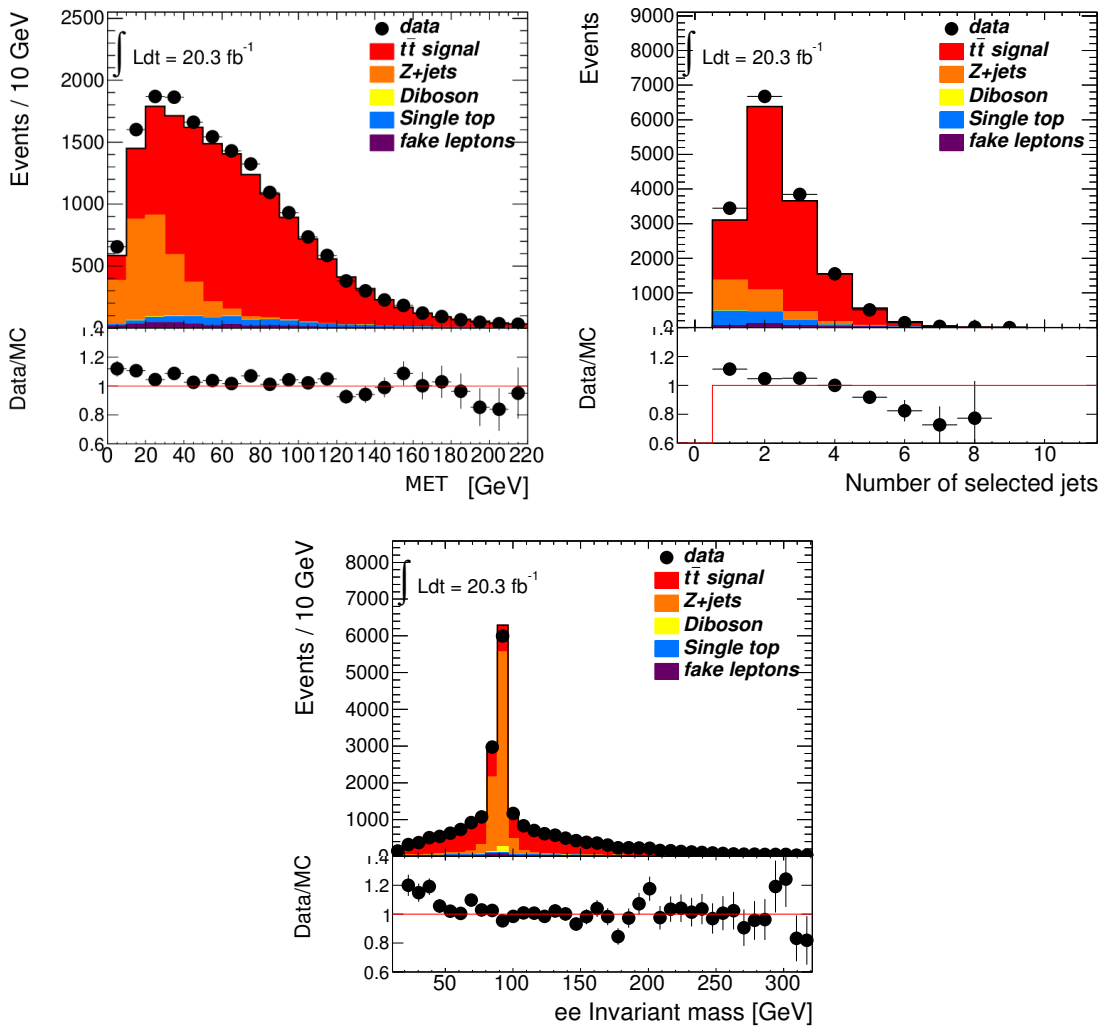

Figure 6.11: Data/Monte Carlo distributions in the e^+e^- channel, using all event selection cuts except the one on the variable which is being plotted. These comparisons are made after the Z+jets normalisation factors have been applied (see section 6.4.2).

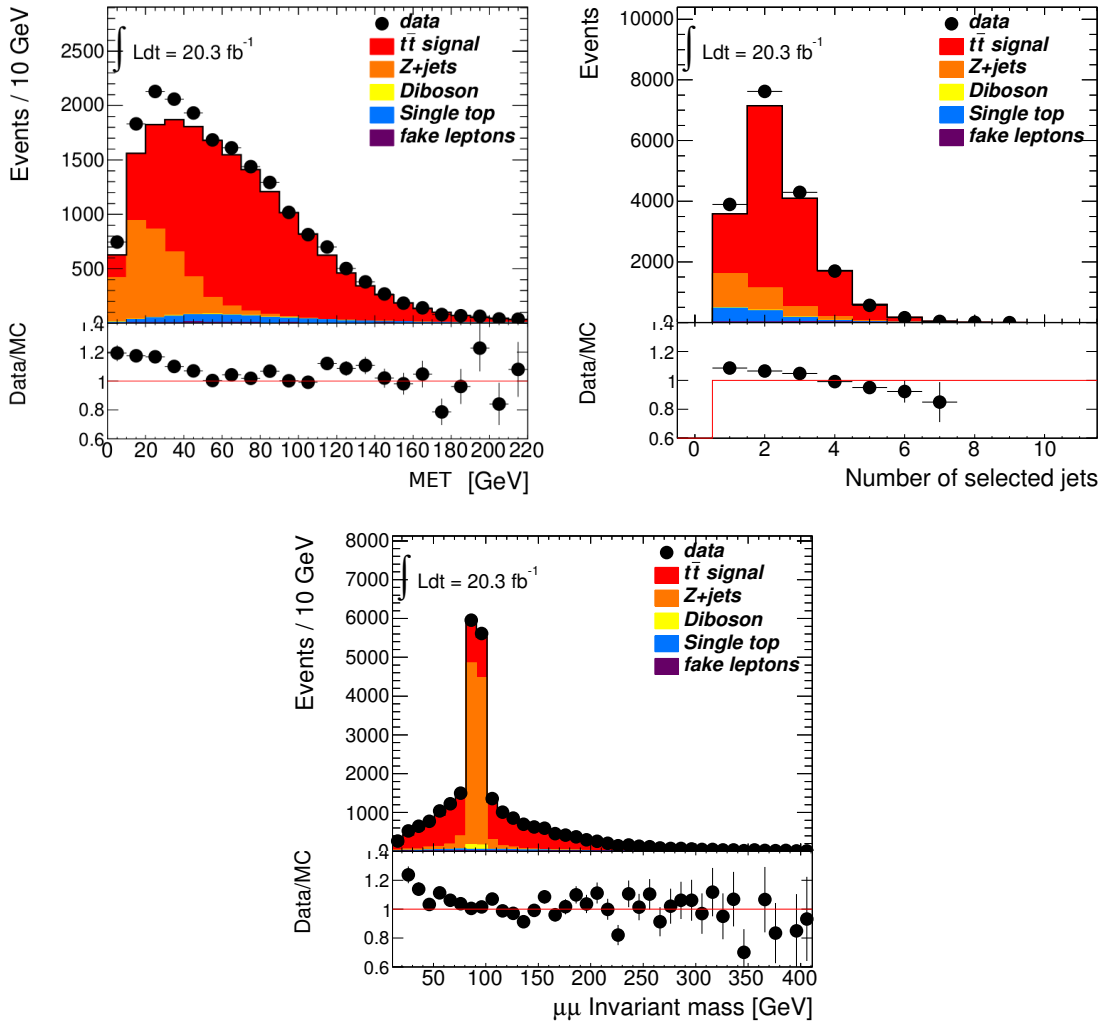

Figure 6.12: Data/Monte Carlo distributions in the $\mu^+\mu^-$ channel, using all event selection cuts except the one on the variable which is being plotted. These comparisons are made after the Z+jets normalisation factors have been applied (see sections 6.4.2).

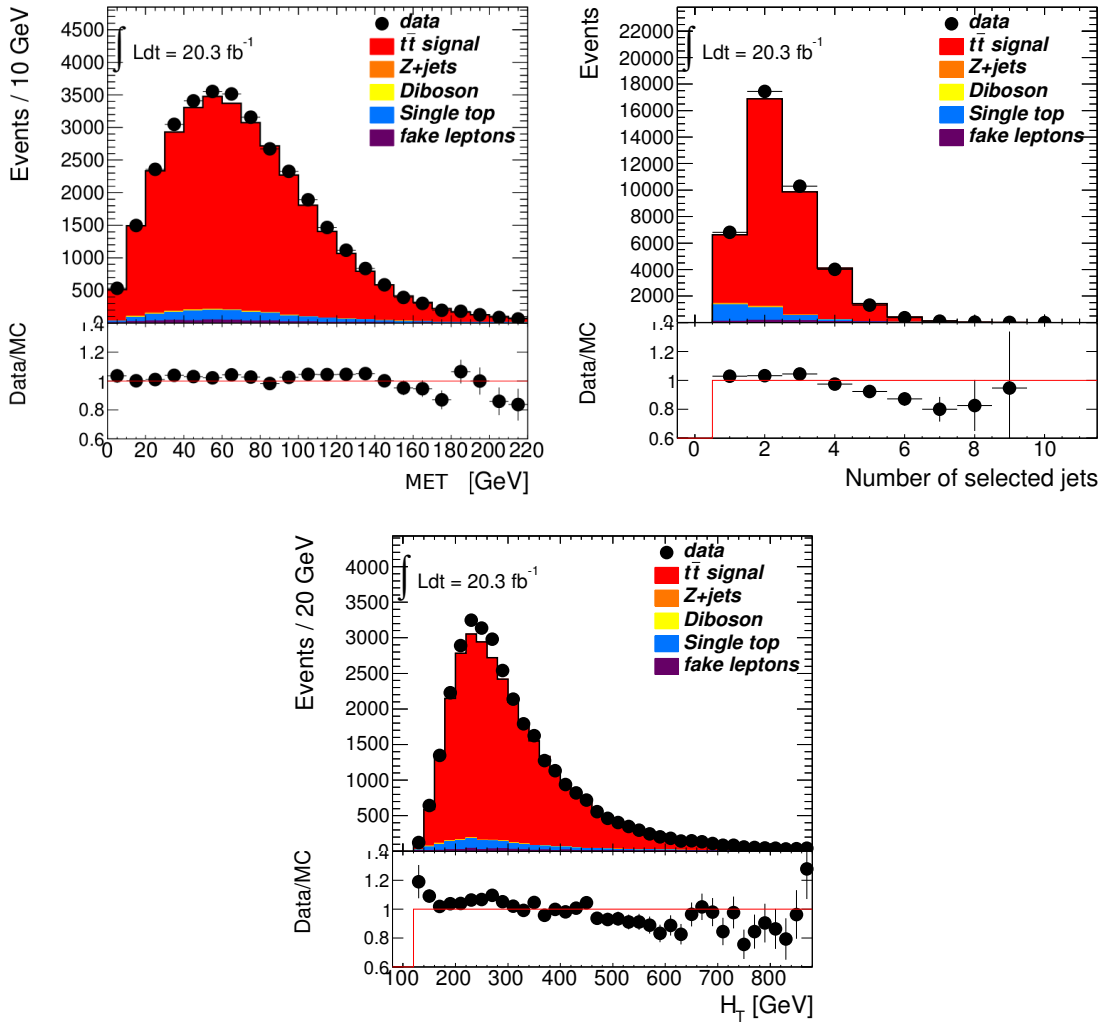

Figure 6.13: Data/Monte Carlo distributions in the $e^{\pm}\mu^{\mp}$ channel, using all event selection cuts except the one on the variable which is being plotted. These comparisons are made after the Z+jets normalisation factors have been applied (see section 6.4.2). Here, H_T is defined as the scalar sum of all jet and charged lepton p_T values.

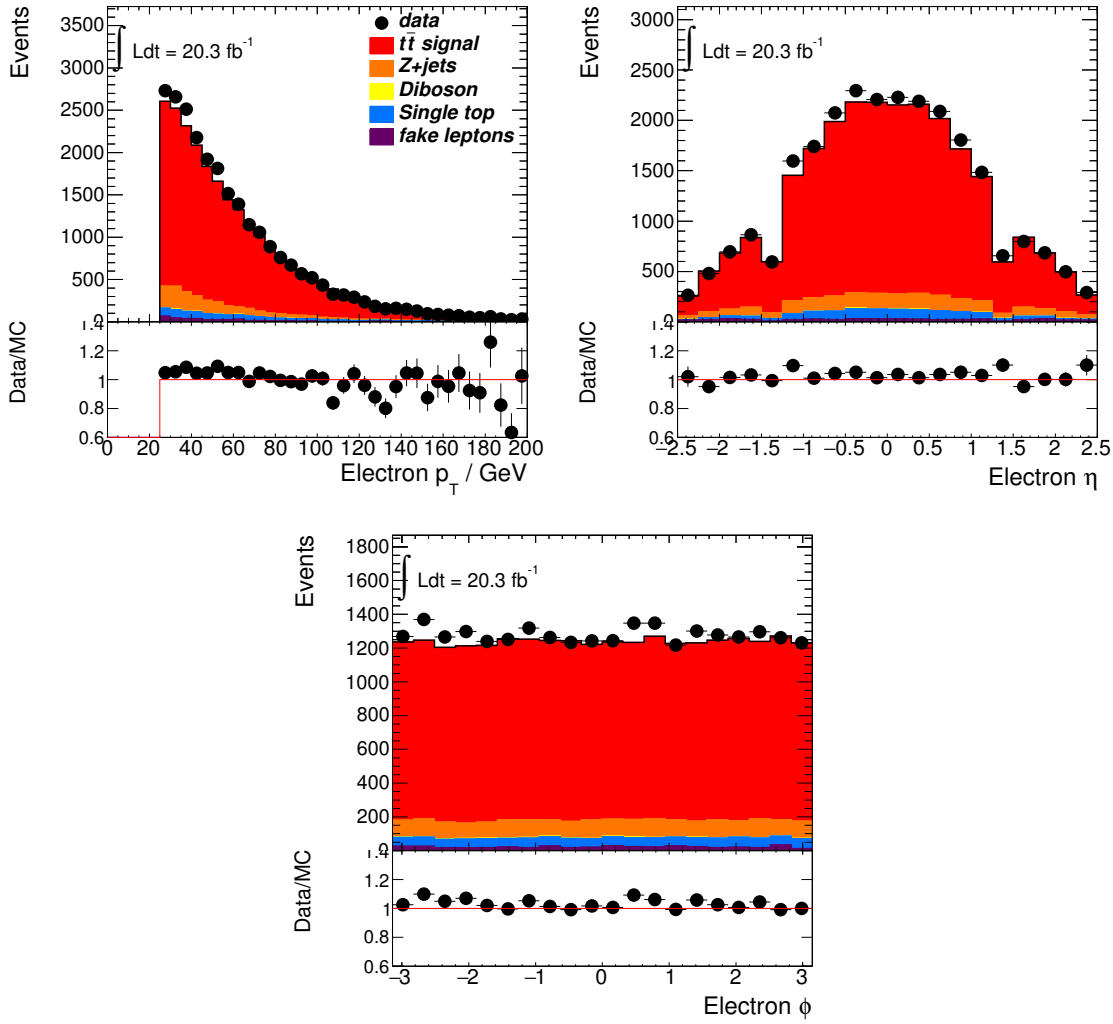

Figure 6.14: Data/Monte Carlo distributions in the e^+e^- channel, using all event selection cuts, for the leading and subleading leptons. These comparisons are made after the Z+jets normalisation factors have been applied (see section 6.4.2).

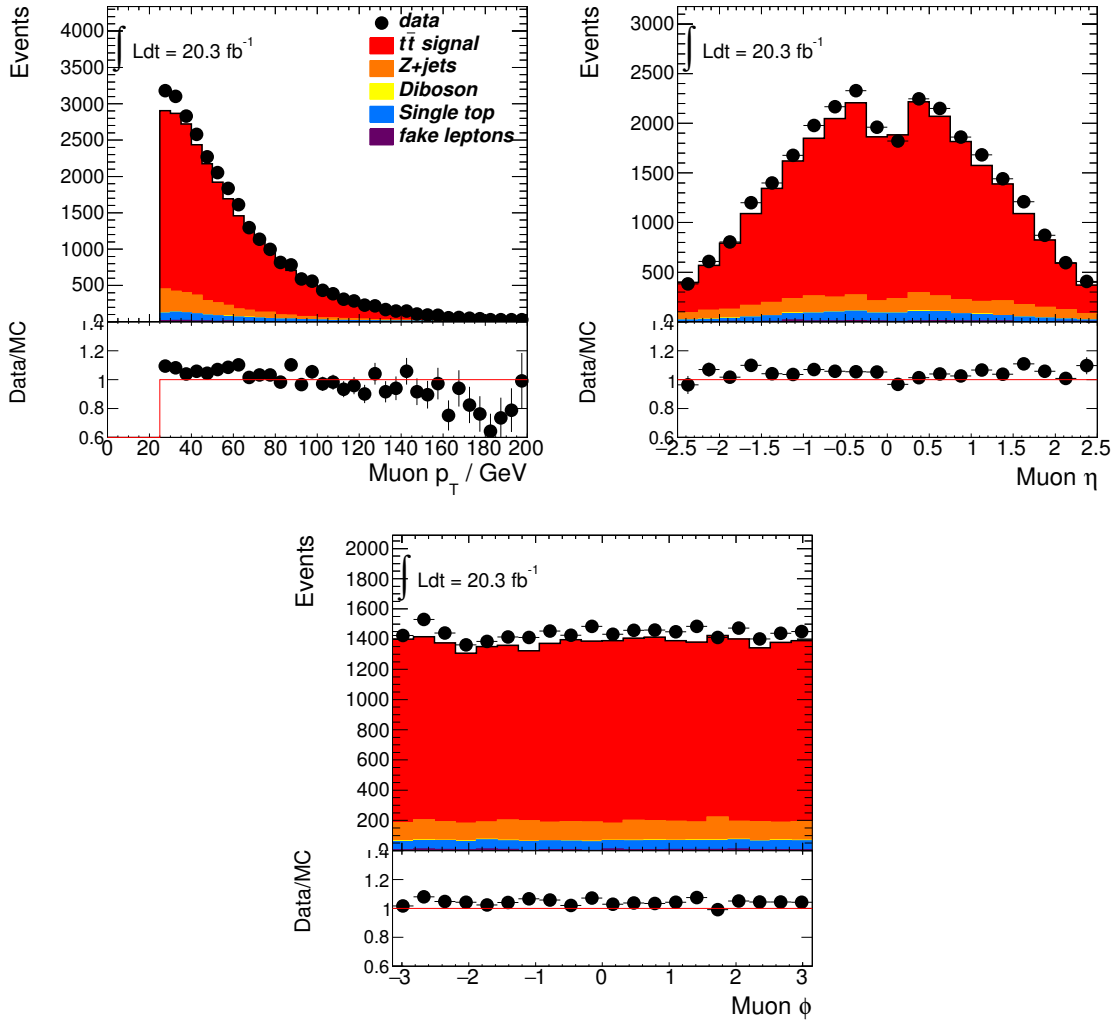

Figure 6.15: Data/Monte Carlo distributions in the $\mu^+\mu^-$ channel, using all event selection cuts, for the leading and subleading leptons. These comparisons are made after the Z+jets normalisation factors have been applied (see section 6.4.2).

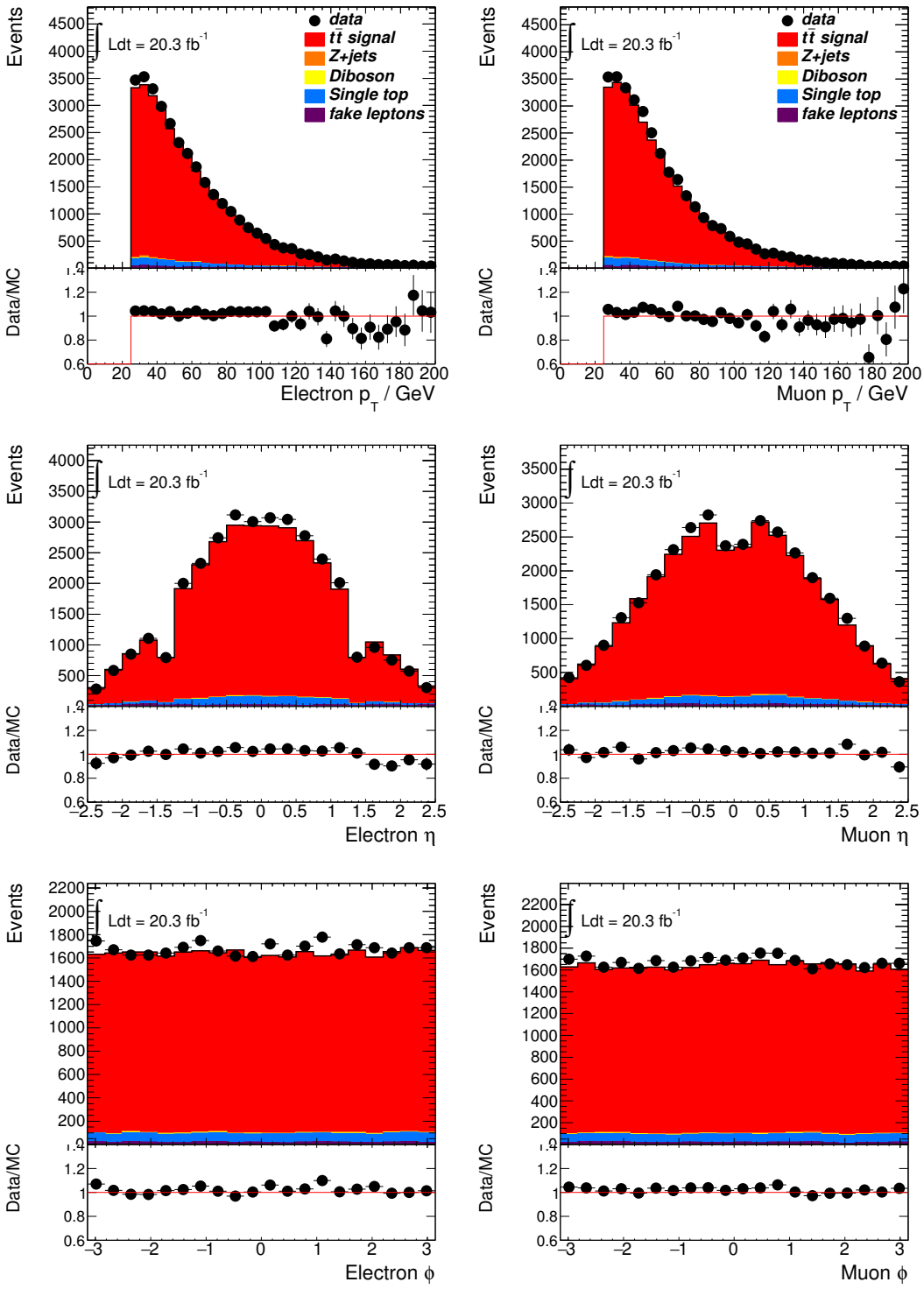

Figure 6.16: Data/Monte Carlo distributions in the $e^{\pm}\mu^{\mp}$ channel, using all event selection cuts, for the leading and subleading leptons. These comparisons are made after the Z+jets normalisation factors have been applied (see section 6.4.2).

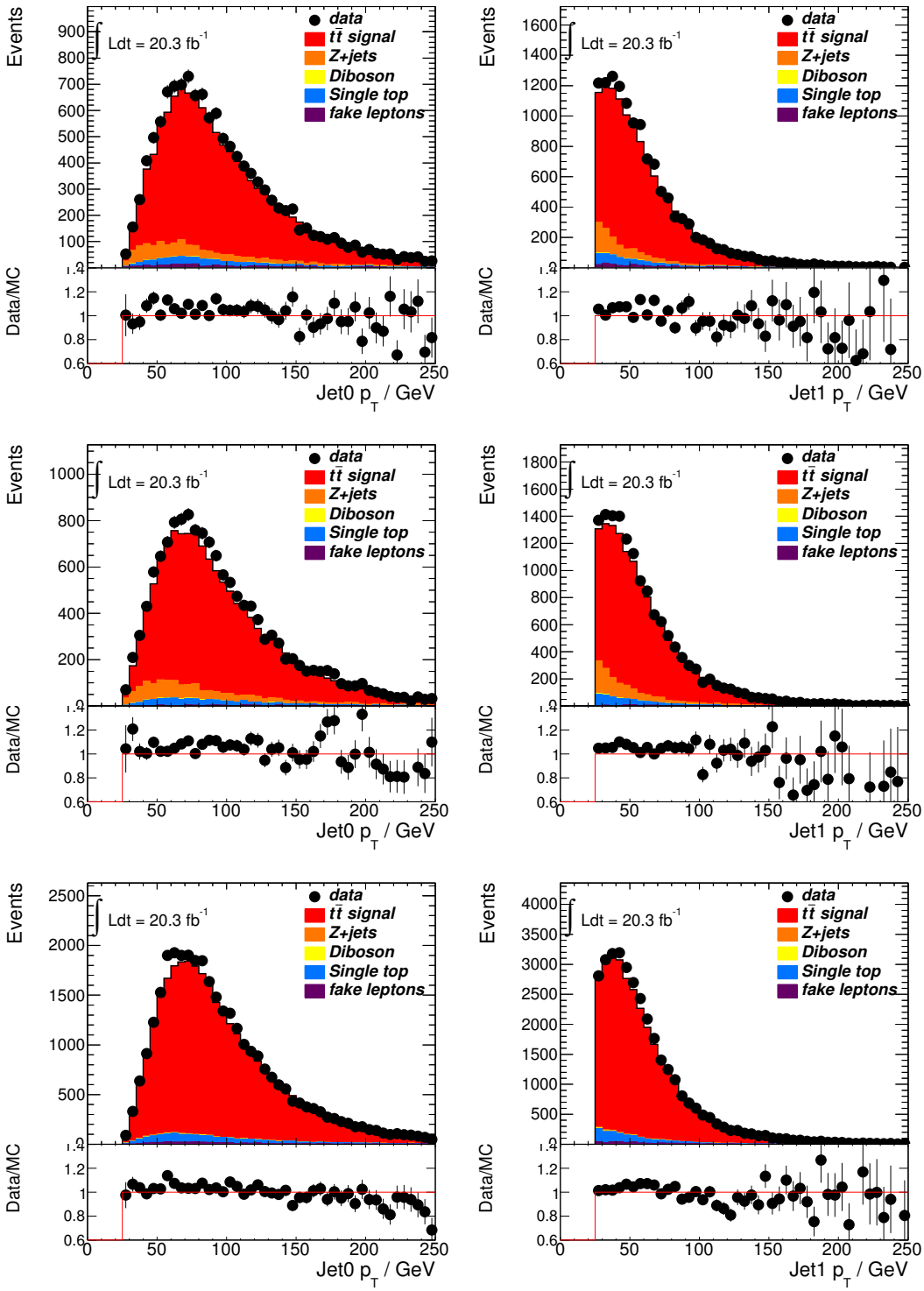

Figure 6.17: Data/Monte Carlo distributions for leading jet (Jet0) and subleading jet (Jet1) p_T using all event selection cuts. These comparisons are made after the Z+jets normalisation factors have been applied (see section 6.4.2). The top row is the ee channel , the second row is the $\mu\mu$ channel and the bottom row is the $e\mu$ channel.

Table 6.4: The yields for data and simulated Monte Carlo in the signal region for the inclusive measurement as well as the expected yields for relevant background sources. For each MC yield, a statistical uncertainty is listed, as well as an associated normalisation error, which is listed as the second of the two errors given.

	Channel		
Event source	ee	$\mu\mu$	eμ
$t\bar{t}$ signal	10587.6 ± 28.7 ± 296.5	11868.7 ± 30.2 ± 332.3	30736.3 ± 48.9 ± 860.1
Z/γ^*+jets	1011.9 ± 24.3 ± 75.1	1257.6 ± 30.5 ± 93.6	117.1 ± 11.3 ± 8.9
Fake leptons	221.6 ± 15.2 ± 221.6	60.1 ± 7.8 ± 60.1	391.8 ± 20.1 ± 391.8
Single top	534.7 ± 6.4 ± 36.4	576.8 ± 6.6 ± 39.2	1491.5 ± 10.7 ± 101.4
Diboson	33.3 ± 3.4 ± 11.3	39.7 ± 3.8 ± 13.5	83.6 ± 5.5 ± 28.4
Total background	1801.5 ± 29.6 ± 237.1	1934.2 ± 32.3± 118.7	2084.0 ± 26.0 ± 405.8
Expected (E)	12389.1 ± 41.2 ± 379.6	13802.9 ± 44.3 ± 352.9	32820.3 ± 55.4 ± 951.0
Observed (O)	12768	14397	33531
O-E	378.9	594.1	710.7
O/E (%)	1.03	1.04	1.02

Table 6.5: The yields for data and simulated Monte Carlo in the signal region for the region $M_{t\bar{t}} \leq 415$ GeV as well as the expected yields for relevant background sources. For each MC yield, a statistical uncertainty is listed, as well as an associated normalisation error, which is listed as the second of the two errors given.

	Channel		
Event source	ee	$\mu\mu$	eμ
$t\bar{t}$ signal	2349.1 ± 13.5 ± 65.8	2690.9 ± 14.5 ± 75.3	6724.4 ± 22.9 ± 188.2
Z/γ^*+jets	239.3 ± 12.8 ± 17.7	251.7 ± 12.8 ± 18.8	28.9 ± 5.9 ± 2.1
Fake leptons	35.5 ± 6.1 ± 35.5	10.8 ± 3.3 ± 10.8	83.5 ± 9.3 ± 83.5
Single top	94.0 ± 2.7 ± 6.4	101.6 ± 2.8 ± 6.9	263.7 ± 4.5 ± 17.9
Diboson	4.1 ± 1.0 ± 1.4	9.3 ± 1.8 ± 3.2	13.1 ± 2.3 ± 4.5
Total background	372.9 ± 14.5 ± 40.2	373.4 ± 13.6 ± 23.0	389.2 ± 12.1 ± 85.5
Expected (E)	2722.0 ± 19.8 ± 77.1	3064.3 ± 19.9 ± 78.7	7113.6 ± 25.9 ± 206.7
Observed (O)	2823	3258	7326
O-E	101.0	193.7	212.4
O/E (%)	1.04	1.06	1.03

Table 6.6: The yields for data and simulated Monte Carlo in the signal region for the region 415 GeV$< M_{t\bar{t}} \leq$ 505 GeV as well as the expected yields for relevant background sources. For each MC yield, a statistical uncertainty is listed, as well as an associated normalisation error, which is listed as the second of the two errors given.

	Channel		
Event source	ee	$\mu\mu$	eμ
$t\bar{t}$ signal	2289.9 ± 13.3 ± 64.1	2571.4 ± 14.1 ± 72.0	6527.0 ± 22.6 ± 182.8
Z/γ^*+jets	121.0 ± 7.9 ± 9.0	145.9 ± 8.7 ± 10.8	8.4 ± 2.7 ± 0.6
Fake leptons	30.5 ± 5.7 ± 30.5	4.9 ± 2.2 ± 4.9	65.7 ± 8.2 ± 65.7
Single top	84.6 ± 2.6 ± 5.8	88.7 ± 2.6 ± 6.0	230.5 ± 4.2 ± 15.7
Diboson	4.8 ± 1.3 ± 1.6	2.8 ± 0.9 ± 1.0	11.1 ± 2.0 ± 3.8
Total background	240.9 ± 10.2 ± 32.3	242.3 ± 9.4 ± 13.3	315.7 ± 9.8 ± 67.7
Expected (E)	2590.0 ± 16.7 ± 71.8	2813.7 ± 16.9 ± 73.2	6842.7 ± 24.6 ± 194.9
Observed (O)	2579	2892	7069
O-E	-11.0	78.3	226.3
O/E (%)	1.00	1.03	1.03

Table 6.7: The yields for data and simulated Monte Carlo in the signal region for the region $M_{t\bar{t}} >$ 505 GeV. For each MC yield, a statistical uncertainty is listed, as well as an associated normalisation error, which is listed as the second of the two errors given.

	Channel		
Event source	ee	$\mu\mu$	eμ
$t\bar{t}$ signal	3249.3 ± 15.9 ± 91.0	3671.9 ± 16.8 ± 102.8	8493.3 ± 25.7 ± 237.8
Z/γ^*+jets	87.7 ± 6.1 ± 6.5	117.1 ± 10.9 ± 8.7	8.3 ± 2.7 ± 0.7
Fake leptons	69.0 ± 8.5 ± 69.0	15.7 ± 4.0 ± 15.7	102.2 ± 10.3 ± 102.2
Single top	93.2 ± 2.6 ± 6.3	107.1 ± 2.8 ± 7.3	239.6 ± 4.3 ± 16.3
Diboson	2.8 ± 1.0 ± 1.0	3.1 ± 0.9 ± 1.1	8.2 ± 1.5 ± 2.8
Total background	252.7 ± 10.8 ± 69.6	243.0 ± 11.9 ± 19.4	358.3 ± 11.6 ± 103.5
Expected (E)	3682.0 ± 19.2 ± 114.6	3914.9 ± 20.6 ± 104.6	8851.6 ± 28.2 ± 259.4
Observed (O)	3585	4061	9049
O-E	-97.0	146.1	197.4
O/E (%)	0.97	1.04	1.02

Chapter 7

ANALYSIS RESULTS

This chapter presents the methodology for extracting the spin correlation from the $\Delta\phi$ distributions at detector level, followed by a presentation of the results. The unfolded distributions are also presented. Additionally, a description of all sources of systematic uncertainty is given, with an outline of the procedures used to assess these. A summary of these uncertainties is given both in this chapter and in Appendix A.

7.1 Extracting Spin Correlation

For the detector level measurement, a technique is developed in order to extract a value for the amount of spin correlation found in the data. This is done using a template method, used with two signal templates (one with Standard Model levels of spin correlation and one with zero spin correlation) and one template for the background (which is the sum of all non $t\bar{t}$ events). To extract a value, a fit is performed with the templates using a binned maximum likelihood methodology, with two free parameters. The fitting is performed using the *ROOFIT* software package [115]. The free parameters affect the expected numbers of signal events in each bin. One parameter affects the overall normalisation of the signal events ($f_{t\bar{t}}$) and allows it to float freely. The other (f_{SM}), alters the mix of SM-like and uncorrelated events. It is this parameter which determines the degree of spin correlation seen. The log likelihood fit is of the form

$$\mathcal{L}(f_{t\bar{t}}, f_{SM}) = \prod_{i=1}^{N} \frac{(S_i + B_i)^{n_i}}{n_i!} e^{-(S_i+B_i)}, \tag{7.1}$$

where n_i is the number of data events observed in bin i, B_i is the number of background events expected from simulation in bin i and S_i is the number of expected signal events in bin i, defined as

$$S_i = f_{t\bar{t}}(s_i^0 + f_{SM}(s_i^{SM} - s_i^0)), \tag{7.2}$$

where s_i^{SM} is the number of signal events expected in bin i from the Standard Model template, and s_i^0 is the number of signal events in bin i from an uncorrelated scenario. The equation has been formulated in such a way that $f_{SM} = 1$ means that the expected number of events is given by the SM template, and $f_{SM} = 0$ implies the number of expected events is taken from the uncorrelated template. In order to determine the best fit values for both $f_{t\bar{t}}$ and f_{SM}, the minimum value of $-\ln\mathcal{L}(f_{t\bar{t}}, f_{SM})$ is found.

In order to verify the method used, a linearity test is performed. Here, sets of pseudo-data are created using Monte Carlo simulation with varying values of f_{SM} and $f_{t\bar{t}}$. From this, each bin in the created distribution is fluctuated 10000 times according to Poisson statistics. Each of these sets of pseudo-data is fitted as if it were data according to the procedure above and a Gaussian distribution of f_{SM} or $f_{t\bar{t}}$ values is formed. The mean values of these Gaussians are taken as the results of the linearity test. The output value for the free parameters is compared to the input parameter and the result is shown in figures 7.1 and 7.2. As can be seen, there is good agreement between the input and output values.

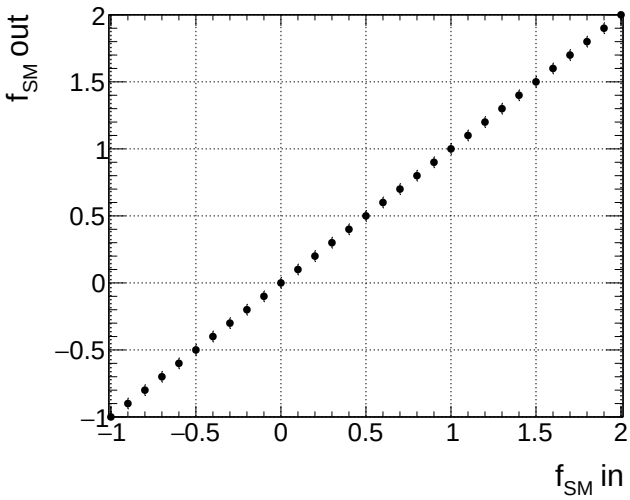

Figure 7.1: Linearity test of the f_{SM} fitting procedure in the eμ channel. Input values of f_{SM} were tested in the range -1 to 2 in intervals of 0.1.

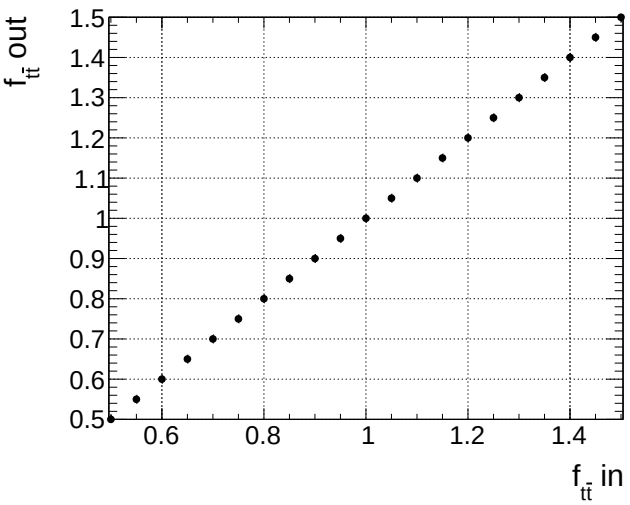

Figure 7.2: Linearity test of the $f_{t\bar{t}}$ fitting procedure in the eμ channel. Input values of $f_{t\bar{t}}$ were tested in the range 0.5 to 1.5 in intervals of 0.05.

7.2 Systematic Uncertainties

7.2.1 Procedure to Assess Systematic Uncertainties in Detector Measurement

In order to assess the systematic uncertainty on f_{SM}, a similar procedure is utilised to that used to validate the fitting procedure in the previous section. For each source of systematic uncertainty, a new MC simulation template is created with the appropriate systematic variation applied to the template (both to the signal, and where appropriate, the background). From this, 10000 pseudo-datasets are created by varying each bin with a Poisson fluctuation. For each of the pseudo-datasets, the fitting procedure is carried out. At the same time, another 10000 pseudoexperiments are generated by Poisson fluctuating the nominal Standard Model template with the same fluctuation as for the systematic template. Another Gaussian of the generated f_{SM} values is created. The absolute difference between the mean values of the two Gaussians is taken as being the error assigned to that systematic variation.

For some of the variations, there will be both an up and down modification. In these cases, the variation is calculated for both possibilities as described above. The larger of the two absolute differences is taken as being the uncertainty associated with this source and will be symmetrised. If there is a one sided variation, the uncertainty will still be calculated as above and symmetrised. The list of uncertainties, and any special procedures needed to assess specific sources of error, are described below. The full list of systematic uncertainties on the f_{SM} measurement are shown in table 7.3.

7.2.2 Sources of Systematic Uncertainties

7.2.2.1 Jet Uncertainties

Jet uncertainties will have an impact on both the inclusive and differential elements of this analysis. For the differential binning, the $t\bar{t}$ system for the event needs to be reconstructed, which requires using jet four-vectors. In addition, in both the inclusive and differential measurements, event selection has some reliance on the jet information (e.g. jet $p_T > 25$ GeV). Therefore if the properties of the jets change within the event, it is expected that the number of accepted events will change and that reconstructed objects will also change. In order to account for this, a systematic uncertainty is assigned to jet uncertainties, split into jet energy scale (JES) uncertainty, jet energy resolution (JER) uncertainty and jet vertex fraction (JVF) uncertainty.

Jet Energy Resolution (JER)

In order to assess the jet energy resolution (JER) uncertainty, the ATLAS *JetEnergyResolutionProvider* tool is used [116]. The jet energy is then smeared within its uncertainties and an alternative distribution is produced for $\Delta\phi$.

The JER uncertainty is evaluated using a number of elements, to include uncertainties from calibration studies using Noise Data/MC studies and also including a number of nuisance parameters (varying from 0-8) [117]. Each of these is treated as a separate systematic variation and the methodology described in section 7.2.1 is employed to evaluate these. For the summary tables, an overall JER systematic uncertainty is presented, being the individual components summed in quadrature.

Jet and b-jet Energy Scales (JES)

Whilst attempts are made to model the detector response in simulation, there are still differences between data and MC. In order to correct for this, calibrations of the jet objects are made using a variety of noise studies, test-beam data and simulation [118].

As a result of these studies, 26 uncorrelated sources of systematic uncertainty are found which can be attributed to the jet energy scale. A template is made for each of these which varies the particular source up and down by 1σ. The approach described in section 7.2.1 is used for each of these sources. The total uncertainty due to variations in JES can be seen in table 7.3, which has been calculated by summing in quadrature the systematic uncertainties from each source.

One of the sources of uncertainty included in the JES systematic evaluation is specifically related to the b-tagged jets. For this source, jets which have come from a b quark are compared to those which originate from other flavours (the origin of the jet is determined using information from the MC truth). This analysis requires at least one b-tagged jet and variations in the b quark JES will affect the tagging performance, so this particular source is of importance.

Jet Vertex Fraction (JVF)

To assess the systematic uncertainty associated with the choice of the jet vertex fraction (defined in section 6.2.3), the JVF value is varied from its nominal value of 0.5 up and down within its uncertainties, and templates are created for each. The approach described in section 7.2.1 is used.

7.2.2.2 Lepton Momentum Resolution and Scale

Charged leptons (specifically electrons and muons) are the key objects used in this analysis. Calibrations are performed on the muon momentum resolution and scale in order to obtain the best possible agreement between MC simulation and data. This calibration leads to associated systematic uncertainties which need to be assessed.

In order to make a measurement of the muon momentum, information is used and combined from the ATLAS muon spectrometers and various subdetectors in the inner detector. Subsequent MC smearing is performed to improve the data/MC agreement (see section 6.2) in these components. There is an uncertainty on the calculation of the smearing required in each of these components and to evaluate the impact of these on the measurement, the resolution is varied within these uncertainties. The analysis is then performed fully again with these variations and the systematic uncertainty is calculated in accordance with the methodology described in section 7.2.1. There is also an overall momentum scaling which is applied to MC, again with uncertainties which are propagated within the analysis to evaluate an uncertainty on the final result.

For electrons, a similar scaling and smearing is performed on the electron energy calculation, with information obtained from the calorimeters and the effects these have on the final measurements of f_{SM} are assessed.

7.2.2.3 Lepton and b-tagging Scale Factors

Scale factors are introduced in the analysis to account for differences in the identification, reconstruction and triggering efficiencies for data and simulation for lepton objects. These scale factors aim to improve the agreement between the two but also have associated uncertainties in their calculation. New templates are created which

vary each of these within their uncertainties (with both an up and down variation).

Additionally, there is a separate scale factor used to improve the agreement between data and simulation when introducing the b-tagging algorithm. This scale factor includes a number of parameters relating to the tagging of b-quarks, c-quarks and an overall mistagging rate. To calculate the systematic uncertainty on the overall b-tag scale factor, each of these parameters is varied up and down within its uncertainties and these are summed in quadrature to give overall up and down variations. The largest of these variations is taken to be the systematic uncertainty and is symmetrised.

7.2.2.4 Missing Transverse Energy

A number of the systematic uncertainties that have been discussed involve varying the resolutions used when creating physics objects (e.g. electrons, jets). A subsequent effect of this is that the missing transverse energy (MET) object also needs to be recalculated. The uncertainties arising from the variations to the physics objects are collected as two terms relating to an uncertainty in the MET resolution and the MET scale, with each term having an up and down variation. An uncertainty is calculated for each of these variations using the technique described in section 7.2.1.

7.2.2.5 Luminosity

The uncertainty on the luminosity is $\pm$ 2.8%, as prescribed by the ATLAS Luminosity group. The derivation of this uncertainty is described in [119] and [120] and was calculated by using a preliminary calibration of the luminosity scale from beam separation scans performed in November 2012.

7.2.2.6 Colour Reconnection (CR) and Underlying Event (UE)

Within the $t\bar{t}$ signal simluation model, there is an inherent assumption of the value of the colour reconnection (CR) strength. This strength is a result of the colour flow along parton lines within a hard scattering multi-parton interaction (MPI). The modelling of the CR strength is therefore a source of systematic uncertainty. In order to evaluate this uncertainty, a sample is produced where the colour reconnection strength is reduced [121]. From this sample, the pseudo-data approach described in section 7.2.1 is used to evaluate the systematic uncertainty, which is one sided but symmetrised.

Similarly, simulation of the underlying event (UE) provides a source of uncertainty. Varying the number of initial MPIs which occur in addition to the main hard scattering interaction can alter the kinematics of the event and thus subsequently affect the measurement. In order to estimate the uncertainty resulting from this, a sample was produced which increases the number of MPI within the underlying event. The pseudo-data approach is then used as above to evaluate and assign a systematic uncertainty. Each of the additional samples is generated using the *POWHEG+PYTHIA 6.4* generators.

7.2.2.7 ISR/FSR Radiation

Within the $t\bar{t}$ signal modelling, an uncertainty arises due to the amount of initial and final state radiation (ISR and FSR respectively) present in the event before and after hard scattering. A change in these can affect the number of jets, which are reconstructed and can in turn affect the event selection. To assess the impact that this has, additional samples were produced using the *POWHEG+PYTHIA 6.4* generators which vary the renormalisation and factorisation scales (defined at the characteristic energy scale of the interaction and used to prevent divergent contributions from loop processes) to $\mu = 0.5$ and $\mu = 2$, from $\mu = 1$ [78]. This varies

multiplicative factors used in the hard scattering calculation which in turn alters the amount of additional radiation produced. Additionally, the strong interaction coupling, α_s, which is the parameter used to govern the amount of additional radiation generated, is varied (to "radLo" and "radHi").

These samples also have a different value for the tunable damping parameter (known as “hdamp”) which is not tuned in the nominal sample used in the analysis, because a corresponding uncorrelated sample is not available. Therefore in order to assess the systematic uncertainty attributed to ISR/FSR, the mean value of f_{SM} for each of the varied samples is compared. The uncertainty is chosen to be half of the difference between the two samples and is symmetrised.

7.2.2.8 Monte Carlo Simulation

For the simulation of signal events in this analysis, a choice of Monte Carlo generator is made from a selection of possibilities. In order to fully model the event, a generator is used to model the initial $t\bar{t}$ production and the result of this production and decay is then interfaced with a separate generator which models the final parton showering. The chosen generators were *POWHEG* (for initial production), interfaced with *PYTHIA 6.4* to model the parton showering. To take account of differences which may occur as a result of the choice of generator, the analysis has been repeated using the *MC@NLO* generator interfaced with *HERWIG++* for the parton showering.

An uncorrelated sample is also available for *MC@NLO+HERWIG++*, so the analysis was repeated, fitting the data to simulation but using the *MC@NLO+HERWIG++* sample for both the SM correlated and uncorrelated templates. The difference between the values of f_{SM} for each of the generators is symmetrised and treated as

the systematic uncertainty.

7.2.2.9 Parton Distribution Function

When the nominal simulation templates are created, an underlying assumption that is used is the choice of parton distribution function (PDF). If different PDF sets are used, it is expected to cause a difference in the simulation and therefore can create a difference to the f_{SM} value obtained.

In order to assess the impact that the choice of PDF has on the result, three alternative sets of PDFs (CT10 [122], MWST2008 [21] and NNPDF23 [123]), with different central values and associated error sets, are used to create alternative templates and the f_{SM} values for these are obtained. The total number of variations for each of the sets is shown in table 7.1.

Table 7.1: The alternative PDF sets used for assessing the PDF systematic uncertainties and the total number of variations for each set.

PDF set	Total number of variations
CT10	1 central value + 52 error sets
MWST2008	1 central value + 42 error sets
NNPDF23	100 (with central value taken as the RMS of the 100 sets)

Rather than produce a new template for each set of the PDF variations (as has been done with other systematic variations), it is more efficient to use a reweighting method, due to the amount of processing time that would be required to make all of the variations.

The reweighting is performed according to the following function

$$w = \frac{PDF(x_1, id_1, Q)PDF(x_2, id_2, Q)}{PDF_0(x_1, id_1, Q)PDF_0(x_2, id_2, Q)}, \tag{7.3}$$

where x_i is the fractional momentum of the incoming parton, id_i is the particle id of the incoming parton and Q is the scale of the event. In addition, PDF_0 refers to the PDF used to generate the initial MC sample and PDF is the name of the set being used to calculate the variation. The calculation for the new PDF is obtained by use of the LHAPDF program [124] and follows the PDF4LHC recommendations [125].

In order to generate a systematic uncertainty for each distribution, an "envelope" method is employed. The error sets for each PDF are combined to give an overall value of the variation for that PDF. The method of combination is different for each of the PDF choices.

For the CT10 PDF, there exists an up and down variation for each error within the set and so the errors are combined using a symmetric Hessian

$$\Delta x = \frac{1}{2}\sqrt{\sum (x_i^+ - x_i^-)^2}, \tag{7.4}$$

where x_i^+/x_i^- are the up and down variations for a particular error in the set and the sum runs over the whole error set.

For the MWST2008 PDF, the up and down variations for each error are expected to give an asymmetric result, and so to assess the uncertainty an asymmetric Hessian is used which compares the variations to the central value for the PDF:

$$\Delta x^+ = \sqrt{\sum (x_i - x_0)^2}, \qquad x_i - x_0 > 0 \tag{7.5}$$

and

$$\Delta x^{-} = \sqrt{\sum (x_i - x_0)^2}, \qquad x_i - x_0 < 0 \tag{7.6}$$

where x_i is the variation for a particular error in the set, x_0 is the central value for the PDF and the sum runs over the whole error set.

For NNPDF23, the errors are not in the form of up and down shifts. Instead, a number of parameters are varied within the set and so the errors are combined using the root mean squared (RMS) method.

In order to assess the overall impact of the choice of PDF, the three error bands are combined and the largest value covered by an error band is compared to the smallest. The systematic variation is taken to be half of the difference between these two. The envelope plots illustrating the f_{SM} values yielded from each PDF variation are shown for the inclusive measurements for each channel in figure 7.3.

7.2.2.10 Template Statistics

The Monte Carlo templates used to generate the $t\bar{t}$ samples have a finite number of events. In addition to creating a statistical error on the expected yields (as shown in tables 6.4 - 6.7), it also creates a systematic uncertainty which needs to be evaluated. This occurs because a statistical fluctuation in each bin of the simulated $\Delta\phi$ distribution may affect its shape, and subsequently alter the fitted f_{SM} value.

This is studied by Gaussian smearing each bin within its statistical uncertainty in both the SM and uncorrelated templates 10,000 times, creating a set of varied templates which are used in place of the nominal templates. The data are then fitted to these templates in the same manner as for the standard analysis. This generates a Gaussian distribution of f_{SM} values, the width of which is taken to be the uncertainty associated with the limited template statistics.

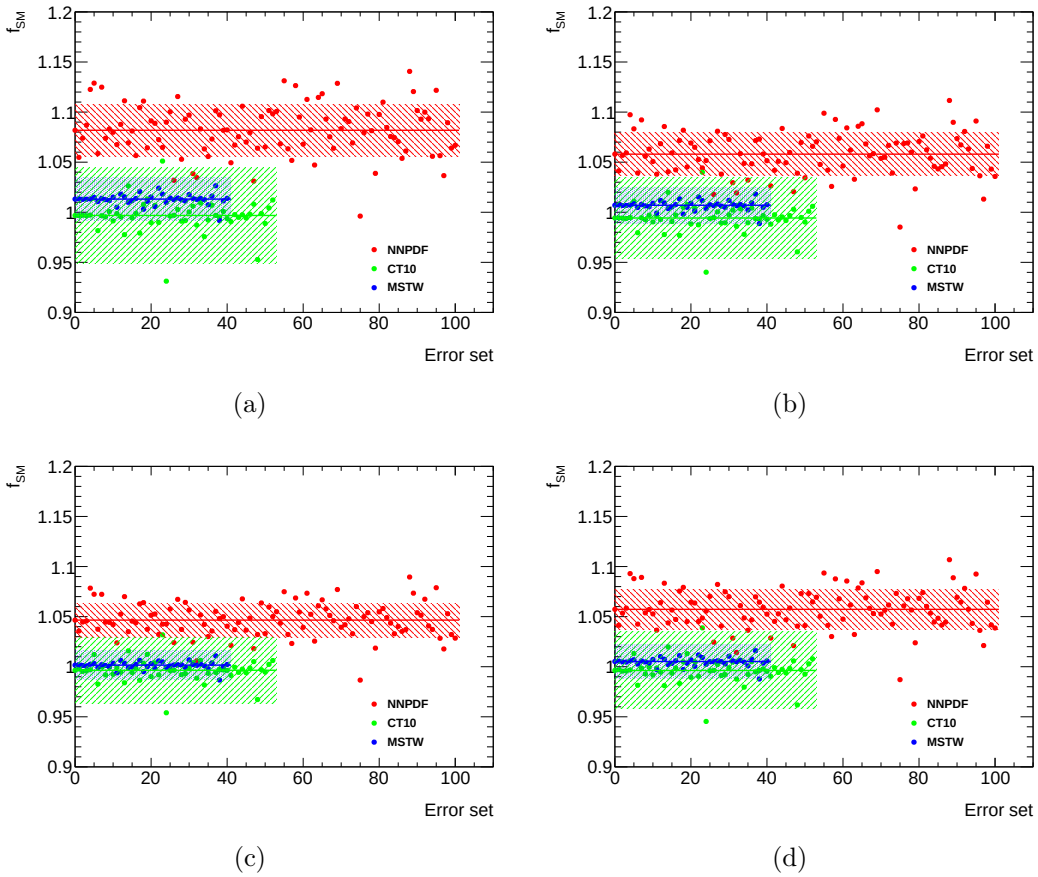

Figure 7.3: Envelope plots showing the values of f_{SM} obtained when using variations in the underlying PDF for the inclusive measurement. Each PDF set has an error band uncertainty calculated using the methodology explained in section 7.2.2.9. The total uncertainty is calculated as being half of the difference between the greatest valued uncertainty band and the smallest valued: a) shows the ee channel, b) shows the $\mu\mu$ channel, c) shows the eμ channel and d) shows the combined dilepton channel.

7.2.2.11 Top Mass Dependence

During event generation, a top quark mass of $m_t = 172.5$ GeV is assumed in both the template samples which are used (SM levels of correlation and uncorrelated). However, the current best estimate of the top mass is $m_t = 173.21 \pm 0.51 \pm 0.71$ GeV [1]. The cross section of top-antitop production is inherently dependent on its mass and so a change will alter the number of events produced and subsequently may cause a change to the measured value of the spin correlation.

In order to estimate the effect of the top mass, a number of samples were produced which used the same generator as the nominal analysis but have varying values for the top mass. These masses range from $165 - 180$ GeV at 2.5 GeV intervals (when including the nominal sample as well). Each sample is treated as pseudo-data and is used to generate a value of f_{SM} when compared to the nominal templates. Each template is then Poisson fluctuated 10000 times using the procedure described in section 7.2.1. The mean value of the Gaussian distribution created by the pseudoexperiments is taken as being the f_{SM} value for that template (with the value of f_{SM} at $m_t = 172.5$ GeV being set to 1 by design). These are then plotted and a linear fit is performed for each channel and observable. The values of f_{SM} are calculated for values $m_t = 171.5$ GeV and $m_t = 173.5$ GeV (to allow a ± 1 GeV uncertainty on the presumed top mass). The symmetric systematic uncertainty is taken as being half of the variation over this range. This follows the approach taken in [66]. The fits performed can be seen in figure 7.4 and the value of the uncertainties are in table 7.3.

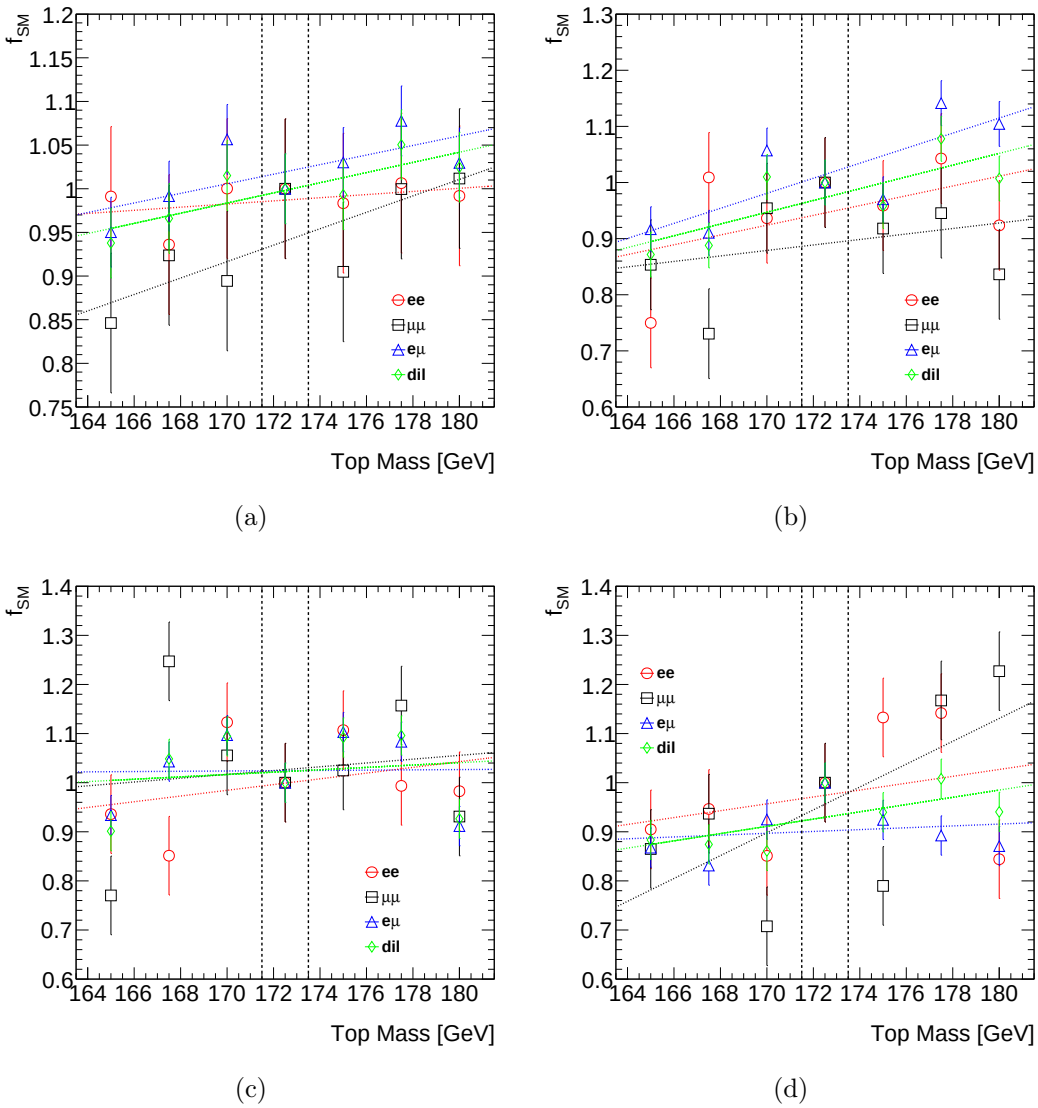

Figure 7.4: Linear fits illustrating the values for f_{SM} when varying the assumed top mass. Each plot shows the three separate dilepton channels and the combined channel where a) is the inclusive measurement and b) - d) are the differential measurements in bins 1-3 respectively. Lines are included showing the uncertainty on the top mass used in the analysis at 171.5 and 173.5 GeV.

7.2.2.12 Background Uncertainties

In addition to systematic errors arising as a result of detector and signal modelling uncertainties, the uncertainties in the backgrounds must also be taken into account. Due to the event selection cuts, the contribution from backgrounds is small and so should not be a large source of error for this analysis. The dominant background is the contribution from $\mathrm{Z}/\gamma^* + jets$.

$\mathrm{Z}/\gamma^* + jets$ Background

As discussed in section 6.4.2, a scale factor has been calculated when estimating the contribution from $\mathrm{Z}/\gamma^* + jets$ background. This normalisation comes with an associated uncertainty. In order to assess the value of this uncertainty, the scale factor is varied by ± 0.1 for events with 1 b-tagged jet, and by ± 0.07 for events with 2 or more b-tagged jets. This range is used so that the maximum scale factors calculated in table 6.1 are being taken into account and the maximum deviation from a scale factor of 1 has been calculated. With these up and down variations, the pseudo-data methodology discussed in section 7.2.1 is then applied to assess the systematic uncertainty.

The normalisation approach taken in section 6.4.2 assumes the shape already prescribed by the Monte Carlo is correct and only modifies the yield, but there is some degree of uncertainty in the shape as well. In order to assign an uncertainty to the shape, a reweighting approach has been used based upon the p_T of the dilepton system for each event.

The reweighting function is calculated within the same control regions as described in section 6.4.2, with the exception that no distinction is made between events with exactly 1 b-tagged jet and those with 2 or more b-tagged jets (i.e. the calculation is made in the ee and $\mu\mu$ channels with the same event selection as the signal region

but in the Z boson window, with or without a missing E_T cut). Within this event selection, the p_T of the dilepton system is calculated and plotted for the data and simulation. The non $Z/\gamma^* + jets$ background is subtracted from data and the p_T spectra are normalised to 1 (in order to directly compare the shapes). A ratio of the two normalised plots is then calculated and a linear fit is made to the ratio plots to give a reweighting function. The fit values are shown in table 7.2. In addition, plots illustrating this procedure are shown in figure 7.5.

Table 7.2: Calculated values for each parameter in the fit function used for the Z p_T reweighting. The fit function is of the form $w = mZ_{p_T} + c$

Channel	Region	Gradient parameter m [GeV^{-1}]	Constant parameter c
ee	CR1	(-1.47 ± 0.02) x 10^{-4}	1.01 ± 0.03
	CR2	(-1.31 ± 0.02) x 10^{-4}	1.01 ± 0.02
$\mu\mu$	CR1	(-2.54 ± 0.02) x 10^{-5}	1.00 ± 0.03
	CR2	(-6.08 ± 0.02) x 10^{-4}	1.04 ± 0.01
l^+l^-	CR1	(2.35 ± 0.01) x 10^{-5}	1.00 ± 0.02
	CR2	(-3.72 ± 0.01) x 10^{-4}	1.03 ± 0.01

For the e^+e^- and $\mu^+\mu^-$ channels, the reweighting functions used were those from the CR1 region (as these use an MET cut) for the corresponding channel. For the $e\mu$ channel, the reweighting function uses the parameters from the combined CR2 channel (as the $e\mu$ channel does not have an MET cut in the event selection). The reweighted $Z/\gamma^* + jets$ background is then used in place of the nominal $Z/\gamma^* + jets$ background and a fit is made. In each case, the effect of the reweighting is negligible on the value of f_{SM} obtained.

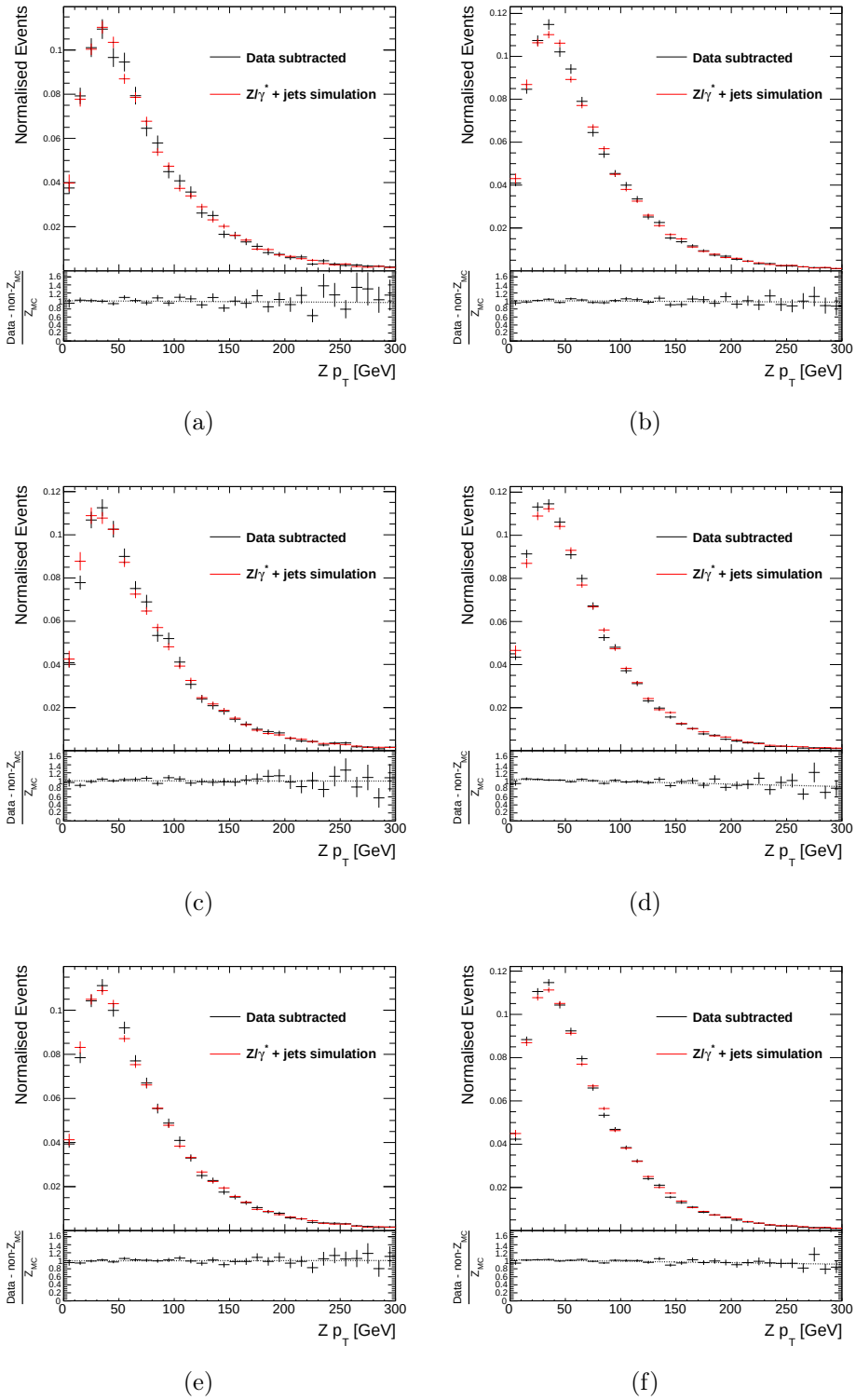

Figure 7.5: Plots showing the normalised p_T distribution for the $Z/\gamma^* + jets$ background MC and data in the Z boson window for the control regions described in section 7.2.2.12. a) and b) show the plots for the e^+e^- channel in the CR1 and CR2 region respectively, c) and d) show the plots for the $\mu^+\mu^-$ channel in the CR1 and CR2 region respectively and e) and f) show the plots for the sum of the two channels in the CR1 and CR2 region respectively. Underneath the distributions is a ratio of the two with a linear fit applied.

Diboson Background

For this background, a systematic uncertainty is assigned based on the normalisation uncertainty of the background. The theoretical uncertainty of the diboson background is 5%, with an extra uncertainty of 24% for each additional jet, added in quadrature [126]. In this analysis, the event selection requires two jets, so the total uncertainty for the diboson background is $34\% = \sqrt{(5\%)^2 + 2(24\%)^2}$.

Single Top Background

Two elements of uncertainty arise as a result of the single top background. The first is the cross section uncertainty, reflected as an uncertainty in the normalisation of the background. The source of the background for this analysis comes from the Wt channel single top process, with an associated up and down uncertainty of 6.8% in the cross section [126].

The second source comes from the method used to remove interference between the $t\bar{t}$ and the Wt final states. The nominal sample uses the diagram removal (DR) approach in order to estimate the background, but it is also possible to use a diagram subtraction (DS) method. The choice of method introduces a systematic uncertainty which must be evaluated. For this case, the nominal DR sample is replaced by the DS sample and 10000 templates are created using Poisson fluctuations.

Fake Lepton Background

The fake lepton background has been estimated by using an entirely data driven approach, with a normalisation uncertainty of $\pm$ 100%. The systematic error is assessed by varying the background up and down by this normalisation uncertainty and the largest variation from the nominal f_{SM} is symmetrised and taken to be the systematic uncertainty.

7.2.3 Total Systematic Uncertainty

The total systematic uncertainty is obtained by summing each individual source of systematic uncertainty in quadrature. A list of these sources for each of the distributions is shown in table 7.3, with the total systematic uncertainty calculated. The total statistical uncertainty is provided for reference. The largest systematic uncertainties arise from sources which alter the underlying generator information (i.e. ISR/FSR, choice of generator and the choice of PDF). Additionally, the systematic uncertainties are larger for the high $M_{t\bar{t}}$ region. This is expected as in this region, the difference between the SM correlated and uncorrelated sample distributions is small, with a small change leading to a large variation in the f_{SM} calculation.

7.3 Procedure to Assess Systematic Uncertainties in Unfolded Distributions

For the unfolded measurement, a different approach is taken. The sources of systematic uncertainties and the samples used to assess them remain the same as in section 7.2, but for each case, the samples are used to perform a modified unfolding. The methodology used for this unfolding is dependent on the source of the uncertainty. These are described below.

7.3.1 Uncertainties Arising from Detector Modelling

In the case where the source of systematic uncertainty arises from modifying the detector modelling, this will cause a slight change to the response matrix yielded from the Monte Carlo signal sample. Therefore, a new response matrix is generated for each uncertainty using the modified sample. Subsequently, the background subtracted data is unfolded with this modified response matrix using the same method-

ology as for the nominal result. The difference between the value yielded by the modified matrix and the nominal result is taken for each bin and then symmetrised to give the error for that bin.

Table 7.3: The systematic error in f_{SM} value for each source of systematic uncertainty for the detector level measurement. The first four columns show the values for each channel for the inclusive measurement. The subsequent columns show the value of the uncertainty for the corresponding channels for the differential measurement bins. A dash indicates the absolute value of the uncertainty is less than 0.005. These values are still taken into account for the overall uncertainty.

	Inclusive measurement				$M_{t\bar{t}} \leq 415$ GeV				415 GeV$< M_{t\bar{t}} \leq 505$ GeV				$M_{t\bar{t}} > 505$ GeV			
Uncertainty source	ee	$\mu\mu$	eμ	Combined	ee	$\mu\mu$	eμ	Combined	ee	$\mu\mu$	eμ	Combined	ee	$\mu\mu$	eμ	Combined
JER	0.04	0.01	0.01	0.01	0.07	0.08	0.02	0.03	0.04	0.04	0.04	0.02	0.05	0.08	0.03	0.02
JES	0.05	0.05	0.02	0.03	0.07	0.08	0.02	0.04	0.05	0.07	0.05	0.05	0.06	0.12	0.05	0.03
JVF	-	-	-	-	0.01	-	-	-	-	0.01	-	-	-	-	-	-
Electron energy scale	0.01	-	0.01	0.01	0.03	-	0.01	0.01	0.02	-	0.01	0.01	0.02	0.01	0.01	0.01
Electron energy resolution	0.01	-	-	-	0.01	-	0.01	-	0.02	-	-	-	-	0.01	0.01	-
Muon ID resolution	-	0.01	-	-	-	0.01	-	-	-	0.01	-	-	0.01	0.02	-	-
Muon spectrometer resolution	-	0.01	-	-	-	-	-	-	-	0.01	0.01	-	-	0.01	-	-
Muon scale	-	0.01	-	-	-	0.01	-	-	-	0.01	-	-	0.01	0.01	-	-
Lepton scale factors	-	-	-	-	-	-	-	-	-	-	-	-	-	-	-	-
B tag scale	0.02	0.02	0.01	0.01	0.02	0.02	0.02	0.02	0.02	0.01	0.01	0.01	0.03	0.05	0.02	0.01
MET resolution	0.01	0.01	-	-	0.01	0.01	0.01	0.01	0.01	-	0.02	0.01	0.01	0.02	0.02	0.01
MET scale	0.01	0.01	-	-	0.02	0.01	0.01	0.01	0.02	0.01	-	-	0.02	0.03	0.01	0.01
Luminosity	-	-	-	-	0.01	0.01	-	-	-	-	-	-	-	-	-	-
Underlying Event	0.06	0.06	0.04	0.05	0.03	0.13	0.02	0.05	0.1	0.02	0.07	0.03	0.26	0.07	0.14	0.15
Colour Reconnection	0.06	0.01	0.03	-	0.07	0.06	0.03	0.01	0.02	0.03	0.01	0.01	0.01	0.08	0.04	0.04
ISR/FSR	0.09	0.01	0.05	0.03	0.08	0.06	0.04	0.05	0.06	0.03	0.11	0.08	0.15	0.09	0.04	0.04
Generator	0.09	0.06	0.05	0.06	0.03	0.03	0.04	0.02	0.07	0.01	0.09	0.06	0.31	0.05	0.29	0.28
PDF	0.08	0.06	0.05	0.06	0.03	0.01	0.01	0.01	0.02	0.07	0.01	0.02	0.14	0.07	0.09	0.11
Template statistics	0.03	0.03	0.02	0.01	0.04	0.03	0.02	0.02	0.05	0.05	0.03	0.02	0.08	0.1	0.04	0.04
Top mass	-	0.01	0.01	0.01	0.01	-	0.01	0.01	0.01	-	-	-	0.01	0.03	-	0.01
Z normalisation	0.01	-	-	-	0.02	0.02	-	0.01	-	-	-	-	-	0.02	-	0.01
Diboson normalisation	-	-	-	-	-	-	-	-	-	-	-	-	-	-	0.01	-
Single Top normalisation	-	-	-	-	-	-	-	-	-	-	-	-	-	0.01	-	-
Single Top alternative sample	0.03	-	0.01	0.01	0.01	0.01	0.01	-	0.01	-	-	-	0.05	0.01	0.01	0.02
Fake Leptons	-	0.01	0.01	-	0.03	-	0.01	0.01	0.01	0.01	0.01	-	0.02	0.02	-	0.01
Total	0.19	0.13	0.11	0.11	0.17	0.20	0.09	0.10	0.17	0.14	0.17	0.12	0.48	0.27	0.35	0.35
Statistical error	0.08	0.08	0.05	0.04	0.12	0.10	0.06	0.05	0.15	0.14	0.08	0.07	0.21	0.23	0.13	0.10

7.3.2 Uncertainties Arising from Signal Modelling

When the source of uncertainty arises from a modification to the underlying truth distribution, the detector response should remain the same and therefore a new response matrix does not need to be created. However, a difference is expected as a result of having a modified distribution. In order to estimate the size of this error, the modified sample is passed through detector simulation and this is then unfolded using the nominal response matrix, using the Monte Carlo as pseudo-data. Note that as there is no background included within these pseudo-data, no background subtraction is performed.

The unfolded distribution is compared to the truth distribution for the modified sample and the difference between the content for the unfolded and truth distributions is symmetrised and taken as being the error for the bin for that source of uncertainty.

For some of the uncertainties of this type, different approaches are taken. These are:

- *PDF Uncertainties*: As in section 7.2.2.9, a number of error sets are provided and an envelope method is used to determine the total PDF uncertainty. For the unfolded case, each reweighted PDF set is unfolded with the nominal response matrix. The value for each bin then undergoes the envelope procedure to determine the total uncertainty on the value of that bin.

- *Top Mass*: For each of the varied top mass samples, the sample is passed through detector simulation and unfolded with the nominal response matrix. The unfolded number of events in each bin is plotted for each of these samples and then fitted with a straight line. A value is read at $m_t = 171.5$ GeV and $m_t = 173.5$ GeV (for the reasons discussed in section 7.2.2) and the uncertainty

is taken as being the half of the difference between these two values, which is then symmetrised.

7.3.3 Uncertainties Arising from Normalisations

Some systematic errors arise from uncertainties in normalisations used when generating signal and background samples. For the case where the normalisation is performed on the signal sample, the approach shown in section 7.3.1 is taken. Where the normalisation is altered in the background sample, the detector response does not change and the only difference is expected in the total number of background events. To estimate the effect of these changes in normalisation, the altered background is subtracted from the data before unfolding. The difference between the modified and nominal distributions is taken for each bin and symmetrised to give the uncertainty attributed to this source.

7.3.4 Uncertainties Arising from Choice of Response Matrix

Section 6.6.4 shows that perfect closure is not obtained when using the response matrices calculated with the SM sample to unfold the uncorrelated sample. To assess the potential bias this may have on the result, the analysis has been repeated using response matrices obtained from the uncorrelated sample. The matrices are created using the full procedure described in section 6.6.1.1 and the data are unfolded using this matrix. The difference between the unfolded distribution obtained from this method and the nominal unfolded distribution is calculated for each bin. This difference is symmetrised and taken to be the systematic error for this source of uncertainty.

The total systematic uncertainty for each bin and distribution is listed in Appendix

A and figures showing the unfolded distributions and total associated errors for each bin can be seen in section 7.5.

7.4 Detector Level Measurement Results

The plots showing the data/MC agreement for each distribution can be seen in figures 7.6 to 7.9.

The fits of data to simulation can be seen in figures 7.10 to 7.13. The fitted value of f_{SM} for each sample is shown in table 7.4. The floating $t\bar{t}$ normalisation factor is also included.

Table 7.4: The f_{SM} value found for each channel and distribution after performing a simultaneous template fit to a simulated sample with SM levels of spin correlation and a simulated sample with no spin correlation at detector level. In addition, the value of $f_{t\bar{t}}$ is included, which is a parameter in the fit which allows the normalisation of the signal to float.

Channel	f_{SM} value	$f_{t\bar{t}}$
Inclusive		
ee	1.18 ± 0.08 (stat) ± 0.19 (syst)	1.04 ± 0.01
$\mu\mu$	1.33 ± 0.08 (stat) ± 0.13 (syst)	1.05 ± 0.01
eμ	1.12 ± 0.05 (stat) ± 0.11 (syst)	1.02 ± 0.01
dilepton	1.18 ± 0.04 (stat) ± 0.11 (syst)	1.03 ± 0.00
$M_{t\bar{t}} \leq 415$ GeV		
ee	1.14 ± 0.12 (stat) ± 0.17 (syst)	1.04 ± 0.02
$\mu\mu$	1.04 ± 0.10 (stat) ± 0.20 (syst)	1.07 ± 0.02
eμ	1.10 ± 0.06 (stat) ± 0.09 (syst)	1.03 ± 0.01
dilepton	1.10 ± 0.05 (stat) ± 0.10 (syst)	1.04 ± 0.01
415 GeV$< M_{t\bar{t}} \leq 505$ GeV		
ee	1.04 ± 0.15 (stat) ± 0.17 (syst)	1.02 ± 0.02
$\mu\mu$	1.19 ± 0.14 (stat) ± 0.14 (syst)	1.03 ± 0.02
eμ	1.08 ± 0.08 (stat) ± 0.17 (syst)	1.04 ± 0.01
dilepton	1.11 ± 0.07 (stat) ± 0.12 (syst)	1.03 ± 0.01
$M_{t\bar{t}} > 505$ GeV		
ee	1.24 ± 0.21 (stat) ± 0.48 (syst)	1.03 ± 0.02
$\mu\mu$	1.57 ± 0.23 (stat) ± 0.27 (syst)	1.05 ± 0.02
eμ	1.21 ± 0.13 (stat) ± 0.35 (syst)	1.03 ± 0.01
dilepton	1.29 ± 0.10 (stat) ± 0.35 (syst)	1.03 ± 0.01

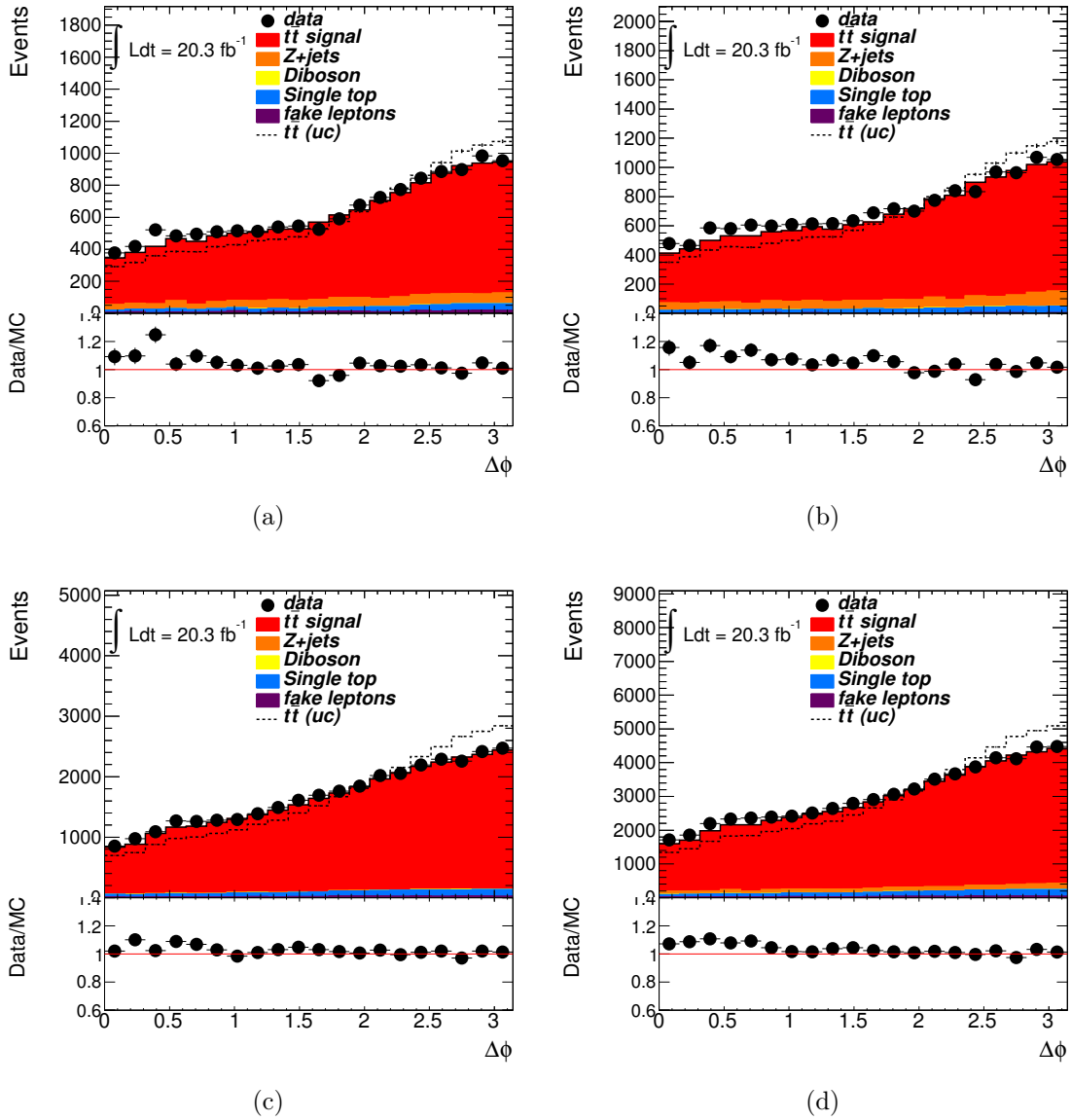

Figure 7.6: Data/Monte Carlo comparisons of the azimuthal opening angle between the two charged leptons in a dileptonic decay chain, using all event selection cuts. These comparisons are made after the Z+jets normalisation factors have been applied (see section 6.4.2) and include statistical uncertainties on data. These distributions are for the inclusive measurement. a) is the distribution for the ee channel, b) is the $\mu\mu$ channel, c) is the eμ channel and d) is the combined channel. Also included is a comparison to the MC prediction using the uncorrelated (UC) sample (plus backgrounds).

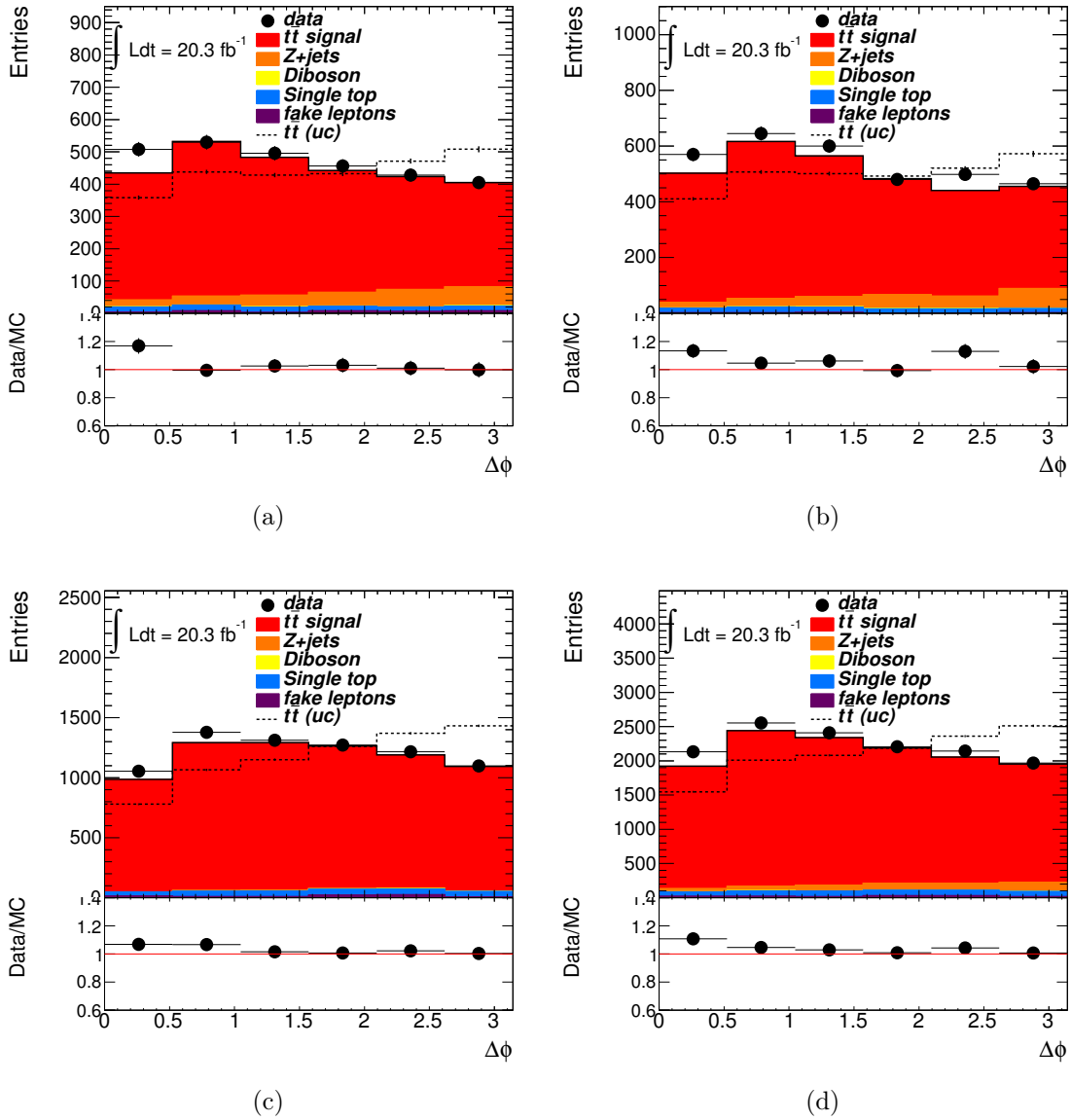

Figure 7.7: Data/Monte Carlo comparisons of the azimuthal opening angle between the two charged leptons in a dileptonic decay chain, using all event selection cuts. These comparisons are made after the Z+jets normalisation factors have been applied (see section 6.4.2) and include statistical uncertainties on data. These distributions are for the opening angle where $M_{t\bar{t}} \leq 415$ GeV. a) is the distribution for the ee channel, b) is the $\mu\mu$ channel, c) is the eμ channel and d) is the combined channel. Also included is a comparison to the MC prediction using the uncorrelated (UC) sample (plus backgrounds).

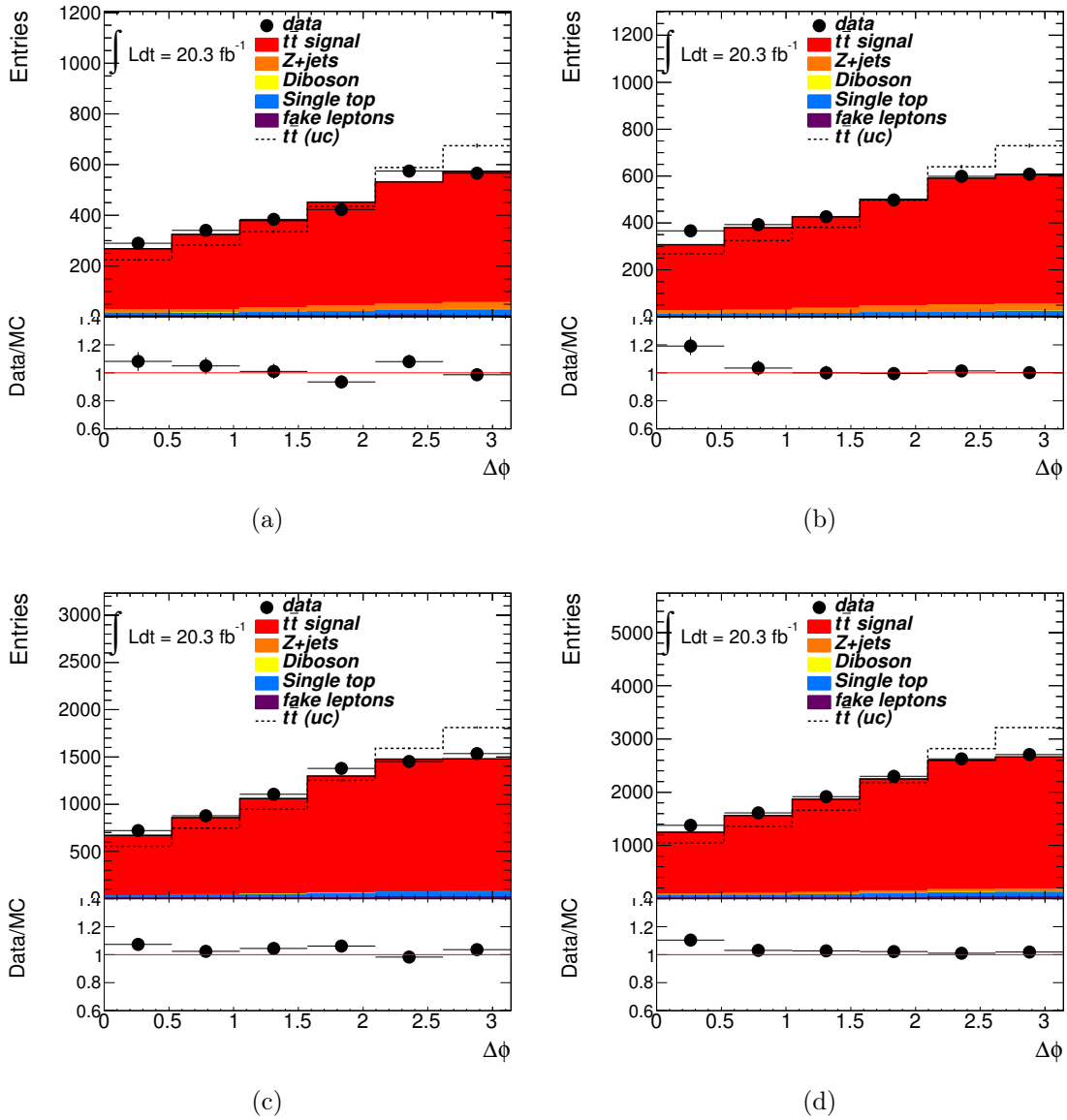

Figure 7.8: Data/Monte Carlo comparisons of the azimuthal opening angle between the two charged leptons in a dileptonic decay chain, using all event selection cuts. These comparisons are made after the Z+jets normalisation factors have been applied (see section 6.4.2) and include statistical uncertainties on data. These distributions are for the opening angle where 415 GeV$< M_{t\bar{t}} \leq$ 505 GeV. a) is the distribution for the ee channel, b) is the $\mu\mu$ channel, c) is the eμ channel and d) is the combined channel. Also included is a comparison to the MC prediction using the uncorrelated (UC) sample (plus backgrounds).

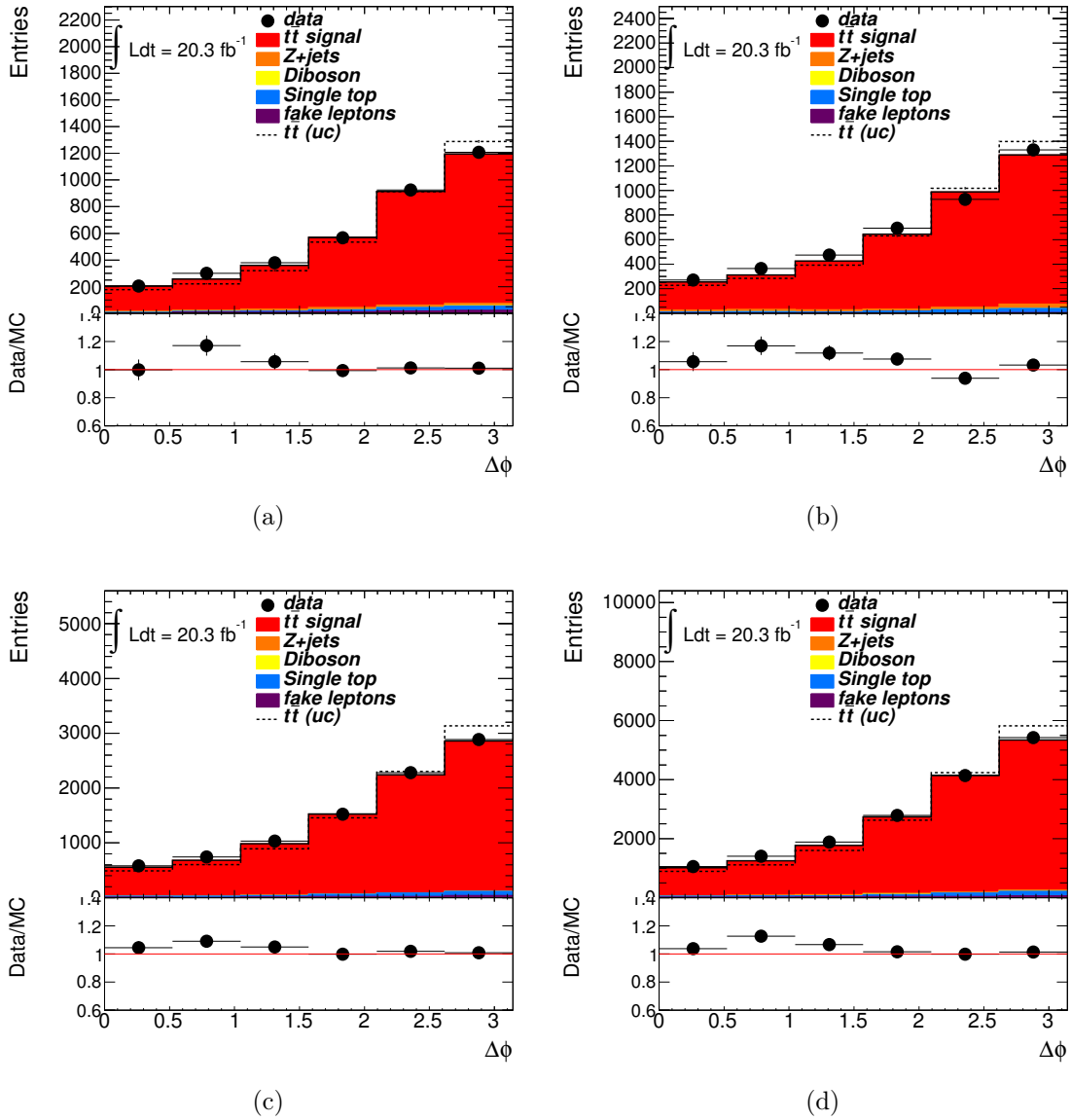

Figure 7.9: Data/Monte Carlo comparisons of the azimuthal opening angle between the two charged leptons in a dileptonic decay chain, using all event selection cuts. These comparisons are made after the Z+jets normalisation factors have been applied (see section 6.4.2) and include statistical uncertainties on data. These distributions are for the opening angle where $M_{t\bar{t}} > 505$ GeV. a) is the distribution for the ee channel, b) is the $\mu\mu$ channel, c) is the eμ channel and d) is the combined channel. Also included is a comparison to the MC prediction using the uncorrelated (UC) sample (plus backgrounds).

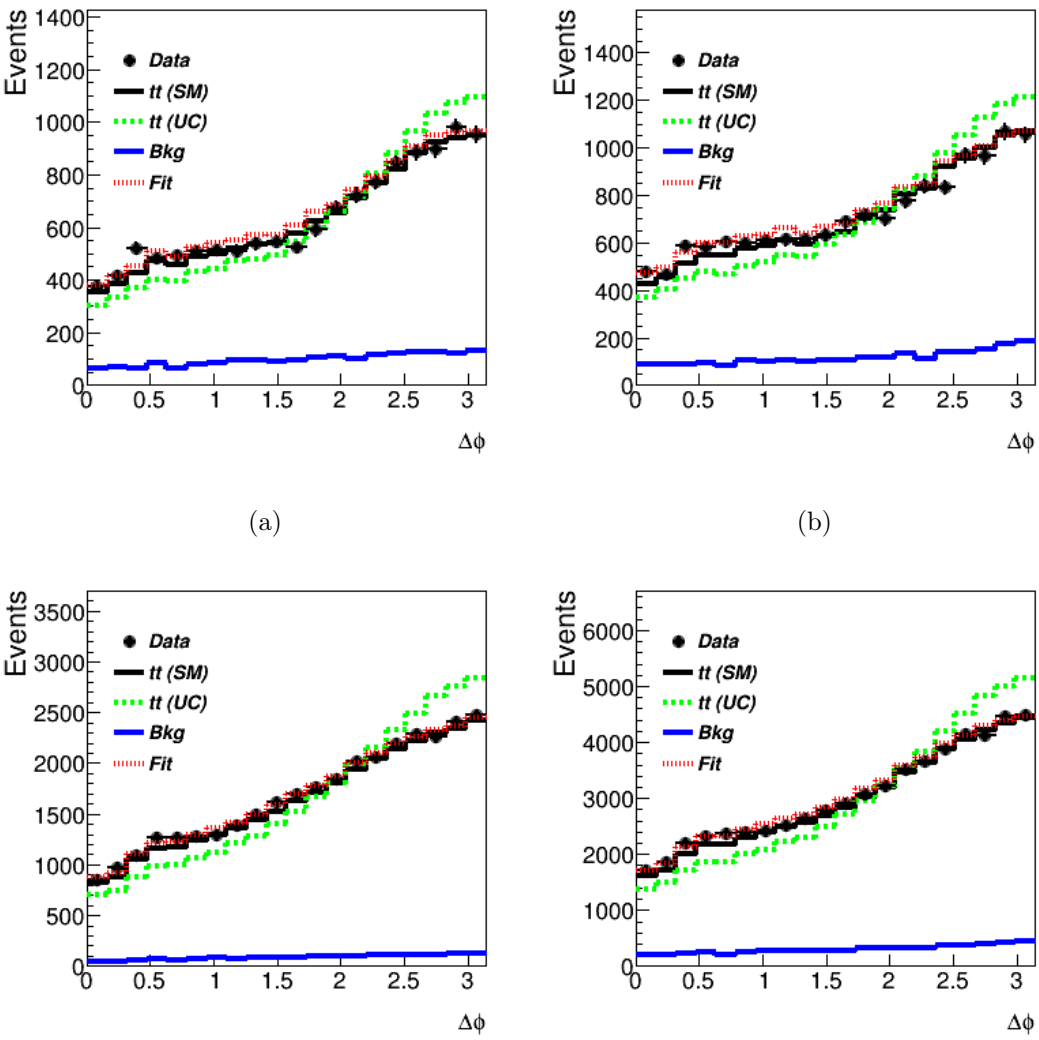

(a) (b)

(c) (d)

Figure 7.10: Data/Monte Carlo comparisons of the azimuthal opening angle between the two charged leptons in a dileptonic decay chain, illustrating the fitting to the SM correlated and uncorrelated templates as a dashed red line. These comparisons are made after the Z+jets normalisation factors have been applied (see section 6.4.2) and include statistical uncertainties on data. These distributions are for the inclusive measurement. a) is the distribution for the ee channel, b) is the $\mu\mu$ channel, c) is the eμ channel and d) is the combined channel. Also included is a comparison to the MC prediction using the uncorrelated (UC) sample (plus backgrounds).

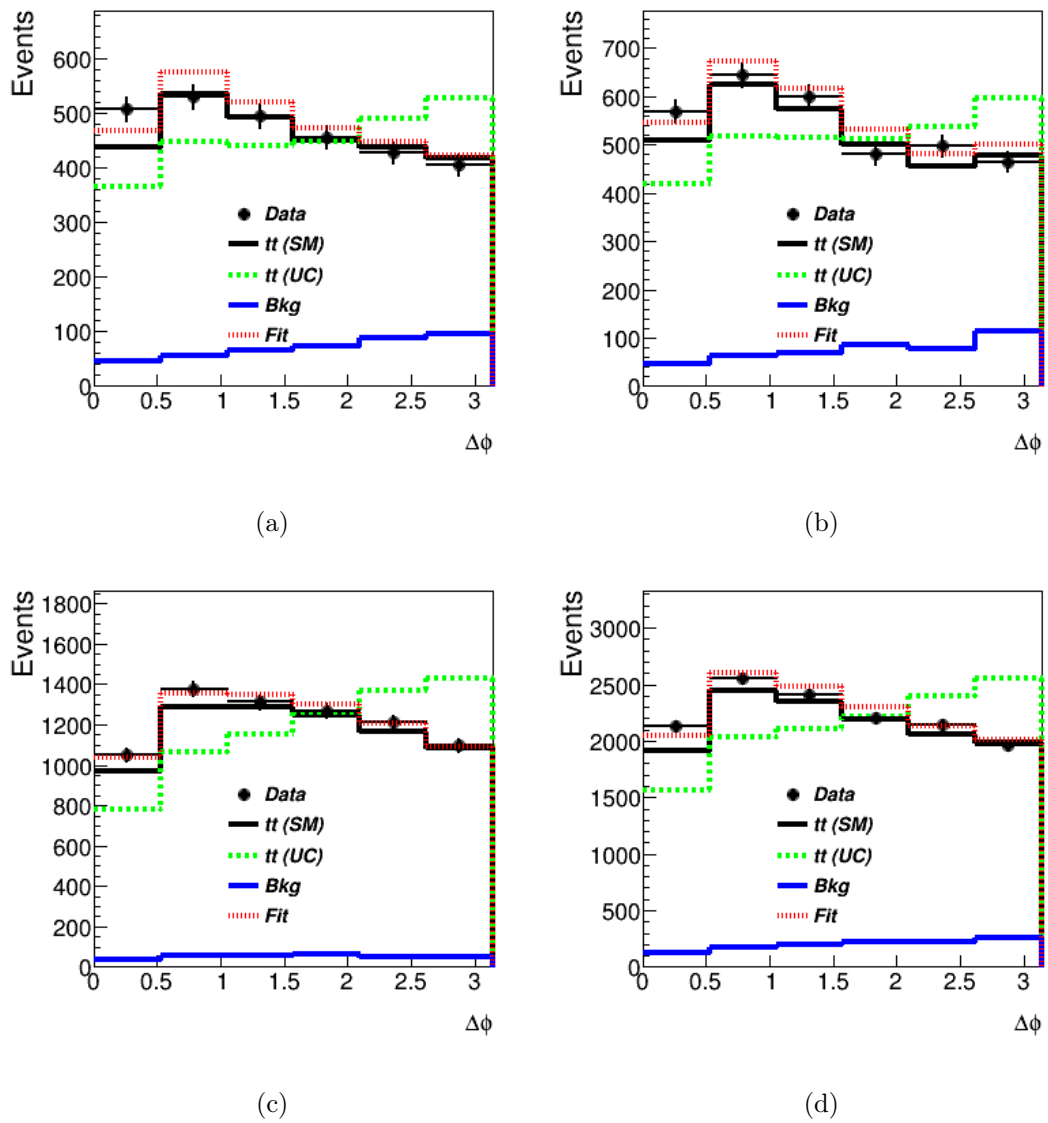

Figure 7.11: Data/Monte Carlo comparisons of the azimuthal opening angle between the two charged leptons in a dileptonic decay chain, illustrating the fitting to the SM correlated and uncorrelated templates as a dashed red line. These comparisons are made after the Z+jets normalisation factors have been applied (see section 6.4.2) and include statistical uncertainties on data. These distributions are for the opening angle where $M_{t\bar{t}} \leq 415$ GeV. a) is the distribution for the ee channel, b) is the $\mu\mu$ channel, c) is the eμ channel and d) is the combined channel. Also included is a comparison to the MC prediction using the uncorrelated (UC) sample (plus backgrounds).

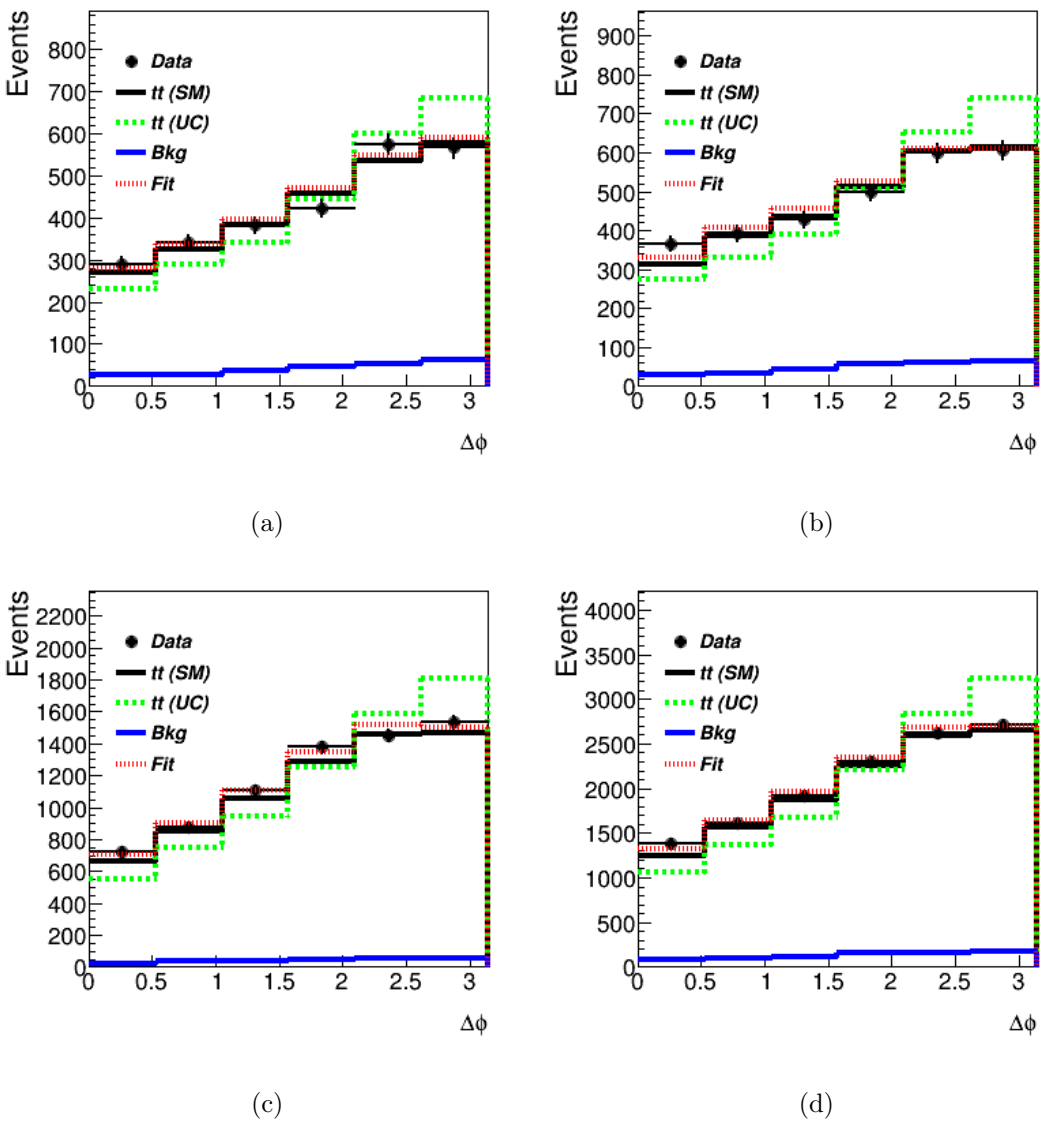

Figure 7.12: Data/Monte Carlo comparisons of the azimuthal opening angle between the two charged leptons in a dileptonic decay chain, illustrating the fitting to the SM correlated and uncorrelated templates as a dashed red line. These comparisons are made after the Z+jets normalisation factors have been applied (see section 6.4.2) and include statistical uncertainties on data. These distributions are for the opening angle where 415 GeV$< M_{t\bar{t}} \leq$ 505 GeV. a) is the distribution for the ee channel, b) is the $\mu\mu$ channel, c) is the eμ channel and d) is the combined channel. Also included is a comparison to the MC prediction using the uncorrelated (UC) sample (plus backgrounds).

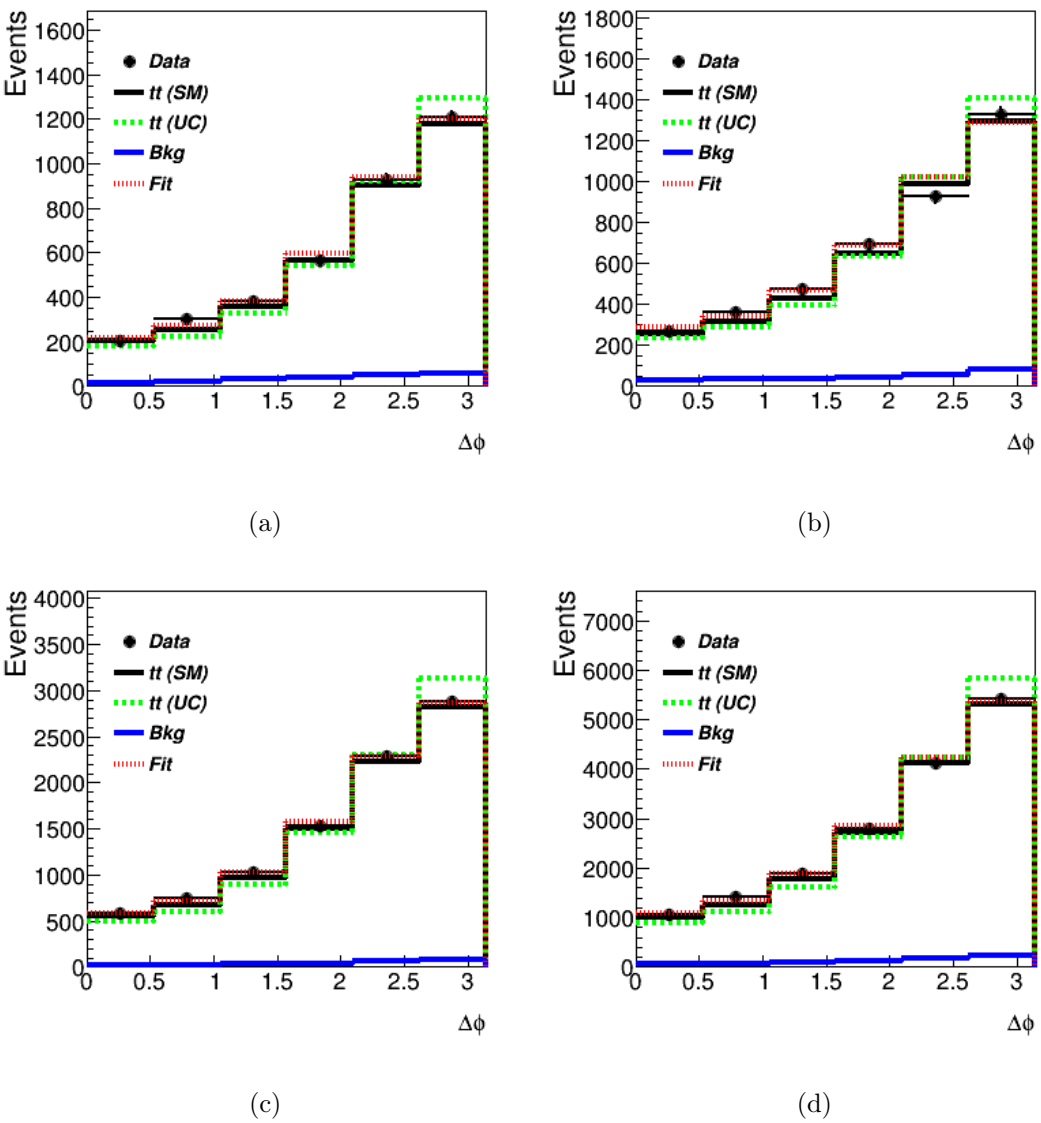

Figure 7.13: Data/Monte Carlo comparisons of the azimuthal opening angle between the two charged leptons in a dileptonic decay chain, illustrating the fitting to the SM correlated and uncorrelated templates as a dashed red line. These comparisons are made after the Z+jets normalisation factors have been applied (see section 6.4.2) and include statistical uncertainties on data. These distributions are for the opening angle where $M_{t\bar{t}} > 505$ GeV. a) is the distribution for the ee channel, b) is the $\mu\mu$ channel, c) is the eμ channel and d) is the combined channel. Also included is a comparison to the MC prediction using the uncorrelated (UC) sample (plus backgrounds).

7.5 Unfolded Measurement Results

Plots showing the normalised unfolded distributions for the eμ and combined dileptonic channels can be seen in figures 7.14 to 7.15. The unnormalised unfolded bin contents can be seen in Appendix A. The plots also include the associated statistical and systematic errors calculated for each bin.

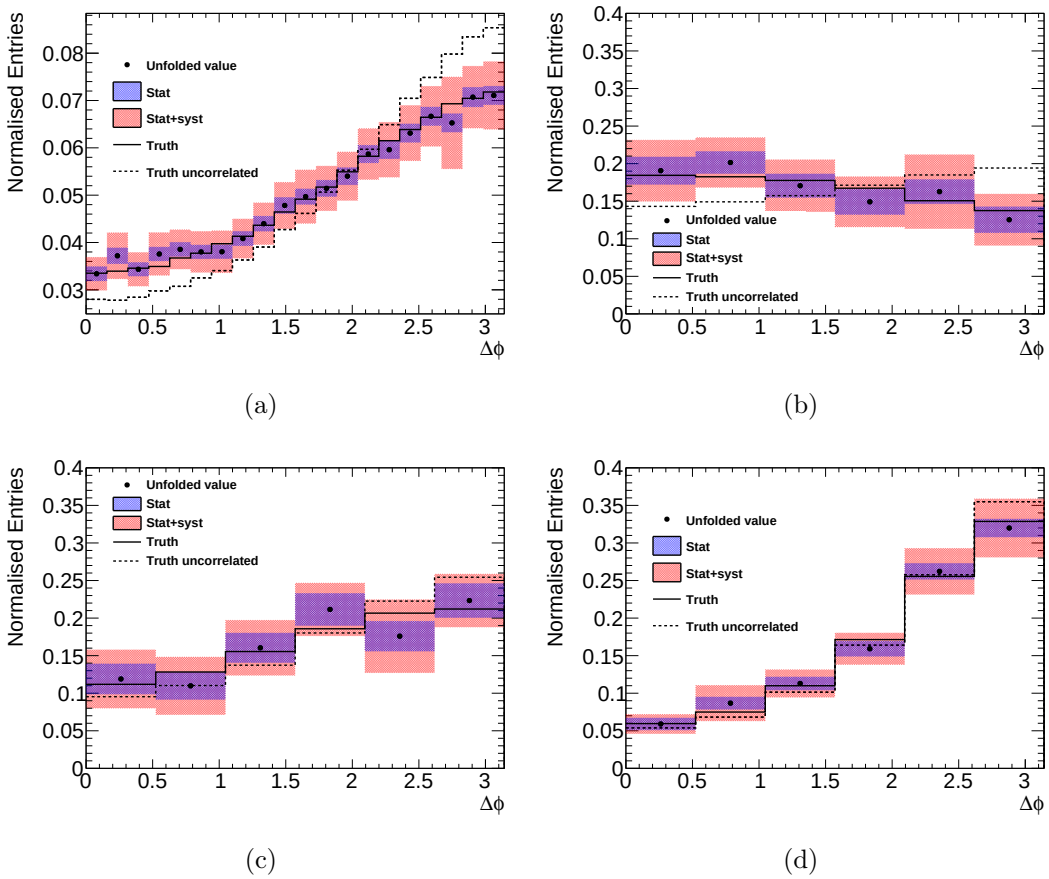

Figure 7.14: Plots showing the unfolded azimuthal lepton opening angle data distributions in the eμ channel, each normalised within its mass range. Plots include the associated statistical and systematic errors for each bin. Before unfolding, the background contributions have been subtracted from the data and the data are adjusted for expected contributions arising from objects measured in the detector which have no corresponding object in the truth distribution: a) is the unfolded inclusive distribution, b) is the distribution where $M_{t\bar{t}} \leq 415$ GeV, c) is the distribution where 415 GeV$< M_{t\bar{t}} \leq 505$ GeV and d) is the distribution where $M_{t\bar{t}} > 505$ GeV.

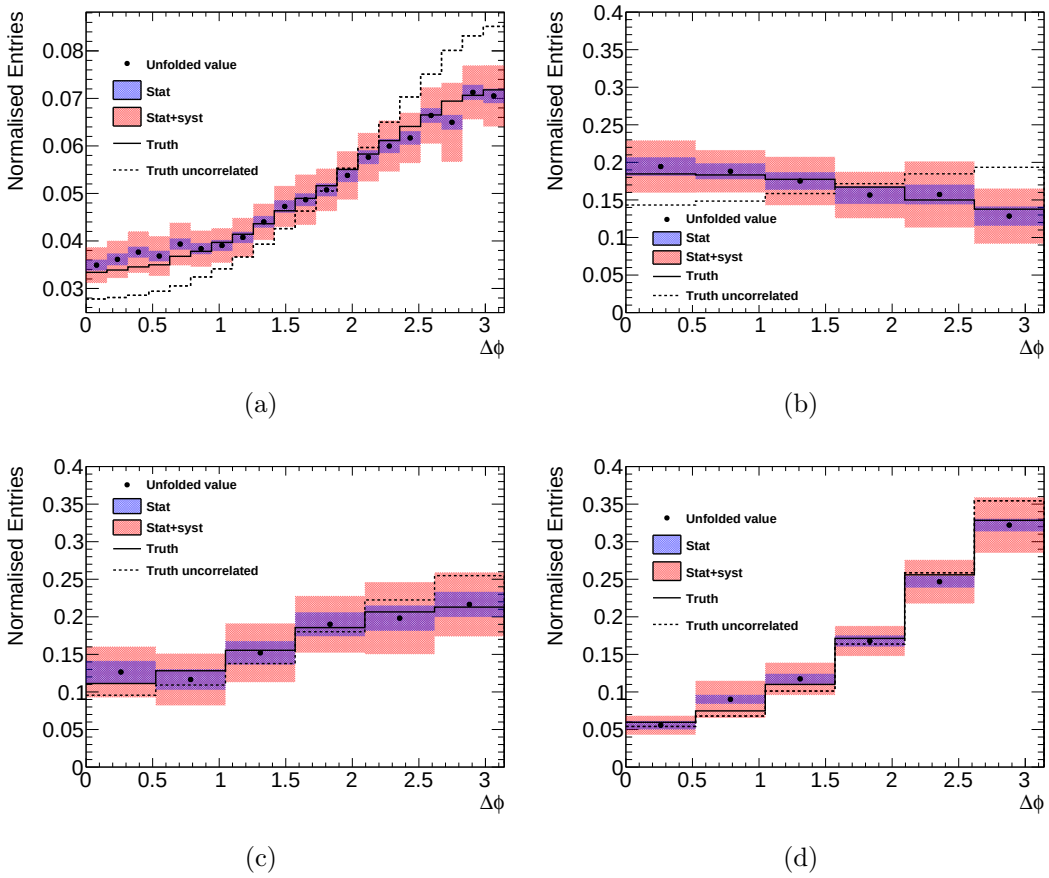

Figure 7.15: Plots showing the unfolded azimuthal lepton opening angle data distributions in the combined dileptonic channel, each normalised within its mass range. Plots include the associated statistical and systematic errors for each bin. Before unfolding, the background contributions have been subtracted from the data and the data are adjusted for expected contributions arising from objects measured in the detector which have no corresponding object in the truth distribution: a) is the unfolded inclusive distribution, b) is the distribution where $M_{t\bar{t}} \leq 415$ GeV, c) is the distribution where 415 GeV$< M_{t\bar{t}} \leq 505$ GeV and d) is the distribution where $M_{t\bar{t}} > 505$ GeV.

7.6 Discussion of Results

7.6.1 Detector Level Results

The fitted f_{SM} values for the inclusive measurement in each channel are shown in figure 7.16, with a comparison to the previous spin correlation combined channel measurement made from the same data sample at ATLAS [66]. The measurements shown favour a SM level of correlation over the uncorrelated scenario, although it is of interest to note that all of the channel measurements give a value of f_{SM} greater than 1, which may imply that there are BSM effects. The combined measurement made in this thesis is in agreement with ATLAS and CMS measurements [66] [67] and is 10.1 standard deviations from the $f_{SM} = 0$ scenario.

The fitted values for each of the $M_{t\bar{t}}$ binned distributions are shown graphically in figures 7.17 - 7.19. As in the case of the inclusive measurement, the results favour a SM level of spin correlation, with a tendency to produce results where the f_{SM} value is larger than 1. The size of the errors is generally larger for higher $M_{t\bar{t}}$ values. This is to be expected, as the choice of $M_{t\bar{t}}$ binning allows for less differentiation between the SM and uncorrelated predictions at higher values of $M_{t\bar{t}}$, so changes in the distributions due to systematic uncertainties are prone to cause larger fluctuations in the f_{SM} results than when considering lower invariant mass ranges. As expected, the shape of the $\Delta\phi$ distribution varies significantly as a function of $M_{t\bar{t}}$, with the lowest mass range showing a negative gradient in contrast to the positive gradient in the other two ranges (see figures 7.7 - 7.9). The results for the combined dilepton channel are within one standard deviation of the SM model for each of the $M_{t\bar{t}}$ ranges and are 9.8, 8.0 and 3.5 standard deviations from the $f_{SM} = 0$ scenario for the $M_{t\bar{t}} \leq 415$ GeV, 415 GeV$< M_{t\bar{t}} \leq 505$ GeV and $M_{t\bar{t}} > 505$ GeV ranges, respectively.

Whilst the results of this analysis do give fitted values of $f_{SM} \geq 1$ in all cases, the size of the uncertainties do not allow for any real conclusion about the possibility of BSM physics and the discrepancy from a value of $f_{SM} = 1$ is more likely to be a result of possible deficiencies in the simulation (for example, missing higher order contributions). However, the results would suggest that any BSM models which would predict a lower degree of spin correlation than the SM (such as a top quark decay to a charged Higgs) may be less likely.

7.6.2 Unfolded Results

The unfolded $\Delta\phi$ distributions for the inclusive analysis and the invariant mass range $M_{t\bar{t}} \leq 415$ GeV favour the SM prediction over the uncorrelated scenario, as the SM prediction is within the error bands whereas the uncorrelated scenario is not (see figures 7.14 - 7.15). For the 415 GeV$< M_{t\bar{t}} \leq 505$ GeV and $M_{t\bar{t}} > 505$ GeV ranges, the result is not as clear due to the decreased differentiation between the two spin scenarios.

For the purposes of discrimination between the SM and uncorrelated cases, a χ^2 goodness of fit approach has been taken, using the full uncertainty for each bin rather than the statistical uncertainty alone. For this reason, the measurement made is not a true χ^2 value, but only acts as an estimation of the goodness of fit for both correlation scenarios. Therefore, the value of χ^2 is expected to be smaller than one would usually expect (i.e. a value of ~ 1 per degree of freedom for a "good" fit). The calculation made is

$$\chi^2 = \sum_{i=1}^{N} \frac{(U_i - E_i)^2}{\sigma_i^2}, \tag{7.7}$$

where N is the number of bins in the distribution, U_i is the number of events in the

unfolded distribution in bin i, E_i is the number of events in the predicted distribution in bin i and σ_i is the total uncertainty in bin i. This value is then adjusted for the assumed number of degrees of freedom, which is taken to be N-1. The values for each channel and scenario are shown in tables 7.5 and 7.6. The χ^2 results all favour a SM scenario over an uncorrelated one, with greater distinction between the two scenarios found in the inclusive measurement and the $M_{t\bar{t}} \leq 415$ GeV range.

Table 7.5: Calculated χ^2 values for each unfolded distribution in the eμ channel.

Channel	χ^2	Degrees of freedom	χ^2/Degrees of Freedom
Inclusive			
SM	2.69	19	0.14
Uncorrelated	36.56		1.92
$M_{t\bar{t}} \leq 415$ GeV			
SM	0.90	5	0.18
Uncorrelated	8.51		2.13
415 GeV$< M_{t\bar{t}} \leq 505$ GeV			
SM	1.85	5	0.37
Uncorrelated	3.24		0.81
$M_{t\bar{t}} > 505$ GeV			
SM	0.70	5	0.14
Uncorrelated	2.06		0.52

Table 7.6: Calculated χ^2 values for each unfolded distribution in the combined dilepton channel.

Channel	χ^2	Degrees of freedom	χ^2/Degrees of Freedom
Inclusive			
SM	4.76	19	0.25
Uncorrelated	47.64		2.51
$M_{t\bar{t}} \leq 415$ GeV			
SM	0.74	5	0.15
Uncorrelated	8.68		2.17
415 GeV$< M_{t\bar{t}} \leq 505$ GeV			
SM	0.43	5	0.09
Uncorrelated	2.12		0.53
$M_{t\bar{t}} > 505$ GeV			
SM	0.82	5	0.16
Uncorrelated	2.44		0.61

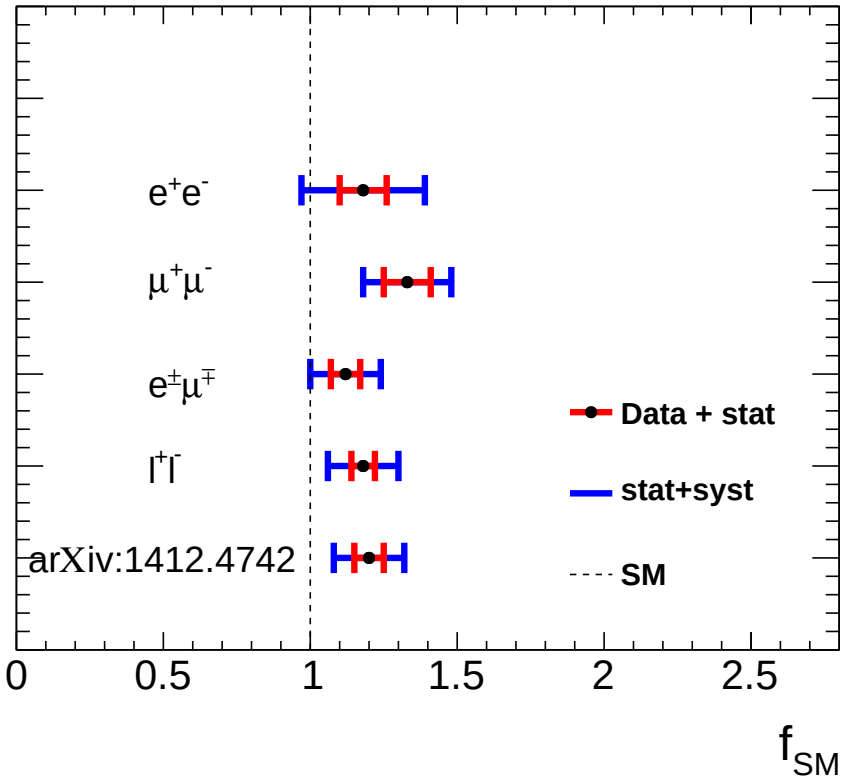

Figure 7.16: Values of f_{SM} for the inclusive measurement for each of the channels and the combined dilepton channel with associated statistical and systematic uncertainties. A line is drawn at $f_{SM} = 1$ to highlight the SM prediction. The result of [66] is included for comparison.

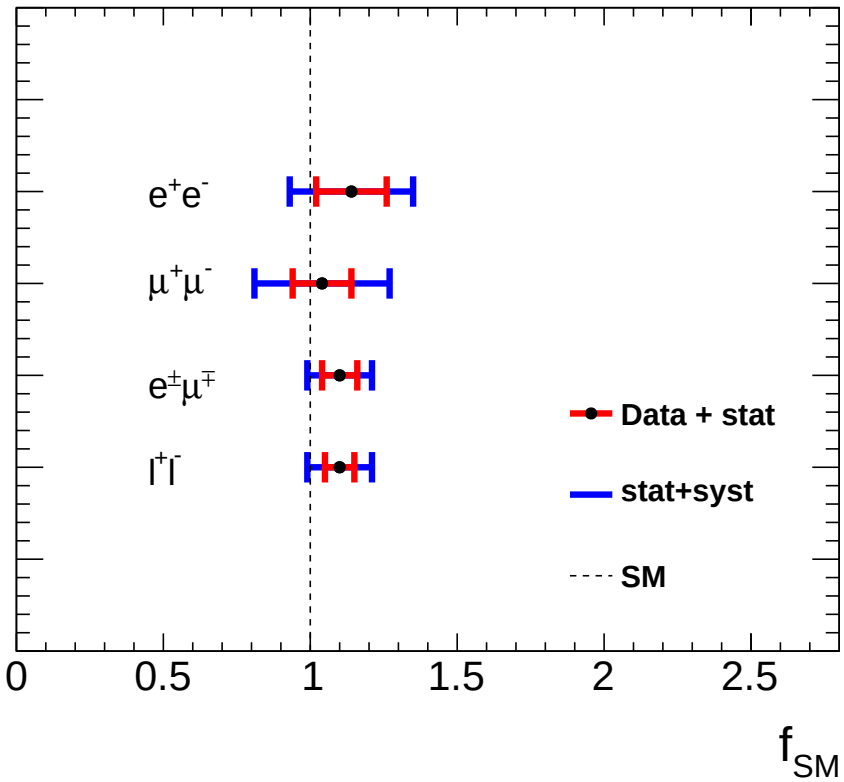

Figure 7.17: Values of f_{SM} measured for each of the channels and the combined dilepton channel with associated statistical and systematic uncertainties in the range $M_{t\bar{t}} \leq 415$ GeV . A line is drawn at $f_{SM} = 1$ to highlight the SM prediction.

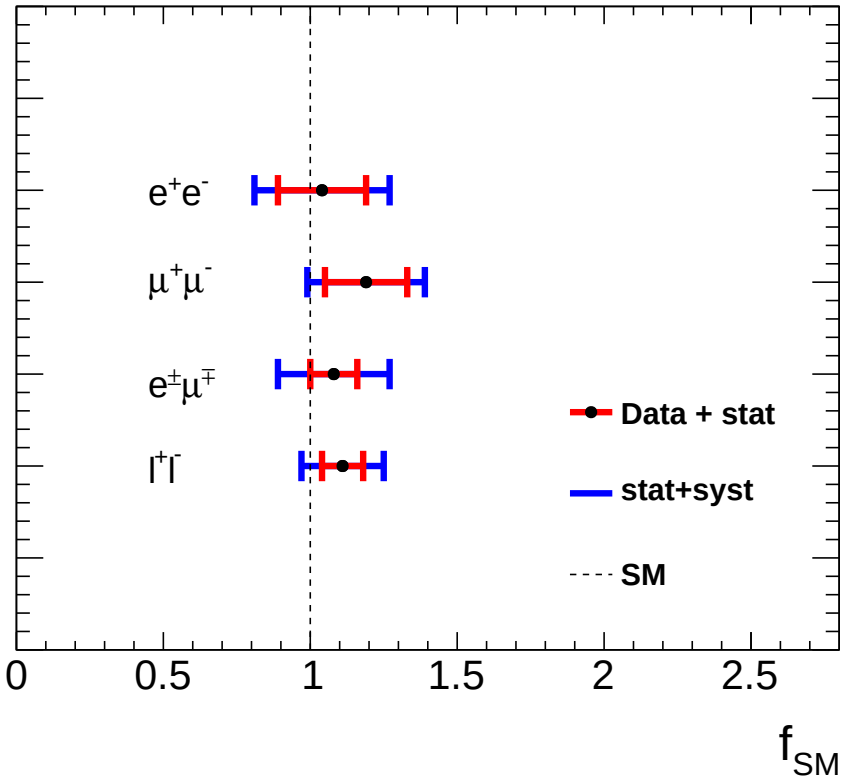

Figure 7.18: Values of f_{SM} measured for each of the channels and the combined dilepton channel with associated statistical and systematic uncertainties in the range 415 GeV$< M_{t\bar{t}} \leq$ 505 GeV. A line is drawn at $f_{SM} = 1$ to highlight the SM prediction.

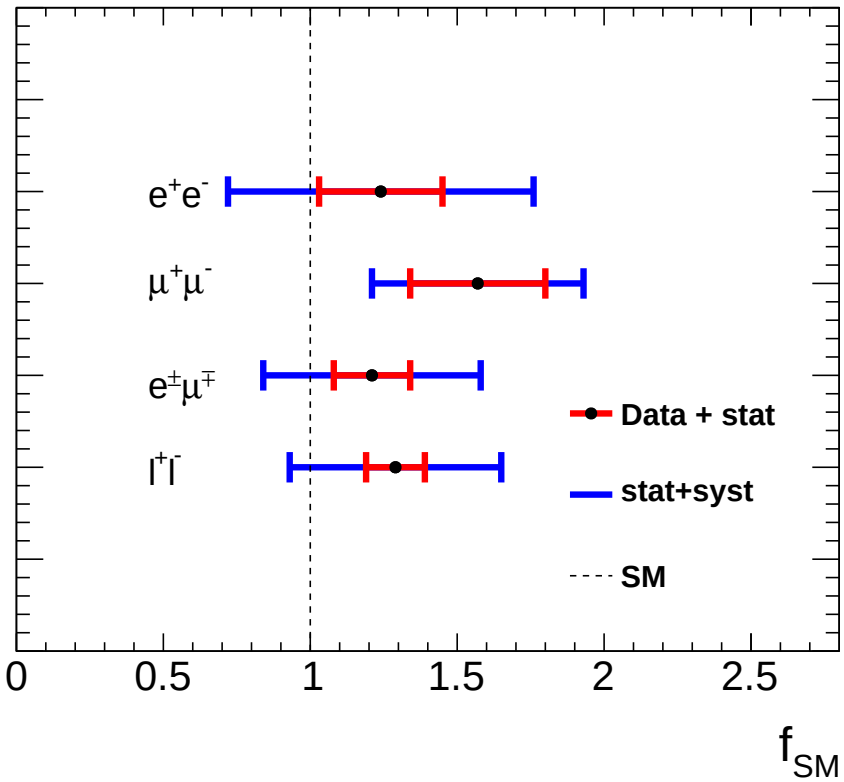

Figure 7.19: Values of f_{SM} measured for each of the channels and the combined dilepton channel with associated statistical and systematic uncertainties in the range $M_{t\bar{t}} > 505$ GeV. A line is drawn at $f_{SM} = 1$ to highlight the SM prediction.

Chapter 8

CONCLUDING REMARKS

The spin correlation in $t\bar{t}$ pairs has been measured by analysing the azimuthal opening angle $\Delta\phi$ of charged leptons in the laboratory frame, originating from a dileptonic decay of $t\bar{t}$ pairs ($t\bar{t} \rightarrow b\bar{b}W^+W^-(\rightarrow l^+l^-\nu\bar{\nu})$). This distribution was chosen as it has been shown to be sensitive to the spin correlation in top-antitop quark pairs produced by gluon-gluon fusion.

The proton-proton collision data used to make this measurement were recorded by the ATLAS detector at the LHC during the 2012 data taking period. Several measurements of the spin correlation have been made previously at the LHC (ATLAS and CMS) and at the Fermilab Tevatron (CDF and D$\emptyset$), and all show good agreement with the SM predictions [63] [64] [65] [66] [67].

This analysis has investigated the $\Delta\phi$ distributions both inclusively and differentially as a function of the invariant mass of the $t\bar{t}$ pair, $M_{t\bar{t}}$. This is the first time this differential measurement of spin correlation has been made at ATLAS and allows an insight into whether the value of spin correlation is anomalous in certain regions of $M_{t\bar{t}}$. Furthermore, these measurements have been made at detector level and also after correcting for detector effects (unfolding). Where reconstruction of the $t\bar{t}$ system was required, the M_{T2} variable was used to estimate the transverse energies of neutrinos in the system. The measurement is split into separate chan-

nels based on the flavour of the leptons (ee, $\mu\mu$, eμ), as well as a combined dilepton channel.

For the detector level measurements, the spin correlation is extracted by using a template fit method which compares the data to simulated $t\bar{t}$ events with an SM level of correlation and one which assumes there is no correlation. From this, the fraction of SM like events (f_{SM}) is found, and for the combined dilepton channel, the results are:

$$\begin{aligned}
\text{Inclusive} \qquad & f_{SM} = 1.18 \pm 0.04 \text{ (stat)} \pm 0.11 \text{ (syst)}, \\
M_{t\bar{t}} \leq 415 \text{ GeV} \qquad & f_{SM} = 1.10 \pm 0.05 \text{ (stat)} \pm 0.10 \text{ (syst)}, \\
415 \text{ GeV} < M_{t\bar{t}} \leq 505 \text{ GeV} \qquad & f_{SM} = 1.11 \pm 0.07 \text{ (stat)} \pm 0.12 \text{ (syst)}, \\
M_{t\bar{t}} > 505 \text{ GeV} \qquad & f_{SM} = 1.29 \pm 0.10 \text{ (stat)} \pm 0.35 \text{ (syst)},
\end{aligned}$$

which all favour a SM scheme for spin correlation over the uncorrelated hypothesis, with the measurements 10.1, 9.8, 8.0 and 3.5 standard deviations away from the uncorrelated scenario respectively. This suggests that the degree of spin correlation is as expected and that there is a minimal contribution from BSM phenomena, although due to the tendency for the f_{SM} value to be slightly larger than 1, these effects cannot be ruled out entirely.

For the unfolded measurements, the data were corrected for detector effects by use of a Fully Bayesian Unfolding technique, and an unfolded $\Delta\phi$ distribution was obtained in the eμ and combined dilepton channels. To assess a favoured model, a χ^2 goodness of fit test was performed using the SM and uncorrelated predictions as templates. It was found that in all cases the SM scenario was favoured over the uncorrelated one, with a stronger distinction between the two models found in the inclusive measurement and in the $M_{t\bar{t}} \leq 415$ GeV mass range.

Due to the similarity of the two models at higher values of $M_{t\bar{t}}$, the ability to dis-

tinguish between the scenarios is hampered by the limited amount of data available and the size of the systematic uncertainties associated with the measurement. As the LHC continues at increased energies, there will be a far larger number of $t\bar{t}$ pairs produced. As of July 2016, running with a c.m. energy of $\sqrt{s} = 13$ TeV, ATLAS has a recorded integrated luminosity of ~ 14 fb^{-1}, and with the increased production cross section of $t\bar{t}$ pairs at this c.m. energy, approximately twice as many $t\bar{t}$ pairs have already been produced than the full dataset used in this thesis. With further understanding of the correlations between the systematic uncertainties involved by modifications to the FBU techniques, there will be scope to produce a more precise measurement, particularly for top-antitop quark pairs produced with a larger invariant mass.

References

[1] **Particle Data Group**, J. Beringer et al., *Review of Particle Physics (RPP)*, *Phys. Rev.* **D86** (2012) 010001.

[2] **The IceCube Collaboration**, G. Sullivan, *Results from the IceCube Experiment*, *Nucl. Phys. Proc. Suppl.* **235-236** (2013) 346–351, [arXiv:1210.4195].

[3] **Super-Kamiokande**, Y. Fukuda et al., *The Super-Kamiokande detector*, *Nucl. Instrum. Meth.* **A501** (2003) 418–462.

[4] O. W. Greenberg, *Spin and Unitary Spin Independence in a Paraquark Model of Baryons and Mesons*, *Phys. Rev. Lett.* **13** (1964) 598–602.

[5] D. B. Lichtenberg, *Unitary Symmetry and Elementary Particles, pp212-261.* Academic Press, 1978.

[6] D. Griffiths, *Introduction to elementary particles, p245, p408.* Wiley-VCH, 2008.

[7] M. Thomson, *Modern particle physics, p178, p296.* Cambridge University Press, New York, 2013.

[8] E. Fermi, *An attempt of a theory of beta radiation. 1.*, UCRL-TRANS-726, *Z. Phys.* **88** (1934) 161–177.

[9] **The UA1 Collaboration**, G. Arnison et al., *Experimental Observation of Isolated Large Transverse Energy Electrons with Associated Missing Energy at $\sqrt{s}$ = 540 GeV*, CERN-EP-83-13, *Phys. Lett.* **B122** (1983) 103–116. [,611(1983)].

[10] **The UA1 Collaboration**, G. Arnison et al., *Experimental Observation of Lepton Pairs of Invariant Mass Around 95-GeV/c^2 at the CERN SPS Collider*, CERN-EP-83-73, *Phys. Lett.* **B126** (1983) 398–410.

[11] **The CDF Collaboration**, D. Acosta et al., *First evidence for $B_s^0 \to \phi\phi$ decay and measurements of branching ratio and A_{CP} for $B^+ \to \phi K^+$*, FERMILAB-PUB-05-027-E, *Phys. Rev. Lett.* **95** (2005) 031801, [hep-ex/0502044].

[12] F. Englert and R. Brout, *Broken Symmetry and the Mass of Gauge Vector Mesons*, *Phys. Rev. Lett.* **13** (1964) 321–323.

[13] G. S. Guralnik, C. R. Hagen, and T. W. B. Kibble, *Global Conservation Laws and Massless Particles*, *Phys. Rev. Lett.* **13** (1964) 585–587.

[14] P. W. Higgs, *Broken Symmetries and the Masses of Gauge Bosons*, *Phys. Rev. Lett.* **13** (1964) 508–509.

[15] **The ATLAS Collaboration**, G. Aad et al., *Observation of a new particle in the search for the Standard Model Higgs boson with the ATLAS detector at the LHC*, CERN-PH-EP-2012-218, *Phys. Lett.* **B716** (2012) 1–29, [arXiv:1207.7214].

[16] **The CMS Collaboration**, S. Chatrchyan et al., *Observation of a new boson at a mass of 125 GeV with the CMS experiment at the LHC*, CMS-HIG-12-028, CERN-PH-EP-2012-220, *Phys. Lett.* **B716** (2012) 30–61, [arXiv:1207.7235].

[17] M. Kobayashi and T. Maskawa, *CP-Violation in the Renormalizable Theory of Weak Interaction*, *Prog. Theor. Phys. 49* **652-657** (1973).

[18] **CKMfitter Group**, J. C. et al. *Eur. Phys. J.* **C41** (2005) 1–131, updated results and plots available at: http://ckmfitter.in2p3.fr, [hep-ph/0406184].

[19] **The CDF Collaboration**, F. Abe et al., *Observation of top quark production in $\bar{p}p$ collisions*, FERMILAB-PUB-95-022-E, CDF-PUB-TOP-PUBLIC-3040, ANL-HEP-PR-95-44, *Phys. Rev. Lett.* **74** (1995) 2626–2631, [hep-ex/9503002].

[20] S. Holmes, R. S. Moore, and V. Shiltsev, *Overview of the Tevatron collider complex: goals, operations and performance*, *Journal of Instrumentation* **6** (2011), no. 08 T08001.

[21] A. D. Martin, W. J. Stirling, R. S. Thorne, and G. Watt, *Parton distributions for the LHC*, IPPP-08-95, DCPT-08-190, CAVENDISH-HEP-08-16, *Eur. Phys. J.* **C63** (2009) 189–285, [arXiv:0901.0002].

[22] **The ATLAS Collaboration**, G. Aad et al., *Expected performance of the atlas experiment: detector, trigger and physics*, CERN-OPEN-2008-020, arXiv:0901.0512.

[23] M. Cacciari, M. Czakon, M. Mangano, A. Mitov, and P. Nason, *Top-pair production at hadron colliders with next-to-next-to-leading logarithmic soft-gluon resummation*, CERN-PH-TH-2011-277, TTK-11-54, *Phys. Lett.* **B710** (2012) 612–622, [arXiv:1111.5869].

[24] M. Czakon and A. Mitov, *Top++: A Program for the Calculation of the Top-Pair Cross-Section at Hadron Colliders*, CERN-PH-TH-2011-303, TTK-11-58, *Comput. Phys. Commun.* **185** (2014) 2930, [arXiv:1112.5675].

[25] M. Czakon, P. Fiedler, and A. Mitov, *Total Top-Quark Pair-Production Cross Section at Hadron Colliders Through $O(\frac{4}{S})$*, CERN-PH-TH-2013-056, TTK-13-08, *Phys. Rev. Lett.* **110** (2013) 252004, [arXiv:1303.6254].

[26] M. Mohammadi Najafabadi, *Single Top production at LHC*, in *Proceedings, 41st Rencontres de Moriond, 2006 QCD and high energy hadronic interactions*, pp. 173–178, 2006. hep-ex/0605034.

[27] A. Giammanco, *Single top quark production at the LHC*, CP3-15-40, *Rev. Phys.* **1** (2016) 1–12, [arXiv:1511.06748].

[28] N. Kidonakis, *Next-to-next-to-leading-order collinear and soft gluon corrections for t-channel single top quark production*, *Phys. Rev.* **D83** (2011) 091503, [arXiv:1103.2792].

[29] N. Kidonakis, *Differential and total cross sections for top pair and single top production*, in *Proceedings, 20th International Workshop on Deep-Inelastic Scattering and Related Subjects (DIS 2012)*, pp. 831–834, 2012. arXiv:1205.3453.

[30] N. Kidonakis, *NNLL resummation for s-channel single top quark production*, *Phys. Rev.* **D81** (2010) 054028, [arXiv:1001.5034].

[31] N. Kidonakis, *Two-loop soft anomalous dimensions for single top quark associated production with a W^- or H^-*, *Phys. Rev.* **D82** (2010) 054018, [arXiv:1005.4451].

[32] **The ATLAS Collaboration**, G. Aad et al., *Search for flavour-changing neutral current top-quark decays to qZ in pp collision data collected with the ATLAS detector at $\sqrt{s} = 8$ TeV*, CERN-PH-EP-2015-183, *Eur. Phys. J.* **C76** (2016), no. 1 12, [arXiv:1508.05796].

[33] **The ATLAS Collaboration**, G. Aad et al., *Measurement of colour flow with the jet pull angle in $t\bar{t}$ events using the ATLAS detector at $\sqrt{s} = 8$ TeV*, CERN-PH-EP-2015-128, *Phys. Lett.* **B750** (2015) 475–493, [arXiv:1506.05629].

[34] **The ATLAS Collaboration**, *The ATLAS Detector*, tech. rep., CERN, Geneva, 2011, http://www.atlas.ch/photos/index.html.

[35] **The ATLAS Collaboration**, *The ATLAS Experiment at the CERN Large Hadron Collider*, *Journal of Instrumentation* **3** (2008), no. 08 S08003.

[36] **The CMS Collaboration**, *The CMS experiment at the CERN LHC*, *Journal of Instrumentation* **3** (2008), no. 08 S08004.

[37] **The LHCb Collaboration**, *The LHCb Detector at the LHC*, *Journal of Instrumentation* **3** (2008), no. 08 S08005.

[38] **The ALICE Collaboration**, *The ALICE experiment at the CERN LHC*, *Journal of Instrumentation* **3** (2008), no. 08 S08002.

[39] K. Schindl, *The injector chain for the LHC*, in *LEP performance. Proceedings, 9th Workshop, Chamonix, France, January 26-29, 1999*, pp. 47–52, 1999.

[40] *LHC Injection System*, tech. rep., `http://slhcpp.web.cern.ch/SLHCPP/news_pages/news_courier1.php`.

[41] C. E. Hill, A. Lombardi, R. Scrivens, M. Vretenar, A. Feschenko, and A. Liou, *Tests of the CERN proton linac performance for LHC - type beams*, LINAC2000-TUD17, *eConf* **C000821** (2000) TUD17, [`physics/0008102`]. [,590(2000)].

[42] K. H. Reich, *The CERN Proton Synchrotron Booster*, *IEEE Trans. Nucl. Sci.* **16** (1969) 959–961.

[43] A. Newborough, M. Buzio, and R. Chritin, *Upgrade of the CERN Proton Synchrotron Booster Bending Magnets for 2 GeV Operation*, *IEEE Trans. Appl. Supercond.* **24** (2014), no. 3 0500304.

[44] F. Djama, *Overview of the ATLAS insertable B-layer project*, *Journal of Instrumentation* **8** (2013), no. 01 C01034.

[45] **ATLAS**, G. Aad et al., *Readiness of the ATLAS Liquid Argon Calorimeter for LHC Collisions*, *Eur. Phys. J.* **C70** (2010) 723–753, [`arXiv:0912.2642`].

[46] F. U. Bernlochner, *The ATLAS Trigger System: Ready for Run 2*, Tech. Rep. ATL-DAQ-PROC-2015-032, CERN, Geneva, Oct, 2015, https://cds.cern.ch/record/2056973.

[47] R. Achenbach et al. *Journal of Instrumentation* **3** (2008), no. 03 P03001.

[48] **The ATLAS Collaboration**, *Performance of the ATLAS Trigger System in 2010*, *Eur. Phys. J. C* **72** (Oct, 2011).

[49] F. Pastore, *ATLAS Run-2 status and performance*, ATL-PHYS-SLIDE-2015-373.

[50] B. Barnett, J. Bracinik, S. Hillier, M. Levy, R. Mudd, R. Owen, and M. Watson, *Investigation into the Effect of Isolation on Trigger Rate and Efficiency of Acceptance on Electromagnetic Events in the ATLAS Level-1 Calorimeter*, Tech. Rep. ATL-COM-DAQ-2013-057, CERN, Geneva, Jul, 2013, https://cds.cern.ch/record/1564863.

[51] R. M. Harris, C. T. Hill, and S. J. Parke, *Cross-section for topcolor Z-prime(t) decaying to top-antitop: Version 2.6*, FERMILAB-FN-0687, CDF-ANAL-EXOTIC-PUBLIC-5064, `hep-ph/9911288`.

[52] M. Arai, N. Okada, K. Smolek, and V. Simak, *Influence of Z' boson on top quark spin correlations at the LHC*, HIP-2008-08-TH, KEK-TH-1242, *Acta Phys. Polon.* **B40** (2009) 93–110, [`arXiv:0804.3740`].

[53] W. Bernreuther, M. Flesch, and P. Haberl, *Signatures of Higgs bosons in the top quark decay channel at hadron colliders*, PITHA-97-34, *Phys. Rev.* **D58** (1998) 114031, [`hep-ph/9709284`].

[54] J. S. Lee, Y. Peters, A. Pilaftsis, and C. Schwanenberger, *Strangephilic Higgs Bosons in the MSSM*, MAN-HEP-2009-32, *Eur. Phys. J.* **C66** (2010) 261–269, [arXiv:0909.1749].

[55] M. Carena, S. Heinemeyer, C. E. M. Wagner, and G. Weiglein, *Suggestions for benchmark scenarios for MSSM Higgs boson searches at hadron colliders*, ANL-HEP-CP-02-017, DCPT-02-24, FERMILAB-PUB-02-024-T, BNL-HET-02-7, EFI-02-64, IPPP-02-11, *Eur. Phys. J.* **C26** (2003) 601–607, [hep-ph/0202167].

[56] T. McLaughlan, *Measurement of Spin Correlation in Top Quark Pair Production at ATLAS*. PhD thesis, Birmingham University, 2014. presented 9 Jan 2014.

[57] A. Brandenburg, Z. Si, and P. Uwer, *QCD-corrected spin analysing power of jets in decays of polarized top quarks*, *Phys.Lett.* **B539** (2002) 235–241.

[58] **The CDF Collaboration**, T. Aaltonen et al., *Measurement of $t\bar{t}$ Spin Correlation in $p\bar{p}$ Collisions Using the CDF II Detector at the Tevatron*, FERMILAB-PUB-10-513-E, *Phys. Rev.* **D83** (2011) 031104, [arXiv:1012.3093].

[59] P. Uwer, *Maximizing the spin correlation of top quark pairs produced at the Large Hadron Collider*, CERN-PH-TH-2004-246, *Phys. Lett.* **B609** (2005) 271–276, [hep-ph/0412097].

[60] S. Frixione, F. Stoeckli, P. Torrielli, B. R. Webber, and C. D. White, *The MC@NLO 4.0 Event Generator*, arXiv:1010.0819.

[61] G. Mahlon and S. J. Parke, *Spin Correlation Effects in Top Quark Pair Production at the LHC*, FERMILAB-PUB-09-662-T, *Phys. Rev.* **D81** (2010) 074024, [arXiv:1001.3422].

[62] G. Mahlon and S. J. Parke, *Angular correlations in top quark pair production and decay at hadron colliders*, FERMILAB-PUB-95-362-T, UM-TH-95-26, *Phys. Rev.* **D53** (1996) 4886–4896, [hep-ph/9512264].

[63] **The D0 Collaboration**, B. Abbott et al., *Spin correlation in $t\bar{t}$ production from $p\bar{p}$ collisions at $\sqrt{s} = 1.8$ TeV*, FERMILAB-PUB-00-046-E, *Phys. Rev. Lett.* **85** (2000) 256–261, [hep-ex/0002058].

[64] **The ATLAS Collaboration**, G. Aad et al., *Observation of spin correlation in $t\bar{t}$ events from pp collisions at $\sqrt{s} = 7$ TeV using the ATLAS detector*, CERN-PH-EP-2012-074, *Phys. Rev. Lett.* **108** (2012) 212001, [arXiv:1203.4081].

[65] **The ATLAS Collaboration**, G. Aad et al., *Measurements of spin correlation in top-antitop quark events from proton-proton collisions at $\sqrt{s} = 7$ TeV using the ATLAS detector*, CERN-PH-EP-2014-116, *Phys. Rev.* **D90** (2014), no. 11 112016, [arXiv:1407.4314].

[66] **The ATLAS Collaboration**, G. Aad et al., *Measurement of Spin Correlation in Top-Antitop Quark Events and Search for Top Squark Pair Production in pp Collisions at $\sqrt{s} = 8$ TeV Using the ATLAS Detector*, CERN-PH-EP-2014-257, *Phys. Rev. Lett.* **114** (2015), no. 14 142001, [arXiv:1412.4742].

[67] **The CMS Collaboration**, V. Khachatryan et al., *Measurements of $t\bar{t}$ spin correlations and top quark polarization using dilepton final states in pp collisions at $\sqrt{s} = 8$ TeV*, CMS-TOP-14-023, CERN-PH-EP-2015-333, *Phys. Rev.* **D93** (2016), no. 5 052007, [arXiv:1601.01107].

[68] A. Buckley, *Soft QCD in ATLAS: Measurements and modelling of multi-parton interactions*, *Acta Phys. Polon.* **B42** (2011) 2669–2696, [arXiv:1112.5477].

[69] **GEANT4**, S. Agostinelli et al., *GEANT4: A Simulation toolkit*, SLAC-PUB-9350, FERMILAB-PUB-03-339, *Nucl. Instrum. Meth.* **A506** (2003) 250–303.

[70] C. Oleari, *The POWHEG-BOX*, *Nucl. Phys. Proc. Suppl.* **205-206** (2010) 36–41, [arXiv:1007.3893].

[71] H.-L. Lai, M. Guzzi, J. Huston, Z. Li, P. M. Nadolsky, J. Pumplin, and C. P. Yuan, *New parton distributions for collider physics*, MSUHEP-100707, SMU-HEP-10-10, *Phys. Rev.* **D82** (2010) 074024, [arXiv:1007.2241].

[72] J. Gao, M. Guzzi, J. Huston, H.-L. Lai, Z. Li, P. Nadolsky, J. Pumplin, D. Stump, and C. P. Yuan, *CT10 next-to-next-to-leading order global analysis of QCD*, SMU-HEP-12-23, *Phys. Rev.* **D89** (2014), no. 3 033009, [arXiv:1302.6246].

[73] E. Re, *Single-top Wt-channel production matched with parton showers using the POWHEG method*, IPPP-10-74, DCPT-10-148, *Eur. Phys. J.* **C71** (2011) 1547, [arXiv:1009.2450].

[74] W. Lukas, *Fast Simulation for ATLAS: Atlfast-II and ISF*, Tech. Rep. ATL-SOFT-PROC-2012-065, CERN, Geneva, Jun, 2012, https://cds.cern.ch/record/1458503.

[75] E. Richter-Was, D. Froidevaux, and L. Poggioli, *ATLFAST 2.0 a fast simulation package for ATLAS*, Tech. Rep. ATL-PHYS-98-131, CERN, Geneva, Nov, 1998, http://cds.cern.ch/record/683751.

[76] M. L. Mangano, F. Piccinini, A. D. Polosa, M. Moretti, and R. Pittau, *ALPGEN, a generator for hard multiparton processes in hadronic collisions*, *Journal of High Energy Physics* **2003** (2003), no. 07 001.

[77] J. Pumplin, D. R. Stump, J. Huston, H. L. Lai, P. M. Nadolsky, and W. K. Tung, *New generation of parton distributions with uncertainties from global QCD analysis*, MSU-HEP-011101, *JHEP* **07** (2002) 012, [hep-ph/0201195].

[78] T. Sjostrand, S. Mrenna, and P. Z. Skands, *PYTHIA 6.4 Physics and Manual*, FERMILAB-PUB-06-052-CD-T, LU-TP-06-13, *JHEP* **05** (2006) 026, [hep-ph/0603175].

[79] J. Alwall et al., *Comparative study of various algorithms for the merging of parton showers and matrix elements in hadronic collisions*, SLAC-PUB-12604, CERN-PH-TH-2007-066, LU-TP-07-13, KA-TP-06-2007, DCPT-07-62, IPPP-07-31, *Eur. Phys. J.* **C53** (2008) 473–500, [arXiv:0706.2569].

[80] **The ATLAS Collaboration**, G. Aad et al., *Study of heavy-flavor quarks produced in association with top-quark pairs at $\sqrt{s} = 7$ TeV using the ATLAS detector*, CERN-PH-EP-2013-030, *Phys. Rev.* **D89** (2014), no. 7 072012, [arXiv:1304.6386].

[81] **The ATLAS Collaboration**, *First tuning of HERWIG/JIMMY to ATLAS data*, ATL-PHYS-PUB-2010-014.

[82] S. Frixione, E. Laenen, P. Motylinski, B. R. Webber, and C. D. White, *Single-top hadroproduction in association with a W boson*, CERN-TH-2008-104, ITP-UU-08-27, NIKHEF-2008-005, ITFA-2008-16, CAVENDISH-HEP-08-06, *JHEP* **07** (2008) 029, [arXiv:0805.3067].

[83] *The ATLAS top Physics Working Group Home Page*, https://twiki.cern.ch/twiki/bin/view/AtlasProtected/TopWorkingGroup.

[84] **The ATLAS Collaboration**, G. Aad et al., *Electron performance measurements with the ATLAS detector using the 2010 LHC proton-proton collision data*, CERN-PH-EP-2011-117, *Eur. Phys. J.* **C72** (2012) 1909, [arXiv:1110.3174].

[85] **The ATLAS Collaboration**, G. Aad et al., *Electron and photon energy calibration with the ATLAS detector using LHC Run 1 data*, CERN-PH-EP-2014-153, *Eur. Phys. J.* **C74** (2014), no. 10 3071, [arXiv:1407.5063].

[86] **The ATLAS Collaboration**, B. Resende, *Muon identification algorithms in ATLAS*, *PoS* **EPS-HEP2009** (2009) 431.

[87] **The ATLAS Collaboration**, S. Leontsinis, *Performance of the muon identification and reconstruction with the ATLAS detector*, *EPJ Web Conf.* **95** (2015) 05009.

[88] **The ATLAS Collaboration**, G. Aad et al., *Measurement of the muon reconstruction performance of the ATLAS detector using 2011 and 2012 LHC proton proton collision data*, CERN-PH-EP-2014-151, *Eur. Phys. J.* **C74** (2014), no. 11 3130, [arXiv:1407.3935].

[89] M. Cacciari, G. P. Salam, and G. Soyez, *The Anti-k(t) jet clustering algorithm*, LPTHE-07-03, *JHEP* **04** (2008) 063, [arXiv:0802.1189].

[90] M. Cacciari, G. P. Salam, and G. Soyez, *FastJet User Manual*, CERN-PH-TH-2011-297, *Eur. Phys. J.* **C72** (2012) 1896, [arXiv:1111.6097].

[91] **The ATLAS Collaboration**, *Tagging and suppression of pileup jets*, ATLAS-CONF-2014-018.

[92] **The ATLAS Collaboration**, G. Aad et al., *Calibration of the b-tagging efficiency for c jets with the ATLAS detector using events with a W boson produced in association with a single c quark*, ATLAS-CONF-2013-109.

[93] **The ATLAS Collaboration**, G. Aad et al., *Commissioning of the ATLAS high-performance b-tagging algorithms in the 7 TeV collision data*, Tech. Rep. ATLAS-CONF-2011-102, CERN, Geneva, Jul, 2011.

[94] **The ATLAS Collaboration**, G. Aad et al., *Measurement of the Mistag Rate with 5 fb^{-1} of Data Collected by the ATLAS Detector*, Tech. Rep. ATLAS-CONF-2012-040, CERN, Geneva, Mar, 2012, https://cds.cern.ch/record/1435194.

[95] **The ATLAS Collaboration**, G. Aad et al., *Measurements of the charge asymmetry in top-quark pair production in the dilepton final state at $\sqrt{s} = 8$ TeV with the ATLAS detector*, CERN-EP-2016-051, *Submitted to Physical Review D.* (2016) [arXiv:1604.05538].

[96] **The ATLAS Collaboration**, G. Aad et al., *Performance of Missing Transverse Momentum Reconstruction in Proton-Proton Collisions at 7 TeV with ATLAS*, CERN-PH-EP-2011-114, *Eur. Phys. J.* **C72** (2012) 1844, [arXiv:1108.5602].

[97] *The ATLAS Good Run Lists Homepage*, https://twiki.cern.ch/twiki/bin/view/Atlas/GoodRunsLists.

[98] *The ATLAS Trigger Menu Homepage*, https://twiki.cern.ch/twiki/bin/view/Atlas/TriggerPhysicsMenu.

[99] **The ATLAS Collaboration**, G. Aad et al., *Measurement of the $t\bar{t}$ production cross-section using $e\mu$ events with b -tagged jets in pp collisions at $\sqrt{s} = 7$ and 8 TeV with the ATLAS detector*, CERN-PH-EP-2014-124, CERN-EP-2014-124, *Eur. Phys. J.* **C74** (2014), no. 10 3109, [arXiv:1406.5375].

[100] R. Mahbubani, K. T. Matchev, and M. Park, *Re-interpreting the Oxbridge Stransverse mass variable MT2 in general cases*, CERN-PH-TH-2012-333, *JHEP* **03** (2013) 134, [arXiv:1212.1720].

[101] C. G. Lester and D. J. Summers, *Measuring masses of semiinvisibly decaying particles pair produced at hadron colliders*, CAVENDISH-HEP-99-07, *Phys. Lett.* **B463** (1999) 99–103, [hep-ph/9906349].

[102] **The ATLAS Collaboration**, G. Aad et al., *Search for direct top-squark pair production in final states with two leptons in pp collisions at $\sqrt{s} = 8TeV$ with the ATLAS detector*, CERN-PH-EP-2014-014, *JHEP* **06** (2014) 124, [arXiv:1403.4853].

[103] **The CMS Collaboration**, V. Khachatryan et al., *Searches for Supersymmetry using the M_{T2} Variable in Hadronic Events Produced in pp Collisions at 8 TeV*, CMS-SUS-13-019, CERN-PH-EP-2015-017, *JHEP* **05** (2015) 078, [arXiv:1502.04358].

[104] D. Guadagnoli and C. B. Park, *M_{T2}-reconstructed invisible momenta as spin analizers, and an application to top polarization*, LAPTH-042-13, CERN-PH-TH-2013-190, *JHEP* **01** (2014) 030, [arXiv:1308.2226].

[105] J. A. Nelder and R. Mead, *A Simplex Method for Function Minimization*, *Comput. J.* **7** (1965) 308–313.

[106] *The Oxbridge Kinetics library of packages for performing an M_{T2} calculation*, http://www.hep.phy.cam.ac.uk/∼lester/mt2/.

[107] W. S. Cho, K. Choi, Y. G. Kim, and C. B. Park, *M(T2)-assisted on-shell reconstruction of missing momenta and its application to spin measurement at the LHC*, *Phys. Rev.* **D79** (2009) 031701, [arXiv:0810.4853].

[108] K. Choi, D. Guadagnoli, and C. B. Park, *Reducing combinatorial uncertainties: A new technique based on MT2 variables*, LPT-ORSAY-11-77, IFT-UAM-CSIC-11-64, *JHEP* **11** (2011) 117, [arXiv:1109.2201].

[109] V. Blobel, *An Unfolding Method for High Energy Physics Experiments*, hep-ex/0208022.

[110] O. Behnke, K. Kröninger, T. Schörner-Sadenius, and G. Schott, eds., *Data analysis in high energy physics.* Wiley-VCH, Weinheim, Germany, 2013.

[111] **The ATLAS Collaboration**, G. Choudalakis, *Unfolding in ATLAS*, arXiv:1104.2962.

[112] G. Choudalakis, *Fully Bayesian Unfolding*, arXiv:1201.4612.

[113] T. Salimans, D. P. Kingma, and M. Welling, *Markov Chain Monte Carlo and Variational Inference: Bridging the Gap*, arXiv:1410.6460.

[114] *The pyFBU package for implementing a Fully Bayesian Unfolding in analyses*, https://pypi.python.org/pypi/fbu/0.0.2.

[115] W. Verkerke and D. P. Kirkby, *The RooFit toolkit for data modeling*, CHEP-2003-MOLT007, *eConf* **C0303241** (2003) MOLT007, [physics/0306116].

[116] *The* JetEnergyResolutionProvider *Tool Homepage*, https://twiki.cern.ch/twiki/bin/view/AtlasProtected/JetEnergyResolutionProvider2012.

[117] G. Romeo, A. Schwartzman, R. Piegaia, T. Carli, and R. Teuscher, *Jet Energy Resolution from In-situ Techniques with the ATLAS Detector Using Proton-Proton Collisions at a Center of Mass Energy $\sqrt{s}$ = 7 TeV*, Tech. Rep. ATL-COM-PHYS-2011-240, CERN, Geneva, Mar, 2011, ATL-COM-PHYS-2011-240, https://cds.cern.ch/record/1334193.

[118] **The ATLAS Collaboration**, G. Aad et al., *Jet energy measurement with the ATLAS detector in proton-proton collisions at $\sqrt{s} = 7$ TeV*, CERN-PH-EP-2011-191, *Eur. Phys. J.* **C73** (2013), no. 3 2304, [arXiv:1112.6426].

[119] **The ATLAS Collaboration**, G. Aad et al., *Improved luminosity determination in pp collisions at $\sqrt{s}$ = 7 TeV using the ATLAS detector at the LHC*, CERN-PH-EP-2013-026, *Eur. Phys. J.* **C73** (2013), no. 8 2518, [arXiv:1302.4393].

[120] T. Luminosity Group, *Preliminary Luminosity Determination in pp Collisions at sqrt(s) = 8 TeV using the ATLAS Detector in 2012*, Tech. Rep. ATL-COM-LUM-2012-013, CERN, Geneva, Nov, 2012, ATL-COM-LUM-2012-013, https://cds.cern.ch/record/1494059.

[121] P. Z. Skands, *Tuning Monte Carlo Generators: The Perugia Tunes*, MCNET-10-08, CERN-PH-TH-2010-113, *Phys. Rev.* **D82** (2010) 074018, [arXiv:1005.3457].

[122] H.-L. Lai, M. Guzzi, J. Huston, Z. Li, P. M. Nadolsky, J. Pumplin, and C. P. Yuan, *New parton distributions for collider physics*, MSUHEP-100707, SMU-HEP-10-10, *Phys. Rev.* **D82** (2010) 074024, [arXiv:1007.2241].

[123] S. Forte, L. Garrido, J. I. Latorre, and A. Piccione, *Neural network parametrization of deep inelastic structure functions*, GEF-TH-3-02, RM3-TH-02-01, *JHEP* **05** (2002) 062, [hep-ph/0204232].

[124] *The LHAPDF software package for reweighting PDFs*, http://lhapdf.hepforge.org/.

[125] M. Botje et al., *The PDF4LHC Working Group Interim Recommendations*, arXiv:1101.0538.

[126] *The ATLAS Top Working Group Systematics Recommendations Homepage*, https://twiki.cern.ch/twiki/bin/view/AtlasProtected/TopSystematics2012.

Appendices

Appendix A

SYSTEMATIC ERRORS FOR UNFOLDED MEASUREMENTS

The tables included within this appendix show the unfolded contents, as well as the size of the systematic errors associated with the unfolded measurement for each bin and distribution.

Table A.1: The unfolded results and uncertainties for each bin of the inclusive unfolded measurement in the eμ channel for bins 1-10.

Uncertainty source	Bin 1	Bin 2	Bin 3	Bin 4	Bin 5	Bin 6	Bin 7	Bin 8	Bin 9	Bin 10
JER	23.4	22.47	9.53	17.71	7.7	20.83	13.39	11.74	13.79	10.61
JES	34.47	24.23	30.45	26.55	27.22	29.37	27.30	29.10	35.08	27.28
JVF	1.97	1.05	0.95	4.24	2.14	3.01	5.07	2.35	4.37	4.90
Electron energy scale	11.42	1.30	10.12	6.98	6.21	7.28	8.13	3.76	8.15	6.32
Electron energy resolution	2.78	5.71	0.97	2.19	5.88	4.00	5.05	5.34	4.16	4.19
Muon ID resolution	1.19	0.56	1.95	0.24	1.27	5.87	4.12	3.01	2.90	0.21
Muon spectrometer resolution	1.99	2.18	1.32	0.17	1.42	6.54	0.88	2.40	0.21	1.96
Muon scale	7.00	1.29	2.74	3.32	2.60	4.50	3.05	4.13	4.33	2.40
Lepton scale factors	5.32	2.13	3.14	2.67	3.89	5.19	6.12	8.64	11.65	9.00
B tag scale	19.74	19.46	12.94	15.53	16.57	13.14	15.28	16.08	21.26	15.81
MET resolution	8.13	3.83	5.72	5.02	1.97	1.65	1.41	1.70	1.43	3.68
MET scale	9.92	2.06	3.15	6.62	0.25	3.94	1.10	1.69	1.63	1.49
Luminosity	5.55	3.46	1.97	2.02	2.41	4.24	3.38	1.41	6.14	4.84
Underlying Event	41.97	24.65	22.44	35.11	61.60	65.12	2.70	7.13	86.37	32.53
Colour Reconnection	2.47	11.47	48.04	40.31	52.94	0.71	7.86	27.19	37.38	9.63
ISR/FSR	54.07	124.12	65.92	110.06	53.35	101.18	65.32	92.29	60.19	79.50
Generator	11.52	78.44	1.64	67.25	73.13	8.52	112.54	39.36	14.67	97.44
PDF	88.91	89.02	89.65	89.43	88.80	102.22	99.13	105.04	106.88	123.21
Top mass	24.29	24.38	28.86	31.03	30.96	30.18	26.07	34.70	35.68	39.28
Z normalisation	8.87	3.49	0.21	0.74	5.15	0.54	5.83	2.04	4.75	2.77
Diboson normalisation	4.78	6.95	7.73	4.65	1.60	3.11	1.41	3.80	7.72	7.19
Single Top normalisation	10.55	10.11	5.34	9.24	6.53	5.28	10.40	5.84	3.97	5.12
Single Top alternative sample	0.79	15.87	3.10	8.12	1.52	6.68	13.31	7.65	11.42	7.29
Fake leptons	27.67	19.41	17.47	21.36	13.14	15.61	22.47	24.07	19.52	27.34
Closure	2.59	48.76	13.01	21.50	22.40	15.87	12.15	16.12	26.97	5.12
Total systematic error	130	189	134	176	160	168	173	160	170	190
Statistical error	63	70	60	61	62	61	61	64	67	71
Unfolded result	1371	1527	1410	1542	1582	1561	1562	1676	1805	1963

Table A.2: The unfolded results and uncertainties for each bin of the inclusive unfolded measurement for each bin of the inclusive unfolded measurement in the eμ channel for bins 11-20.

Uncertainty source	Bin 11	Bin 12	Bin 13	Bin 14	Bin 15	Bin 16	Bin 17	Bin 18	Bin 19	Bin 20
JER	17.69	14.44	20.57	11.57	8.98	22.21	12.48	15.54	35.49	15.96
JES	44.69	47.27	42.44	53.82	40.47	57.30	53.28	46.61	73.25	71.41
JVF	1.98	4.53	0.62	1.17	2.85	3.92	4.16	3.41	1.27	5.81
Electron energy scale	7.55	4.96	5.57	6.51	3.84	9.54	8.75	8.14	13.84	6.50
Electron energy resolution	5.73	6.62	6.72	2.19	9.07	4.09	2.38	5.51	6.35	3.86
Muon ID resolution	2.16	4.32	2.62	2.66	4.99	4.92	6.87	4.39	6.66	0.34
Muon spectrometer resolution	3.49	2.23	1.21	0.41	1.18	4.05	0.12	1.00	10.98	7.03
Muon scale	5.70	2.10	3.76	1.63	3.39	4.97	5.68	3.13	8.80	8.13
Lepton scale factors	12.11	10.20	9.78	1.42	8.76	10.97	13.45	17.21	14.36	2.10
B tag scale	25.52	18.93	21.83	21.09	18.48	24.27	17.22	17.17	42.13	26.81
MET resolution	3.87	4.25	4.99	3.26	0.89	0.49	3.75	2.46	8.52	6.50
MET scale	2.68	2.63	3.29	3.00	2.19	2.90	4.61	4.05	6.23	4.39
Luminosity	11.55	7.16	3.58	4.31	6.44	9.26	3.08	4.83	23.47	10.71
Underlying Event	67.64	7.70	8.12	21.86	1.54	11.35	23.09	7.37	60.08	23.16
Colour Reconnection	22.49	16.95	18.64	13.89	18.85	36.64	0.38	30.92	30.32	70.81
ISR/FSR	149.84	87.24	63.29	122.63	87.24	108.44	156.38	82.76	130.43	162.47
Generator	14.07	29.98	99.24	5.44	113.70	32.86	24.17	326.41	24.33	90.15
PDF	122.64	132.00	129.42	139.86	150.10	158.71	165.77	173.48	167.23	166.10
Top mass	47.06	37.46	48.23	50.26	58.97	58.74	61.87	55.48	59.34	61.18
Z normalisation	7.88	6.63	8.93	4.57	5.56	7.06	1.89	4.92	8.66	7.81
Diboson normalisation	3.18	2.92	7.62	4.99	1.70	4.94	2.51	2.72	7.14	8.28
Single Top normalisation	7.49	15.71	10.13	6.28	11.54	12.91	12.93	12.57	20.56	11.76
Single Top alternative sample	3.07	18.14	8.86	20.85	13.71	7.91	16.94	21.29	12.56	18.96
Fake leptons	28.02	35.66	42.80	36.38	36.43	42.79	27.42	39.51	37.40	29.91
Closure	21.67	8.12	26.38	0.17	10.77	40.26	0.15	16.80	4.83	26.79
Total systematic error	223	181	198	208	226	227	249	391	256	283
Statistical error	69	72	76	78	80	81	82	81	86	81
Unfolded result	2040	2111	2217	2409	2447	2591	2736	2679	2903	2917

Table A.3: The unfolded results and uncertainties for each bin of the inclusive unfolded measurement in the combined dileptonic channel in bins 1-10.

Uncertainty source	Bin 1	Bin 2	Bin 3	Bin 4	Bin 5	Bin 6	Bin 7	Bin 8	Bin 9	Bin 10
JER	18.09	24.62	38.74	11.08	12.25	22.31	21.24	12.49	20.33	11.24
JES	54.06	70.03	57.60	44.92	55.55	50.17	66.13	60.70	74.30	65.67
JVF	5.12	8.71	5.37	0.81	1.62	3.10	0.76	3.51	8.12	1.11
Electron energy scale	10.70	16.66	13.56	11.76	14.02	13.89	12.9	16.74	10.45	9.98
Electron energy resolution	5.13	8.11	1.43	2.08	2.63	7.78	4.66	2.43	4.93	5.05
Muon ID resolution	1.73	8.81	5.14	1.01	0.53	1.32	7.36	0.78	5.60	2.14
Muon spectrometer resolution	6.11	0.08	5.72	6.45	2.59	10.29	2.65	3.56	6.12	9.57
Muon scale	7.76	6.77	6.56	4.62	3.39	3.20	7.99	11.51	6.96	3.44
Lepton scale factors	2.33	5.39	2.19	4.90	4.18	5.41	6.32	1.96	2.22	7.90
B tag scale	28.54	37.59	25.04	26.14	25.94	26.75	27.63	26.34	34.25	25.75
MET resolution	4.24	9.76	7.17	7.95	4.42	0.97	6.21	4.98	3.72	11.94
MET scale	2.92	3.62	5.23	3.51	3.05	3.90	8.29	7.15	5.53	4.73
Luminosity	6.40	19.63	11.59	6.76	10.29	13.35	14.65	8.96	11.84	12.54
Underlying Event	65.85	35.59	11.25	84.32	88.24	118.34	12.88	7.82	70.91	42.55
Colour Reconnection	19.31	33.98	81.99	71.74	87.91	16.17	24.44	68.68	65.04	10.10
ISR/FSR	161.47	149.57	109.74	177.98	120.97	152.08	124.72	188.66	93.58	168.78
Generator	130.35	159.33	246.48	159.04	226.51	67.72	104.83	84.65	38.59	129.19
PDF	174.72	169.60	171.39	175.30	185.67	189.71	201.69	210.25	220.42	233.57
Top mass	51.28	49.68	53.69	64.42	56.17	64.06	55.98	74.30	71.48	75.88
Z normalisation	13.23	23.10	16.08	13.31	13.11	15.98	21.01	19.15	19.61	28.78
Diboson normalisation	7.25	12.78	9.09	5.18	5.86	0.81	9.44	6.78	4.08	2.13
Single Top normalisation	6.51	12.73	12.58	12.76	8.43	8.16	14.04	12.22	11.84	15.80
Single Top alternative sample	2.70	18.65	14.82	13.15	3.06	13.92	12.74	16.76	12.23	12.31
Fake leptons	43.97	42.48	33.50	44.14	35.31	39.86	51.21	40.96	43.94	41.72
Closure	3.96	46.13	40.90	30.34	56.07	29.36	21.20	21.60	73.90	1.13
Total systematic error	296	307	348	333	358	299	285	325	298	341
Statistical error	95	103	95	92	97	97	95	98	101	108
Unfolded result	2894	2994	3121	3052	3262	3181	3237	3378	3649	3918

Table A.4: The unfolded results and uncertainties for each bin of the inclusive unfolded measurement in the combined dileptonic channel in bins 11-20.

Uncertainty source	Bin 11	Bin 12	Bin 13	Bin 14	Bin 15	Bin 16	Bin 17	Bin 18	Bin 19	Bin 20
JER	13.99	20.87	25.77	22.20	39.65	18.19	31.35	28.63	43.60	40.96
JES	81.05	93.34	89.12	91.58	113.77	107.43	132.25	134.95	132.11	173.21
JVF	5.98	6.53	2.52	6.42	4.04	1.75	3.42	0.04	5.47	3.70
Electron energy scale	11.08	12.52	10.04	20.09	19.34	13.87	15.93	11.31	20.13	10.73
Electron energy resolution	5.05	4.00	6.84	4.53	6.90	3.80	3.51	4.79	3.94	2.08
Muon ID resolution	2.76	3.85	3.69	8.74	3.24	2.75	1.48	2.49	0.93	0.39
Muon spectrometer resolution	0.94	1.23	3.00	0.33	2.84	2.79	0.72	1.07	3.76	1.00
Muon scale	7.16	5.80	4.92	4.48	4.67	8.84	3.39	6.74	4.98	3.36
Lepton scale factors	5.64	9.27	8.86	2.91	4.78	3.19	3.76	9.21	4.00	1.70
B tag scale	26.21	45.70	31.21	31.31	38.76	40.31	48.30	36.08	51.13	30.16
MET resolution	3.75	20.23	7.85	7.87	1.27	4.29	4.54	11.47	2.97	15.25
MET scale	8.70	7.02	5.67	5.77	3.46	15.77	12.63	9.41	17.82	14.81
Luminosity	13.76	16.19	18.41	15.49	18.79	19.45	17.77	13.57	14.82	18.67
Underlying Event	111.36	77.38	8.93	14.33	2.64	17.22	12.34	31.93	28.84	13.66
Colour Reconnection	2.23	4.29	6.34	57.70	22.24	20.92	0.06	34.96	16.66	92.76
ISR/FSR	270.34	155.90	202.99	228.27	205.76	177.58	263.27	218.71	191.71	255.03
Generator	127.03	23.64	153.77	20.18	129.37	80.77	90.28	505.91	88.86	142.20
PDF	240.95	254.74	272.44	282.21	295.22	309.69	322.72	326.00	334.99	338.10
Top mass	88.06	73.63	85.64	102.48	111.49	120.90	118.09	116.93	118.10	124.88
Z normalisation	17.30	26.57	23.54	23.17	20.84	24.50	21.07	23.52	28.74	27.85
Diboson normalisation	3.32	13.74	11.20	9.33	14.18	8.16	7.45	7.18	3.29	8.38
Single Top normalisation	11.45	18.30	17.91	26.12	25.26	23.81	22.85	20.65	24.45	19.02
Single Top alternative sample	15.28	49.18	8.95	39.40	29.69	30.88	38.46	48.64	35.38	42.90
Fake leptons	53.16	64.26	69.91	62.07	47.99	82.39	56.44	76.90	70.61	63.81
Closure	25.24	54.08	24.46	17.06	36.20	72.69	17.87	39.05	15.42	59.06
Total systematic error	424	352	404	405	426	422	473	677	450	518
Statistical error	111	112	116	120	123	118	128	128	131	126
Unfolded result	4035	4207	4459	4777	4971	5113	5504	5385	5907	5846

Table A.5: The unfolded results and uncertainties for each bin of the inclusive unfolded measurement where $M_{t\bar{t}} \leq 415$ GeV in the eμ channel.

Uncertainty source	Bin 1	Bin 2	Bin 3	Bin 4	Bin 5	Bin 6
JER	174.86	41.69	45.88	78.87	59.86	52.09
JES	111.81	105.30	95.56	91.73	161.38	69.99
JVF	20.26	8.26	0.03	11.20	8.43	7.96
Electron energy scale	32.82	4.07	18.22	15.75	10.55	8.43
Electron energy resolution	32.83	12.29	10.20	8.12	7.11	11.22
Muon ID resolution	20.87	12.22	4.05	1.57	6.95	0.29
Muon spectrometer resolution	18.51	0.98	7.30	20.63	9.21	0.52
Muon scale	34.93	4.37	12.39	4.70	3.95	5.02
Lepton scale factors	20.18	16.21	5.72	18.97	11.98	10.21
B tag scale	97.28	29.35	42.71	55.40	30.75	47.48
MET resolution	36.55	11.80	12.80	5.61	7.90	31.92
MET scale	20.05	16.35	10.85	14.28	23.82	10.69
Luminosity	18.46	14.26	11.99	17.90	6.73	10.50
Underlying Event	74.70	48.22	136.85	96.08	47.87	38.97
Colour Reconnection	53.15	35.64	62.86	50.37	75.01	37.19
ISR/FSR	141.50	120.25	194.90	146.48	160.07	238.96
Generator	195.19	179.85	194.39	184.32	427.23	199.68
PDF	228.95	225.35	138.39	137.12	212.21	99.87
Top Mass	77.42	66.02	91.35	85.33	88.73	90.15
Z normalisation	19.03	3.37	7.41	17.96	3.07	6.27
Diboson normalisation	28.16	11.13	4.81	8.35	4.33	2.03
Single Top normalisation	29.56	5.65	16.63	18.57	15.88	2.86
Single Top alternative sample	22.65	28.21	19.97	13.23	2.62	17.63
Fake leptons	80.27	17.48	28.09	67.22	69.65	10.69
Closure	66.41	99.84	2.50	79.81	126.81	6.64
Total systematic error	445	363	376	353	567	361
Statistical error	225	181	194	208	199	212
Unfolded result	2320	2452	2076	1816	1980	1525

Table A.6: The unfolded results and uncertainties for each bin of the differential unfolded measurement where 415 GeV$< M_{t\bar{t}} \leq$ 505 GeV in the eμ channel.

Uncertainty source	Bin 1	Bin 2	Bin 3	Bin 4	Bin 5	Bin 6
JER	180.46	67.17	66.98	108.11	112.97	105.68
JES	97.45	181.85	187.44	170.52	248.12	162.04
JVF	15.02	7.58	1.44	16.82	5.20	18.63
Electron energy scale	46.14	5.63	9.02	32.25	5.35	14.20
Electron energy resolution	29.30	7.23	7.47	17.58	4.37	6.99
Muon ID resolution	13.60	5.18	9.42	3.69	6.97	0.67
Muon spectrometer resolution	8.92	6.04	19.83	27.48	29.49	6.32
Muon scale	33.59	0.91	14.59	7.71	6.71	7.69
Lepton scale factors	28.50	23.17	8.30	25.41	41.98	10.00
B tag scale	85.67	56.07	55.20	83.60	89.33	76.12
MET resolution	33.39	20.35	7.97	22.96	32.58	39.73
MET scale	15.27	15.01	7.52	22.55	15.91	10.12
Luminosity	15.07	8.76	19.63	28.86	14.39	7.09
Underlying Event	58.68	34.18	256.57	129.73	33.29	69.42
Colour Reconnection	57.86	99.74	102.08	18.26	10.05	30.12
ISR/FSR	175.89	133.44	120.86	128.82	152.93	104.51
Generator	251.71	272.40	54.18	77.59	328.79	115.98
PDF	215.80	232.16	202.43	191.96	358.22	181.03
Top Mass	15.43	19.43	6.45	36.47	30.07	17.29
Z normalisation	18.55	7.91	13.44	31.14	9.51	13.90
Diboson normalisation	28.15	7.78	10.69	6.17	18.05	3.14
Single Top normalisation	19.78	4.73	21.25	20.37	36.45	11.18
Single Top alternative sample	17.23	18.66	16.25	0.46	24.29	8.44
Fake leptons	39.85	31.39	8.79	32.15	75.78	51.54
Closure	3.50	116.94	3.38	116.12	120.04	159.18
Total systematic error	456	463	424	383	609	371
Statistical error	278	251	272	295	275	312
Unfolded result	1626	1501	2193	2891	2405	3053

Table A.7: The unfolded results and uncertainties for each bin of the differential unfolded measurement where $M_{t\bar{t}} > 505$ GeV in the eμ channel.

Uncertainty source	Bin 1	Bin 2	Bin 3	Bin 4	Bin 5	Bin 6
JER	53.44	26.60	50.93	24.91	66.18	42.63
JES	40.16	100.03	63.53	71.40	119.90	87.07
JVF	1.50	4.37	11.16	0.92	11.57	9.28
Electron energy scale	9.33	8.35	15.32	17.67	9.93	6.77
Electron energy resolution	8.40	6.50	9.73	5.96	5.39	6.06
Muon ID resolution	0.27	1.20	10.60	4.96	6.92	5.76
Muon spectrometer resolution	9.16	6.16	16.40	4.69	17.94	11.55
Muon scale	9.21	3.61	9.95	18.28	7.86	6.72
Lepton scale factors	15.21	19.87	11.12	1.32	5.43	7.91
B tag scale	20.49	37.02	56.70	22.84	73.26	53.56
MET resolution	14.66	6.63	8.44	2.35	18.78	29.17
MET scale	6.14	10.08	4.79	10.14	4.70	7.86
Luminosity	3.94	9.74	11.59	10.49	9.69	6.40
Underlying Event	31.99	21.52	25.12	71.93	12.96	71.20
Colour Reconnection	26.57	57.40	30.69	66.19	73.90	33.59
ISR/FSR	75.61	84.37	113.57	74.69	261.05	267.22
Generator	19.82	286.79	139.35	117.96	29.96	343.80
PDF	95.45	106.49	119.39	196.85	290.36	314.83
Top Mass	23.97	23.03	42.16	47.05	101.98	113.84
Z normalisation	5.05	7.22	17.23	4.89	12.17	6.82
Diboson normalisation	7.32	2.36	7.17	2.69	14.03	4.05
Single Top normalisation	5.97	6.83	17.47	4.39	25.81	18.66
Single Top alternative sample	5.88	1.72	3.08	9.96	5.09	9.81
Fake leptons	25.79	14.80	39.33	60.29	37.55	66.67
Closure	24.79	35.03	0.16	34.32	41.58	50.53
Total systematic error	157	346	252	287	446	574
Statistical error	127	131	138	160	168	189
Unfolded result	913	1342	1747	2462	4055	4948

Table A.8: The unfolded results and uncertainties for each bin of the differential unfolded measurement where $M_{t\bar{t}} \leq 415$ GeV in the combined dilepton channel.

Uncertainty source	Bin 1	Bin 2	Bin 3	Bin 4	Bin 5	Bin 6
JER	195.21	99.96	137.69	141.92	193.70	229.95
JES	266.64	314.10	372.35	337.30	357.72	430.96
JVF	4.58	14.27	17.58	12.36	11.46	3.05
Electron energy scale	25.41	30.89	10.20	28.95	40.18	4.33
Electron energy resolution	71.09	50.17	55.94	139.47	42.66	104.92
Muon ID resolution	0.20	4.62	15.15	2.88	32.93	17.01
Muon spectrometer resolution	40.72	16.87	6.15	52.61	7.69	13.88
Muon scale	20.52	18.75	2.75	21.72	23.18	12.03
Lepton scale factors	31.21	35.76	15.29	31.62	39.50	1.32
B tag scale	110.26	81.90	100.38	170.48	133.56	165.49
MET resolution	47.63	12.89	40.41	32.56	61.17	37.68
MET scale	60.17	25.90	27.50	23.29	30.17	22.01
Luminosity	49.46	47.00	127.99	19.73	85.31	233.76
Underlying Event	277.07	130.04	167.52	104.78	75.32	117.21
Colour Reconnection	142.07	193.50	17.67	26.09	56.49	46.43
ISR/FSR	346.19	299.71	362.31	215.13	424.34	286.62
Generator	332.77	65.51	94.11	350.14	742.13	404.42
PDF	401.80	294.08	393.42	274.38	296.44	275.91
Top Mass	154.99	149.58	178.09	167.08	173.25	190.76
Z normalisation	22.92	27.07	34.92	56.54	69.70	62.01
Diboson normalisation	4.14	20.17	26.03	21.86	31.75	10.43
Single Top normalisation	21.51	102.62	90.04	116.36	49.25	95.12
Single Top alternative sample	31.82	28.81	22.92	28.05	29.65	16.49
Fake leptons	62.15	119.37	39.35	106.10	113.34	50.04
Closure	76.74	144.48	85.14	94.50	164.04	129.47
Total systematic error	814	655	752	715	1050	861
Statistical error	308	265	294	295	329	322
Unfolded result	4879	4720	4395	3928	3946	3223

Table A.9: The unfolded results and uncertainties for each bin of the differential unfolded measurement where 415 GeV$< M_{t\bar{t}} \leq$ 505 GeV in the combined dilepton channel.

Uncertainty source	Bin 1	Bin 2	Bin 3	Bin 4	Bin 5	Bin 6
JER	255.10	179.69	217.22	182.88	262.02	272.53
JES	387.77	480.47	639.81	561.40	586.19	709.13
JVF	16.52	27.47	18.30	21.89	18.93	8.75
Electron energy scale	65.50	41.03	14.23	41.39	54.24	3.95
Electron energy resolution	121.50	81.03	86.40	223.89	83.62	165.28
Mu ID scale	6.67	8.12	35.43	5.49	43.19	26.92
Mu ms scale	43.22	10.56	4.52	72.17	2.69	19.83
Muon scale	9.73	23.12	11.14	28.74	23.52	31.21
Lepton scale factors	59.11	26.81	36.72	31.88	34.90	6.77
B tag scale	136.44	121.49	200.29	244.60	171.66	245.44
MET resolution	50.76	10.66	87.50	52.41	70.69	14.14
MET scale	64.60	38.42	64.48	19.10	49.15	14.09
Luminosity	123.95	69.67	209.45	14.01	73.47	347.07
Underlying Event	120.90	148.20	262.02	187.35	88.96	224.23
Colour Reconnection	249.60	306.43	213.79	62.82	155.05	34.03
ISR/FSR	244.70	92.92	140.85	246.61	364.45	68.56
Generator	221.36	404.05	237.87	191.19	768.56	118.80
PDF	426.00	235.77	319.86	389.88	389.13	405.19
Top Mass	10.35	32.01	29.94	54.67	70.99	19.65
Z normalisation	17.80	16.38	35.37	35.04	35.98	44.00
Diboson normalisation	16.92	46.75	67.71	24.18	28.94	31.27
Single Top normalisation	24.72	195.21	209.58	148.19	75.49	82.25
Single Top alternative sample	13.93	40.22	1.10	77.82	13.82	6.85
Fake leptons	11.66	120.05	12.77	35.55	173.55	141.85
Closure	62.02	110.89	18.23	180.81	58.39	175.35
Total systematic error	809	841	953	909	1190	1040
Statistical error	393	363	414	422	447	443
Unfolded result	3365	3100	4045	5055	5272	5759

Table A.10: The unfolded results and uncertainties for each bin of the differential unfolded measurement where $M_{t\bar{t}} > 505$ GeV in the combined dilepton channel.

Uncertainty source	Bin 1	Bin 2	Bin 3	Bin 4	Bin 5	Bin 6
JER	117.10	78.15	119.96	64.51	96.75	100.10
JES	166.95	150.12	222.43	203.34	177.89	254.49
JVF	8.58	0.34	4.61	7.48	9.69	2.20
Electron energy scale	13.31	10.89	37.94	14.82	37.90	25.00
Electron energy resolution	60.39	38.72	26.49	67.70	38.86	83.7
Mu ID scale	7.23	0.39	26.42	9.23	17.22	10.30
Muon spectrometer resolution	3.87	7.60	3.19	34.72	9.01	8.30
Muon scale	13.84	19.75	15.63	11.16	11.40	8.20
Lepton scale factors	12.98	8.00	25.67	21.90	22.38	19.83
B tag scale	49.42	80.04	105.04	100.82	79.18	120.90
MET res	19.80	6.33	38.23	0.93	9.56	11.00
MET scale	27.85	3.19	32.25	15.34	17.20	19.8
Luminosity	35.09	36.36	52.62	2.88	20.56	123.20
Underlying Event	86.06	101.39	11.11	149.24	76.80	201.76
Colour Reconnection	83.47	64.72	113.87	137.83	211.13	50.55
ISR/FSR	27.50	146.37	224.39	234.68	561.70	428.98
Generator	60.42	653.65	400.31	78.67	165.08	624.10
PDF	221.78	205.12	287.83	373.26	526.06	669.46
Top Mass	50.75	55.19	81.71	105.62	191.97	246.40
Z normalisation	11.38	21.81	33.02	24.08	21.48	3.50
Diboson normalisation	14.25	24.89	28.83	12.84	21.49	16.00
Single Top normalisation	13.32	72.60	79.38	66.85	29.77	62.50
Single Top alternative sample	6.87	12.42	0.20	36.03	19.94	21.50
Fake leptons	50.96	87.55	68.84	95.51	90.19	131.60
Closure	2.84	40.01	17.44	82.00	8.63	77.53
Total systematic error	353	750	641	581	877	1130
Statistical error	176	188	211	232	245	263
Unfolded result	1749	2831	3687	5269	7747	10113

Appendix B

MC SAMPLES USED IN ANALYSIS

B.1 MC Samples Used for Analysis

Listed below are the MC samples used in the measurement of spin correlation. These are split by the general type of process that they simulate.

Table B.1: MC simulation samples for processes involving one or more top quarks. This includes the Wt-channel single top background and the signal samples for an SM and an uncorrelated model. The signal sample for the SM correlated model includes both dileptonic and semi-leptonic decays. The Wt-channel single top sample uses the diagram removal (DR) scheme.

Process	Dataset ID	Generator	Events
$t\bar{t} \to l^+l^-\nu\bar{\nu}b\bar{b}/t\bar{t} \to l\nu q\bar{q}b\bar{b}$ (A=1)	117050	*POWHEG+PYTHIA 6.4*	99,930,891
$t\bar{t} \to l^+l^-\nu\bar{\nu}b\bar{b}$ (A=0)	117072	*POWHEG+PYTHIA 6.4*	9,999,991
$tW \to l^+l^-\nu\bar{\nu}b$ (DR)	110141	*POWHEG+PYTHIA 6.4*	999,894

Table B.2: MC simulation samples for diboson backgrounds (WW, WZ and ZZ). Samples have been generated with up to 3 additional partons in the matrix element calculation.

Process	Additional partons	Dataset ID	Generator	Events
$W^+W^- \to ll\nu\nu$	0	107100	*ALPGEN+HERWIG++*	205,100
$W^+W^- \to ll\nu\nu$	1	107101	*ALPGEN+HERWIG++*	125,000
$W^+W^- \to ll\nu\nu$	2	107102	*ALPGEN+HERWIG++*	60,000
$W^+W^- \to ll\nu\nu$	3	107103	*ALPGEN+HERWIG++*	35,000
$WZ \to llqq$	0	107104	*ALPGEN+HERWIG++*	399,999
$WZ \to llqq$	1	107105	*ALPGEN+HERWIG++*	225,999
$WZ \to llqq$	2	107106	*ALPGEN+HERWIG++*	149,998
$WZ \to llqq$	3	107107	*ALPGEN+HERWIG++*	94,899
$ZZ \to llqq$	0	107108	*ALPGEN+HERWIG++*	609,898
$ZZ \to llqq$	1	107109	*ALPGEN+HERWIG++*	290,000
$ZZ \to llqq$	2	107110	*ALPGEN+HERWIG++*	119,900
$ZZ \to llqq$	3	107111	*ALPGEN+HERWIG++*	59,999
$W^+W^- \to l\nu qq$	0	110829	*ALPGEN+HERWIG++*	994,999
$W^+W^- \to l\nu qq$	1	110830	*ALPGEN+HERWIG++*	494,899
$W^+W^- \to l\nu qq$	2	110831	*ALPGEN+HERWIG++*	234,998
$W^+W^- \to l\nu qq$	3	110832	*ALPGEN+HERWIG++*	130,000

Table B.3: MC simulation samples for Z/γ^* + jets backgrounds in the dilepton invariant mass range $10 < M_{ll} \leq 40$ GeV. Samples have been generated with up to 4 additional partons in the matrix element calculation.

Process	Additional partons	Dataset ID	Generator	Events
$Z \to ee$	0	178354	*ALPGEN+PYTHIA 6.4*	5,594,990
$Z \to ee$	1	178355	*ALPGEN+PYTHIA 6.4*	2,229,887
$Z \to ee$	2	178356	*ALPGEN+PYTHIA 6.4*	3,303,492
$Z \to ee$	3	178357	*ALPGEN+PYTHIA 6.4*	231,000
$Z \to ee$	4	178358	*ALPGEN+PYTHIA 6.4*	82,089
$Z \to \mu\mu$	0	178359	*ALPGEN+PYTHIA 6.4*	5,559,153
$Z \to \mu\mu$	1	178360	*ALPGEN+PYTHIA 6.4*	2,114,696
$Z \to \mu\mu$	2	178361	*ALPGEN+PYTHIA 6.4*	3,306,093
$Z \to \mu\mu$	3	178362	*ALPGEN+PYTHIA 6.4*	230,748
$Z \to \mu\mu$	4	178363	*ALPGEN+PYTHIA 6.4*	83,219
$Z \to \tau\tau$	0	178364	*ALPGEN+PYTHIA 6.4*	350,000
$Z \to \tau\tau$	1	178365	*ALPGEN+PYTHIA 6.4*	239,999
$Z \to \tau\tau$	2	178366	*ALPGEN+PYTHIA 6.4*	301,299
$Z \to \tau\tau$	3	178367	*ALPGEN+PYTHIA 6.4*	53,180
$Z \to \tau\tau$	4	178368	*ALPGEN+PYTHIA 6.4*	13,410

Table B.4: MC simulation samples for Z/γ^* + jets backgrounds in the dilepton invariant mass range $40 < M_{ll} \leq 60$ GeV. Samples have been generated with up to 4 additional partons in the matrix element calculation.

Process	Additional partons	Dataset ID	Generator	Events
$Z \to ee$	0	178369	*ALPGEN+PYTHIA 6.4*	4,563,894
$Z \to ee$	1	178370	*ALPGEN+PYTHIA 6.4*	779,998
$Z \to ee$	2	178371	*ALPGEN+PYTHIA 6.4*	769,998
$Z \to ee$	3	178372	*ALPGEN+PYTHIA 6.4*	298,998
$Z \to ee$	4	178373	*ALPGEN+PYTHIA 6.4*	80,749
$Z \to \mu\mu$	0	178374	*ALPGEN+PYTHIA 6.4*	4,799,191
$Z \to \mu\mu$	1	178375	*ALPGEN+PYTHIA 6.4*	779,899
$Z \to \mu\mu$	2	178376	*ALPGEN+PYTHIA 6.4*	769,798
$Z \to \mu\mu$	3	178377	*ALPGEN+PYTHIA 6.4*	299,799
$Z \to \mu\mu$	4	178378	*ALPGEN+PYTHIA 6.4*	80,900
$Z \to \tau\tau$	0	178379	*ALPGEN+PYTHIA 6.4*	4,799,889
$Z \to \tau\tau$	1	178380	*ALPGEN+PYTHIA 6.4*	879,498
$Z \to \tau\tau$	2	178381	*ALPGEN+PYTHIA 6.4*	871,996
$Z \to \tau\tau$	3	178382	*ALPGEN+PYTHIA 6.4*	304,797
$Z \to \tau\tau$	4	178383	*ALPGEN+PYTHIA 6.4*	45,400

Table B.5: MC simulation samples for Z/γ^* + jets backgrounds in the dilepton invariant mass range $60 < M_{ll} \leq 2000$ GeV. Samples have been generated with up to 5 additional partons in the matrix element calculation.

Process	Additional partons	Dataset ID	Generator	Events
$Z \to ee$	0	147105	*ALPGEN+PYTHIA 6.4*	6,298,998
$Z \to ee$	1	147106	*ALPGEN+PYTHIA 6.4*	8,184,476
$Z \to ee$	2	147107	*ALPGEN+PYTHIA 6.4*	389,996
$Z \to ee$	3	147108	*ALPGEN+PYTHIA 6.4*	894,995
$Z \to ee$	4	147109	*ALPGEN+PYTHIA 6.4*	398,597
$Z \to ee$	5	147110	*ALPGEN+PYTHIA 6.4*	229,700
$Z \to \mu\mu$	0	147113	*ALPGEN+PYTHIA 6.4*	6,298,796
$Z \to \mu\mu$	1	147114	*ALPGEN+PYTHIA 6.4*	8,193,384
$Z \to \mu\mu$	2	147115	*ALPGEN+PYTHIA 6.4*	389,999
$Z \to \mu\mu$	3	147116	*ALPGEN+PYTHIA 6.4*	894,799
$Z \to \mu\mu$	4	147117	*ALPGEN+PYTHIA 6.4*	393,200
$Z \to \mu\mu$	5	147118	*ALPGEN+PYTHIA 6.4*	229,200
$Z \to \tau\tau$	0	147121	*ALPGEN+PYTHIA 6.4*	19,392,764
$Z \to \tau\tau$	1	147122	*ALPGEN+PYTHIA 6.4*	10,674,582
$Z \to \tau\tau$	2	147123	*ALPGEN+PYTHIA 6.4*	3,765,893
$Z \to \tau\tau$	3	147124	*ALPGEN+PYTHIA 6.4*	1,096,994
$Z \to \tau\tau$	4	147125	*ALPGEN+PYTHIA 6.4*	398,798
$Z \to \tau\tau$	5	147126	*ALPGEN+PYTHIA 6.4*	229,799

Table B.6: MC simulation samples for Z/γ^* + jets backgrounds produced with additional heavy flavour quark pairs ($b\bar{b}$ and $c\bar{c}$) in the dilepton invariant mass range $60 < M_{ll} \leq 1000$ GeV. Samples have been generated with up to 3 additional partons in the matrix element calculation.

Process	Additional partons	Dataset ID	Generator	Events
$Z \to ee + b\bar{b}$	0	200332	*ALPGEN+PYTHIA 6.4*	1,799,992
$Z \to ee + b\bar{b}$	1	200333	*ALPGEN+PYTHIA 6.4*	999,896
$Z \to ee + b\bar{b}$	2	200334	*ALPGEN+PYTHIA 6.4*	999,594
$Z \to ee + b\bar{b}$	3	200335	*ALPGEN+PYTHIA 6.4*	885,392
$Z \to \mu\mu + b\bar{b}$	0	200340	*ALPGEN+PYTHIA 6.4*	1,799,797
$Z \to \mu\mu + b\bar{b}$	1	200341	*ALPGEN+PYTHIA 6.4*	999,897
$Z \to \mu\mu + b\bar{b}$	2	200342	*ALPGEN+PYTHIA 6.4*	999,395
$Z \to \mu\mu + b\bar{b}$	3	200343	*ALPGEN+PYTHIA 6.4*	885,894
$Z \to \tau\tau + b\bar{b}$	0	200348	*ALPGEN+PYTHIA 6.4*	300,000
$Z \to \tau\tau + b\bar{b}$	1	200349	*ALPGEN+PYTHIA 6.4*	100,000
$Z \to \tau\tau + b\bar{b}$	2	200350	*ALPGEN+PYTHIA 6.4*	50,000
$Z \to \tau\tau + b\bar{b}$	3	200351	*ALPGEN+PYTHIA 6.4*	49,800
$Z \to ee + c\bar{c}$	0	200432	*ALPGEN+PYTHIA 6.4*	284,999
$Z \to ee + c\bar{c}$	1	200433	*ALPGEN+PYTHIA 6.4*	499,500
$Z \to ee + c\bar{c}$	2	200434	*ALPGEN+PYTHIA 6.4*	498,997
$Z \to ee + c\bar{c}$	3	200435	*ALPGEN+PYTHIA 6.4*	443,697
$Z \to \mu\mu + c\bar{c}$	0	200440	*ALPGEN+PYTHIA 6.4*	298,998
$Z \to \mu\mu + c\bar{c}$	1	200441	*ALPGEN+PYTHIA 6.4*	499,799
$Z \to \mu\mu + c\bar{c}$	2	200442	*ALPGEN+PYTHIA 6.4*	499,500
$Z \to \mu\mu + c\bar{c}$	3	200443	*ALPGEN+PYTHIA 6.4*	443,999
$Z \to \tau\tau + c\bar{c}$	0	200448	*ALPGEN+PYTHIA 6.4*	299,000
$Z \to \tau\tau + c\bar{c}$	1	200449	*ALPGEN+PYTHIA 6.4*	199,998
$Z \to \tau\tau + c\bar{c}$	2	200450	*ALPGEN+PYTHIA 6.4*	99,800
$Z \to \tau\tau + c\bar{c}$	3	200451	*ALPGEN+PYTHIA 6.4*	49,400

B.2 MC Samples Used in Systematic Uncertainty Assessment

Listed below are additional MC samples used for assessing certain systematic uncertainties in the analysis. These are split by the systematic uncertainty that they used to assess.

Table B.7: $t\bar{t}$ MC simulation signal samples using an alternative generator (*MC@NLO+ HERWIG++*). Samples include both an SM model (A = 1) and an uncorrelated model (A = 0).

Process	Dataset ID	Generator	Events
$t\bar{t} \to l^+l^-\nu\bar{\nu}b\bar{b}$ (A=1)	110001	*MC@NLO + HERWIG++*	9,984,981
$t\bar{t} \to l^+l^-\nu\bar{\nu}b\bar{b}$ (A=0)	117200	*MC@NLO + HERWIG++*	9,990,989

Table B.8: $t\bar{t}$ MC simulation signal samples with altered amounts of ISR and FSR as discussed in section 7.2.2.7.

Process	Dataset ID	Generator	Events
$t\bar{t} \to l^+l^-\nu\bar{\nu}b\bar{b}/t\bar{t} \to l\nu q\bar{q}b\bar{b}$ (Lower additional radiation)	110407	*POWHEG+PYTHIA 6.4*	14,999,480
$t\bar{t} \to l^+l^-\nu\bar{\nu}b\bar{b}/t\bar{t} \to l\nu q\bar{q}b\bar{b}$ (Higher additional radiation)	110408	*POWHEG+PYTHIA 6.4*	14,990,989

Table B.9: $t\bar{t}$ MC simulation signal samples with altered amounts of colour reconnection (CR) strength and multiple parton interactions (MPI) in the underlying event, as described in section 7.2.2.6.

Process	Dataset ID	Generator	Events
$t\bar{t} \to l^+l^-\nu\bar{\nu}b\bar{b}/t\bar{t} \to l\nu q\bar{q}b\bar{b}$ (Lower CR strength)	117426	*POWHEG+PYTHIA 6.4*	14,998,982
$t\bar{t} \to l^+l^-\nu\bar{\nu}b\bar{b}/t\bar{t} \to l\nu q\bar{q}b\bar{b}$ (Higher number of MPI)	117429	*POWHEG+PYTHIA 6.4*	14,998,988

Table B.10: $t\bar{t}$ MC simulation signal samples with altered top mass values, as described in section 7.2.2.11.

Process	Dataset ID	Generator	Events
$t\bar{t} \to l^+l^-\nu\bar{\nu}b\bar{b}/t\bar{t} \to l\nu q\bar{q}b\bar{b}$ ($m_t = 165$ GeV)	117836	*POWHEG+PYTHIA 6.4*	5,998,267
$t\bar{t} \to l^+l^-\nu\bar{\nu}b\bar{b}/t\bar{t} \to l\nu q\bar{q}b\bar{b}$ ($m_t = 167.5$ GeV)	117838	*POWHEG+PYTHIA 6.4*	5,998,058
$t\bar{t} \to l^+l^-\nu\bar{\nu}b\bar{b}/t\bar{t} \to l\nu q\bar{q}b\bar{b}$ ($m_t = 170$ GeV)	117840	*POWHEG+PYTHIA 6.4*	5,999,470
$t\bar{t} \to l^+l^-\nu\bar{\nu}b\bar{b}/t\bar{t} \to l\nu q\bar{q}b\bar{b}$ ($m_t = 175$ GeV)	117842	*POWHEG+PYTHIA 6.4*	5,998,875
$t\bar{t} \to l^+l^-\nu\bar{\nu}b\bar{b}/t\bar{t} \to l\nu q\bar{q}b\bar{b}$ ($m_t = 177.5$ GeV)	117844	*POWHEG+PYTHIA 6.4*	5,996,769
$t\bar{t} \to l^+l^-\nu\bar{\nu}b\bar{b}/t\bar{t} \to l\nu q\bar{q}b\bar{b}$ ($m_t = 180$ GeV)	117846	*POWHEG+PYTHIA 6.4*	5,998,382

Table B.11: Alternative Wt-channel single top MC simulation sample which uses a diagram subtraction (DS) scheme to remove interference between the Wt-channel and $t\bar{t}$ final states.

Process	Dataset ID	Generator	Events
$tW \to l^+l^-\nu\bar{\nu}b$ (DS)	110143	*POWHEG+PYTHIA 6.4*	999,997